

UNIVERSITY OF CALIFORNIA

Los Angeles

Computational Fluid Dynamics Modeling and Simulation of Steam Methane Reforming  
Reactors and Furnaces

A dissertation submitted in partial satisfaction of the  
requirements for the degree Doctor of Philosophy  
in Chemical Engineering

by

Andres Aguirre

2017



# ABSTRACT OF THE DISSERTATION

Computational Fluid Dynamics Modeling and Simulation of Steam Methane Reforming  
Reactors and Furnaces

by

Andres Aguirre

Doctor of Philosophy in Chemical Engineering

University of California, Los Angeles, 2017

Professor Panagiotis D. Christofides, Chair

This work develops a computational fluid dynamics (CFD) framework for high-fidelity modeling of steam methane reforming reactors and furnaces. Initially, a CFD model for a steam methane reforming reactor is developed and its results are shown to closely match industrial plant data. Subsequently, CFD models of steam methane reforming furnaces are developed for both pilot-scale and full industrial scale furnaces. These furnace CFD models capture the physical dimension, transport phenomena, and core components of a reformer utilized in an industrial plant. Comparison of the CFD models with industrial plant data demonstrates that model predictions are within 1% of industrial measurements for consistent reformer conditions. Finally, to automate the use of the CFD models for reformer furnace balancing, we develop a workflow for reformer simulation on the Smart Manufacturing platform. The workflow is designed to be executed without the need of an expert user, to be deployed in a cloud environment and to be fully or partially used.

The dissertation of Andres Aguirre is approved.

Tsu-Chin Tsao

Dante A. Simonetti

James Davis

Panagiotis D. Christofides, Committee Chair

University of California, Los Angeles

2017



# Contents

<b>1</b>	<b>Introduction</b>	<b>1</b>
1.1	Smart Manufacturing . . . . .	1
1.2	Steam Methane Reforming (SMR) . . . . .	2
1.3	Dissertation Objectives and Structure . . . . .	4
<b>2</b>	<b>CFD modeling for a single reforming tube</b>	<b>6</b>
2.1	Hydrogen production . . . . .	6
2.2	Single Reforming Tube Model . . . . .	8
2.2.1	Industrial Level Geometry . . . . .	8
2.2.2	Tube Geometry and Meshing . . . . .	9
2.2.3	Reforming Reaction Mechanism . . . . .	11
2.2.4	Compressible Gas Flow . . . . .	14
2.2.5	Porous Zone Design . . . . .	15
2.2.6	Reforming Tube Wall Boundary Conditions . . . . .	16
2.2.7	Governing equations . . . . .	19
2.2.8	Simulation Results . . . . .	24
2.3	Feedback control design and closed-loop simulation results . . . . .	28
2.3.1	Open-loop dynamics . . . . .	28
2.3.2	Feedback controller design . . . . .	31
2.3.3	Closed-loop simulation results . . . . .	35
2.3.4	Integrating dynamic optimization and feedback . . . . .	37
2.4	Conclusions . . . . .	45
<b>3</b>	<b>CFD modeling of the pilot scale furnace</b>	<b>46</b>
3.1	Motivation . . . . .	46
3.2	Background . . . . .	47
3.3	Industrial Steam Methane Reformer Geometry . . . . .	52
3.3.1	Geometry of Pilot-scale SMR Unit . . . . .	53
3.3.2	Mesh of Pilot-scale SMR Unit . . . . .	58
3.4	Furnace Chamber Modeling . . . . .	60
3.4.1	Combustion Reaction Kinetic Model and Turbulence Chemistry Model . . . . .	62
3.4.2	Radiation Heat Transfer Modeling . . . . .	68
3.5	Reforming Tube Modeling . . . . .	70

3.5.1	Reforming Reaction Kinetic Model . . . . .	70
3.5.2	Porous Zone Design . . . . .	74
3.6	Equation of State of Pilot-scale SMR Unit . . . . .	75
3.7	Turbulence-Chemistry Interaction Model of Pilot-scale SMR Unit . . . . .	77
3.8	Governing Equation of Pilot-scale SMR Unit . . . . .	80
3.8.1	Furnace Chamber . . . . .	80
3.8.2	Reforming Tube . . . . .	85
3.9	Simulation Results . . . . .	86
3.10	Sample Parametric Study Case . . . . .	90
3.11	Conclusion . . . . .	92
<b>4</b>	<b>CFD of the full-scale furnace</b>	<b>105</b>
4.1	Introduction . . . . .	105
4.2	Industrial-scale Steam Methane Reformer Geometry . . . . .	108
4.3	Industrial-scale Steam Methane Reformer Mesh . . . . .	109
4.4	Furnace Chamber Modeling . . . . .	114
4.4.1	Combustion Reaction Kinetic Model and Turbulence-Chemistry Model . . . . .	114
4.4.2	Radiative Heat Transfer Modeling . . . . .	118
4.5	Reforming Tube Modeling . . . . .	125
4.5.1	Reforming Reaction Kinetic Model . . . . .	125
4.5.2	Porous Zone Design . . . . .	128
4.6	Equation of State and Turbulence-Chemistry Interaction Model . . . . .	130
4.7	Governing Equations of Industrial-scale SMR Unit . . . . .	135
4.7.1	Furnace Chamber . . . . .	137
4.7.2	Reforming Tube . . . . .	141
4.8	Process Simulation . . . . .	143
4.9	Simulation Results . . . . .	145
4.10	Discussion . . . . .	146
4.11	Conclusion . . . . .	163
<b>5</b>	<b>Smart Manufacturing Workflow to Model a Steam Methane Reforming Furnace Using Computational Fluid Dynamics</b>	<b>167</b>
5.1	Introduction . . . . .	167
5.2	Smart Manufacturing . . . . .	168
5.3	Steam Methane Reforming (SMR) . . . . .	169
5.3.1	Steam Methane Reformer . . . . .	171
5.4	Smart Manufacturing Workflow . . . . .	171
5.4.1	Smart Manufacturing Workflow Convergence Criterion . . . . .	175
5.5	Internal Balancing Workflow . . . . .	176
5.5.1	Fluent User-Defined Function (UDF) and Implementation Scheme . . . . .	177
5.5.2	Model Identification . . . . .	178
5.5.3	Valves and flow rate relation . . . . .	183
5.5.4	Model-based furnace-balancing optimizer . . . . .	187
5.5.5	Internal Balancing Workflow Convergence Criterion . . . . .	192

5.6	Results . . . . .	193
5.7	Conclusion . . . . .	198
<b>6</b>	<b>Conclusion</b>	<b>199</b>
	<b>Bibliography</b>	<b>201</b>

# List of Figures

1.1	Steam methane reforming process diagram. <sup>34</sup> . . . . .	3
2.1	Overall view of furnace geometry . . . . .	10
2.2	Two-dimensional axisymmetric reforming tube geometry & mesh structure . .	12
2.3	Outer reforming tube wall temperature along the axial direction . . . . .	18
2.4	Temperature profile from the reforming tube CFD simulation . . . . .	25
2.5	Hydrogen mole fraction profiles . . . . .	26
2.6	Inner and outer wall temperature profiles of the reforming tube . . . . .	27
2.7	Heat flux profile across the reforming tube wall . . . . .	28
2.8	Pre-determined outer reforming tube wall temperature trajectory . . . . .	30
2.9	Expected steady-state value of $\bar{x}_{H_2}^{outlet}$ . . . . .	31
2.10	Propagation of $\bar{x}_{H_2}^{outlet}$ with time under open-loop control . . . . .	32
2.11	Tube wall temperature in the absence of feed disturbance . . . . .	41
2.12	The propagation of $\bar{x}_{H_2}^{outlet}$ with time in the absence of a tube-side feed disturbance under P control and under PI control . . . . .	42
2.13	The outer reforming tube wall temperature profile trajectory in the presence of a disturbance under PI control . . . . .	42
2.14	The propagation of $\bar{x}_{H_2}^{outlet}$ with time in the presence of a disturbance in the tube-side feed under PI control and under open-loop control . . . . .	43
2.15	Dynamic optimization and integral feedback control scheme . . . . .	43
2.16	The outer reforming tube wall temperature profile trajectory in the presence of a tube-side feed disturbance under the dynamic optimization with integral feedback control scheme . . . . .	44
2.17	The propagation of $\bar{x}_{H_2}^{outlet}$ with time in the presence of a tube-side feed disturbance under the dynamic optimization with integral feedback control scheme and under PI control . . . . .	44
3.1	The top view of an industrial-scale, top-fired, co-current reformer with 336 reforming tubes, which are symbolized by 336 smaller circles, and 96 burners, which are denoted by 96 larger circles. The outer-lane burners are shown as the circles on the right and left boundaries of the figure, while the inner-lane burners are shown as slightly larger circles within the figure. . . . .	54

3.2	The front view of an industrial-scale, top-fired, co-current reformer. It is important to note that the refractory wall of the combustion chamber is modeled to be transparent, so that the interior components, which include eight rectangular boxes located on the floor representing the flue gas tunnels, eight frustums of cones located on the ceiling representing the corresponding rows of burners and seven slender rectangles connecting the ceiling and floor representing the corresponding rows of reforming tubes, can be seen. . . . .	55
3.3	CAD geometry of pilot-scale furnace model. . . . .	57
3.4	Isometric view of the hexahedral structured mesh of the pilot-scale reformer. .	61
3.5	Top view of the hexahedral structured mesh of the pilot-scale reformer. This figure demonstrates that the geometries of the outer-lane burners, inner-lane burners and reforming tubes are successfully preserved by means of the O-grid Block function of <i>ANSYS ICEM</i> . . . . .	62
3.6	Isometric view of the hexahedral structured mesh of the inner-lane burner. . .	63
3.7	Side view of the hexahedral structured mesh of a reforming tube. In this figure, the radial direction is scaled up by 20 times for display purposes only. . . . .	64
3.8	Isometric view of the hexahedral structured mesh of a reforming tube. In this figure, the radial direction is scaled up by 20 times for display purposes only. .	64
3.9	Temperature field inside the combustion chamber from the pilot-scale reformer CFD simulation, where the parameters of the tube-side feed, furnace-side feed and combustion chamber refractory walls are consistent with typical plant data. <sup>38</sup>	89
3.10	Methane mole fraction profile inside the combustion chamber from the pilot-scale reformer CFD simulation, where the parameters of the tube-side feed, furnace-side feed and combustion chamber refractory walls are consistent with typical plant data. <sup>38</sup> . . . . .	93
3.11	Hydrogen mole fraction profile inside the combustion chamber from the pilot-scale reformer CFD simulation, where the parameters of the tube-side feed, furnace-side feed and combustion chamber refractory walls are consistent with typical plant data. <sup>38</sup> . . . . .	94
3.12	Carbon monoxide mole fraction profile inside the combustion chamber from the pilot-scale reformer CFD simulation, where the parameters of the tube-side feed, furnace-side feed and combustion chamber refractory walls are consistent with typical plant data. <sup>38</sup> . . . . .	95
3.13	Temperature profile inside the reforming tube from the pilot-scale reformer CFD simulation, where the parameters of the tube-side feed, furnace-side feed and combustion chamber refractory walls are consistent with typical plant data. <sup>38</sup> .	96
3.14	Pressure profile inside the reforming tube from the pilot-scale reformer CFD simulation, where the parameters of the tube-side feed, furnace-side feed and combustion chamber refractory walls are consistent with typical plant data. <sup>38</sup> .	97
3.15	Hydrogen mole fraction profile inside the reforming tube from the pilot-scale reformer CFD simulation, where the parameters of the tube-side feed, furnace-side feed and combustion chamber refractory walls are consistent with typical plant data. <sup>38</sup> . . . . .	98

3.16	Methane mole fraction inside the reforming tube from the pilot-scale reformer CFD simulation, where the parameters of the tube-side feed, furnace-side feed and combustion chamber refractory walls are consistent with typical plant data. <sup>38</sup>	99
3.17	Superheated steam mole fraction profile inside the reforming tube from the pilot-scale reformer CFD simulation, where the parameters of the tube-side feed, furnace-side feed and combustion chamber refractory walls are consistent with typical plant data. <sup>38</sup>	100
3.18	Temperature profiles of flue gas in the vicinity of the reforming tube (solid line), of the outer reforming tube wall (dashed line) and of the inner reforming tube wall (dotted line) from the pilot-scale reformer CFD simulation, where the parameters of tube-side feed, furnace-side feed and combustion chamber refractory walls are consistent with typical plant data. <sup>38</sup>	101
3.19	Heat flux profile (solid line), and average heat flux (dashed line) across the reforming tube wall from the pilot-scale reformer CFD simulation, where the parameters of the tube-side feed, furnace-side feed and combustion chamber refractory walls are consistent with typical plant data. <sup>38</sup>	102
3.20	Flame length inside the combustion chamber	103
3.21	Temperature profiles of the flue gas in the vicinity of the reforming tube (solid line), of the outer reforming tube wall (dashed line) and of the inner reforming tube wall (dotted line) from the pilot-scale reformer CFD simulation, where the furnace-side feed mass flow rate is increased by 20% from its nominal value and all other parameters of the tube-side feed, furnace-side feed and combustion chamber refractory walls are consistent with typical plant data. <sup>38</sup>	104
4.1	The isometric view of an industrial-scale, top-fired, co-current reformer with 336 reforming tubes, which are symbolized by 336 smaller circles, 96 burners, which are denoted by 96 larger circles, and 8 flue gas tunnels, which are represented by 8 rectangular intrusions. The outer-lane burners are burners on the right and left boundaries of the figure, while the inner-lane burners are slightly larger than the outer-lane burners in the figure.	109
4.2	Isometric view of the hexahedral structured mesh of the outer-lane burner (a), inner-lane burner (b) and reforming tube (c). This figure demonstrates that the meshes of both the inner-lane and outer-lane burners, as well as the mesh of the reforming tubes, created by the O-grid Block function of ANSYS ICEM have the exact geometries of the corresponding components. In Fig. 4.2(c), the radial direction of the reforming tube is scaled up by 20 times for display purposes.	113
4.3	A sample of the top view of the hexahedral structured mesh of the reformer, where a row of reforming tubes is adjacent to two inner-lane burners. In Fig. 4.3, the reforming tube inlets and burner inlets are assigned with different color for display purposes.	113
4.4	A sample of the vertical cross section of the hexahedral structured mesh of the reformer.	114
4.5	Step-by-step converging strategy	146
4.6	The frontal and lateral cross-sectional plane of the combustion chamber.	147

4.7	Lateral (left) and frontal (right) furnace-side temperature contour maps predicted by the reformer CFD simulation in which the parameters of the tube-side feed, furnace-side feed and combustion chamber refractory walls are consistent with typical plant data. <sup>38</sup>	147
4.8	Lateral (left) and frontal (right) contour maps of energy released by the furnace-side oxidation predicted by the reformer CFD simulation in which the parameters of the tube-side feed, furnace-side feed and combustion chamber refractory walls are consistent with typical plant data. <sup>38</sup>	148
4.9	Lateral (left) and frontal (right) contour maps of the furnace-side velocity magnitude predicted by the reformer CFD simulation in which the parameters of the tube-side feed, furnace-side feed and combustion chamber refractory walls are consistent with typical plant data. <sup>38</sup>	148
4.10	Lateral (left) and frontal (right) methane mole fraction contour maps inside the combustion chamber predicted by the reformer CFD simulation in which the parameters of the tube-side feed, furnace-side feed and combustion chamber refractory walls are consistent with typical plant data. <sup>38</sup>	149
4.11	Lateral (left) and frontal (right) hydrogen mole fraction contour maps inside the combustion chamber predicted by the reformer CFD simulation in which the parameters of the tube-side feed, furnace-side feed and combustion chamber refractory walls are consistent with typical plant data. <sup>38</sup>	149
4.12	Lateral (left) and frontal (right) carbon monoxide mole fraction contour maps inside the combustion chamber predicted by the reformer CFD simulation in which the parameters of the tube-side feed, furnace-side feed and combustion chamber refractory walls are consistent with typical plant data. <sup>38</sup>	150
4.13	Lateral (left) and frontal (right) oxygen mole fraction contour maps inside the combustion chamber predicted by the reformer CFD simulation in which the parameters of the tube-side feed, furnace-side feed and combustion chamber refractory walls are consistent with typical plant data. <sup>38</sup>	150
4.14	Tube-side pressure contour map predicted by the reformer CFD simulation in which the parameters of the tube-side feed, furnace-side feed and combustion chamber refractory walls are consistent with typical plant data. <sup>38</sup>	151
4.15	Radial-weighted average tube-side compositions predicted by the reformer CFD simulation in which the parameters of the tube-side feed, furnace-side feed and combustion chamber refractory walls are consistent with typical plant data. <sup>38</sup>	151
4.16	Average temperature profiles of the furnace-side mixture (solid line), outer reforming tube wall (dashed line), inner reforming tube wall (dash-dotted line) and tube-side mixture (dotted line) predicted by the reformer CFD simulation in which the parameters of the tube-side feed, furnace-side feed and combustion chamber refractory walls are consistent with typical plant data. <sup>38</sup>	152
4.17	Radial-weighted average tube-side compositions along the reforming tubes produced by the reformer CFD model (black) versus those derived from typical plant data of the SMR process (red). <sup>38</sup>	160
4.18	Average temperature profiles of the furnace-side mixture and outer reforming tube wall produced by the reformer CFD model (black) versus those derived from typical plant data of the SMR process (red). <sup>39</sup>	160

4.19	Description of the layout of the outer reforming tube wall temperature distribution, in which each grid contains an average outer reforming tube wall temperature of the corresponding reforming tube recorded by a system of IR cameras situated around the reformer. . . . .	161
4.20	Distribution of the percent difference in the outer reforming tube wall temperature between the reformer CFD data and the plant data provided by the third party. The percent difference of each reforming tube is computed by the ratio of the deviation of the CFD data from the corresponding plant data to the corresponding plant data. . . . .	162
5.1	The isometric view of an industrial-scale, top-fired, co-current reformer with 336 reforming tubes, which are represented by 336 slender cylinders, 96 burners, which are represented by 96 frustum cones, and 8 flue-gas tunnels, which are represented by 8 rectangular intrusions. . . . .	172
5.2	Smart Manufacturing workflow . . . . .	172
5.3	Kepler workflow and elements . . . . .	174
5.4	Inner workflow schematic . . . . .	176
5.5	The velocity vector field of the furnace-side flow pattern in the vicinity of the 4 <sup>th</sup> burner row in the reformer is constructed from the reformer CFD data. <sup>64</sup> The outlets of the reformer are situated at the bottom right corner and are placed in the direction of the velocity vectors inside the flue-gas tunnels. . . . .	183
5.6	The temperature contour map of the 4 <sup>th</sup> flue-gas tunnel, which is situated directly under the 4 <sup>th</sup> burner row in the reformer, is shown. This contour map is created from the reformer CFD data in. <sup>64</sup> In Fig. 5.6, the outlets of the reformer are situated at the bottom right corner. . . . .	184
5.7	A representation of a burner heating zone which is created by the highlighted burner in red. The burner heating zones are displayed by a blue cylindrical volume (where the reforming tubes are heated via thermal radiation from the furnace-side flow) and a green rectangular volume (where the reforming tubes are heated via thermal radiation from the neighboring flue-gas tunnels). It is assumed that only the reforming tubes located within the burner heating zones have the outer wall temperature values dependent on the FSF flow rate of the burner. . . . .	185
5.8	Evolution of the OTWT standard deviation at 6.5 m from the top and its percent change going from trial 3 to 4. . . . .	194
5.9	Standard deviation (red-gold) and percent reduction of the standard deviation (grey) during the internal balancing workflow execution. . . . .	194
5.10	Tube outer tube wall temperature measured at the end of trials . . . . .	196
5.11	Temperature distribution inside the furnace for the OTWT. . . . .	197



## ACKNOWLEDGEMENTS

First, I would like to express my gratitude to my advisor, Professor Panagiotis D. Christofides, for his unwavering support throughout my doctoral work. I was very fortunate to have him as my advisor. I couldn't have imagined a better advisor; his mentoring style finds a way to adjust to all of his student's personalities including mine. I would also like to thank Vice Provost and Professor James Davis, Professor Tsu-Chin Tsao and Professor Dante Simonetti for serving on my doctoral committee.

Also, I am grateful to my mother Matilde, my sister, Carolina, my brother, Oswaldo, grandmother, Carmen, and my girlfriend, Serena for all their support, encouragement and love.

In addition, I would like to thank Prakashan Korambath, Liangfeng Lao, Anh Tran, Yangyao Ding and Yufan Cheng with whom I worked closely. Also I would like to thank all my colleagues, visiting scholars, and friends at UCLA. Moreover, my gratitude to Helen Durand, Maddie Pont and Anh Tran for proofreading my thesis.

I gratefully acknowledge the funding from the Department of Energy (DoE) and a Eugene Cota-Robles Fellowship from UCLA's Graduate Division.

Chapter 2 is a version of: Lao, L., A. Aguirre, A. Tran, Z. Wu, H. Durand and P. D. Christofides, CFD Modeling and Control of a Steam Methane Reforming Reactor. *Chem. Eng. Sci.*, **148**, 78-92, 2016.

Chapter 3 is a version of: Aguirre, A., A. Tran, L. Lao, H. Durand, M. Crose and P. D. Christofides, CFD Modeling of a Pilot-Scale Steam Methane Reforming Furnace. *Advances in Energy Systems Engineering*, G. Kopanos, P. Liu and M. Georgiadis (Eds.), Chapter 4, 75-117, Springer, Switzerland, 2017.

Chapter 4 is a version of: Tran, A., A. Aguirre, H. Durand, M. Crose and P. D. Christofides, CFD Modeling of an Industrial-scale Steam Methane Reforming Furnace. *Chemical Engineering Science.*, **171**, 576-598, 2017.

Chapter 5 is a version of: Tran, A., A. Aguirre, H. Durand, M. Crose and P. D. Christofides, Temperature balancing in steam methane reforming furnace via an integrated CFD/ optimization approach. *Computers & Chemical Engineering*, **104**, 185-200, 2017.

## VITA

2009–2012	Bachelor of Science, Chemical Engineering Department of Chemical Engineering and Material Science University of California, Irvine
2013–2014 & 2016–2017	Eugene V. Cota-Robles Fellowship Teaching Assistant Fellow Department of Chemical and Biomolecular Engineering University of California, Los Angeles
2013–2017	Ph.D., Chemical Engineering Department of Chemical and Biomolecular Engineering University of California, Los Angeles

## Publications

1. Tran, A., **A. Aguirre**, H. Durand, M. Crose and P. D. Christofides, “CFD Modeling of an Industrial-Scale Steam Methane Reforming Furnace,” *Chemical Engineering Science*, **171**, 576-598, 2017.
2. Wu, Z., **A. Aguirre**, A. Tran, H. Durand, D. Ni and P. D. Christofides, “Model Predictive Control of a Steam Methane Reforming Reactor Described by a Computational Fluid Dynamics Model,” *Industrial & Engineering Chemistry Research*, **56**, 6002-6011, 2017.
3. Tran, A., **A. Aguirre**, M. Crose, H. Durand and P. D. Christofides, “Temperature Balancing in Steam Methane Reforming Furnace via an Integrated CFD/Data-Based Optimization Approach,” *Computers & Chemical Engineering*, **104**, 185-200, 2017.

4. Lao, L., **A. Aguirre**, A. Tran, Z. Wu, H. Durand and P. D. Christofides, “CFD Modeling and Control of a Steam Methane Reforming Reactor,” *Chemical Engineering Science*, **148**, 78-92, 2016.
5. Tran, A., **A. Aguirre**, H. Durand, M. Crose and P. D. Christofides, “Steam Methane Reforming Furnace Temperature Balancing via CFD Model-Based Optimization,” *Proceedings of the American Control Conference*, 4165-4170, Seattle, Washington, 2017.
6. **Aguirre, A.**, A. Tran, L. Lao, H. Durand, M. Crose and P. D. Christofides, “CFD Modeling of a Pilot-Scale Steam Methane Reforming Furnace,” *Advances in Energy Systems Engineering*, G. Kopanos, P. Liu and M. Georgiadis (Eds.), Chapter 4, 75-117, Springer, Switzerland, 2017.

# Chapter 1

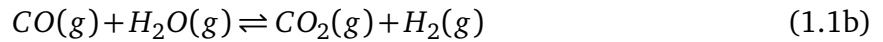
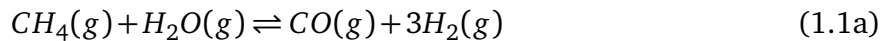
## Introduction

### 1.1 Smart Manufacturing

Smart manufacturing (SM) is the practice of generating and applying manufacturing intelligence to the manufacturing life cycle and supply chain enterprise, allowing for an increase of operational freedom. Manufacturing intelligence (MI) includes two components: (1) the intensified and pervasive application of networked information based technologies, and (2) the extensive use of data analysis, modeling and optimization. The application of manufacturing intelligence requires the real-time understanding, reasoning, planning, and management of all aspects of the manufacturing process. Smart Manufacturing<sup>11,12</sup> aims to address manufacturing needs driven by competitive markets that are influenced by legislation and social pressures. Manufacturing needs include producing the best value for customers in a short and flexible time frame, maintaining a flexible and agile production, while decreasing maintenance, incidents, and operational cost. Davis *et al.*<sup>11</sup> refer to manufacturing test beds as a concept to classify and identify industrial needs, proposing four potential test bed scenarios in which smart manufacturing can be implemented using the Smart Manufacturing Platform (SM Platform).

## 1.2 Steam Methane Reforming (SMR)

The steam methane reforming (SMR) process, which produces bulk hydrogen gas from methane through catalytic reactions Eqns.1.1a-1.1c, is the most common commercial method of industrial hydrogen production. A general industrial-scale SMR process can be described by the schematic in Fig. 1.1. The steam methane reformer (for simplicity, it is denoted as “reformer” in the following text) is the core unit in a SMR process and is composed of a process (tube) side and a furnace side, which interact via heat exchange through the walls of reforming reactors (for simplicity, they are denoted as the “reforming tubes”). In the furnace side, combustion of the furnace-side feed, usually a mixture of methane, hydrogen, carbon dioxide, carbon monoxide and air, heats the reforming tubes via radiative heat exchange; inside the reforming tubes, catalytic reactions take place, converting steam and methane into hydrogen and carbon oxides (including  $CO$  and  $CO_2$ ). In addition to reforming tubes a traditional top-fired, co-current furnace usually includes top burners that are fed with the furnace-side feed, refractory walls that envelop the combustion products, flue gas tunnels that transport the flue gas out of the reformer, and reforming tubes.



For the last 50 years, extensive work has been performed on the development of first principles reformer models. The mathematical modeling methodology of the complete reformer was first proposed and developed in the 1960s.<sup>46</sup> An increased understanding of both physical and chemical phenomena inside the reformer, led to the development of more comprehensive mathematical models which consider more detailed and precise radiation mechanisms, com-

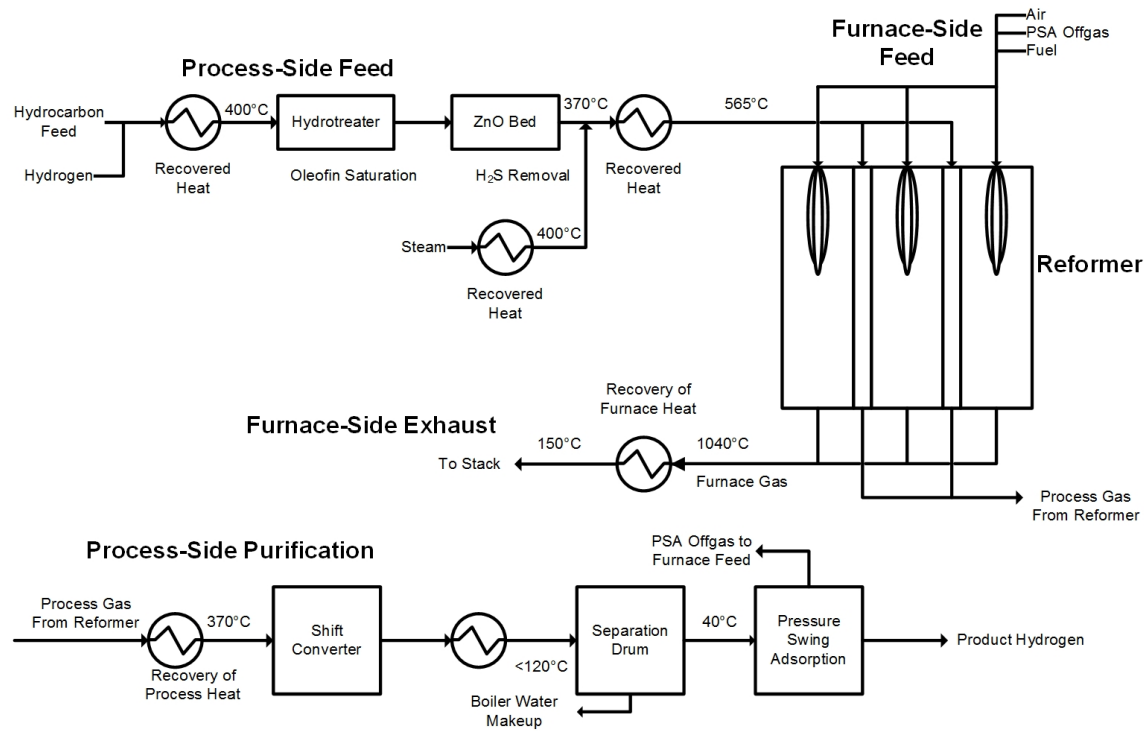


Figure 1.1: Steam methane reforming process diagram.<sup>34</sup>

bustion models, flue gas flow patterns, SMR reaction kinetics and packed bed reactor models.<sup>38</sup> However, solving these complete reformer models is computationally expensive due to the increasing complexity of the fundamental nonlinear partial differential equations describing reformer physicochemical phenomena. Additionally, large reformers with complicated geometry give rise to various boundary conditions that make mathematical modeling very difficult<sup>38</sup>

On the other hand, with the dramatic increase of computing power, computational fluid dynamics (CFD) modeling is able to combine physical and chemical models with detailed representations of the reformer geometry and has therefore become an increasingly important platform for reformer modeling and design. When compared with first-principles modeling, CFD is a modeling technique with powerful visualization capabilities to deal with various geometry characteristics and boundary conditions. Moreover, CFD modeling provides flexibility to modify design parameters without the expense of hardware changes which brings substantial economic and time savings.<sup>67</sup> CFD technology has been successful in carrying out the sim-

ulation of industrial furnaces<sup>5,24,50,62</sup> and SMR tube reactors, i.e., reforming tubes modeled as packed-bed reactors.<sup>8,10,15,23</sup> Specifically, recent attempts to use CFD modeling to characterize the physico-chemical phenomena of transport and reaction processes inside reforming tubes have been done exclusively on a microscopic or bench-scale level, e.g., the effect of catalyst orientation on catalytic performance is investigated with a CFD model of a single catalyst particle,<sup>15</sup> and the validation of CFD simulation results to experimental data is performed with a CFD model of a bench-scale reforming tube.<sup>8</sup> In the present work, we focus on an industrial-scale reforming tube, i.e, the external diameter, internal diameter and exposed length of the reforming tube are 14.6 cm, 12.6 cm, 12.5 m respectively.

### 1.3 Dissertation Objectives and Structure

Motivated by future manufacturing needs addressed by smart manufacturing these works was set to develop a workflow and Computational Fluid Dynamics (CFD) of an operational steam methane reformer for the SM platform development. The goals of chapters 2-4, which focus on the development of the steam methane reforming process are twofold: to accurately capture the transport phenomena relevant to the process, and to maintain an adequate simulation size with a computational time reasonable for our design target to run on the Hoffman2.

Chapter 2 presented a two-dimensional axisymmetric model of a single reforming tube with a uniform temperature profile. To ensure the validity of this limited-scale model, the output was compared to expected results based on global intrinsic kinetics models of the steam methane reforming process in *J. Xu and G. F. Froment*.<sup>70</sup> Upon confirmation of the accuracy of the model, we increased both its scale and complexity in Chapter 3; the model comprised four three-dimensional reforming tubes and included the effects of combustion from three burners two-outer lane and one inner-lane. This more sophisticated model lent insight into the complexities associated with the combination of two computational domains as well as the implementation



of both combustion and steam methane reforming in a single model. In Chapter 4, the scale of the model was increased to encompass the full Sela-Linde GmbH steam methane reformer. For effective use of this model, a convergence strategy was implemented that addressed issues of instability in the early steps of the simulation and significantly enhanced model performance. Chapter 5 presents a workflow designed for use by a non-expert user. To balance the furnace temperature, such a user can simply visit our Smart Manufacturing (SM) Platform resource, choose an appropriate input resource, and run the model.

## Chapter 2

# CFD modeling for a single reforming tube

### 2.1 Hydrogen production

The production rate of hydrogen fuel from a typical SMR process depends strongly on the operating temperature of the furnace, in which the aforementioned reforming tubes are encapsulated, and more specifically the outer reforming tube wall temperature. Because of the endothermic nature of SMR reactions, a higher outer reforming tube wall temperature theoretically results in a higher production rate of hydrogen fuel. However, operating the reforming tubes at excessively high temperature can lead to disastrous consequences and significant capital loss. Particularly, the formation of carbon on the catalyst surface and on the inner reforming tube surface prevents the reactants from entering the catalyst active sites and reduces the rate of heat transfer to the tube-side gas mixture, respectively, which hinders reaction progress and hydrogen production. Additionally, the expected lifetime of reforming tubes is extremely sensitive to changes in operating temperatures, i.e., an increase in tube wall temperature of 20 K can reduce the tube lifetime by half<sup>38,54</sup>. Moreover, reforming tubes are one of the most expensive plant components, as they account for approximately 10% of the capital cost of an entire hydrogen plant,<sup>38</sup> and the total replacement of a typical industrial-scale reformer is ex-

pected to cost 5–8 million USD.<sup>54</sup> Consequently, the outer reforming tube wall temperature is required to be closely monitored and kept slightly below the design tube wall temperature in industrial standard operation in order to eliminate the potential stress-to-rupture of tube materials.<sup>9</sup> Through CFD simulation, critical issues discussed above can be detected and predicted, and corresponding changes can be applied to improve the reforming tube design and operating parameters.

Motivated by the above considerations, we initially develop a CFD model of an industrial-scale reforming tube in ANSYS Fluent with realistic tube geometry characteristics to simulate the transport and reaction phenomena with a detailed representation of the catalyst packing inside the reforming tube. Next, we utilize publicly available SMR plant data to construct the proper boundary conditions for the reforming tube inlet, the reforming tube outlet and the outer reforming tube wall, so that the simulation results and the available industrial plant data are consistent.<sup>38</sup> Due to the high Reynolds number of the tube-side gas mixture, significant pressure gradients across the reforming tube and well-acknowledged radial gradients near the reforming tube inlet, the standard  $k-\epsilon$  turbulence model with enhanced wall treatment is implemented. Furthermore, an intrinsic SMR reaction kinetic mechanism,<sup>70</sup> widely accepted in academia and industry, is used to derive the chemical conversion rate equations, which account for the effect of internal and external diffusion limitations on the observed rates as well as for the presence of the catalyst particles inside the reforming tube. Subsequently, to adjust the hydrogen production of the reforming tube in real-time, we propose the design and implementation of feedback control schemes into the CFD model. Specifically, the manipulated input and controlled output are chosen as the outer reforming tube wall temperature and the area-weighted average hydrogen mole fraction measured at the reforming tube outlet ( $\bar{x}_{H_2}^{outlet}$ ) respectively, and the objective is to drive  $\bar{x}_{H_2}^{outlet}$  to the desired set-point ( $\bar{x}_{H_2}^{set}$ ) under the influence of a tube-side feed disturbance. On the problem of feedback control, firstly, a proportional (P) control scheme and a proportional-integral (PI) control scheme generating the outer reforming tube wall temperature trajectory based on the desired  $\bar{x}_{H_2}^{set}$  are designed to realize the closed-

loop CFD simulation. Finally, motivated by industrial concerns, we also design a feedback control scheme that combines dynamic optimization and integral feedback control. The control performance of these three control schemes is evaluated with respect to tracking the set-point, improving the speed of the closed-loop responses and compensating for the effect of the tube-side feed disturbance on  $\bar{x}_{H_2}^{outlet}$ .

## 2.2 Single Reforming Tube Model

### 2.2.1 Industrial Level Geometry

This work focuses on modeling one of the 336 reforming tubes in an industrial-scale top-fired, co-current reformer designed by Sela Fluid Processing Corporation (Fig. 2.1). The furnace of this reformer contains seven rows of forty-eight reforming tubes whose external diameter, internal diameter and exposed length are 14.6 cm, 12.6 cm, 12.5 m respectively. Each reforming tube is tightly packed with specially designed nickel oxide over alpha alumina support (i.e.,  $Ni-\alpha Al_2O$ ) catalyst particles, which not only facilitate the formation of hydrogen fuel from steam and methane through the highly endothermic SMR reactions, but also play a role as an intermediate medium to enhance the rate of heat transfer to the tube-side gas mixture. These rows of tubes are separated by eight rows of twelve burners that are fed with the furnace-side gas composed of three parts, i.e., natural gas, combustion air ( $Ar$ ,  $N_2$  and  $O_2$ ) and tail gas ( $CO$  and  $H_2$ ). Based on the composition of a typical furnace-side gas that is given in Table 2.1, the combustion is a fuel lean process so that the fuel can be completely combusted over a flame length of 4.5-6 m releasing the thermal energy needed to drive the highly endothermic SMR reactions.<sup>38</sup> The thermal energy released by the combustion of furnace fuel is transferred to the reforming tubes predominantly by radiation inside the high-temperature furnace chamber. At the bottom of the furnace, the rows of tubes are separated by the rectangular intrusions known as flue gas tunnels or coffin boxes. The flue gas tunnels extend from the front to the

back of the furnace with a height of 2.86 m from the floor and allow the furnace flue gas to exit the furnace. Thirty-five extraction ports are distributed in a row along the sides of each flue gas tunnel as shown in Fig. 2.1. The furnace flue gas enters the tunnels from the furnace chamber through the extraction ports and then exits the furnace through the front openings of the coffin boxes. It is worth noting that the dynamics of all aforementioned components are tightly coupled inside the furnace during operation. Nonetheless, the scope of this study only aims to develop a CFD model with realistic dimensions, geometry and characteristics of an industrial-scale steam methane reforming tube, and in this regard, we develop and evaluate all essential simulation settings of the reforming tube model to accomplish the modeling objective in the following sections.

Table 2.1: Furnace-side inlet operating conditions.

Pressure (kPa)	132.4
Temperature (K)	524
Flow rate ( $\text{kg s}^{-1}$ )	1.08
$x_{CH_4}$	0.0517
$x_{H_2O}$	0.0306
$x_{CO}$	0.0211
$x_{H_2}$	0.0540
$x_{O_2}$	0.1530
$x_{Ar}$	0.0077
$x_{N_2}$	0.5793

## 2.2.2 Tube Geometry and Meshing

Mesh quality is the most critical issue for accurate and successful CFD modeling, i.e., a low quality mesh requires the most robust CFD solver and significantly greater computing resources to determine a converged solution. Due to the axisymmetric geometry property of the reforming tube as shown in Fig. 2.2(a), a two-dimensional 2D axisymmetric reforming tube geometry and its corresponding mesh structure were employed. The 2D axisymmetric reforming tube mesh, which is shown in Fig. 2.2(b), was constructed in the meshing software ICEM-CFD. The 2D axisymmetric reforming tube mesh only contains 24690 quadrilateral cells, with a 100%

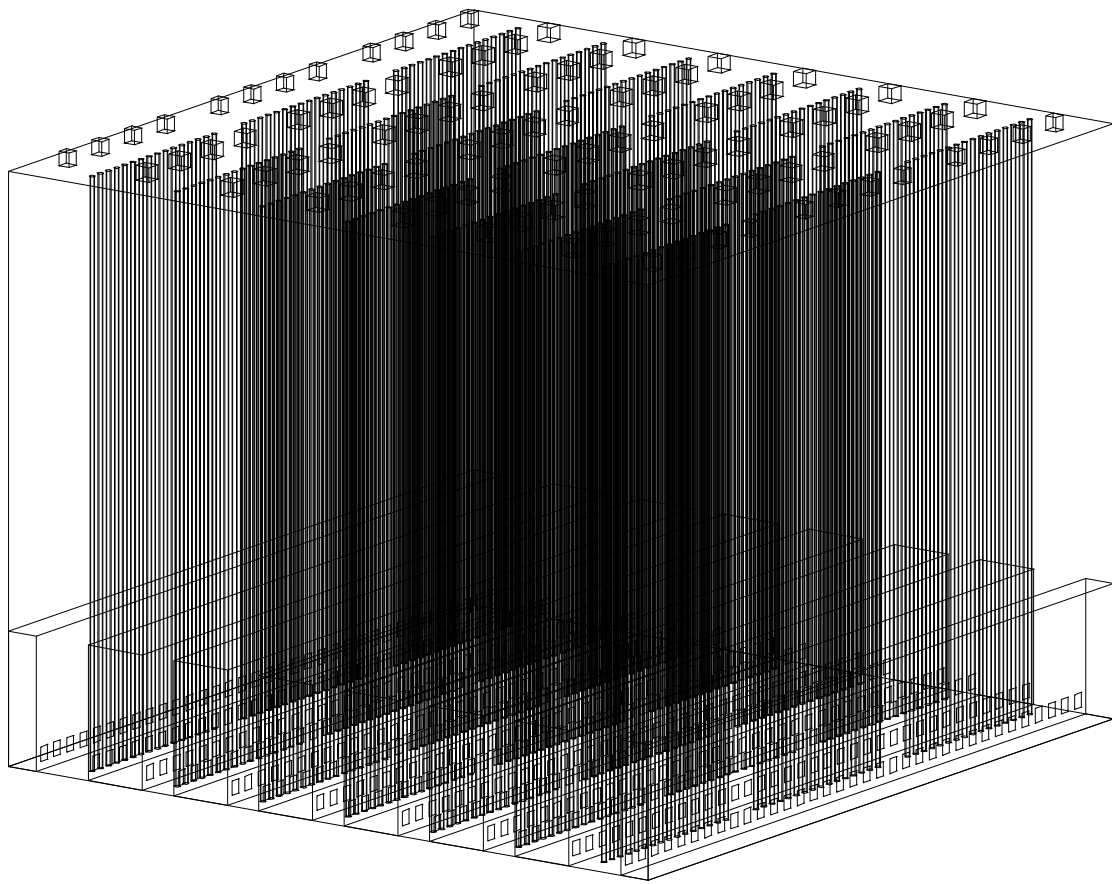


Figure 2.1: Overall view of furnace geometry.

orthogonal quality. Also, the CFD simulation of the single reforming tube only performs calculations for half of the tube mesh considering its 2D axisymmetric properties. Consequently, this 2D axisymmetric reforming tube mesh is much more computationally efficient than is a three-dimensional reforming tube CFD model.

For this reforming tube CFD model, boundary layer design is very critical to the modeling of the heat convection from the inner reforming tube wall to the tube-side gas mixture and the heat conduction from the inner reforming tube wall to the catalyst particles. To calculate the first node height from the inner reforming tube wall for the boundary layer design, NASA's Viscous Grid Spacing Calculator<sup>2</sup> is adopted based on a suitable  $Y^+$  value.<sup>26</sup> For this specific single reforming tube geometry, five nodes are applied in the boundary layer at the inner reforming tube wall as requested by the two-equation  $k-\epsilon$  turbulence model with the enhanced wall treatment function (which will be discussed below). The first node height is  $8.26 \times 10^{-4}$  m, and the node spacing ratio in the boundary layer is 6 : 5. The detailed mesh structure for the boundary layer design is demonstrated in Fig. 2.2(b). We note here that NASA's Viscous Grid Spacing Calculator<sup>2</sup> uses fixed viscosity, pressure and temperature values for the fluid properties which may not be suitable for most SMR calculations. Through a decompiling of the calculator, a revised algorithm based on the original calculator is developed for our specific inlet conditions of the tube-side gas mixture.

### 2.2.3 Reforming Reaction Mechanism

The conversion rates of reactants, i.e., steam and methane, into products, i.e., hydrogen fuel, and the direction of the reforming reactions and the water-gas shift reaction under different conditions (reactant concentration, temperature and pressure) must be accurately accounted for by using a reaction kinetics model. In a reforming tube, the reforming reactions and water-gas shift reaction occur at the catalyst active sites. In particular, reactants need to diffuse from the bulk tube-side gas mixture to the surface of the catalyst particle and then into the

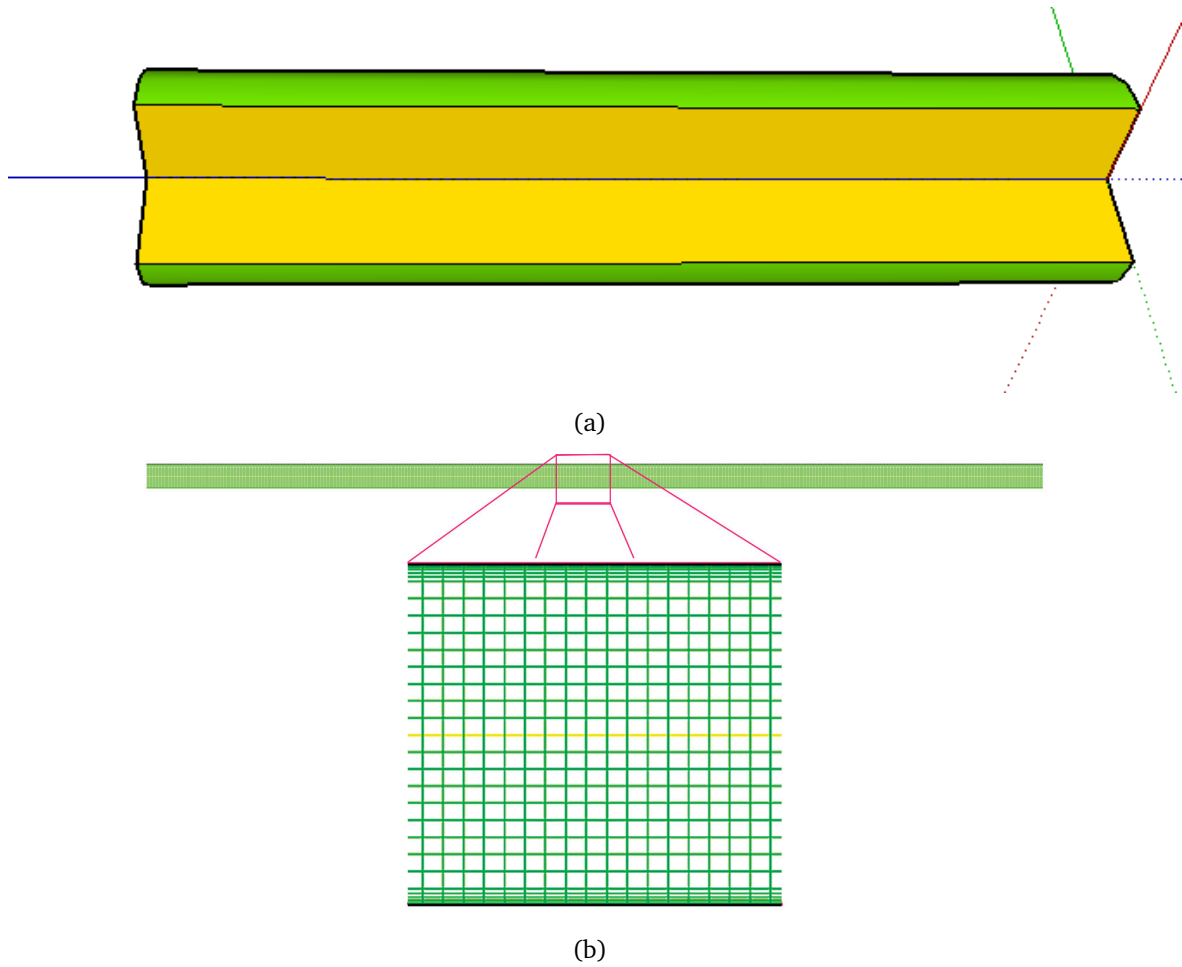
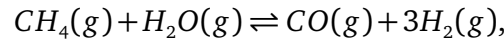


Figure 2.2: Two-dimensional axisymmetric reforming tube geometry (Fig. 2.2(a)) and mesh structure (Fig. 2.2(b)).

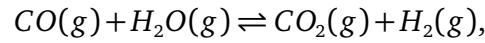


catalyst pores; after the formation of the products, products need to desorb from the catalyst cores and reenter the bulk tube-side gas mixture. However, a reaction kinetics model that provides a detailed treatment of these catalyst-specific phenomena is unnecessarily complex. For the purposes of this work, as the catalyst particles and the detailed packing pattern inside an industrial-scale packed-bed reactor are not explicitly modeled in this study.

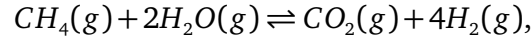
To deal with this issue, in this single reforming tube CFD model, an intrinsic SMR reaction mechanism<sup>70</sup> is used to describe the reactions happening inside the reforming tube. The SMR reaction kinetics are given in Eq. 2.1 below which is widely adopted in both CFD modeling and mathematical modeling of reforming tubes:



$$r_1 = \frac{k_1}{p_{H_2}^{2.5}} \left( p_{CH_4} p_{H_2O} - \frac{p_{H_2}^3 p_{CO}}{K_1} \right) / DEN^2 \quad (2.1a)$$



$$r_2 = \frac{k_2}{p_{H_2}} \left( p_{CO} p_{H_2O} - \frac{p_{H_2} p_{CO_2}}{K_2} \right) / DEN^2 \quad (2.1b)$$



$$r_3 = \frac{k_3}{p_{H_2}^{3.5}} \left( p_{CH_4} p_{H_2O}^2 - \frac{p_{H_2}^4 p_{CO_2}}{K_3} \right) / DEN^2 \quad (2.1c)$$

$$DEN = 1 + \frac{K_{H_2O} p_{H_2O}}{p_{H_2}} + K_{CO} p_{CO} + K_{H_2} p_{H_2} + K_{CH_4} p_{CH_4} \quad (2.1d)$$

where  $p_{H_2}$ ,  $p_{CH_4}$ ,  $p_{H_2O}$ ,  $p_{CO}$  and  $p_{CO_2}$  are the partial pressures of  $H_2$ ,  $CH_4$ ,  $H_2O$ ,  $CO$  and  $CO_2$  respectively in the bulk tube-side gas mixture inside the reforming tube,  $K_{H_2}$ ,  $K_{CH_4}$  and  $K_{CO}$  are adsorption constants for  $H_2$ ,  $CH_4$  and  $CO$ , respectively,  $K_{H_2O}$  is a dissociative adsorption constant of  $H_2O$ ,  $k_1$ ,  $k_2$  and  $k_3$  are rate coefficients of the SMR reactions and  $DEN$  is a dimensionless parameter. To realize this reaction mechanism in CFD simulations by Fluent, each reversible

reaction in Eq. 2.1 is split into two irreversible reactions. The reaction rates in Eq. 2.1 are implemented in Fluent by designing a user defined function (UDF) file. Since these intrinsic reaction kinetics do not consider the internal and external diffusion resistances of the catalyst particles, the reaction rates in Eq. 2.1 are multiplied by an effectiveness factor, 0.1,<sup>69</sup> to account for the overall diffusion effects on the intrinsic reaction rates.

#### 2.2.4 Compressible Gas Flow

The tube-side inlet operating conditions of the reforming tubes are given in Table 2.2.<sup>38</sup> Based on the inlet conditions of the tube-side gas mixture, the Mach number is determined to be greater than 0.3, and therefore, the density variations of the fluid flow due to high static pressure cannot be ignored. From the point of view of CFD simulation, when a pressure-based solver is used, like the one we chose for the simulation in this work, an accurate gas state equation is very critical to simulation accuracy. Based on this consideration, the compressible ideal gas state equation is adopted to describe the compressibility of the tube-side gas mixture.

Table 2.2: Process-side gas inlet operating conditions.

Pressure (kPa )	3038.5
Temperature (K)	887
Flow rate (kgs <sup>-1</sup> )	0.1161
$x_{CH_4}$	0.2487
$x_{H_2O}$	0.7377
$x_{CO}$	0.0001
$x_{H_2}$	0.0018
$x_{CO_2}$	0.0117

A pressure-based solver that enables the pressure-based Navier-Stokes solution algorithm<sup>28</sup> is chosen over a density-based solver. The pressure-based solver is more suited for a wider range of physical models and has features that are unavailable to the density-based solver, e.g., the physical velocity formulation for porous media which is adopted by this work to simulate the flow through the catalyst network in the reforming tube (this will be discussed later). It also

provides more freedom for the simulations while converging to the same results obtained by the density-based solver.

## 2.2.5 Porous Zone Design

Table 2.3: Johnson Matthey's Katalco 23–4Q catalyst properties.

Density, $\rho_c$	3960 kg/m <sup>3</sup>
Heat Capacity, $C_{p,c}$	880 J/kgK
Thermal Conductivity, $k_c$	33 W/mK
Particle Diameter, $D_p$	3.5 mm (average)

Pressure drop is significant in industrial-scale reforming tubes when the tube-side gas mixture flows through the catalyst network made of many tightly packed catalyst particles. To estimate the pressure drop across the porous zone in the CFD modeling of turbulent flows, a semi-empirical expression, the Ergun equation,<sup>18</sup> which is applicable over a wide range of Reynolds numbers and for many packing patterns, is adopted as follows:

$$\frac{\Delta P}{L} = \frac{150\mu}{D_p^2} \frac{(1-\gamma)^2}{\gamma^3} v_\infty + \frac{1.75\rho}{D_p} \frac{(1-\gamma)}{\gamma^3} v_\infty^2 \quad (2.2)$$

where  $\Delta P$  is the pressure drop through the porous media,  $L$  is the depth of the porous media,  $\mu$  is the viscosity of the fluid,  $\gamma$  is the porosity of the packed bed,  $v_\infty$  is the bulk velocity of the fluid,  $\rho$  is the density of the porous media,  $\frac{150\mu}{D_p^2} \frac{(1-\gamma)^2}{\gamma^3}$  is the viscous resistance coefficient and  $\frac{1.75\rho}{D_p} \frac{(1-\gamma)}{\gamma^3}$  is the inertial resistance coefficient. We assume that the viscous and inertial resistance coefficients are defined along the direction vectors  $v_1 = [1, 0]$  (i.e., the principal axis direction) and  $v_2 = [0, 1]$  (i.e., the radius direction) in the Cartesian two-dimensional (2D) coordinate system.

## 2.2.6 Reforming Tube Wall Boundary Conditions

For an industrial-scale reformer, the outer reforming tube wall temperature is usually in the range of 1100 K to 1178 K.<sup>38</sup> In this single reforming tube simulation, to construct the temperature boundary condition of the outer reforming tube wall, the available plant data<sup>38</sup> are fit with a fourth order polynomial function by using a least squares linear regression method. The result of the fit shown in Fig. 2.3(a) is

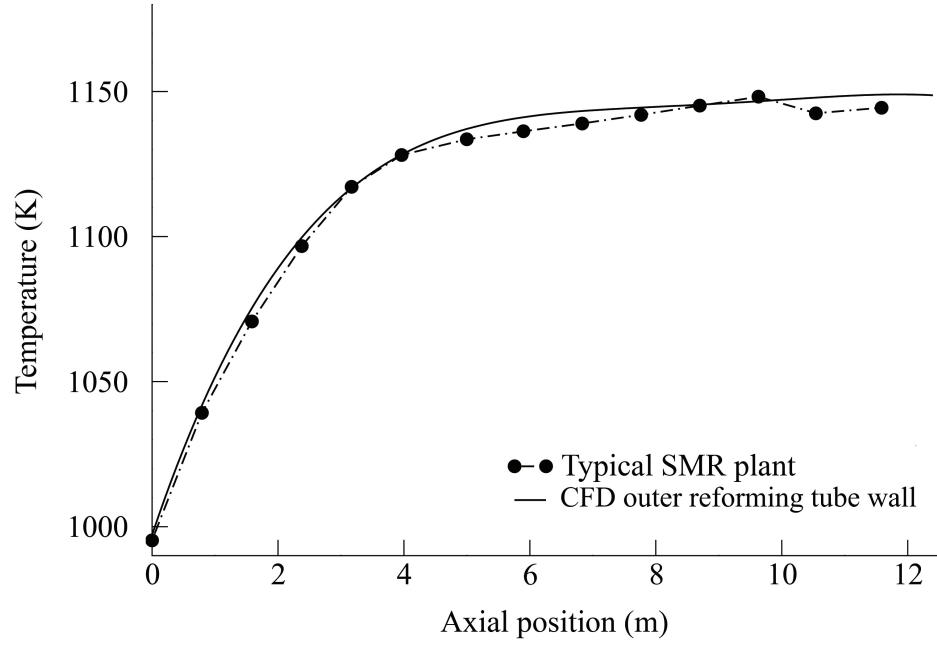
$$T_{wall}(x) = \begin{bmatrix} x^4 & x^3 & x^2 & x^1 & x^0 \end{bmatrix} \begin{bmatrix} -0.0221 \\ 0.8003 \\ -10.734 \\ 64.416 \\ 997.16 \end{bmatrix} \quad (2.3)$$

where  $T_{wall}(x)$  is the outer reforming tube wall temperature at a location  $x$  (m) away from the reforming tube inlet,  $x = 0$  m. Using the boundary condition in Eq. 2.3, the reforming tube here is modeled as a heat sink, and thermal energy is transferred from the outer reforming tube wall to the inner reforming tube wall by heat conduction. The corresponding tube material properties are listed in Table 2.4<sup>13</sup> which assumes that all the tube properties are temperature independent and the values at  $T = 1144$  K are adopted in the CFD simulation. However, a constant outer reforming tube wall temperature profile is neither sufficient to maintain the current  $\bar{x}_{H_2}^{outlet}$  when the reforming tube operating condition is subjected to a change in the tube-side mass flow rate (e.g., tube-side feed disturbance), nor capable of driving the current  $\bar{x}_{H_2}^{outlet}$  to a new desired  $\bar{x}_{H_2}^{set}$ . To fulfill the overall scope of this work, which is to design and implement feedback control schemes to drive  $\bar{x}_{H_2}^{outlet}$  to the desired  $\bar{x}_{H_2}^{set}$  under the influence of a tube-side feed disturbance, additional temperature profiles are constructed based on the most essential criterion that the shapes (in the axial direction) of these additional temperature profiles have to match that of the original outer reforming tube wall temperature profile (owing

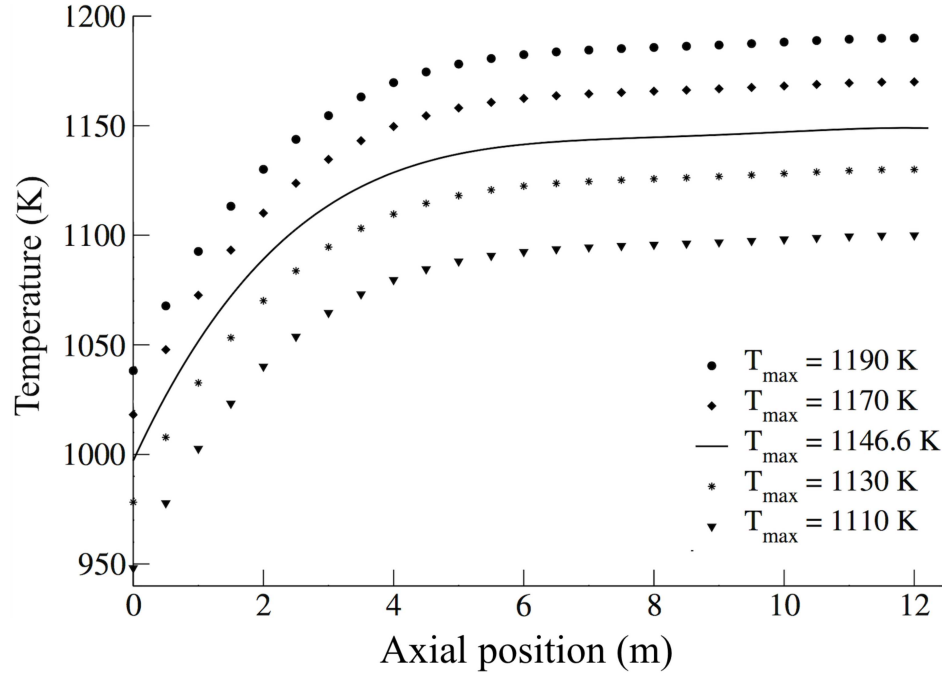
to the overall shape and location of burner flames which does not change appreciably with time). The additional profiles are given by the following fourth-order polynomial,

$$T_{Wall}(x) = \begin{bmatrix} x^4 & x^3 & x^2 & x^1 & x^0 \end{bmatrix} \begin{bmatrix} -0.0221 \\ 0.8003 \\ -10.734 \\ 64.416 \\ T_{Wall}^{max} - 151.83 \end{bmatrix} \quad (2.4)$$

where  $T_{Wall}^{max}$  is the maximum outer reforming tube wall temperature of the temperature profile. Eq. 2.4 allows one to construct an entire outer reforming tube wall temperature profile along the reforming tube length based on its maximum temperature value and consequently affect the  $\bar{x}_{H_2}^{outlet}$ .



(a)



(b)

Figure 2.3: Outer reforming tube wall temperature versus distance down the reforming tube for the CFD simulations. Fig. 2.3(a) depicts the direct comparison between the fourth order polynomial temperature profile, i.e., Eq. 2.3 and that of publicly available SMR plant data.<sup>38</sup> Fig. 2.3(b) represents the calculated outer reforming tube wall temperature profiles generated by Eq. 2.4 and the fitted outer reforming tube wall temperature profile (solid line) based on the publicly available SMR plant data.<sup>38</sup>

Table 2.4: Reforming tube material properties.

Density, $\rho_t$	7720 kg/m <sup>3</sup>
Heat Capacity, $C_{p,t}$	502 J/(kgK)
Thermal Conductivity, $k_t$	29.58 W/(mK) at 1144 K
Emissivity, $\epsilon_t$	0.85 at 1144 K

### 2.2.7 Governing equations

In the microscopic view of the reforming tube, the physico-chemical phenomena of transport and reaction processes that generate hydrogen fuel from steam and methane are closely coupled and utterly complex. Initially, a convective mass transfer process driven primarily by the reactant concentration gradients between a flowing bulk gas mixture and an infinitesimally thin stationary layer around the catalytic surface takes place. Next, a molecular diffusion process mainly driven by the reactant concentration and temperature gradients (Eq. 2.6g) between an infinitesimally thin stationary layer around the catalyst surface and a catalyst medium allows the reactants to diffuse into the catalyst pores and then finally arrive at the catalyst active sites, where the endothermic SMR reactions take place. Products, once formed, immediately desorb from the catalyst active sites, diffuse back to the catalyst surface and eventually reenter the flowing bulk gas mixture. It is worth noting that the series of consecutive molecular-level elementary steps of the endothermic SMR reactions is still largely unknown. As a result, a kinetic mechanism model that provides a detailed treatment of these catalyst-specific phenomena would be unnecessarily complex from the point of view of CFD modeling; therefore, the kinetic model used in this paper is derived based on a widely-accepted intrinsic SMR reaction kinetic mechanism<sup>70</sup> to lessen the computational burden without sacrificing the accuracy of the simulation results (Sec. 2.2.3).

In the macroscopic view of the reforming tube, the significant axial pressure gradient across the reforming tube length and radial gradients near the reforming tube entrance are well-acknowledged. This, in turn, motivates us to develop two-dimensional (2D) governing equa-

tions that are capable of accounting for the presence of the catalyst network formed by the solidly packed catalyst particles. It is important to thoroughly understand the contribution of the catalyst network to the SMR reactions in order to develop an appropriate process model. Specifically, the catalyst network not only facilitates the formation of hydrogen fuel from the naturally stable and slowly-reacting materials, i.e., steam and methane, but also enhances the rate of convective thermal energy transfer from the heated outer reforming tube wall to the flowing bulk gas mixture by expanding its contact area.

Additionally, due to the intrinsic resistance properties of the catalyst network, i.e., the inertial resistance and viscous resistance previously mentioned in Sec. 2.2.5, the catalyst network acts as a physical obstacle that interferes with the flow of the tube-side gas mixture to generate turbulence. This obstacle enhances mixing efficiency to radially homogenize the moving fluid. Furthermore, under the influence of flow resistances induced by the catalyst network, the residence time of all species in the reforming tube is also increased, which allows the SMR reactions<sup>70</sup> to reach equilibrium prior to the process gas exiting the reforming tube. Based on the aforementioned considerations, the 2D governing equations, i.e., the continuity equation (Eq. 2.5) and the momentum (Eq. 2.6a), energy (Eq. 2.6b) and species material (Eq. 2.6c) balances, of the SMR process taking place inside the reforming tube are formulated as follows, so that the presence of the catalyst network is explicitly accounted for:

$$\frac{\partial}{\partial t}(\gamma \rho_{fluid}) + \nabla \cdot (\gamma \rho_{fluid} \vec{v}) = 0 \quad (2.5)$$



$$\frac{\partial}{\partial t}(\gamma \rho_{fluid} \vec{v}) + \nabla \cdot (\gamma \rho_{fluid} \vec{v} \vec{v}) = \quad (2.6a)$$

$$-\gamma \nabla P + \nabla \cdot (\gamma \vec{\tau}) + \gamma \vec{B}_f - \left( \frac{\gamma^2 \mu}{\alpha} \vec{v} + \frac{\gamma^3 C_2}{2} \rho |\vec{v}| \vec{v} \right)$$

$$\frac{\partial}{\partial t}(\gamma \rho_{fluid} E_{fluid}) + \frac{\partial}{\partial t}((1-\gamma) \rho_{solid} E_{solid}) \quad (2.6b)$$

$$+ \nabla \cdot (\vec{v}(\rho_{fluid} E_{fluid} + P)) =$$

$$\nabla \cdot \left[ k_{eff} \nabla T - \left( \sum_i h_i J_i \right) + \vec{\phi} \right] + \sum_i \Delta H_{rxn,i}$$

$$\frac{\partial}{\partial t}(\gamma \rho_{fluid} Y_i) + \nabla \cdot (\gamma \rho_{fluid} \vec{v} Y_i) = -\nabla \cdot (\gamma \vec{J}_i) + R_i \quad (2.6c)$$

with

$$\vec{v}_{superficial} = \gamma \vec{v} \quad (2.6d)$$

$$\vec{\tau} = \mu \left[ (\nabla \vec{v} + \nabla \vec{v}^T) - \frac{2}{3} \nabla \cdot \vec{v} I \right] \quad (2.6e)$$

$$k_{eff} = \gamma k_{fluid} + (1-\gamma) k_{solid} \quad (2.6f)$$

$$\vec{J}_i = \left( \rho_{fluid} D_{m,i} + \frac{\mu_t}{Sc_t} \right) \nabla Y_i - D_{T,i} \frac{\nabla T}{T} \quad (2.6g)$$

$$\vec{\phi} = 2\mu \left[ \left( \frac{\partial v_x}{\partial x} \right)^2 + \left( \frac{\partial v_y}{\partial y} \right)^2 - \frac{1}{3} (\nabla \cdot \vec{v})^2 \right] \quad (2.6h)$$

$$+ \mu \left[ \frac{\partial v_y}{\partial x} + \frac{\partial v_x}{\partial y} \right]^2$$

where  $\mu$ ,  $\mu_t$ ,  $\vec{v}$ ,  $\vec{v}_{superficial}$  and  $\rho_{fluid}$  are the molecular viscosity, turbulent viscosity, physical velocity vector, superficial velocity vector and the average density of the bulk tube-side gas mixture respectively,  $\gamma$ ,  $\rho_{solid}$  and  $\alpha$  are the porosity, density and absolute permeability of the catalyst network respectively,  $\frac{1}{\alpha}$  and  $C_2$  represent the viscous resistance coefficient and inertial resistance coefficient (previously introduced in Sec. 2.2.5),  $E_{fluid}$  and  $E_{solid}$  are the total energy of the tube-side gas mixture and of the catalyst network,  $P$  is the static pressure,  $\sum_i \Delta H_{rxn,i}$  is the total thermal energy generated by the SMR reactions,  $k_{fluid}$ ,  $k_{solid}$  and  $k_{eff}$  are the thermal conductivities of the tube-side gas mixture, of the catalyst network and of the overall medium,

$Y_i$ ,  $D_{m,i}$ ,  $D_{T,i}$ ,  $\vec{J}_i$  and  $R_i$  are the mass fraction, mass diffusion coefficient, thermal diffusion coefficient, turbulent mass diffusion flux and overall rate of chemical reaction of species  $i$ , and  $\vec{\tau}$  and  $I$  are the stress tensor and unit tensor, respectively. It is important to note that the chemical rate equations are formulated to account for the effects of internal and external diffusion limitations on the observed rates as well as for the presence of the catalyst particles inside the reforming tube, and therefore, it would be unnecessary and incorrect to multiply  $R_i$  in Eq. 2.6c and  $\sum_i \Delta H_{rxn,i}$  in Eq. 2.6b by  $\gamma$  in an attempt to account for the effects of the catalyst network. Additionally, detailed microscopic transport and chemical reaction processes are described by the 2D governing equations, i.e.,  $[\nabla \cdot (\sum_i h_i J_i)]$  in Eq. 2.6b represents the transport of enthalpy due to molecular diffusion, and  $[(\nabla \vec{v} + \nabla \vec{v}^T) - \frac{2}{3} \nabla \cdot \vec{v} I]$  in Eq. 2.6e represents the effect of volume dilation.

Due to the high Reynolds number of the tube-side gas mixture, which is estimated to be  $\sim 5500$  based on the inlet conditions of the tube-side feed as shown in Table 2.2, the semi-empirical standard two-equation turbulent kinetic energy and turbulent dissipation rate ( $k-\epsilon$ ) model<sup>30,40</sup> developed from the Reynolds-averaged Navier-Stokes (RANS) equations is employed to describe the complex turbulence phenomena inside the reforming tube. The  $k-\epsilon$  turbulence model presented in Eq. 2.7 below is applicable for a wide range of flows and is relatively computationally inexpensive, though it still yields reasonably accurate estimates, and it is relatively simple to implement and easy to converge from the point of view of CFD simulation. This model has the form:

$$\begin{aligned} \frac{\partial}{\partial t}(\gamma \rho_{fluid} k) + \nabla \cdot (\gamma \rho_{fluid} \vec{v} k) &= \nabla \cdot \left[ \gamma \left( \mu + \frac{\mu_t}{\sigma_k} \right) \nabla k \right] \\ &+ \gamma G_k + \gamma G_b - \gamma \rho_{fluid} \epsilon - \gamma Y_M \end{aligned} \quad (2.7a)$$

$$\begin{aligned} \frac{\partial}{\partial t}(\gamma \rho_{fluid} \epsilon) + \nabla \cdot (\gamma \rho_{fluid} \epsilon \vec{v}) &= \nabla \cdot \left[ \gamma \left( \mu + \frac{\mu_t}{\sigma_\epsilon} \right) \nabla \epsilon \right] \\ &+ \gamma C_{1\epsilon} \frac{\epsilon}{k} (G_k + C_{3\epsilon} G_b) - \gamma C_{2\epsilon} \rho \frac{\epsilon^2}{k} \end{aligned} \quad (2.7b)$$

$$\left\{ \begin{array}{l} \mu_t = \rho_{fluid} C_\mu \frac{k^2}{\epsilon} \\ C_{3\epsilon} = \tanh \left| \frac{v}{u} \right| \\ G_b = \beta g_i \frac{\mu_t}{Pr_t} \frac{\partial T}{\partial x_i} \\ G_k = -\rho u'_i u'_j \frac{u_j}{x_i} \\ \beta = -\frac{1}{\rho} \left( \frac{\partial \rho}{\partial T} \right)_p \end{array} \right.$$

where  $k$  and  $\epsilon$  are the turbulent kinetic energy and turbulent dissipation rate respectively,  $G_k$  and  $G_b$  are the generation of turbulent kinetic energy due to the mean velocity gradients and buoyancy respectively,  $Y_M$  is the contribution of the fluctuating dilation in compressible turbulence to the overall dissipation rate,  $\sigma_\epsilon = 1.0$  and  $\sigma_k = 1.3$  are the turbulent Prandtl numbers for  $\epsilon$  and  $k$  respectively,  $C_{1\epsilon} = 1.44$ ,  $C_{2\epsilon} = 1.92$  and  $C_\mu = 0.09$  are default constants of the standard  $k-\epsilon$  model,  $Pr_t = 0.85$  is the turbulent Prandtl number for energy,  $g_i$  is the component of the gravitational vector in the  $i$ th direction,  $\beta$  is the thermal expansion coefficient, and  $v$  and  $u$  are the components of the flow velocity parallel and perpendicular, respectively, to the gravitational vector. It is worth noting that all default values of the aforementioned constants are determined empirically by experiments for fundamental turbulent flows, i.e., boundary layers and mixing layers, and have been verified to be suitable for a wide range of wall-bounded and free shear flow applications.<sup>26</sup> Furthermore, turbulent flows are significantly affected by the walls. The accuracy of the near-wall modeling decides the fidelity of

numerical solutions. Specifically, it is in the near-wall region that the solution variables have large gradients, i.e., the momentum, material and energy fluxes have large magnitudes. Therefore, an accurate representation of the flow in the near-wall region is required for successful predictions of wall-bounded turbulent flows. For this single reforming tube CFD model, the enhanced wall treatment function in Fluent is applied as the near wall treatment method. The enhanced wall treatment  $\epsilon$ -Equation is suitable for certain fluid dynamics especially for those with lightly turbulent flow, and it only requires a few nodes in the boundary layer when using the  $k-\epsilon$  model.<sup>26</sup>

## 2.2.8 Simulation Results

### CFD Model of Single Reforming Tube: Results Comparison

Using a parallel computational environment with message passing interface technology, the simulation of the single reforming tube CFD model converges in about 5 minutes with the steady solver in a 4-core CPU desktop computer. The steady-state results of the simulations are displayed in Figs. 2.4-2.5. We note here that due to the large length to diameter ratio of the reforming tube, in all plots of the simulation results, the radius is scaled up by 20 times, which is convenient and is done for display purposes only. It is worth noting that the pressure profile in this simulation is radially uniform, which is the result of the direction definitions of the resistance coefficients in Section 2.2.5. Additionally, based on the wall temperature profile in Fig. 2.3(a), the corresponding inner reforming tube wall temperature profile at the steady-state from the converged model is displayed in Fig. 2.6, and the corresponding steady-state heat flux profile through the tube wall is shown in Fig. 2.7.



Figure 2.4: Temperature profile from the reforming tube CFD simulation, where the outer reforming tube wall temperature profile (Fig. 2.3(a)) is that fitted based on the available SMR plant data.<sup>38</sup>

Reforming tube outlet data (not reported here for proprietary reasons) from a typical hydrogen plant with the same tube-side inlet conditions, the same tube geometric structure and similar catalyst and tube material properties as described in Secs. 2.2.1, 2.2.4 and 2.2.5, and also the same wall temperature profile as that reported in Fig. 2.3(a), is used to validate the CFD single tube model. The validation is performed by comparing the data of the process gas at the reforming tube outlet (Table 2.5) from the CFD simulation to that of the available industrial plant. All mole fraction values in Table 2.5 are area-weighted average values at the tube outlet. We found that our simulation results reported in Table 2.5 closely matched the plant data for both temperature and species compositions.

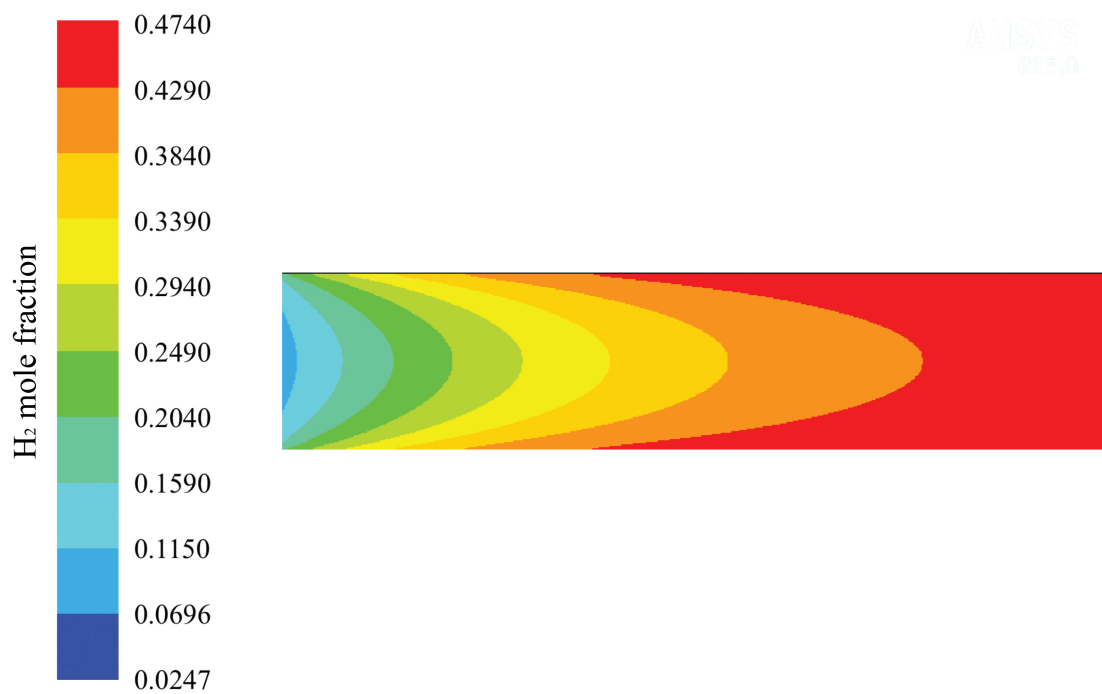


Figure 2.5: Hydrogen mole fraction profiles from the reforming tube CFD simulation, where the outer reforming tube temperature profile (Fig. 2.3(a)) is that fitted based on the available SMR plant data.<sup>38</sup>

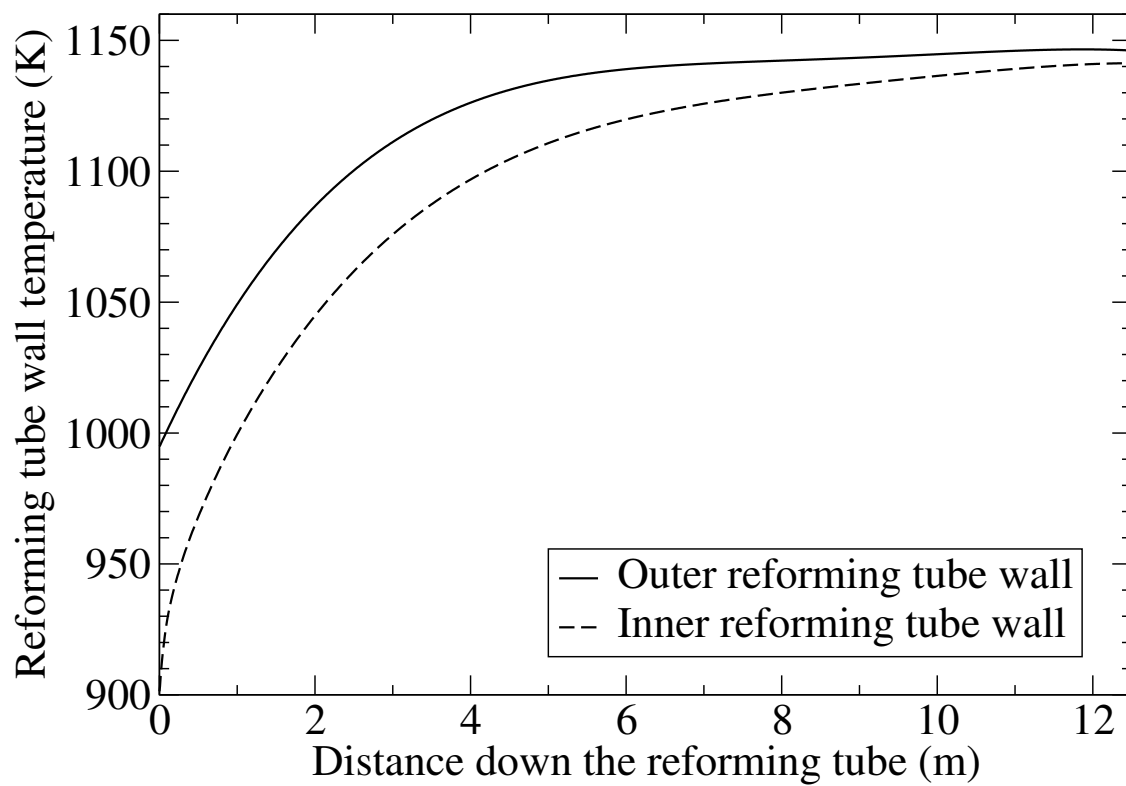


Figure 2.6: Inner (dashed line) and outer (solid line) wall temperature profiles of the reforming tube.

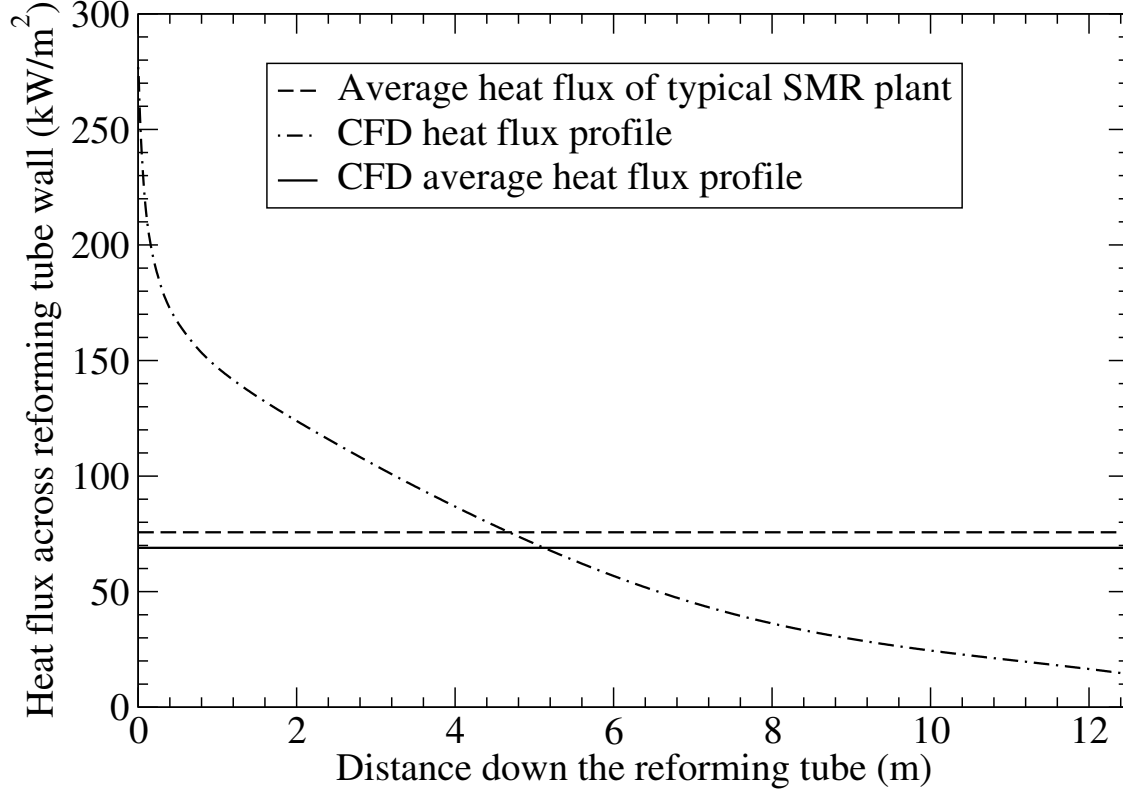


Figure 2.7: Heat flux profile across the reforming tube wall.

## 2.3 Feedback control design and closed-loop simulation results

### 2.3.1 Open-loop dynamics

We are primarily interested in the regulation of  $\bar{x}_{H_2}^{outlet}$  when the reforming tube is subjected to tube-side feed disturbances, where the control objective is to maintain the current  $\bar{x}_{H_2}^{set}$ , or when changes in industrial plant objectives occur, where the control objective is to attain a new  $\bar{x}_{H_2}^{set}$ .

Among all simulation settings described in Section II, the outer reforming tube wall temperature profile is chosen as the single manipulated input due to the endothermic nature of the SMR reactions. As a result,  $\bar{x}_{H_2}^{outlet}$  can be manipulated by adjusting the outer reforming tube wall



Table 2.5: Single reforming tube results.

	CFD Result
$\Delta P$ (kPa)	212.83
$\bar{P}_{outlet}$ (kPa)	3044.0
$\bar{x}_{H_2}^{outlet}$	0.4645
$\bar{x}_{H_2O}^{outlet}$	0.3467
$\bar{x}_{CH_4}^{outlet}$	0.0426
$\bar{x}_{CO}^{outlet}$	0.0873
$\bar{x}_{CO_2}^{outlet}$	0.0588
$Heat\ Flux_{average}$ (kW/m <sup>2</sup> )	68.972

temperature profile, which depends on the fuel flow rates to the burners around the reforming tube. It should be noted that the maximum value of an outer reforming tube wall temperature profile ( $T_{Wall}^{max}$ ) can be used in Eq. 2.4 to construct an entire profile along the reforming tube, and therefore, a specific  $T_{Wall}^{max}$  can represent a unique outer reforming tube wall temperature profile. The temperature dependence of  $\bar{x}_{H_2}^{outlet}$  is demonstrated in Fig. 2.9 for a wide range of outer reforming tube wall temperature profiles for which  $T_{Wall}^{max}$  varies from 1100 K to 1200 K. Due to the endothermic nature of the SMR reactions, higher values of  $\bar{x}_{H_2}^{outlet}$  are observed for temperature profiles with higher  $T_{Wall}^{max}$ .

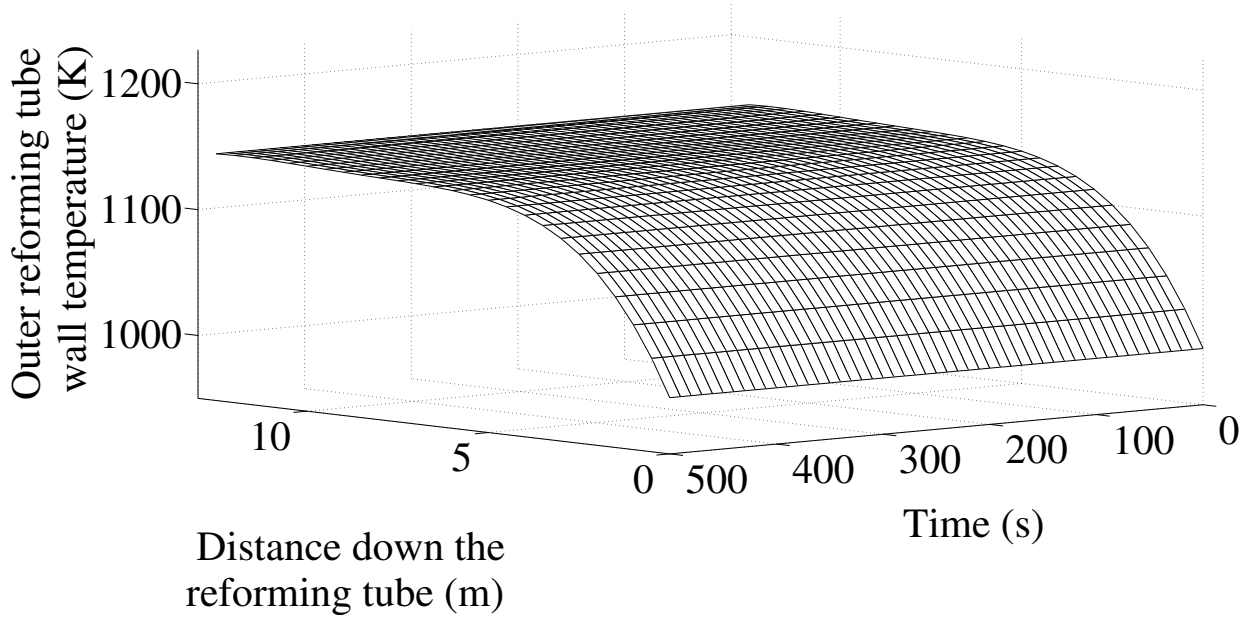


Figure 2.8: The pre-determined outer reforming tube wall temperature trajectory with time for open-loop control with  $\bar{x}_{H_2}^{set} = 0.465$ .

In this work, all CFD reforming tube simulations under feedback control and under open-loop control are carried out in a parallel computational environment with message passing interface technology with a built-in, explicit-time-stepping, transient solver. Transient simulation may reveal dynamics of a system that cannot be obtained under steady-state simulation.<sup>54</sup> In particular, Barton reported that the catalyst core temperatures of the water-gas shift reactors in an IGCC-TIGAS polygeneration plant can exceed the maximum steady-state value by  $100^\circ\text{C}$  during start-up, which would not be detected under steady-state simulation.<sup>1</sup> Additionally, the transient solver can be used to determine the steady-state solution when a steady-state model is highly unstable, e.g., natural convection problems with Rayleigh number in the transition regime.<sup>26</sup> CFD simulations under open-loop control using a constant pre-determined outer wall temperature trajectory (e.g., Fig. 2.8) as the process manipulated input and built with fixed simulation settings can successfully drive  $\bar{x}_{H_2}^{outlet}$  to the desired  $\bar{x}_{H_2}^{set}$  under a strictly disturbance-free environment as shown in Fig. 2.10. However, due to the absence of the feedback mechanism, open-loop control is unable to recognize or handle the tube-side feed dis-

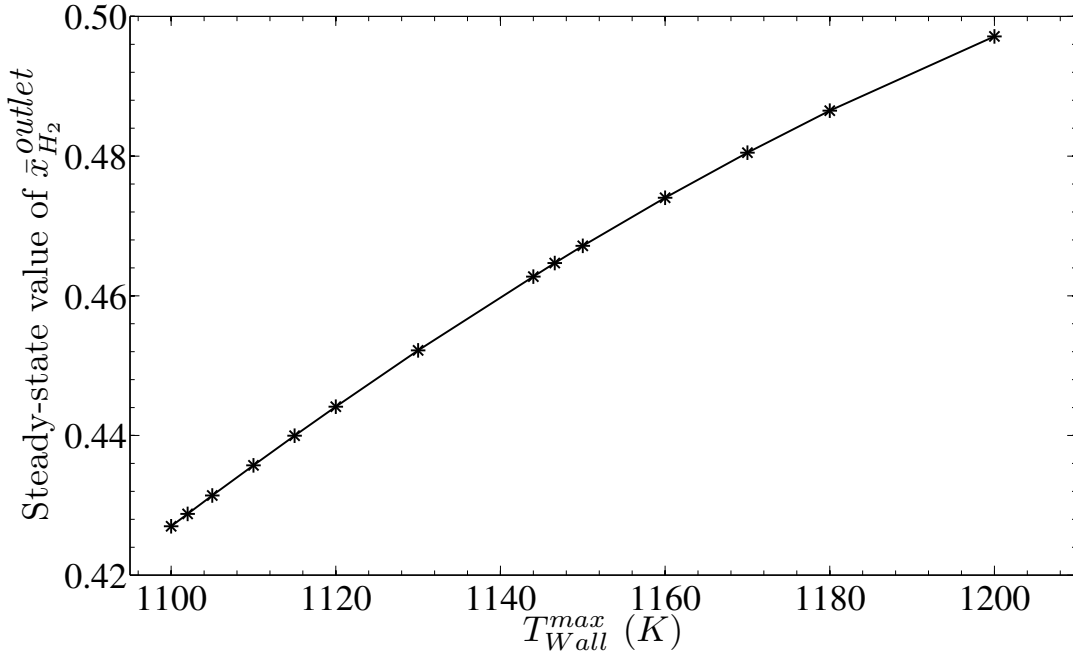


Figure 2.9: The expected steady-state value of  $\bar{x}_{H_2}^{outlet}$  at different constant outer reforming tube temperature profiles which are presented by their corresponding  $T_{Wall}^{max}$ . The relationship between  $\bar{x}_{H_2}^{outlet}$  and  $T_{Wall}^{max}$  is captured by the second-order polynomial,  $T_{Wall}^{max} = 5648.6(\bar{x}_{H_2}^{outlet})^2 - 3814.7\bar{x}_{H_2}^{outlet} + 1699.5$ , which is used to generate an appropriate manipulated input for the open-loop CFD simulations based on the desired  $\bar{x}_{H_2}^{set}$  (Fig. 2.8).

turbances, which results in a substantial deviation of the steady-state  $\bar{x}_{H_2}^{outlet}$  from the desired set-point,  $\bar{x}_{H_2}^{set}$ . The aforementioned robustness issue motivates us to design feedback control schemes including proportional (P), proportional-integral (PI) and optimization-based control schemes, which are utilized to produce a feedback-based manipulated input in order to drive  $\bar{x}_{H_2}^{outlet}$  to the desired  $\bar{x}_{H_2}^{set}$  in the presence of tube-side feed disturbances.

### 2.3.2 Feedback controller design

In this work, the primary objectives of the feedback control schemes are to drive  $\bar{x}_{H_2}^{outlet}$  to the desired  $\bar{x}_{H_2}^{set}$  in the presence of the tube-side feed disturbance, and to speed up the dynamics of the process to allow the system to quickly advance to the optimized steady-state operating condition. All simulation settings of the closed-loop simulations are the same as those

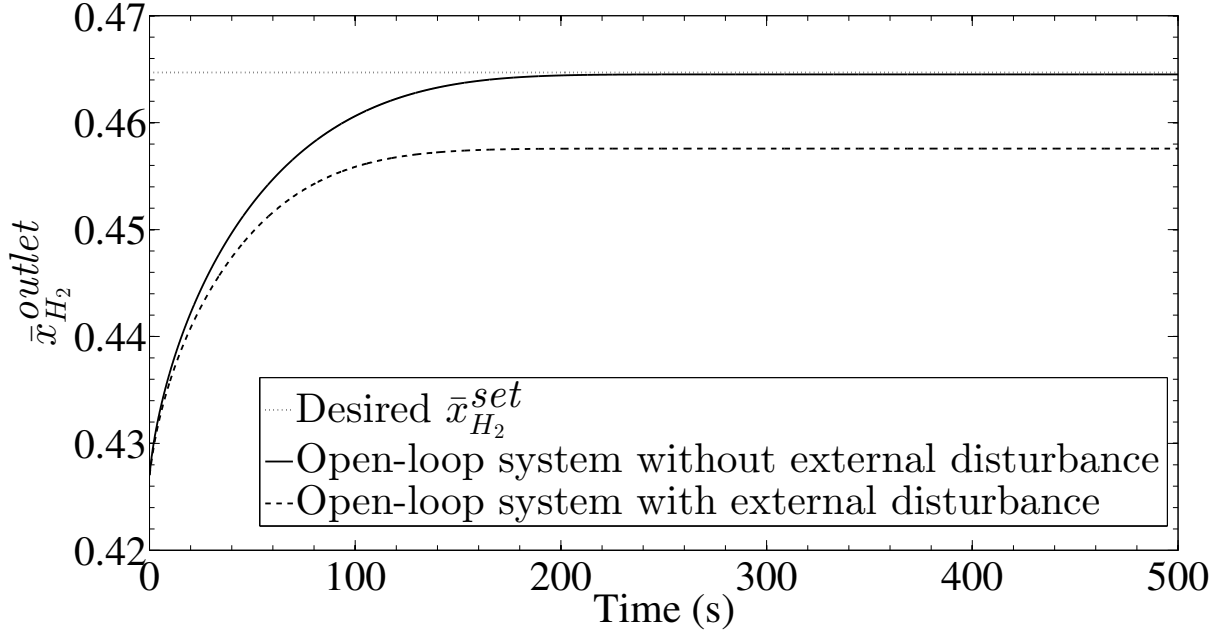


Figure 2.10: The propagation of  $\bar{x}_{H_2}^{outlet}$  with time under open-loop control with  $\bar{x}_{H_2}^{set} = 0.465$ , when the tube-side mass flow rate is kept at its nominal value (solid line), and when it is increased by 20% (dashed line). Fig. 2.10 demonstrates that open-loop control is not robust and cannot be used to maintain  $\bar{x}_{H_2}^{set}$  at 0.465 when a change in the operating condition is imposed.

used in the previously studied open-loop system. These feedback control schemes make the control objectives feasible and provide robustness against the tube-side feed disturbance, and thus resolve the critical drawback of open-loop control. It is desired that under each feedback control scheme, the closed-loop system is initially operated in a high temperature regime favoring the formation of hydrogen fuel resulting in a fast increase of  $\bar{x}_{H_2}^{outlet}$  toward the desired  $\bar{x}_{H_2}^{set}$  due to the endothermic nature of the SMR reactions described in Eq. 2.1. After the initial burst of hydrogen fuel, it is desired that the closed-loop system is then kept in a moderately high temperature regime, which effectively slows down the rapid formation of hydrogen fuel to prevent unnecessary aggressive control action. To design feedback control schemes to accomplish the operating strategy, a data-driven modeling technique is used to obtain a process transfer function describing the evolution of  $\bar{x}_{H_2}^{outlet}$  based on the CFD simulation result for a step-change of the maximum outer reforming tube wall temperature from  $T_{Wall}^{max}(0) = 1100$  K to  $T_{Wall}^{max}(t) = 1110$  K (which is discussed in greater detail below). Then, this approximate model

capturing the dominant dynamics of the reforming tube is combined with classical feedback control to form a closed-loop system. The closed-loop system is utilized in a parametric study (not reported here for brevity) to determine the appropriate control parameters, i.e.,  $K_c$  of P control or  $K_c$  and  $\tau_I$  of PI control.

Furthermore, the maximum allowable temperature value of 1200 K is taken into account in the control schemes to avoid the rupture of the reforming tube which can occur at exceedingly high operating temperatures. Additionally, this upper limit on the outer reforming tube wall temperature prevents the deposition of carbon on the reforming tube wall and on the surfaces of catalyst particles, which would significantly decrease the heat transfer rate to the flowing gas mixture and prevent the reactants from entering the catalyst active sites resulting in a lower  $\bar{x}_{H_2}^{outlet}$ . Next, the minimum allowable temperature value of 987 K at the tube inlet is considered in the formulation of the control schemes to ensure that sufficient heat is transferred to the flowing tube-side gas mixture to facilitate the highly endothermic SMR reactions. Moreover, since the scope of our current work focuses on CFD modeling and controller design of the reforming tube instead of the SMR furnace, we will disregard the dynamics of the outer reforming tube wall temperature. Hence, we suppose that the outer reforming tube wall temperature can reach the predicted profile instantaneously. Lastly, we assume that measurements of  $\bar{x}_{H_2}^{outlet}$  are available at all sampling instances. Classical P and PI control schemes that are based on the deviation of  $\bar{x}_{H_2}^{outlet}$  from the desired set-point and account for input constraints are presented as follows:

P control scheme

$$\begin{cases} e(t_k) = \bar{x}_{H_2}^{set} - \bar{x}_{H_2}^{outlet}(t_k) \\ u_p(t_k) = K'_c e(t_k) \\ T_{wall}^{max}(t_k + \Delta t) = \\ T_{wall}^{max}(t = 0) + u_p(t_k) \end{cases} \quad (2.8a)$$

PI control scheme

$$\begin{cases} e(t_k) = \bar{x}_{H_2}^{set} - \bar{x}_{H_2}^{outlet}(t_k) \\ u_{pi}(t_k) = K_c \left( e(t_k) + \frac{1}{\tau_I} \int_{t_0}^{t_k} e(\tau) d\tau \right) \\ T_{wall}^{max}(t_k + \Delta t) = \\ T_{wall}^{max}(t = 0) + u_{pi}(t_k) \end{cases} \quad (2.8b)$$

$$T_{wall}(x, t_k + \Delta t) \leq T_{max} \quad (2.8c)$$

$$T_{wall}(x = 0, t_k + \Delta t) \geq T_{min} \quad (2.8d)$$

$$T_{wall}(x, t_k + \Delta t) = \quad (2.8e)$$

$$\begin{bmatrix} x^4 & x^3 & x^2 & x^1 & x^0 \end{bmatrix} \begin{bmatrix} -0.0221 \\ 0.8003 \\ -10.734 \\ 64.416 \\ T_{wall}^{max}(t_k + \Delta t) - 151.83 \end{bmatrix}$$

where  $t_k$ ,  $t_0$  and  $\Delta t$  are the current time, the initial time, and the sampling time interval of the CFD simulation respectively,  $e(t_k)$  represents the current deviation of  $\bar{x}_{H_2}^{outlet}$  from the desired set-point  $\bar{x}_{H_2}^{set}$ ,  $T_{min}$  and  $T_{max}$  are the minimum and maximum allowable reforming tube wall temperatures respectively,  $K'_c = 1856.3$  and  $u_p(t_k)$  are the controller gain and current

controller output of the P control scheme,  $K_c = 1856.3$ ,  $\tau_I = 46.4$  and  $u_{PI}(t_k)$  are the controller gain, controller time constant and current controller output of the PI control scheme,  $T_{wall}^{max}(t_k + \Delta t)$  and  $T_{wall}^{max}(t = 0)$  are the predicted (i.e., prior to being saturated with the temperature constraints) and initial maximum outer reforming tube wall temperatures, respectively, and  $T_{wall}(x, t_k + \Delta t)$  is the predicted outer reforming tube wall temperature profile. At the end of each sampling time interval, the measurement of  $\bar{x}_{H_2}^{outlet}$  is acquired from the CFD simulation, and the current deviation from the desired  $\bar{x}_{H_2}^{set}$  ( $e(t_k)$ ) is computed. Then, the control output ( $u_{PI}(t_k)$  or  $u_P(t_k)$ ) is evaluated depending on the implemented control scheme, which allows  $T_{wall}^{max}(t_k + \Delta t)$  to be estimated. The value of  $T_{wall}^{max}(t_k + \Delta t)$  is subjected to Eq. 2.8c; if the constraint is not satisfied,  $T_{wall}^{max}(t_k + \Delta t)$  is set to the value of  $T_{max}$ . Then,  $T_{wall}^{max}(t_k + \Delta t)$  is used to compute the predicted wall temperature profile ( $T_{wall}(x, t_k + \Delta t)$ ), which is applied until the next sampling time, when the new value of  $\bar{x}_{H_2}^{outlet}$  is obtained from the CFD simulation.

### 2.3.3 Closed-loop simulation results

In this section, we investigate the closed-loop performance of the P and PI controllers, which adjust the manipulated input variable chosen to be the outer reforming tube wall temperature, to drive  $\bar{x}_{H_2}^{outlet}$  to the desired  $\bar{x}_{H_2}^{set}$  in the absence or presence of a tube-side feed disturbance. At the end of each sampling time interval, the measurement of  $\bar{x}_{H_2}^{outlet}$  is acquired from the CFD simulation, and the control action, which is formulated following the scheme described in Eq. 2.8, is evaluated. Next, the control action is applied to the closed-loop system until the end of the next sampling time, when the new  $\bar{x}_{H_2}^{outlet}$  is received from the CFD simulation. In our work, the performance of the feedback control schemes is evaluated based on two criteria: the improvement in the process dynamics and the final deviation of  $\bar{x}_{H_2}^{outlet}$  from the desired  $\bar{x}_{H_2}^{set}$ . It is important to note that the process dynamics in this work is defined as the time duration that is needed for the  $\bar{x}_{H_2}^{outlet}$  of the closed-loop system to first attain 99.99% of the desired  $\bar{x}_{H_2}^{set}$ . Unfortunately, due to the well-known drawback of P control, an offset of the final value of

$\bar{x}_{H_2}^{outlet}$  is expected in the system under P control, and hence, the process dynamics cannot be evaluated based on the arrival of  $\bar{x}_{H_2}^{outlet}$  at the desired  $\bar{x}_{H_2}^{set}$ . In the case of the P control scheme, the process dynamics is the time that is required for the closed-loop system to settle at its new steady-state.

In the case of set-point tracking control under a disturbance-free environment, the outer reforming tube wall temperature trajectory propagates differently under P control and PI control than under open-loop control (Fig. 2.8, Fig. 2.11(a) and Fig 2.11(b)). The open-loop control strategy adopts the outer reforming tube wall temperature profile based on the relationship between  $\bar{x}_{H_2}^{outlet}$  and  $T_{Wall}^{max}$  as shown in Fig. 2.9 with  $\bar{x}_{H_2}^{outlet} = \bar{x}_{H_2}^{set} = 0.465$ . Because of the aforementioned closed-loop operating policy described in Section 2.3.2, the process dynamics is greatly enhanced in the closed-loop system shown in Fig. 2.12. In particular, it takes  $\sim 244$  seconds for  $\bar{x}_{H_2}^{outlet}$  to attain the desired  $\bar{x}_{H_2}^{set}$  under open-loop control, while it takes  $\sim 90$  seconds corresponding to an improvement of 63.1% under P control or  $\sim 154$  seconds corresponding to an improvement of 36.9% under PI control, respectively. Nevertheless, the closed-loop system implemented with P control is unable to drive  $\bar{x}_{H_2}^{outlet}$  completely to the desired  $\bar{x}_{H_2}^{set}$ , and the offset is estimated to be 3.18%.

Next, we turn our attention to the case of set-point tracking control under a tube-side feed disturbance to emphasize the importance of feedback control. In this case, a 20% increase in the tube-side inlet mass flow rate is introduced into the simulation settings to simulate the feed disturbance. In the presence of a tube-side feed disturbance, PI control and open-loop control yield significantly different temperature trajectories of the outer reforming tube wall (Fig. 2.8 and Fig. 2.13). Unlike feedback control schemes, open-loop control does not possess a self-correcting mechanism, and therefore, open-loop control fails to recognize the presence of the induced tube-side feed disturbance. As a result, open-loop control fails to drive  $\bar{x}_{H_2}^{outlet}$  to the desired  $\bar{x}_{H_2}^{set}$  (Fig. 2.14) since it blindly applies the pre-determined outer reforming tube wall temperature trajectory, which is independent from  $\bar{x}_{H_2}^{outlet}$ . On the contrary, under PI control,



$\bar{x}_{H_2}^{outlet}$  is driven to the desired  $\bar{x}_{H_2}^{set}$  in the presence of a tube-side feed disturbance within  $\sim 308$  seconds. This result demonstrates that the performance of PI control is superior to that of open-loop control (as well as P control) in the presence of a tube-side feed disturbance. Most importantly, the above analysis confirms that it is possible to utilize CFD software to model, design and implement feedback control schemes into a CFD model to form a closed-loop system to study disturbance compensation.

### 2.3.4 Integrating dynamic optimization and feedback

In previous sections, we demonstrate that we can design closed-loop CFD models under feedback control schemes in Ansys Fluent CFD software, and analyze and evaluate the performance of P control and PI control in the presence and absence of a tube-side feed disturbance. In both scenarios, PI control possesses the most enhanced process dynamics and zero-offset in the final  $\bar{x}_{H_2}^{outlet}$ , and therefore, it is ranked to have the best performance. Nevertheless, we strive to improve the process dynamics further, and in this regard, we would like to formulate more advanced control schemes, i.e., optimization-based control schemes, to design a closed-loop system in CFD software that drives  $\bar{x}_{H_2}^{outlet}$  to the desired  $\bar{x}_{H_2}^{set}$ . Therefore, motivated by industrial practical considerations, we devote the remaining section to the development of a dynamic optimization and integral feedback control scheme (Fig. 2.15) which generates the outer reforming tube wall temperature profile.

The majority of approximate models formulated to capture the dominant dynamics of the reforming tube for the purpose of designing optimization-based control schemes such as model predictive control (MPC) in industry are data-based models. Hence, we first derive a mathematical model capturing the relationship between  $\bar{x}_{H_2}^{outlet}$  and the outer reforming tube wall temperature by utilizing a data-driven modeling technique and CFD simulation results. It is worth emphasizing that all CFD simulation settings from the previous sections are again used in this section. From the CFD simulation result of the step-change of the maximum outer reform-

ing tube wall temperature from  $T_{Wall}^{max}(0) = 1100$  K to  $T_{Wall}^{max}(t) = 1110$  K, the dynamic response of  $\bar{x}_{H_2}^{outlet}$  exhibits a behavior that can be described by a first-order transfer function indicated by the initial non-zero slope. Hence, the discrete first-order single-input-single-output (SISO) model presented in Eq. 2.9a below is formulated to represent the transfer function of the process. Then, based on this first-order SISO model, the maximum likelihood estimation (MLE) method<sup>56,57</sup> presented in Eq. 2.9b is used to identify the appropriate model parameters with a set of outer reforming tube wall temperature and  $\bar{x}_{H_2}^{outlet}$  data from the above CFD simulation. The discrete first order SISO model and MLE formulation are presented as follows:

$$y(k) = \frac{B(s)}{A(s)} u(k) + \frac{1}{A(s)} e(k) \quad (2.9a)$$

$$\begin{cases} A(s) = a_0 + a_1 s \\ B(s) = b_0 \end{cases}$$

$$\tau(y(k), u(k)) = \arg \max_{\theta \in \Theta} \{y(k) | u(k), \theta\} \quad (2.9b)$$

where  $y(k)$  and  $u(k)$  are the process output and process input respectively,  $s$  is an independent variable on the Laplace domain of the transfer function,  $k$  is a discrete time variable,  $\tau(y(k), u(k))$  is the maximum likelihood estimator,  $\theta = [a_0 \ a_1 \ b_0]$  is the parameter vector of the estimated model, and  $e(k)$  is assumed to be a value of a white noise function with zero mean and a standard deviation of 1. Utilizing the aforementioned strategy,  $a_0$ ,  $a_1$  and  $b_0$  are estimated to be  $2.188 \times 10^{-3}$ , 1.000 and  $1.764 \times 10^{-5}$  respectively, and therefore, the approximate model that describes the dominant dynamics of the reforming tube is created.

Subsequently, this dynamic model is applied in the Matlab MPC Design Toolbox for the calculation of an optimal maximum outer reforming tube wall temperature trajectory,  $T_{Wall}^{max,p}(t_k + \Delta t)$ , based on the desired  $\bar{x}_{H_2}^{set}$  and aforementioned constraints on the outer reforming tube wall temperature (Eq. 2.8c-2.8d). Based on this reference manipulated input trajectory, the proposed dynamic optimization and integral feedback control scheme is formulated as follows:

$$\begin{cases} e(t_k) = \bar{x}_{H_2}^{set} - \bar{x}_{H_2}^{outlet}(t_k) \\ u_I(t_k) = \frac{1}{\tau_I} \int_{t_0}^{t_k} e(\tau) d\tau \\ T_{Wall}^{max}(t_k + \Delta t) = \\ \quad T_{Wall}^{max,p}(t_k + \Delta t) + u_I(t_k) \end{cases} \quad (2.10a)$$

$$T_{min} \leq T_{Wall}(x, t_k + \Delta t) \leq T_{max} \quad (2.10b)$$

$$T_{Wall}(x, t_k + \Delta t) = \quad (2.10c)$$

$$\begin{bmatrix} x^4 & x^3 & x^2 & x^1 & x^0 \end{bmatrix} \begin{bmatrix} -0.0221 \\ 0.8003 \\ -10.734 \\ 64.416 \\ T_{Wall}^{max}(t_k + \Delta t) - 151.83 \end{bmatrix}$$

where  $T_{Wall}^{max,p}(t_k + \Delta t)$  is the reference manipulated input trajectory determined at  $t_k + \Delta t$  from the dynamic optimization using the MPC algorithm in Matlab. At the end of each sampling time interval, a measurement of  $\bar{x}_{H_2}^{outlet}$  acquired from CFD simulation is used to evaluate the current deviation of  $\bar{x}^{outlet}$  from the desired  $\bar{x}_{H_2}^{set}$ , and the corresponding integral control action,  $u_I(t_k)$ , is determined. Then,  $T_{Wall}^{max,p}(t_k + \Delta t)$ , obtained from the strategy described in the preceding paragraph, is adjusted by  $u_I(t_k)$  to yield the predicted  $T_{Wall}^{max}(t_k + \Delta t)$  as the manipulated input to the closed-loop CFD model.

We compare the performance of the dynamic optimization and integral feedback control scheme with those of PI feedback control and open-loop control based on the two aforementioned criteria for control performance in Sec. 2.3.2. It is worth mentioning that the primary role of integral control in the dynamic optimization and integral feedback control scheme is to guarantee that  $\bar{x}_{H_2}^{outlet}$  can always attain the desired  $\bar{x}_{H_2}^{set}$  even in the presence of a tube-side

feed disturbance. In the case of set-point tracking control under a tube-side feed disturbance, both the dynamic optimization and integral feedback control scheme and the PI control scheme can drive the system to the desired set-point; however, the dynamic optimization and integral feedback control scheme predicts a slightly different outer reforming tube temperature trajectory than that predicted by PI control as shown in Fig. 2.17. Specifically, the maximum outer reforming tube wall temperature of the closed-loop system under the dynamic optimization with integral control scheme is initially maintained at 1200 K for nearly 40 *seconds* as shown in Fig. 2.16, which speeds up the process dynamic response. Based on the metric that we previously defined in this study, it only takes  $\sim 33$  seconds for  $\bar{x}_{H_2}^{outlet}$  to first achieve the desired  $\bar{x}_{H_2}^{set}$  under the dynamic optimization with integral feedback control scheme as shown in Fig. 2.17, corresponding to an improvement of 89.3% when compared with the system under PI control for which it takes  $\sim 308$  seconds. Nevertheless, the aggressive manipulated input generated by the dynamic optimization with integral feedback control scheme also causes the oscillation of  $\bar{x}_{H_2}^{outlet}$  around the desired  $\bar{x}_{H_2}^{set}$ . Therefore, it is important to notice that although the dynamic optimization with integral control scheme allows  $\bar{x}_{H_2}^{outlet}$  to advance to the desired  $\bar{x}_{H_2}^{set}$  much faster than PI control, it ultimately requires a longer duration to reach the optimized steady-state conditions and results in oscillation; and therefore, its performance is comparable with that of PI feedback control.

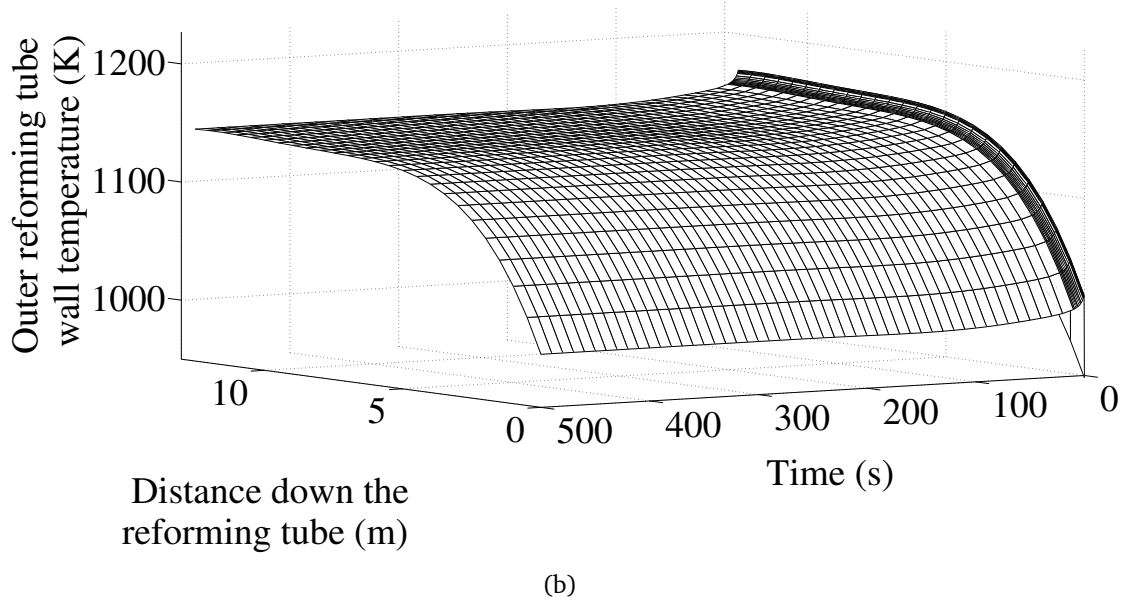
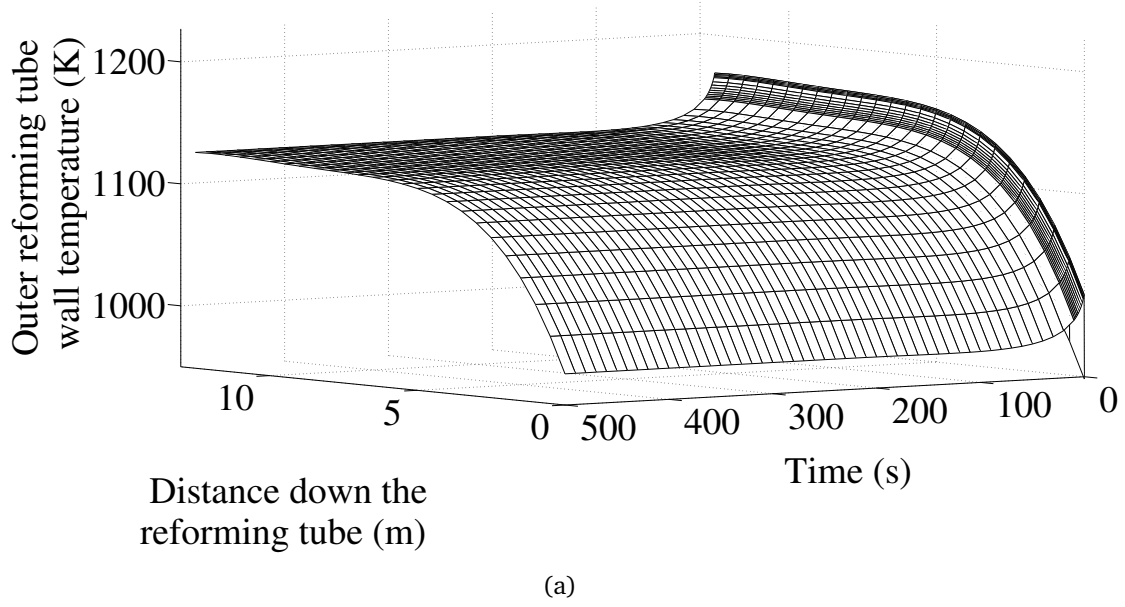


Figure 2.11: The outer reforming tube wall temperature profile trajectory in the absence of a tube-side feed disturbance under P control shown in Fig. 2.11(a) and under PI control shown in Fig. 2.11(b) with  $\bar{x}_{H_2}^{set} = 0.465$ .

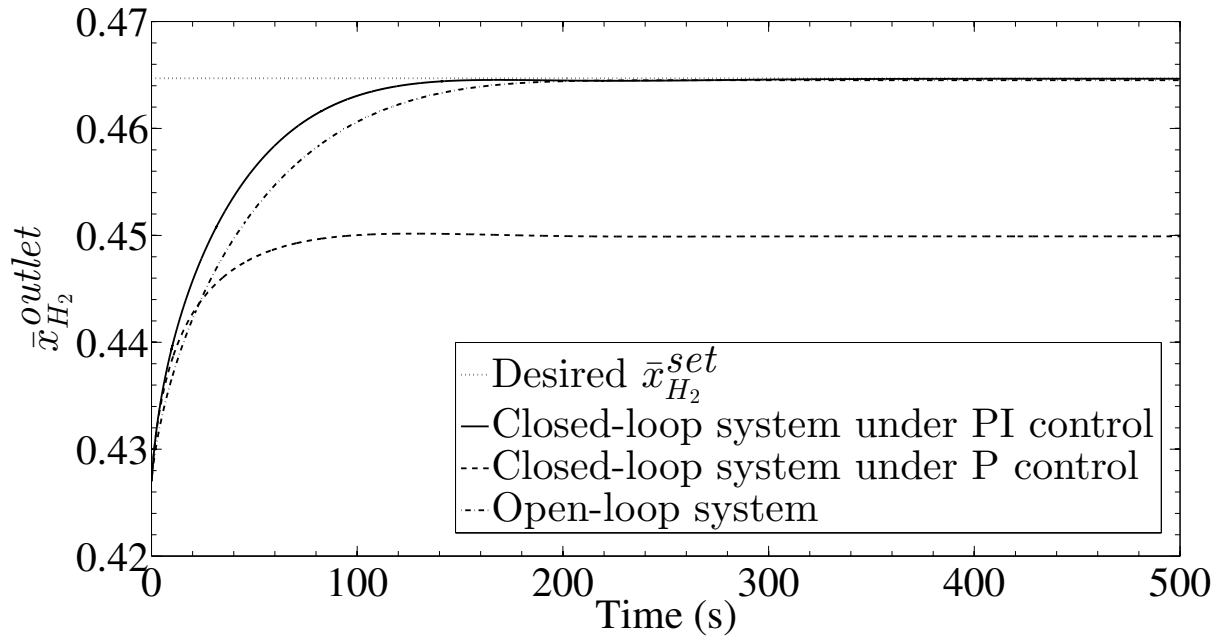


Figure 2.12: The propagation of  $\bar{x}_{H_2}^{outlet}$  with time in the absence of a tube-side feed disturbance under P control (solid line) and under PI control (dashed line). The open-loop system response (dashed-dotted line) is also included for a wall temperature profile for which  $\bar{x}_{H_2}^{set} = 0.465$ .

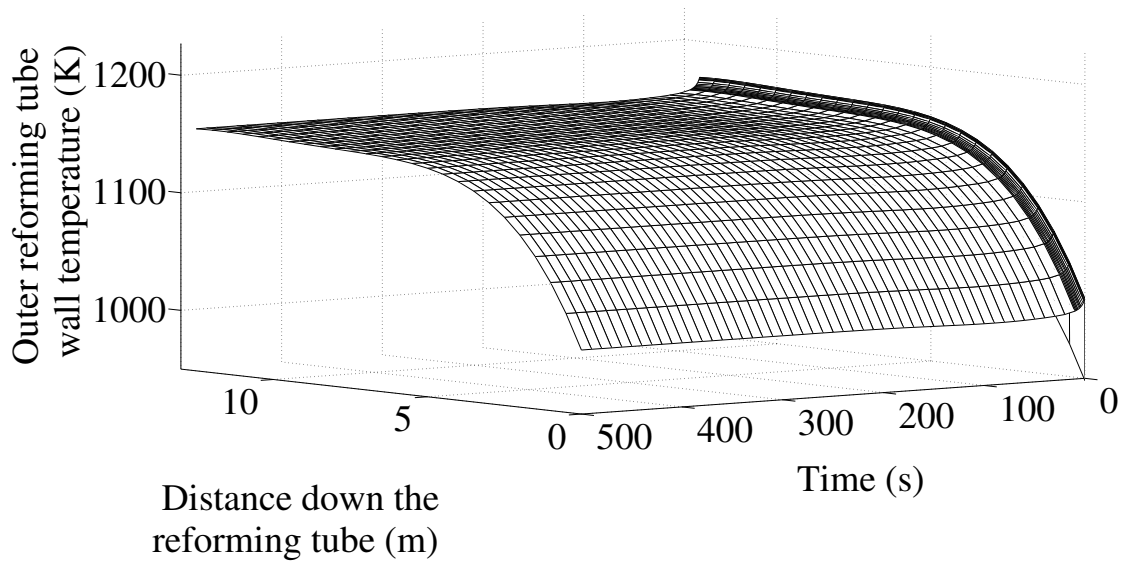


Figure 2.13: The outer reforming tube wall temperature profile trajectory in the presence of a disturbance in the tube-side feed under PI control with  $\bar{x}_{H_2}^{set} = 0.465$ .

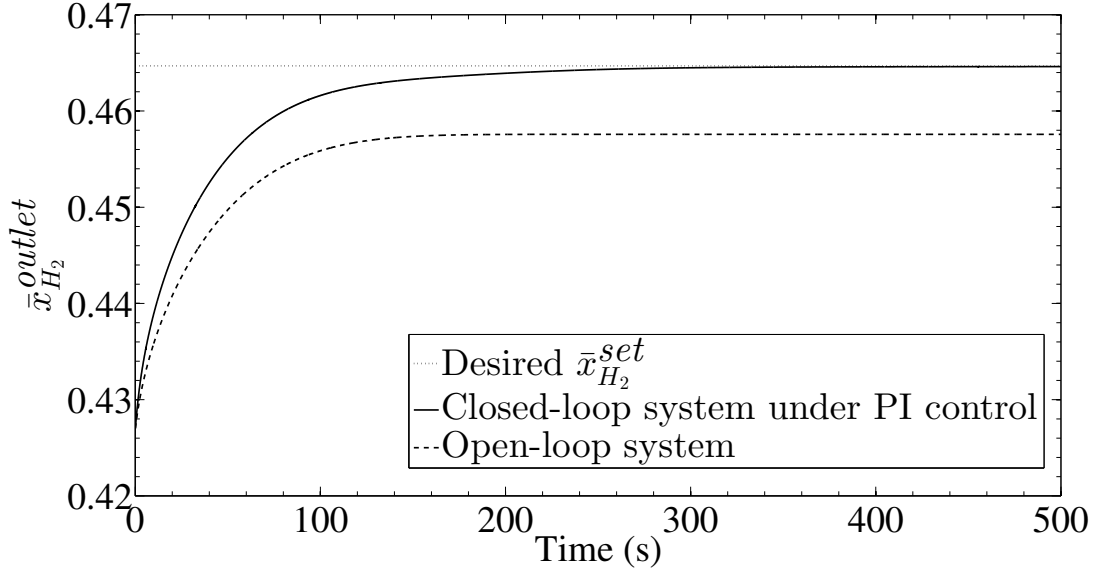


Figure 2.14: The propagation of  $\bar{x}_{H_2}^{outlet}$  with time in the presence of a disturbance in the tube-side feed under PI control (solid line) and under open-loop control (dashed line) for a wall temperature profile for which  $\bar{x}_{H_2}^{set} = 0.465$ .

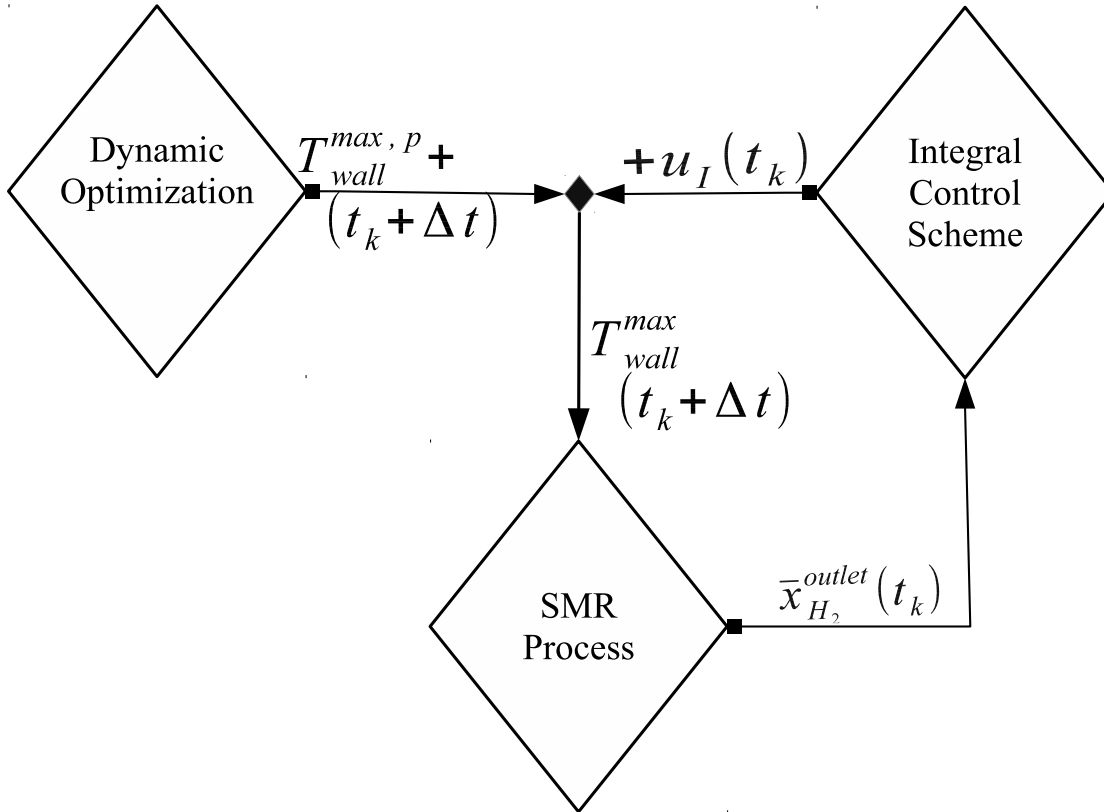


Figure 2.15: Dynamic optimization and integral feedback control scheme, where the manipulated input at  $t_k + \Delta t$  is computed based on the reference manipulated input profile at  $t_k + \Delta t$  and the integral control action at  $t_k$ , which is described in Eq. 2.10.

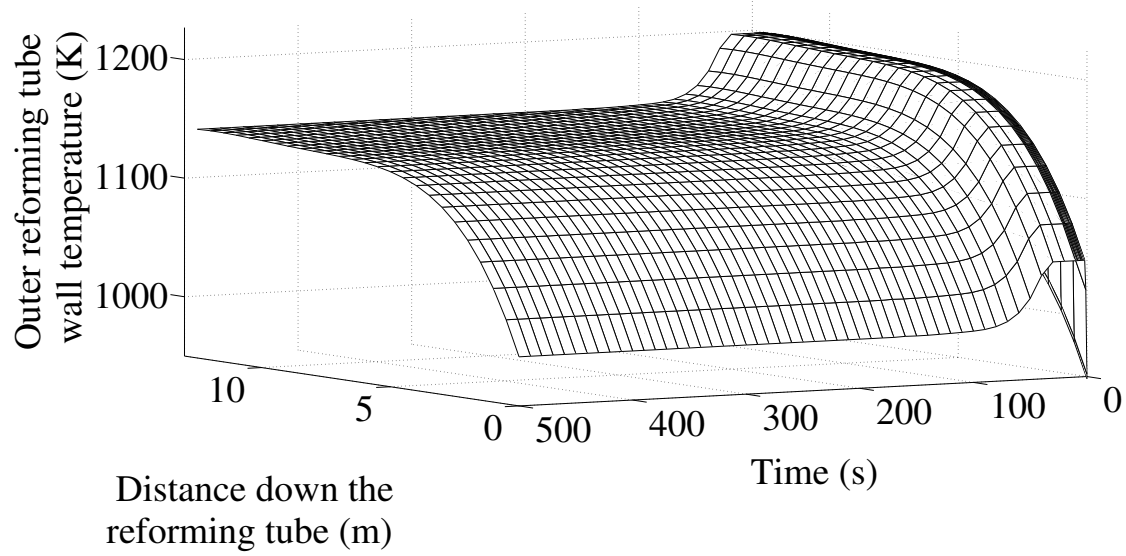


Figure 2.16: The outer reforming tube wall temperature profile trajectory in the presence of a tube-side feed disturbance under the dynamic optimization with integral feedback control scheme with  $\bar{x}_{H_2}^{set} = 0.465$ .

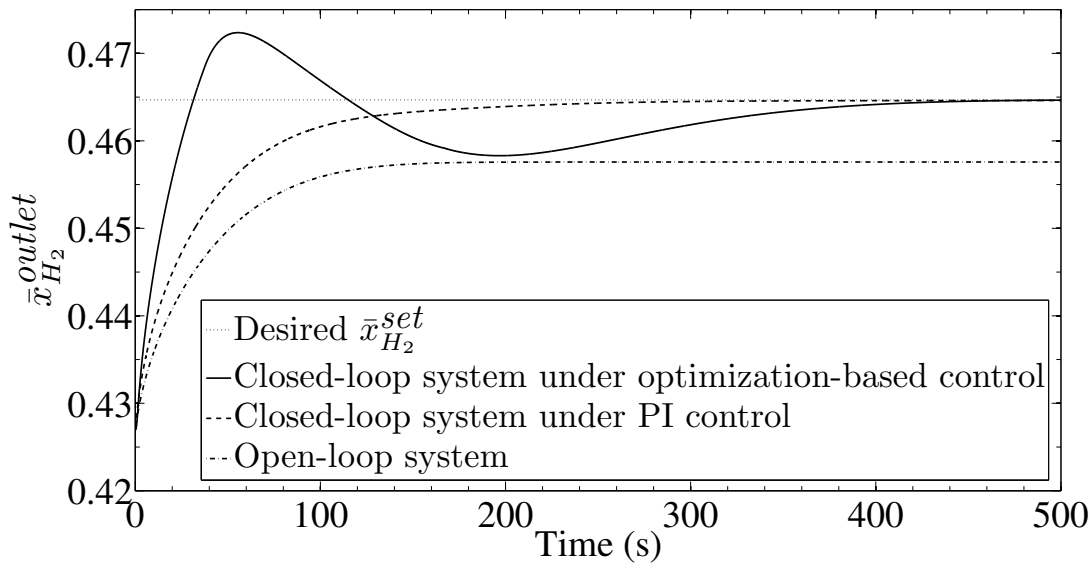


Figure 2.17: The propagation of  $\bar{x}_{H_2}^{outlet}$  with time in the presence of a tube-side feed disturbance under the dynamic optimization with integral feedback control scheme (solid line) and under PI control (dashed line). The open-loop system response (dashed-dotted line) is also included for a wall temperature profile for which  $\bar{x}_{H_2}^{set} = 0.465$ .



## 2.4 Conclusions

This work initially focused on demonstrating that CFD software can be employed to create a detailed CFD model of an industrial-scale steam methane reforming tube, and subsequently focused on the design and implementation of feedback control schemes into the CFD model. The simulation results of the reforming tube CFD model simulating the transport and chemical reaction phenomena with a detailed representation of the catalyst packing matched well with the available industrial plant data. The closed-loop CFD simulation results demonstrated that the proposed PI control scheme and a control scheme combining dynamic optimization and integral feedback control could drive the value of  $\bar{x}_{H_2}^{outlet}$  to a desired  $\bar{x}_{H_2}^{set}$ , and significantly improve the process dynamics compared to that under open-loop control. In the case of set-point tracking control under a tube-side feed disturbance, the dynamic optimization with integral feedback control scheme calculates a more aggressive outer reforming tube wall temperature trajectory compared to that calculated by PI control but both control systems drive the average outlet hydrogen mole fraction to the set-point.

# Chapter 3

## CFD modeling of the pilot scale furnace

### 3.1 Motivation

Energy consumption is frequently the second largest operating cost in many U.S. industries. Approximately 30% of the energy delivered to a manufacturing site is lost as waste heat. One of the aforementioned industries is petroleum refining, which converts crude oil into a variety of products with higher economic value, e.g. gasoline. In chemical process plants and petroleum refineries, hydrogen is produced primarily by the steam methane reforming (SMR) process, synthesizing hydrogen and carbon oxides from methane and super-heated steam in the presence of a nickel-based catalyst network in a steam methane reformer. The necessity for an accurate development of this model stems from the desired smart manufacturing platform, which aims to enable data, modeling and simulation technologies for active real-time decision to manage energy use in conjunction with production performance metrics.

## 3.2 Background

Hydrogen is one of the most important raw materials for petroleum refineries that convert crude oil into a variety of products with higher economic value, e.g., gasoline, jet fuel and diesel, and its unavailability can limit the production rates of these petroleum products. The environmental requirement for low-sulfur-content fuels results in an increasing amount of hydrogen required by hydrotreating processes, and the attempt to process heavier components of the crude oil known as bottom-of-the-barrel processing also increases the demand for hydrogen in hydrocracking processes.<sup>66,71</sup> Additionally, hydrogen can also be used as a fuel. Hydrogen is an efficient energy carrier, e.g, it can be converted into electrical energy by electrochemical reactions taking place inside fuel cells, which consist of three primary components, i.e., a cathode, an anode and an ion exchange membrane separating the electrodes. Particularly, hydrogen molecules are split into electrons and positively charged hydrogen ions at the anode by electrochemical reactions inside the fuel cell, and then the newly generated ions pass through the ion exchange membrane, which generates an electric potential between the electrodes.

Hydrogen is industrially produced primarily by the steam reforming process and partial oxidation of hydrocarbons.<sup>4</sup> Specifically, the steam reforming process is an overall endothermic process in which raw natural gas, e.g., methane, reacts with high-pressure, high-temperature steam (superheated steam) in the presence of a nickel-based catalyst to produce hydrogen, carbon dioxide and carbon monoxide. The partial oxidation of hydrocarbons, e.g., natural gas, petroleum coke and light naphtha, is an exothermic process in which hydrocarbons react with a limited amount of oxygen, typically less than the stoichiometric amount required for complete oxidation of the hydrocarbons to carbon dioxide and water, to produce hydrogen and carbon oxides (predominantly carbon monoxide).

It is worth noting that the amount of hydrogen produced by the partial oxidation process is always less than that produced by the steam reforming process for a fixed amount of raw material. As a result, the steam reforming process, specifically, the steam methane reforming (SMR)

process (shown in Fig. 1.1), remains the most economic and common commercial method for industrial hydrogen production.<sup>60</sup>

A steam methane reformer (it will be referred to as “reformer” in the following text) is the core unit in a SMR process, and it comes in four typical configurations, i.e., top-fired, side-fired, bottom-fired and terrace wall-fired reformers, which are categorized based on the burner arrangements. It is important to note that the terrace wall-fired configuration is a modification of the bottom-fired reformer, and therefore, they possess similar characteristics. Specifically, they are known to produce an approximately constant heat flux profile across the heated reforming tube length.<sup>14</sup> The top-fired reformers are characterized by a temperature field inside the combustion chamber for which the maximum temperature value and maximum heat flux are located in the upper part of the reformer.<sup>14</sup> Lastly, the characteristic of side-fired reformers that differentiates them from the other three configurations is that they allow control of the reforming tube wall temperature, which in turn offers more flexible design and operation to generate a desired temperature distribution throughout the reformer. Nevertheless, the number of burners in side-fired reformers is  $\sim 4$  times as many as that in top-fired units with a similar amount of thermal energy transferred to the reforming tubes.<sup>14</sup> Therefore, a top-fired configuration, which includes burners located at the reformer ceiling, flue gas tunnels located at the reformer floor allowing the furnace-side mixture to exit the reformer, and reforming tubes, is employed most frequently in hydrogen plants and the petroleum refinery industry, and is the subject of this work.

The top-fired reformer is composed of two closed domains including a tube side, which consists of tubular reforming reactors (they will be referred to as the “reforming tubes”) and a furnace side, which is a combustion chamber. The combustion chamber encapsulates the thermal energy released by the oxidation of the furnace-side feed composed of methane, hydrogen, carbon oxides and air, to prevent it from escaping to the surrounding environment through the combustion chamber refractory walls. Typically, only  $\sim 2\% - 4\%$  of the total fired duty is

lost, while a significant percentage of trapped thermal energy, e.g.,  $\sim 50\%$ , is transferred to the reforming tubes, primarily by radiative heat transfer.<sup>14</sup> The remaining energy leaves the reformer by species transport through the chamber outlet. In the tube side, prior to entering the reforming tubes, raw natural gas undergoes a hydro-treating process to remove sulfur compounds to prevent the nickel-based catalyst of the steam methane reforming process from being poisoned and deactivated. Additionally, this hydro-treated natural gas also undergoes a hydro-cracking process to remove unsaturated hydrocarbon compounds, and as a result, the major component of pre-treated natural gas is methane. Subsequently, the pre-treated natural gas is mixed with superheated steam prior to be fed into the reforming tubes where an overall endothermic SMR process driven by the thermal energy absorbed from the furnace side and facilitated by the nickel-based catalyst network converts steam and methane into the desired product, i.e., hydrogen, and byproducts, i.e., carbon oxides (including  $\text{CO}$  and  $\text{CO}_2$ ).

In 2004, the hydrogen production rate and annual growth rate of hydrogen production in North America were estimated to be  $6.7 \times 10^6 \text{ Nm}^3/\text{h}$  and above 4%, respectively,<sup>38</sup> and the largest plant could produce up to  $3.0 \times 10^5 \text{ Nm}^3/\text{h}$ .<sup>38</sup> Due to the aforementioned hydrogen production rate of plants, the annual cost of raw materials alone would be on the order of millions of dollars. For instance, a hydrogen plant with a production rate of  $1.120 \times 10^5 \text{ Nm}^3/\text{h}$  can spend up to 62 million dollars on raw natural gas annually.<sup>38</sup> Therefore, a small improvement in process efficiency results in a great gain in profit margin of a plant. This became the driving force for the development of reformer study, and specifically, reformer parametric study has become a highly researched topic. Since the mid-1900s, extensive work has been conducted on the development of reformer first-principles modeling, and in the 1960s,<sup>46</sup> the first mathematical model of a complete reformer was developed and proposed. This mathematical model of reformers gradually became more sophisticated and highly complex in order to account for physical phenomena, i.e., the transport of turbulence, momentum, materials and energy, and chemical phenomena, i.e., combustion processes and the SMR process, taking place inside the unit. As a result, the mathematical model of the complete reformer composed of two governing

equation sets, i.e., the continuity equation, and momentum, species and energy conservation equations, is a set of highly non-linear coupled differential equations, which are solved simultaneously to characterize the reformer. Unfortunately, solving the mathematical model of the complete reformer is a formidable task.

With the onset of technology evolution, computational fluid dynamics (CFD) modeling became a powerful tool for predicting fluid behavior with a high level of accuracy, and also one of the most effective tools employed in reformer parametric study because the parametric effect can be visualized and quantified through CFD simulations. Additionally, CFD modeling can precisely capture all geometry characteristics of a given reformer through computer-aided design software, which in turn allows CFD models to generate simulation results that can be expected to serve as reasonable substitutes for experimental data. Therefore, CFD modeling has gained popularity and become the primary method for reformer parametric study to replace the traditional on-site experimental approach for optimizing the SMR process, which is time-consuming, expensive and potentially risky.

For example, the SMR process converting superheated steam and methane into carbon oxides and hydrogen is an overall endothermic and reversible process, and therefore, in order to maintain or increase the hydrogen production rate, thermal energy has to be continuously supplied to replenish that consumed by the SMR process. It is important to note that hydrogen conversion for the SMR process depends primarily on the temperature field inside the combustion chamber, and more specifically, the temperature of the outer reforming tube wall, i.e., a higher outer reforming tube wall temperature theoretically results in a higher hydrogen conversion. Nevertheless, operating at excessively high temperature decreases the reforming tube expected life span, i.e., an increase in outer reforming tube wall temperature of 20 K can reduce the reforming tube lifetime by half<sup>54,38</sup>. In addition, it might cause the reforming tube wall to lose its integrity and to rupture, which results in production and capital losses. Specifically, the required total capital investment to replace a typical industrial-scale reformer

is estimated to be 5–8 million USD.<sup>54</sup> Consequently, on-site parametric study to determine the optimized furnace-side feed flow rate to the burners must be carried out with small changes in the parameters, while the outer reforming tube walls are closely monitored in order to avoid the aforementioned production and capital losses. Therefore, this high-risk study usually is conducted over a long time period, and is costly. On the contrary, simulation results generated by a well-developed reformer CFD model are expected to be consistent with experimental data collected from industrial-scale plants because CFD models are capable of capturing not only physical and chemical phenomena, but also the geometry of a reformer. Therefore, CFD modeling can be used as an alternate method for parametric study. Furthermore, a well-developed CFD model of a reformer can provide insights into the system which cannot be captured in experimental data generated by on-site parametric study or by solution of a complete reformer mathematical model, e.g., the species distributions inside the combustion chamber.

Motivated by the above considerations, we initially employ *ANSYS Fluent* CFD software to develop a pilot-scale reformer CFD model that is composed of four industrial-scale reforming tubes of which the external diameter, internal diameter and heated length are 14.6 cm, 12.6 cm, 12.5 m, respectively, three industrial-scale burners (details given in Sec. 3.3) and three flue gas tunnels. It is important to note that the industrial-scale reforming tube modeling strategy is adopted from our previous work,<sup>37</sup> which has an approximate representation of the catalyst network that can account for the presence of catalyst particles inside the reforming tube, and the effect of internal and external diffusion limitations on the observed reaction rates of the SMR process (details given in Sec. 3.5.2). The boundary conditions for the reforming tube inlet (referred to in the following text as “tube-side feed”), burner inlet (referred to in the following text as “furnace-side feed”), and combustion chamber refractory walls are consistent with typical plant data, so that simulation data generated by the pilot-scale reformer is in agreement with the former data.<sup>38</sup> Based on the conditions of the tube-side feed and furnace-side feed, and the expected physical and chemical phenomena taking place inside the reformer, the standard  $k-\epsilon$  turbulence model, finite rate/eddy dissipation turbulence chemistry interaction

model (details given in Sec. 3.7) and global kinetic models of combustion processes<sup>649</sup> and the SMR process<sup>70</sup> are implemented to capture the individual species reaction rates in the turbulent reacting flow. Next, the simulation results generated by the pilot-scale reformer CFD model are rigorously validated by comparing them with available data in the literature and simulation results generated by a well-developed single reforming tube CFD model. Finally, we conduct a parametric study on furnace-side feed flow rate variation, i.e., a 20% increase in the furnace-side inlet mass flow rate is introduced, in order to demonstrate the importance of the pilot-scale CFD model for evaluating conditions that may not be safely accessed experimentally.

### 3.3 Industrial Steam Methane Reformer Geometry

The pilot-scale reformer investigated in this work is developed based on an industrial-scale top-fired, co-current reformer designed by Sela Fluid Processing Corporation (Figs. 3.1-3.2). This industrial-scale reformer produces  $2.83 \times 10^6 \text{ Nm}^3$  of high-purity hydrogen along with 1708800 kg of superheated steam (i.e., 663 K and 4580 kPa) per day.<sup>38</sup> The combustion chamber of this industrial-scale reformer contains seven rows of forty-eight reforming tubes. The external diameter, internal diameter and exposed length of these reforming tubes are 14.6 cm, 12.6 cm, 12.5 m, respectively. Inside these reforming tubes, nickel-based catalyst pellets, specifically, alpha-alumina-supported nickel oxide denoted as  $\text{NiO} - \alpha\text{Al}_2\text{O}_3$ , are used as packing material to facilitate the formation of hydrogen from steam and methane through the endothermic SMR process, and to act as an intermediate medium to enhance the rate of convective heat transfer to the tube-side gas mixture. At the combustion chamber ceiling, these rows of reforming tubes are separated by eight rows of twelve burners which are fed with a furnace-side feed composed of two separate streams, i.e., a fuel stream composed of natural gas and tail gas ( $\text{CO}$  and  $\text{H}_2$ ), and an oxidizer stream composed of combustion air ( $\text{Ar}$ ,  $\text{N}_2$  and  $\text{O}_2$ ). It is important to mention that the rows of burners adjacent to the combustion chamber re-



fractory walls and a single row of reforming tubes (for brevity, these burners are denoted as “outer-lane burners”) are fed with a lower furnace-side feed flow rate than the rows of burners adjacent to two rows of reforming tubes (for brevity, these burners are denoted as “inner-lane burners”). Specifically, the furnace-side feed flow rate of the outer-lane burners is 60% of that of the inner-lane burners to avoid causing “over-firing” in the outer lanes and “under-firing” in the inner lanes, which would occur if the same furnace-side feed flow rate were fed to all burners. Based on typical flow rates and species compositions of the fuel and oxidizer streams of an inner-lane burner, the fuel stream of the furnace-side feed is completely oxidized over a flame length of 4.5–6m releasing the thermal energy needed to drive the SMR process.<sup>38</sup> The thermal energy released by combusting the furnace-side feed is transferred to the reforming tubes predominantly by radiative heat transfer inside the high-temperature furnace chamber. At the reformer floor, the rows of reforming tubes are separated by the rectangular intrusions known as flue gas tunnels or coffin boxes which extend from the front to the back of the combustion chamber along the rows of reforming tubes with a height of 2.86 m from the floor. Additionally, there are thirty-five extraction ports evenly distributed in a row along each side of the flue gas tunnels that allow the furnace flue gas to enter the flue gas tunnels, and then to exit the combustion chamber through the front openings of the flue gas tunnels. In this work, we will focus on the development and analysis of a CFD model of a pilot-scale version of the industrial-scale reformer described above.

### **3.3.1 Geometry of Pilot-scale SMR Unit**

As noted, this work focuses on the development of a pilot-scale version of the industrial-scale reformer described in the previous section. The pilot-scale reformer contains the reforming tubes, inner-lane burners, outer-lane burners and extraction ports, with the same dimensions and geometry as those of the industrial-scale reformer. It is critical for our work to obtain a pilot-scale reformer geometry such that the environment of each individual component is

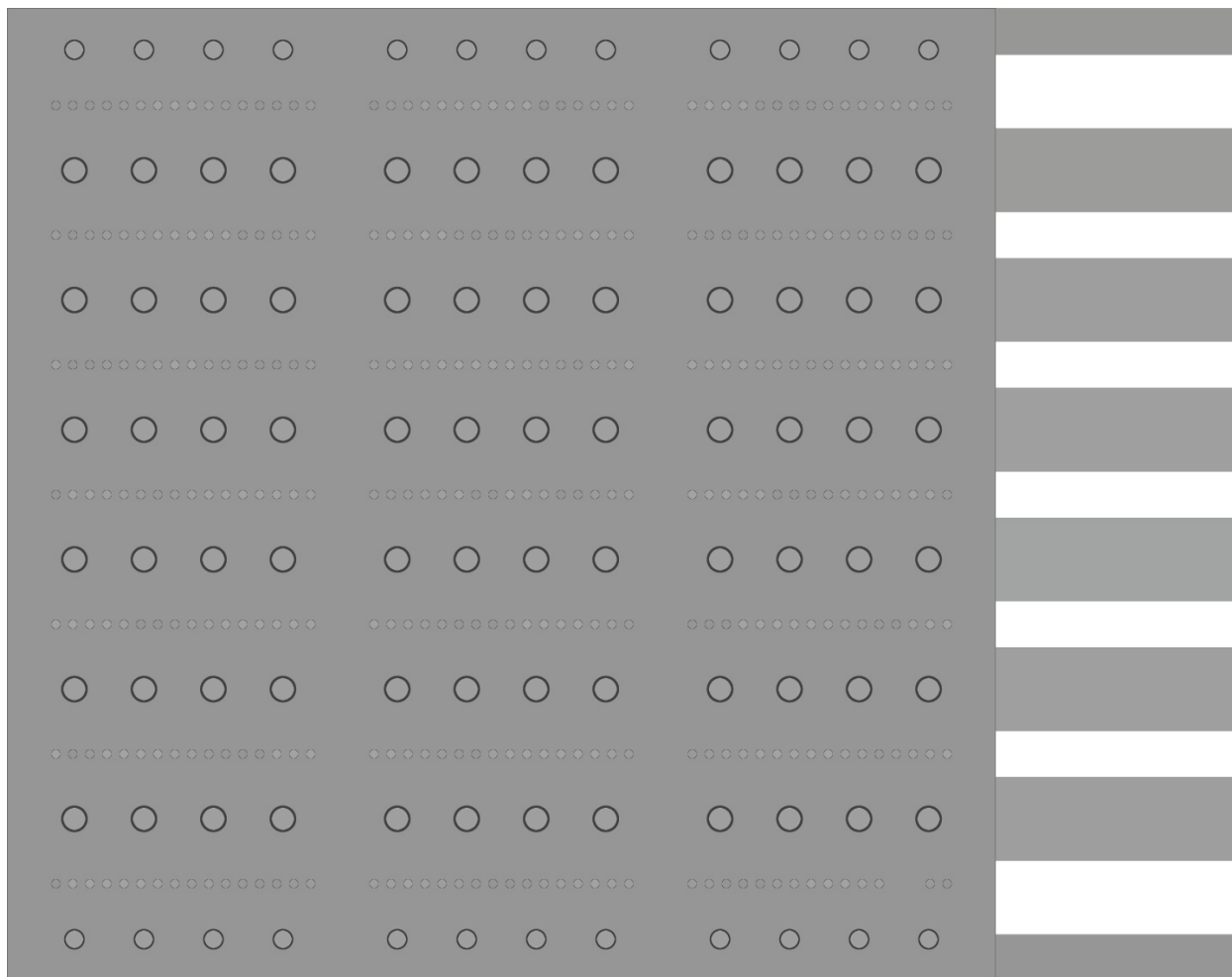


Figure 3.1: The top view of an industrial-scale, top-fired, co-current reformer with 336 reforming tubes, which are symbolized by 336 smaller circles, and 96 burners, which are denoted by 96 larger circles. The outer-lane burners are shown as the circles on the right and left boundaries of the figure, while the inner-lane burners are shown as slightly larger circles within the figure.

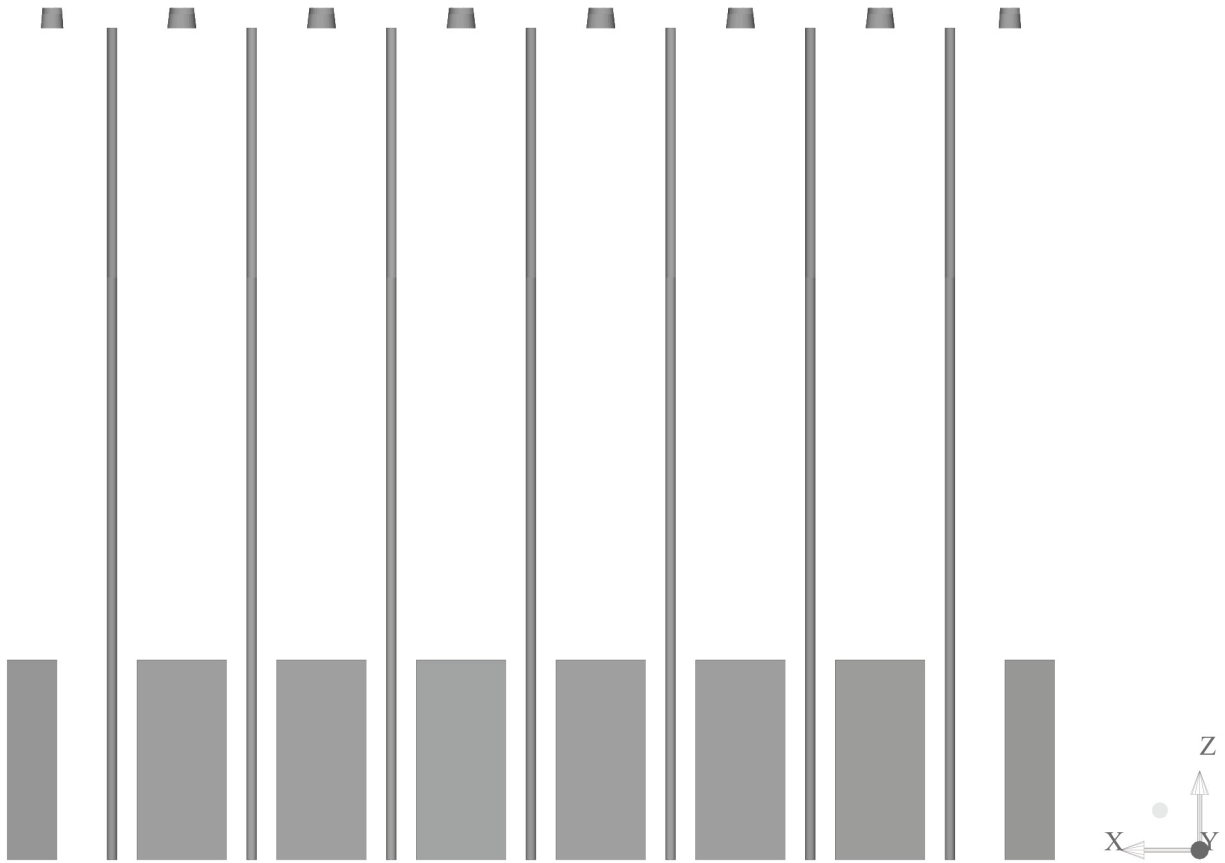


Figure 3.2: The front view of an industrial-scale, top-fired, co-current reformer. It is important to note that the refractory wall of the combustion chamber is modeled to be transparent, so that the interior components, which include eight rectangular boxes located on the floor representing the flue gas tunnels, eight frustums of cones located on the ceiling representing the corresponding rows of burners and seven slender rectangles connecting the ceiling and floor representing the corresponding rows of reforming tubes, can be seen.

as close as possible (if not identical) to that in the industrial-scale unit. Thus, in this pilot-scale reformer CFD model, there are two rows of two reforming tubes, and each is surrounded by two rows of burners. Based on the estimated thermal energy released by combusting the furnace-side feed for one inner-lane burner and the expected thermal energy absorbed by each reforming tube from the available industrial data, it is determined that only one burner is needed in each row of burners in this pilot-scale reformer to provide the desired heat to the reforming tubes. As mentioned in the previous section, there are two types of burners in the industrial-scale reformer, i.e., the outer-lane burners, which are adjacent to one row of reforming tubes and to the refractory wall of the combustion chamber, and the inner-lane burners, which are adjacent to two rows of reforming tubes. Additionally, it is important to note that the outer-lane burners are smaller in size, and are fed with 40% less of the furnace-side feed than the inner-lane burners. Furthermore, in this pilot-scale reformer CFD model, the rows of reforming tubes are also separated by the flue gas tunnels with extraction ports at the floor of the combustion chamber as they are in the industrial-scale reformer. The geometry of the pilot-scale reformer is shown in Fig. 3.3.

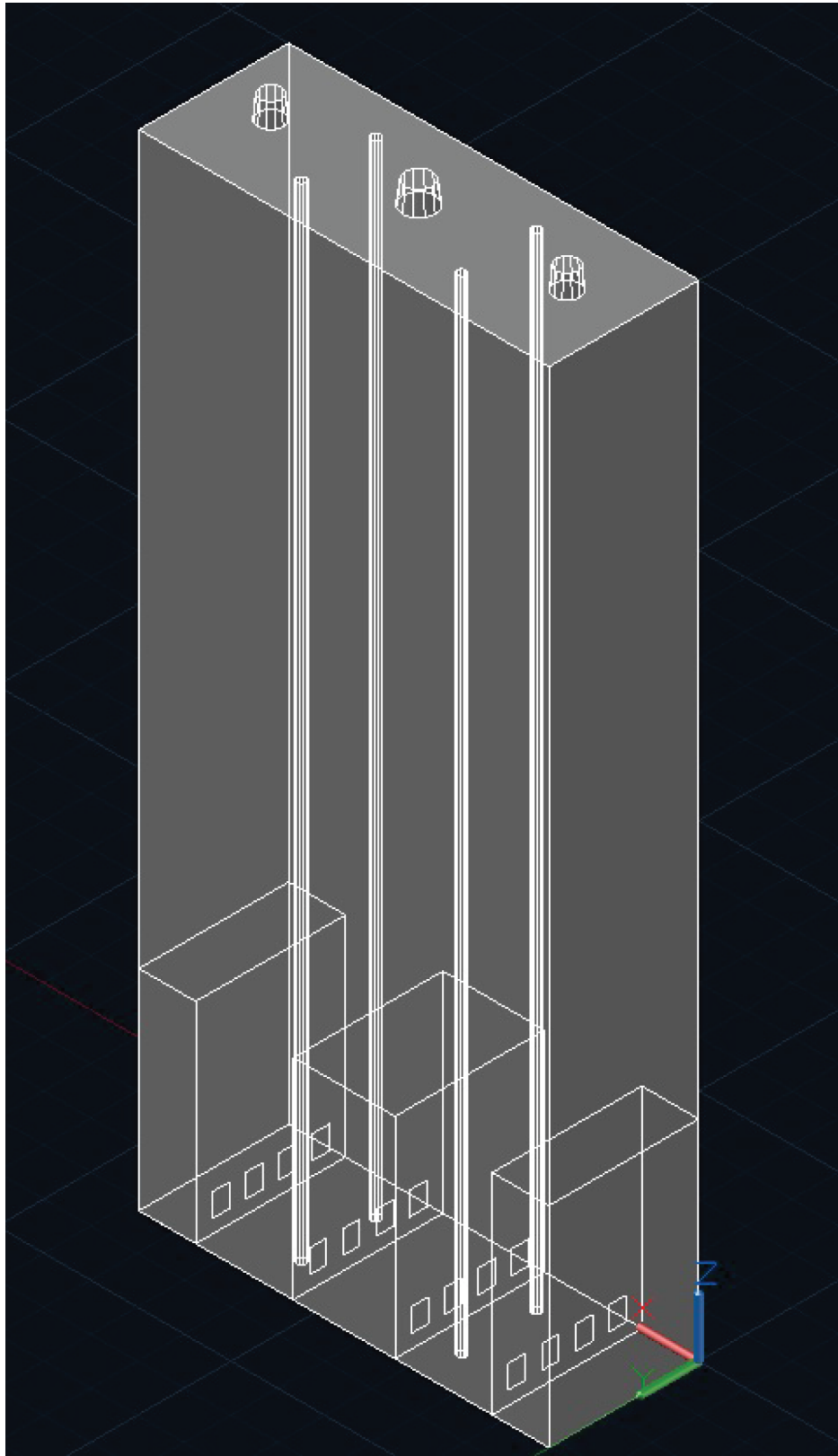


Figure 3.3: CAD geometry of pilot-scale furnace model.

### 3.3.2 Mesh of Pilot-scale SMR Unit

Due to the tightly coupled chemical, physical and transport phenomena taking place inside the pilot-scale reformer and the multi-step complex reaction schemes (i.e., the SMR process<sup>70</sup> and combustion reactions) with corresponding nonlinear empirical kinetic formulas, it is impossible to obtain an analytical solution to characterize the fluid-flow and temperature fields. Instead, the computational domain is divided into fine, discrete elements also known as grids, wherein spatial variations are relatively small. The governing equations (i.e., the continuity equation and the momentum, material, energy and turbulence conservation balances) required for characterizing the heat and fluid-flow fields inside the pilot-scale reformer are numerically solved for each grid. Then, the numerical solutions of the grids are patched together to reconstruct the solution of the original domain. Hence, creating a mesh with acceptable mesh quality is a critical task that determines the success level of CFD modeling because a poor quality mesh needs the most robust CFD solver and demands greater computing resources to determine a converged solution. Additionally, a CFD model with a poor quality mesh has a slow speed of convergence and is more likely to converge to an inaccurate solution because mesh quality directly determines solver discretization error.<sup>26</sup>

There are two major classes of meshing strategies, i.e., the unstructured tetrahedral meshing strategy (for simplicity, it is denoted as “unstructured meshing” in the following text) wherein discrete grids are arranged in an irregular pattern, and the multiblock structured hexahedral meshing strategy (for simplicity, it is denoted as “structured meshing” in the following text). Although unstructured meshing is more proficient at approximating complicated geometries than structured meshing, the latter class is chosen to develop a CFD model of this pilot-scale reformer (Figs. 3.4–3.5) since the pilot-scale reformer geometry shown in Fig. 3.3 is composed primarily of straight edges. Additionally, for wall-bounded systems like the pilot-scale reformer, a CFD model built from structured meshing generally generates a converged solution closer to experimental data and also has a superior speed of convergence compared to

other CFD models built from unstructured meshing when the system is decomposed into the same number of discrete grids.<sup>26</sup> Furthermore, the *ANSYS ICEM* environment provides an O-grid Block function to enhance the structured meshing's ability to approximate curvy geometry characteristics by re-arranging existing grid lines into an *O* shape to effectively improve the overall mesh quality.<sup>26</sup> In the pilot-scale reformer CFD model, the sub-mesh regions of the inner-lane burner, outer-lane burners and reforming tubes shown in Figs. 3.6–3.8 are created by the O-grid Block function due to their unique geometry characteristics. Specifically, the burners have a frustum-like structure, and the reforming tubes have a cylindrical structure. It is important to note that in this pilot-scale reformer the grids are not uniformly distributed but instead they are designed to be more dense in the regions that are expected to have large momentum, material and temperature gradients as shown in Figs. 3.4–3.5.

An example of a cluster of regions within which the grid density is higher, is within and around the reforming tubes, where the process of transferring thermal energy from the furnace-side mixture to the tube-side mixture is very complex. Specifically, the thermal energy released from combusting the furnace-side feed is transferred to the reforming tube outer wall mostly by radiative heat transfer. Then, it is conducted to the inner reforming tube wall and to the catalyst network, and finally, it is transferred to the tube-side mixture by convective heat transfer. Therefore, to capture the process through which thermal energy is transferred from the furnace-side mixture to the tube-side mixture, the grid density in the aforementioned regions is designed to be more dense to account for the large spatial gradients. Similarly, in the flame regions where the combustion process of the furnace-side feed takes place as previously mentioned in Sec. 3.3, large spatial variations of transport variables are expected. Additionally, because the reaction rates for the combustion process are fast and are described by nonlinear empirical kinetic formulas, the formation/consumption rates of the components of the furnace-side feed are directly controlled by the transport rates of these components. Therefore, it is essential that the sub-mesh regions of the burners and their vicinity, shown in Fig. 3.5, and of the flame regions inside the combustion chamber, are composed of finer grids in order to more

accurately predict the species distributions, and to simulate the flame characteristics.

The mesh of the pilot-scale reformer, shown in Fig. 3.4, accounting for all of the above considerations, contains 165,817 hexahedral grids, 516,325 quadrilateral cells and 184,636 nodes. The mesh quality of the pilot-scale reformer mesh chosen to construct the CFD model for the remaining investigation is evaluated based on three suggested criteria including the orthogonal factor, aspect ratio and ortho skew as shown in Table 3.1. It is important to note that a mesh is considered to have poor quality if the mesh quality is outside of the recommended range for any of the three criteria; the mesh quality values of the pilot-scale reformer are above all minimum recommended values and below all maximum recommended values as shown in the table, and thus, can be considered to have reasonably good quality.

Table 3.1: Mesh quality of the pilot-scale reformer mesh.

	<b>Pilot-scale unit mesh value</b>	<b>Recommended value</b>
Minimum orthogonal factor	0.3934	0.1667
Maximum ortho skew	0.6066	0.85
Maximum aspect ratio	16.14	100.0

### 3.4 Furnace Chamber Modeling

In the pilot-scale reformer, the composition of the furnace-side feed is identical to that of the industrial-scale unit, where the furnace-side feed is composed of the fuel stream ( $CH_4$ ,  $CO$  and  $H_2$ ) and the oxidizer stream ( $Ar$ ,  $N_2$  and  $O_2$ ). Nevertheless, due to a significant difference between the industrial-scale and pilot-scale reformers in the ratio of the number of reforming tubes to the number of burners, i.e., the ratios in the industrial-scale and pilot-scale reformers are 3.50 and 1.33, respectively, when the furnace-side feed flow rate of the inner-lane burners from the industrial-scale reformer is implemented in the pilot-scale unit, the reforming tubes will have an excessively high outer reforming tube wall temperature, which can lead to disastrous consequences and significant capital loss as discussed in Ch.3. Therefore, an adjustment



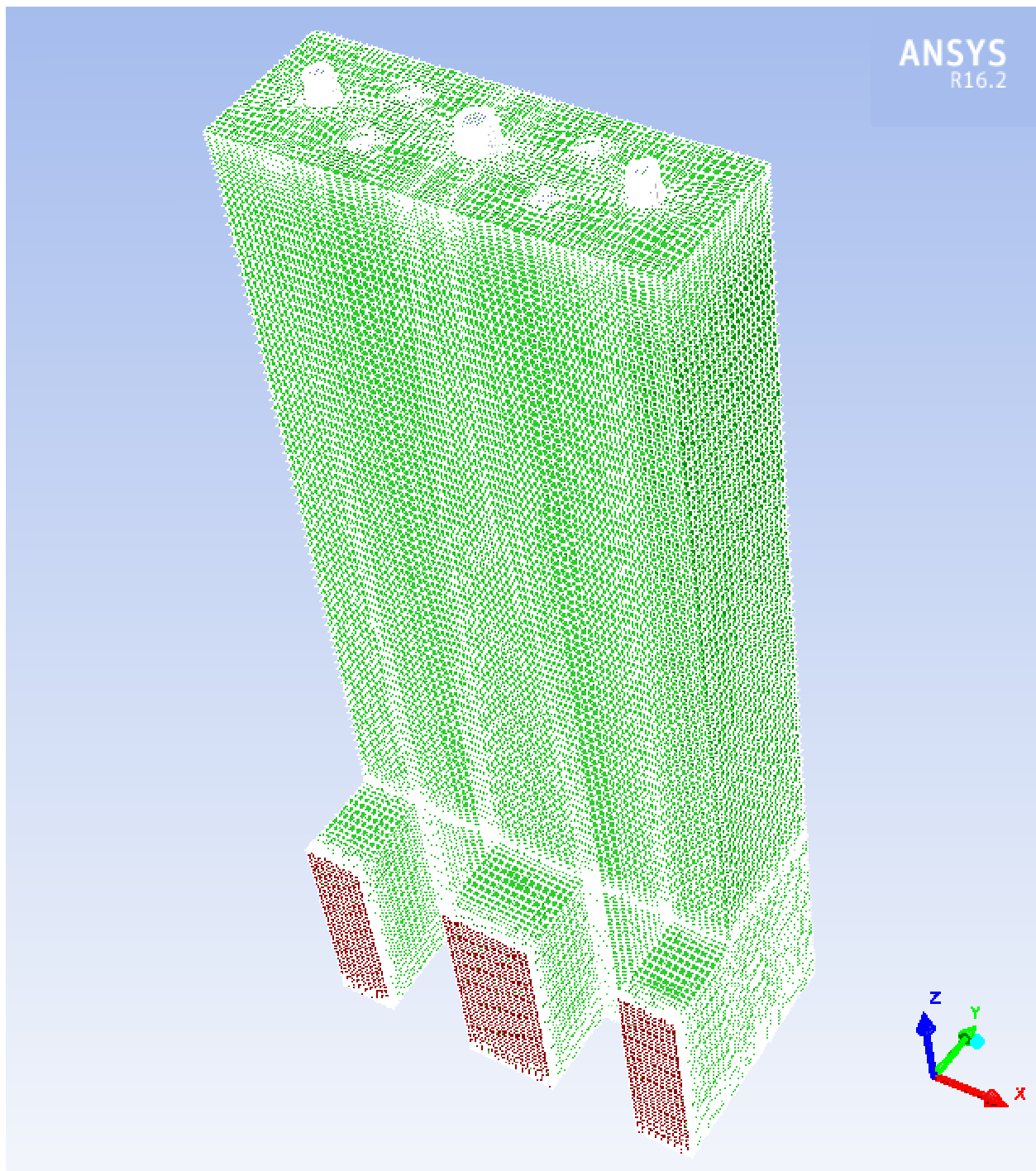


Figure 3.4: Isometric view of the hexahedral structured mesh of the pilot-scale reformer.

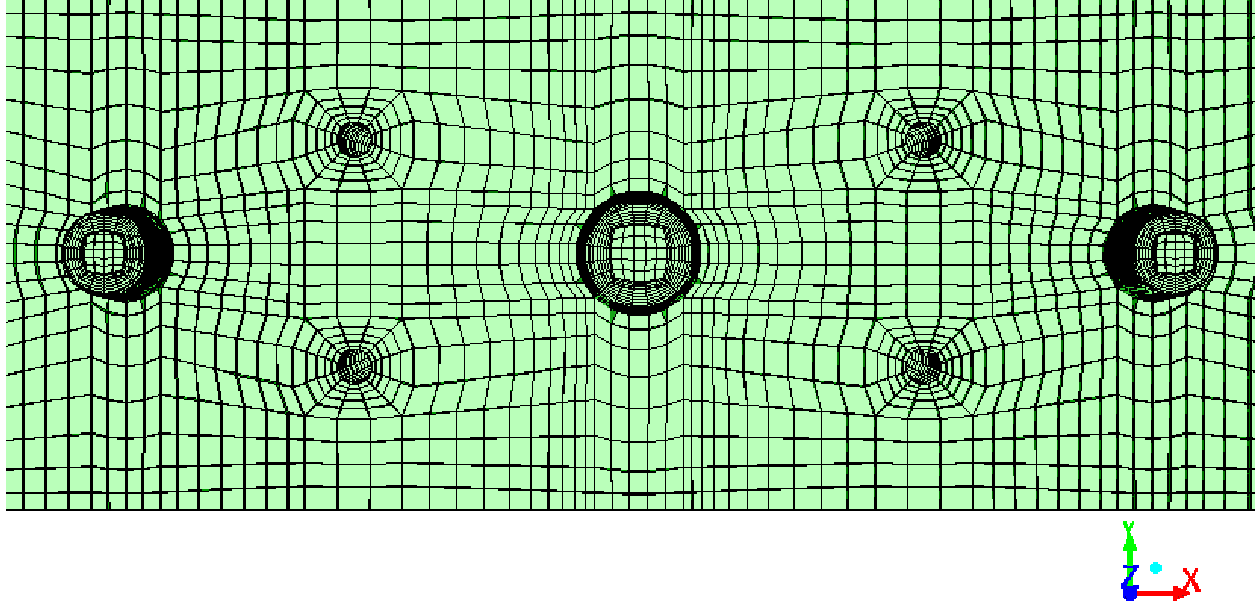


Figure 3.5: Top view of the hexahedral structured mesh of the pilot-scale reformer. This figure demonstrates that the geometries of the outer-lane burners, inner-lane burners and reforming tubes are successfully preserved by means of the O-grid Block function of *ANSYS ICEM*.

is made to the furnace-side feed flow rate of the inner-lane burner in the pilot-scale reformer to avoid the aforementioned issue. Specifically, the furnace-side feed flow rate is decreased to 37.5% of that in the industrial-scale reformer based on the estimated thermal energy released by combusting the furnace-side feed of a single inner-lane burner in the industrial-scale reformer, the expected average heat flux across the reforming tube wall and the amount of heat absorbed by each reforming tube. Additionally, in the pilot-scale reformer CFD model, the ratio of the inner-lane burner and outer-lane burner furnace-side feed flow rates is 0.6 as in the industrial-scale reformer.

### 3.4.1 Combustion Reaction Kinetic Model and Turbulence Chemistry Model

In the combustion chamber, methane and hydrogen in the furnace-side feed are completely oxidized to generate carbon dioxide, water and a large amount of thermal energy required

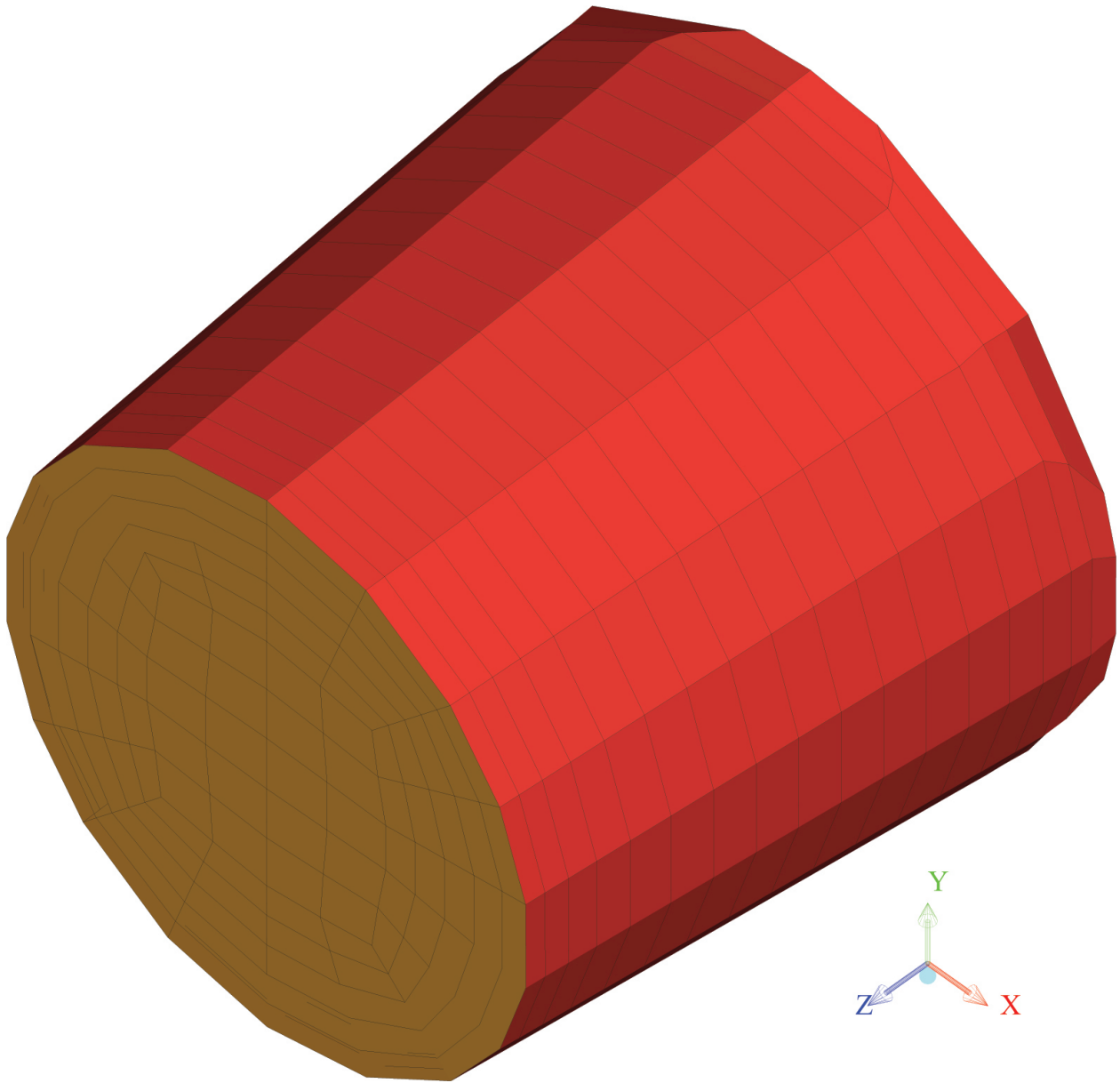


Figure 3.6: Isometric view of the hexahedral structured mesh of the inner-lane burner.

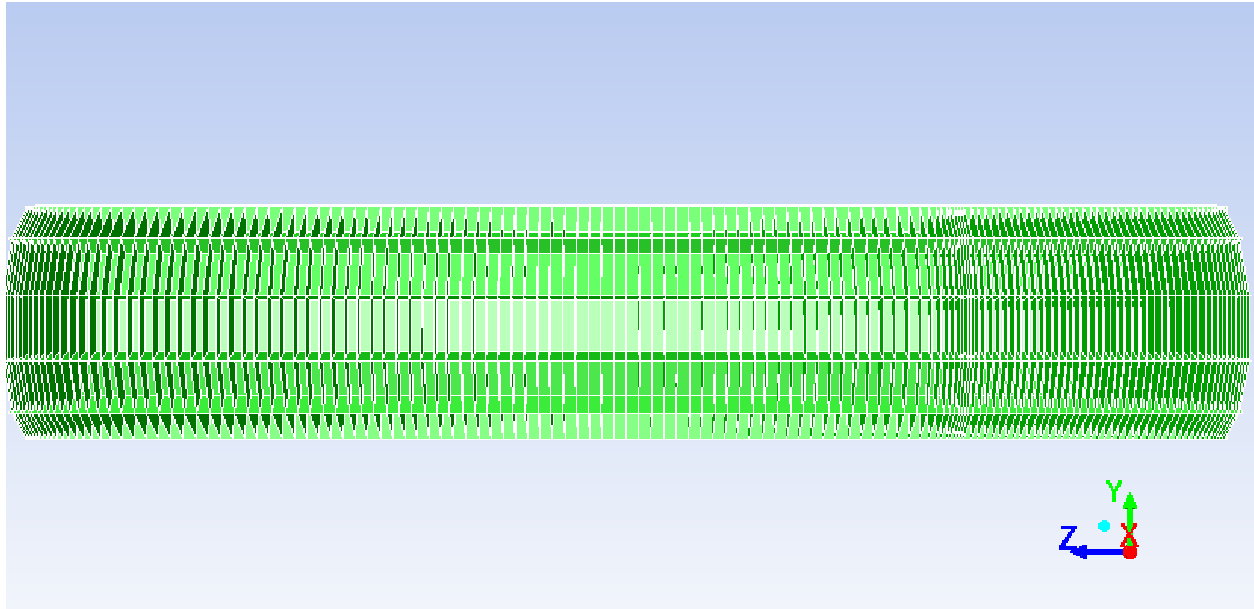


Figure 3.7: Side view of the hexahedral structured mesh of a reforming tube. In this figure, the radial direction is scaled up by 20 times for display purposes only.

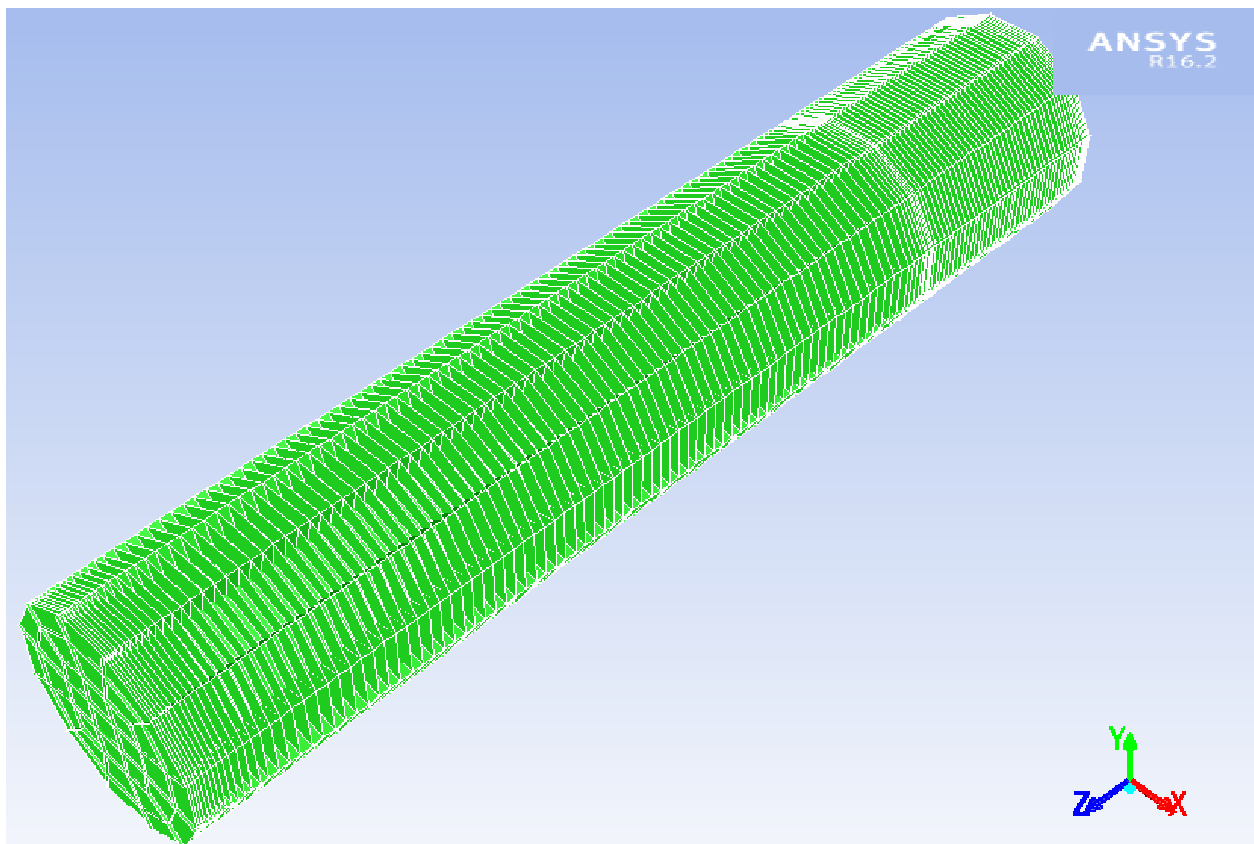
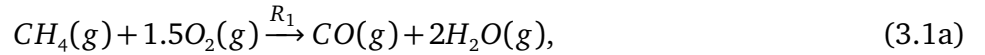


Figure 3.8: Isometric view of the hexahedral structured mesh of a reforming tube. In this figure, the radial direction is scaled up by 20 times for display purposes only.

by the SMR process. It is important to note that the chemistry of the combustion process is a complex network of sequential elementary reactions governed by the concentrations of free radicals, which are reactive molecules with unpaired electrons. For instance, the complete mechanism of the hydrogen combustion process generating water involves more than 20 elementary reactions and various intermediates.<sup>65</sup> Therefore, the computing power required to simulate a pilot-scale reformer CFD model implemented with a complete reaction mechanism providing the detailed descriptions of all elementary steps involved in the formation and consumption rates of free radicals and intermediates of the methane and hydrogen oxidation processes would be too demanding. As a result, simplified global kinetic models for the combustion of methane<sup>49</sup> and hydrogen<sup>6</sup> are adopted to reduce the computational requirement for simulating the pilot-scale reformer CFD model. In detail, the combustion processes for natural gas and hydrogen considered in this work involve a two-step mechanism and a single-step mechanism respectively with reaction rates given by the following global kinetic models:



$$R_1 = 10^{15.22} [CH_4]^{1.46} [O_2]^{0.5217} \exp(-20643/T) \quad (3.1b)$$



$$R_2 = 10^{14.902} [CO]^{1.6904} [O_2]^{1.57} \exp(-11613/T) \quad (3.1d)$$

$$R_3 = 10^{14.349} [CO_2] \exp(-62281/T) \quad (3.1e)$$



$$R_4 = 4.61 \times 10^{15} [H_2][O_2] \exp(-10080/T) \quad (3.2b)$$

where  $R_1$ ,  $R_2$ ,  $R_3$  and  $R_4$  are the intrinsic volumetric reaction rates and are measured in  $\text{kmol/m}^3\text{s}$   $T$  (K) is the temperature of the surrounding environment in which the reactions take place and  $[CO_2]$ ,  $[CO]$ ,  $[O_2]$ ,  $[H_2]$  and  $[CH_4]$  are the molar concentrations of the corresponding species and have the units of  $\text{kmol/m}^3$ . As these empirical kinetic formulas are in the Arrhenius form, they can be directly implemented into the pilot-scale reformer CFD model to simulate the formation and consumption rates of the individual species.

Table 3.2: Furnace-side inlet operating conditions of the inner-lane burner. Pressure (P), temperature (T), flow rate (F)

P (kPa)	132.4
T (K)	525
F (kg/s)	0.4056
$x_{H_2O}$	0.03061
$x_{O_2}$	0.15305
$x_{Ar}$	0.00765
$x_{N_2}$	0.57396
$x_{H_2}$	0.05399
$x_{CO_2}$	0.10797
$x_{CO}$	0.02113
$x_{CH_4}$	0.05164

In the industrial-scale reformer, the furnace-side feed composed of two separate streams, i.e., the fuel stream and the oxidizer stream, is combusted inside the combustion chamber to generate the required fired duty for the SMR process. It is important to note that the intrinsic nature of non-premixed combustion is turbulent mixing-controlled, i.e., the rate of the chemical reactions is relatively faster than that of mixing, and the observed formation and consumption rates of each individual species depends on the rate of mixing. In the remain of this section, we demonstrate the modeling strategy that allows the pilot-scale reformer CFD model with the pre-mixed combustion model to exhibit the nature of non-premixed combustion processes.

Specifically, in the pilot-scale reformer CFD model, the fuel stream and oxidizer stream of the furnace-side feed are assumed to be well-mixed prior to being fed into the combustion chamber where the fuel stream is fully oxidized to generate the needed thermal energy for the SMR process. Thus, the pressure, temperature, flow rate and species composition of the furnace-

side feed of the inner-lane burner are shown in Table 3.2, and the combustion of methane and hydrogen is modeled by the premixed combustion model. However, the intrinsic nature of non-premixed combustion processes must be shown in the simulation result generated by the pilot-scale reformer CFD model with the premixed combustion model. This issue is resolved by using the finite-rate/eddy-dissipation (FR/ED) model as the turbulence-chemistry interaction model to simulate the rates of formation and consumption of each individual species in the turbulent flow. In particular, the FR/ED model estimates the observed reaction rate of species  $i$ , for which  $i$  are components of the furnace-side mixture, based on the global kinetic models shown in Eqs. 3.1–3.2 and the eddy-dissipation reaction rates (as shown in Eq. 3.3):<sup>26</sup>

$$R_{i,j} = \nu_{i,j} M_i A \rho \frac{\epsilon}{k} \min_{\mathcal{R}} \left( \frac{Y_{\mathcal{R}}}{\nu_{\mathcal{R},j} M_{\mathcal{R}}} \right) \quad (3.3a)$$

$$R_{i,j} = \nu_{i,j} M_i B \rho \frac{\epsilon}{k} \frac{\sum_{\mathcal{P}} Y_{\mathcal{P}}}{\sum_n \nu_{n,j} M_n} \quad (3.3b)$$

$$R_{i,j} = \nu_{i,j} M_i R_j \quad (3.3c)$$

where  $R_{i,j}$  (kg/m<sup>3</sup>s) and  $\nu_{i,j}$  are the consumption/formation rate and stoichiometric coefficient of species  $i$  in reaction  $j$ ,  $M_i$  is the molecular weight of species  $i$ ,  $Y_{\mathcal{R}}$  and  $M_{\mathcal{R}}$  are the mass fraction and molecular weight of a specified reactant  $\mathcal{R}$ ,  $\nu_{\mathcal{R},j}$  is the stoichiometric coefficient of a specified reactant  $\mathcal{R}$  in reaction  $j$ ,  $A$  and  $B$  are empirical constants equal to 4.0 and 0.5,  $k$  and  $\epsilon$  are the turbulence kinetic energy and dissipation rate (which will be discussed in a subsequent section),  $Y_{\mathcal{P}}$  is the mass fraction of a product species  $\mathcal{P}$  in reaction  $j$ ,  $R_j$  (kmol/m<sup>3</sup>s) is the consumption/formation rate of reaction  $j$  from Eqs. 3.1–3.2,  $\rho$  is the local average density of the furnace-side mixture and  $n$  is the index of the product species involved in reaction  $j$ .<sup>26</sup>

When the FR/ED model as shown in Eq. 3.3 is adopted in the pilot-scale reformer CFD model, the observed reaction rate of species  $i$  is equal to the minimum reaction rate between Eqs. 3.3a, 3.3b, and 3.3c to reduce the discrepancy between the premixed-combustion model

and non-premixed combustion processes. Particularly, the furnace-side feed is fed into the combustion chamber at 525 K, and at this temperature the species  $i$  reaction rate (Eq. 3.3c), calculated based on the given reaction kinetic models (Eqs. 3.1–3.2), is smaller than that calculated based on the eddy-dissipation reaction rate because of the well-mixed furnace-side feed assumption. Thus, the observed reaction rate of species  $i$  at the burner inlet is estimated based on the former approach. However, within the flame region the species  $i$  rate of change calculated based on the given reaction kinetic models is greater than that calculated based on the eddy-dissipation reaction rate because of the flame temperature. Thus, the observed reaction rate of species  $i$  is determined based on the eddy-dissipation reaction rate. This shows that by using the minimum reaction rate from Eqs. 3.3a-3.3c, the fuel is prevented from being immediately oxidized when it first enters the combustion chamber.<sup>26</sup> As a result, the premixed combustion model coupled with the FR/ED model exhibits the turbulent-mixing controlled characteristics of non-premixed combustion processes. It is worth noting that due to the use of the simplified global kinetic models for the combustion of methane and hydrogen, the FR/ED model is selected as a suitable turbulence-chemistry interaction model for the pilot-scale reformer CFD model. This is because when the global reaction mechanisms for methane and hydrogen combustion consist of less than three elementary reactions, the CFD model implemented with FR/ED model is expected to produce an accurate converged solution.<sup>26</sup>

### 3.4.2 Radiation Heat Transfer Modeling

Inside the combustion chamber, it has been established that thermal energy is transferred predominantly by radiative heat transfer, and as a result, a computationally efficient and accurate radiation model is critical to the success of the pilot-scale reformer CFD model. Due to the complexity of the combustion chamber geometry as described in Sec. 3.3.1 and the complicated thermal coupling of the furnace side and the process side, a differential approximation radiation model, also known as  $P-1$ , is employed to determine the rate at which energy is trans-



ferred by radiative heat transfer inside the combustion chamber.<sup>26</sup> This is because the  $P-1$  model can easily be applied to complicated geometries with curvilinear coordinates, while the radiative energy transfer can be accurately computed with minimal CPU requirement.<sup>26</sup> It is important to note that in this work, the furnace-side mixture is assumed to be a non-scattering medium, and as a result, the  $P-1$  model is formulated as shown in Eq. 3.4:

$$\vec{q}_{rad} = -\frac{1}{3\sigma_a} \nabla G \quad (3.4a)$$

$$-\nabla \cdot \vec{q}_{rad} = \sigma_a G - 4\sigma_a n_{comb}^2 \sigma T^4 \quad (3.4b)$$

$$\nabla \cdot \left( \frac{1}{3\sigma_a} \nabla G \right) = \sigma_a G - 4\sigma_a \sigma T^4 \quad (3.4c)$$

$$\vec{q}_{rad}^{wall} = -\frac{\epsilon_{wall}}{2(2-\epsilon_{wall})} (4n_{comb}^2 \sigma T_{wall}^4 - G_{wall}) \quad (3.4d)$$

where  $\sigma_a$  and  $n_{comb}$  are the absorption coefficient and refractive index of the furnace-side mixture, which are estimated based on the weighted sum of gray gas (WSGG) model,  $\sigma$  is the Stefan-Boltzmann constant,  $\epsilon_{wall}$  is the internal emissivity coefficient of the wall,  $T$  and  $T_{wall}$  are the temperatures at a location inside the furnace chamber and at the wall surface where energy is transferred by radiative heat transfer, respectively  $G$  and  $G_{wall}$  are the incident radiation at a location inside the furnace chamber and at the wall surface where energy is transferred by radiative heat transfer, respectively, and analogously  $\vec{q}_{rad}$  and  $\vec{q}_{rad}^{wall}$  are the radiative heat fluxes at a location inside the furnace chamber and at the wall surface where energy is transferred by radiative heat transfer. It is noteworthy that the transport equation for  $G$  (as shown in Eq. 3.4c) is formed by substituting Eq. 3.4a into Eq. 3.4b, which is solved to determine the local radiation intensity, and to ultimately estimate the local radiative heat transfer ( $\vec{q}_{rad}$ ).<sup>26</sup> Additionally, it is critical to a successful modeling task to realize that the internal emissivity of the wall surface is an intrinsic property of the surface, and therefore, it only depends on the surface's characteristics, e.g., the surface texture, instead of the surface material. In the pilot-scale reformer

CFD model, the assumption of a temperature-independent emissivity coefficient for the wall surfaces is employed. Specifically, the emissivity coefficients of the reforming tubes, refractory wall and tunnel wall are chosen to be 0.85, 0.65 and 0.65, respectively.<sup>38</sup>

Table 3.3: Combustion chamber refractory walls properties.

Density (kg/m <sup>3</sup> )	3950
Heat Capacity (J/kg K)	718
Thermal Conductivity (W/mK)	2.6
Emissivity	0.65

## 3.5 Reforming Tube Modeling

### 3.5.1 Reforming Reaction Kinetic Model

In a reforming tube, the endothermic reforming reactions and water-gas shift reaction taking place at the catalyst active sites to convert reactants, i.e., steam and methane, into products, i.e., hydrogen, reach equilibrium before the tube-side mixture exits the reforming tube. Specifically, reactants are transported from the bulk of the tube-side mixture to the surface of the catalyst network by convective mass transfer driven primarily by the reactant concentration difference, which is generated by the external diffusion resistance of the catalyst network. Then, they diffuse down the reactant concentration gradient from the surface of the catalyst network through the catalyst medium to the catalyst active sites, where the reforming and water-gas shift reactions occur to generate the desired hydrogen along with carbon oxides. This reactant concentration gradient within the catalyst is generated by the internal diffusion resistance of the catalyst network. Next, the products diffuse from the catalyst active sites back to the surface of the catalyst network, and eventually emerge back into the tube-side mixture. A reaction kinetic model that provides a detailed description of all elementary steps involved in these catalyst-specific transport and reaction phenomena would be unnecessarily complex for the purpose of this work. Therefore, a simplified global kinetic model,<sup>70</sup> which is widely-

accepted, and is frequently used in CFD modeling and first-principles modeling of the SMR process, is also used in this paper to lessen the computational demand without sacrificing the accuracy of the simulation results as follows:

$$CH_4(g) + H_2O(g) \rightleftharpoons CO(g) + 3H_2(g),$$

$$R_5 = \frac{k_1}{p_{H_2}^{2.5}} \left( p_{CH_4} p_{H_2O} - \frac{p_{H_2}^3 p_{CO}}{K_1} \right) / DEN^2 \quad (3.5a)$$

$$CO(g) + H_2O(g) \rightleftharpoons CO_2(g) + H_2(g),$$

$$R_6 = \frac{k_2}{p_{H_2}} \left( p_{CO} p_{H_2O} - \frac{p_{H_2} p_{CO_2}}{K_2} \right) / DEN^2 \quad (3.5b)$$

$$CH_4(g) + 2H_2O(g) \rightleftharpoons CO_2(g) + 4H_2(g),$$

$$R_7 = \frac{k_3}{p_{H_2}^{3.5}} \left( p_{CH_4} p_{H_2O}^2 - \frac{p_{H_2}^4 p_{CO_2}}{K_3} \right) / DEN^2 \quad (3.5c)$$

$$DEN = 1 + \frac{K_{H_2O} p_{H_2O}}{p_{H_2}} \quad (3.5d)$$

$$+ K_{CO} p_{CO} + K_{H_2} p_{H_2} + K_{CH_4} p_{CH_4}$$

where  $K_{H_2}$ ,  $K_{CH_4}$  and  $K_{CO}$  are adsorption constants for  $H_2$ ,  $CH_4$  and  $CO$ ,  $K_{H_2O}$  is a dissociative adsorption constant of  $H_2O$ ,  $K_1$ ,  $K_2$ , and  $K_3$  are equilibrium constants of the reactions in Eqs. 3.5a, 3.5b and 3.5c,  $k_1$ ,  $k_2$  and  $k_3$  are kinetic constant coefficients of the reactions in Eqs. 3.5a, 3.5b, and 3.5c, respectively,  $DEN$  is a dimensionless parameter and  $p_{H_2}$ ,  $p_{CH_4}$ ,  $p_{H_2O}$ ,  $p_{CO}$  and  $p_{CO_2}$  are the partial pressures of  $H_2$ ,  $CH_4$ ,  $H_2O$ ,  $CO$  and  $CO_2$  respectively in the tube-side mixture. This kinetic model accounts for the presence of the catalyst network, and it can be reformulated to also account for the external and internal diffusion resistances of the catalyst network by multiplying the formation and consumption rates of each individual species shown in Eq. 3.5 with a universal effectiveness factor of 0.1.<sup>69</sup> However, unlike the global kinetic models of the methane and hydrogen combustion processes, the empirical kinetic for-

mulas shown in Eq. 3.5 are not in the Arrhenius form, and thus, they cannot be directly implemented within the pilot-scale reformer CFD model. Nevertheless, *ANSYS Fluent* allows these non-Arrhenius form kinetic formulas to be incorporated into the CFD model by means of user-defined functions, i.e., *DEFINE\_VR\_RATE* and *DEFINE\_NET\_REACTION\_RATE*, to simulate the formation and consumption rates of the individual components.

Table 3.4: Tube-side gas inlet operating conditions. Pressure (P), temperature (T), Flow rate (F)

P (kPa)	3038.5
T (K)	887
F (kg/s)	0.1161
$x_{CH_4}$	0.2487
$x_{H_2O}$	0.7377
$x_{CO}$	0.0001
$x_{H_2}$	0.0018
$x_{CO_2}$	0.0117

Inside the reforming tubes, the Reynolds number is calculated to be  $\sim 5500$  based on the tube-side feed information shown in Table 3.4. Therefore, a proper turbulence-chemistry interaction model is required to accurately simulate the individual species reaction rates in the turbulent reacting flow. It is worth noting that when the global kinetic model consists of three or more dependent elementary steps as does the global kinetic model of the SMR process as shown in Eq. 3.5, the CFD model implemented with the FR/ED model is likely to converge to an inaccurate solution.<sup>26</sup> This issue is remedied by means of an alternate chemistry-turbulence interaction model known as the eddy dissipation concept (EDC) model. The most important advancement offered by the EDC model is that the detailed multi-step reaction mechanism can be employed to determine the formation and consumption rates of individual species in the turbulent reacting flow with a high level of accuracy. Additionally, the EDC model with default parameters is a robust turbulence-chemistry interaction model, and can be directly applied for a vast variety of reaction-limited and diffusion-limited systems without the need to adjust its parameters.<sup>43</sup> When the EDC model is used to describe the chemistry and turbulence interactions taking place inside the tube-side mixture, the grids in the reforming domain are

decomposed into a special reaction space, which is the collection of turbulence structures.<sup>26</sup> Each turbulence structure is treated as a perfect stirred tank reactor (PSTR) for which the characteristic dimension can be calculated as shown in Eq. 3.6a. Each PSTR is assumed to operate at constant pressure over an interval equal to that of the mean residence time (estimated by Eq. 3.6b) with the initial conditions taken from the corresponding local grid, and the reactions are governed by the chosen kinetic model (Eq. 3.5)<sup>26, 43</sup> The characteristic dimension of the turbulence structure and the mean residence time are as follows:

$$\zeta^* = C_\zeta \left( \frac{\nu \epsilon}{k^2} \right)^{\frac{1}{4}} \quad (3.6a)$$

$$\tau^* = C_\tau \left( \frac{\nu}{\epsilon} \right)^{\frac{1}{2}} \quad (3.6b)$$

where  $\zeta^*$  and  $\tau^*$  are the characteristic dimension and mean residence time of the turbulence structure,  $C_\zeta = 2.1377$  is the volume fraction constant,  $C_\tau = 0.4082$  is the time scale constant,  $k$  and  $\epsilon$  are the turbulence kinetic energy and dissipation rate, respectively, and  $\nu$  is the kinematic viscosity of the turbulent reacting flow. At the end of each reacting time interval, the mass fractions of species  $i$ ,  $Y_i^*$ , evaluated at the scale of the turbulence structures are used to compute the net formation and consumption rates of the corresponding species on grid scale as shown in Eq. 3.7:

$$R_i = \frac{\rho (\zeta^*)^2}{\tau^* [1 - (\zeta^*)^3]} (Y_i^* - Y_i) \quad (3.7)$$

where  $R_i$  is the observed reaction rate of species  $i$  in the tube-side mixture which has the units of  $\frac{kmol}{m^3 s}$ , and  $Y_i$  is the average mass fraction of species  $i$ . Lastly, it is important to note that because of the intensive computational requirement needed to simulate a detailed multi-step kinetic model, the EDC model should only be implemented when the FR/ED model predicts a highly inaccurate converged solution.

Table 3.5: Johnson Matthey's Katalco 23–4Q catalyst properties.

Density, $\rho_c$	3960 kg/m <sup>3</sup>
Heat Capacity, $C_{p,c}$	880 J/(kgK)
Thermal Conductivity, $k_c$	33 W/(mK)
Particle Diameter, $D_p$	3.5 mm (average)

### 3.5.2 Porous Zone Design

In the reforming tubes, the tube-side feed composed of steam and methane enters at the ceiling of the pilot-scale reformer and passes through a wall-bounded, tightly packed catalyst network to be converted into hydrogen and carbon oxides. It is essential to the development of a pilot-scale reformer CFD model that the contribution of the catalyst network to the SMR process is well understood. Specifically, the catalyst network facilitates the formation of hydrogen from the naturally stable and slowly-reacting tube-side reactants, i.e., steam and methane, and it also enhances the rate of convective energy transfer from the inner reforming tube wall to the tube-side mixture by increasing the contact area. Additionally, the presence of the catalyst network inside the reforming tubes interferes with the tube-side flow, generating turbulence which homogenizes the tube-side mixture and prevents the tube-side mixture from quickly exiting, which ensures the SMR reactions<sup>70</sup> reach the desired equilibrium state. Furthermore, a large pressure difference between the tube-side mixture at the reforming tube inlet and outlet is expected due to the presence of the catalyst network inside the reforming tubes. Therefore, it is desirable to also model the catalyst network for the pilot-scale reformer CFD model in order to gain insight into the transport and reaction phenomena inside the reforming tube. Based on the known pressure difference, tube geometry and available intrinsic characteristics of the catalyst network as shown in Table 3.5, a set of modeling parameters required by the pilot-scale reformer CFD model to design a realistic representation of the catalyst network can be estimated through the semi-empirical Ergun equation,<sup>18</sup> which is suitable for a wide range

of Reynolds numbers and various packing patterns:

$$\frac{\Delta P}{L} = \frac{150\mu (1-\gamma)^2}{D_p^2 \gamma^3} v_\infty + \frac{1.75\rho (1-\gamma)}{D_p \gamma^3} v_\infty^2 \quad (3.8)$$

where  $\Delta P$  is the pressure difference between the tube-side mixture at the reforming tube inlet and outlet,  $L$  is the length of the reforming tubes,  $\mu$  is the viscosity of the tube-side mixture,  $\gamma$  is the porosity of the catalyst network,  $v_\infty$  is the bulk velocity of the tube-side mixture,  $\rho$  is the density of the catalyst network, and  $\frac{150\mu (1-\gamma)^2}{D_p^2 \gamma^3} = 8782800 \frac{1}{m^2}$  and  $\frac{1.75\rho (1-\gamma)}{D_p \gamma^3} = 1782 \frac{1}{m}$  are the viscous resistance coefficient and inertial resistance coefficient of the catalyst network. In this CFD model, the assumption of uniform packing is used for the catalyst network. Additionally, the coefficients of viscous resistance and inertial resistance of the catalyst network are assumed to be constant and uniform along the axial and radial directions.

### 3.6 Equation of State of Pilot-scale SMR Unit

In the pilot-scale reformer, the furnace-side mixture can be assumed to possess ideal gas characteristics, and can be described by the ideal gas law, due to its temperature and pressure. It is important to note that the ideal gas equation of state can only be used to model the behavior of a real gas at high temperature and low pressure. The maximum temperature of the furnace-side mixture is approximately  $\sim 2000$  K due to the thermal energy released by the combustion processes inside the furnace chamber. Additionally, the operating pressure of the combustion chamber is nearly at atmospheric pressure, and is  $\sim 25-28$  times smaller than that of the reforming tubes.<sup>38</sup> On the contrary, the thermodynamic behavior of the tube-side mixture deviates significantly from that governed by the ideal gas law due to the severely high operating pressure inside the reforming tubes, i.e.,  $\sim 3000$  kPa. Moreover, the SMR process taking place inside the reforming tubes is driven in the desired direction primarily by the thermal energy generated by the oxidation of methane and hydrogen inside the combustion chamber. Fur-

thermore, in the pilot-scale reformer CFD model, the Mach number of the tube-side feed is estimated to be  $\sim 0.3$  based on the available plant information as shown in Table 3.4,<sup>38</sup> and therefore, the density variations of the tube-side flow due to the high operating pressure cannot be ignored. Hence, an appropriate equation of state must be incorporated into the pilot-scale reformer CFD model to accurately describe the thermodynamics and intrinsic properties of the turbulent tube-side reacting flows.

Due to the tightly coupled chemical, physical and transport phenomena, and the complex interactions between turbulence and the multi-step nonlinear kinetic models taking place inside the pilot-scale reformer, it is extremely challenging to obtain a converged solution of the model. Additionally, simulating the pilot-scale reformer CFD model shown in Fig. 3.4 composed of 165,817 hexahedral grids, 516,325 quadrilateral cells and 184,636 nodes is expected to require large computing power and a long computation time to find a converged solution. Therefore, it is not practical to use the pilot-scale reformer CFD model as a means to obtain the most suitable equation of state that can account for the aforementioned considerations.

From our previous work, we successfully developed the CFD model of an industrial-scale reforming tube that can reproduce publicly available industrial plant data given the plant tube-side feed and outer reforming tube wall temperature.<sup>37</sup> The industrial-scale reforming tube mesh contains 23,030 quadrilateral cells and 24,460 nodes, and is considerably smaller than the pilot-scale reformer mesh, i.e., the number of quadrilateral cells inside the former mesh is approximately 5% of that inside the latter mesh. Additionally, the mesh quality of the industrial-scale reforming tube mesh is nearly ideal based on the three suggested criteria including the orthogonal factor, aspect ratio and ortho skew as shown in Table 3.6. As a result, the CFD model of the industrial-scale reforming tube allows a large reduction in the computation time required to determine a suitable equation of state for the pilot-scale reformer CFD model.

A rigorous study is conducted to select the most suitable equation of state for the CFD model



Table 3.6: Mesh quality of the industrial-scale reforming tube mesh.

	Industrial-scale reforming value	Ideal value	Recommended value
Minimum orthogal factor	1.000	1.000	0.1667
Maximum ortho skew	$4.281 \times 10^{-7}$	0.000	0.8500
Maximum aspec tratio	9.253	1.000	100.00

of the pilot-scale reformer by means of the industrial-scale reforming tube CFD model. In this effort three potential candidates, i.e., the compressible ideal gas, the real gas Soave-Redlich-Kwong (*SRK*) and the real gas Peng-Robinson (*PR*) equations of state, are selected based on the aforementioned modeling challenges and considerations, and the corresponding simulation results are shown in Table 3.7. The differences between the simulation results generated by the CFD model implemented with the compressible ideal gas equation of state and that generated by the CFD model implemented with the more sophisticated equations of state (*SRK* and *PR*) are negligible. Specifically, in the compositions of the tube-side mixture at the reforming tube outlet, the differences occur at the fifth digit after the decimal point. Additionally, the CFD model implemented with the compressible ideal gas equation of state requires less computation time to find the converged solution than the other CFD models with the more complex equations of state, and the simulation results presented in Table 3.7 show that it yields approximately the same converged solution. As a result, the compressible ideal gas equation of state is adopted in the pilot-scale reformer CFD model to describe the thermodynamics and intrinsic properties of both the tube-side and furnace-side mixtures.

### 3.7 Turbulence-Chemistry Interaction Model of Pilot-scale SMR Unit

The discussion presented in Sec. 3.4.1 demonstrates that the FR/ED turbulence-chemistry interaction model and premixed combustion model can successfully describe the characteristics

Table 3.7: Simulation results of industrial-scale reforming tube with the selected equations of state. Heat flux ( $H$ )

Equation of state	Compressible ideal gas	Real gas SRK	Real gas PR
$\Delta P$ (kPa)	212.83	213.99	213.60
$\bar{P}_{outlet}$ (kPa)	3044.0	3044.0	3044.0
$H_{average}$ (kW/m <sup>2</sup> )	68.972	69.380	69.391
$\bar{x}_{H_2}^{outlet}$	0.464485	0.464493	0.464492
$\bar{x}_{H_2O}^{outlet}$	0.346720	0.346716	0.346717
$\bar{x}_{CH_4}^{outlet}$	0.042605	0.042607	0.042608
$\bar{x}_{CO}^{outlet}$	0.087348	0.087347	0.087347
$\bar{x}_{CO_2}^{outlet}$	0.058842	0.058837	0.058837

of the non-premixed combustion process, i.e., the overall reaction rates of the individual species depend only on the rate of mixing. Additionally, the global kinetic models chosen for the combustion of hydrogen and natural gas are compatible with the FR/ED model, and as a result, the FR/ED model is chosen as the turbulence-chemistry interaction model for the furnace-side mixture. However, the SMR process consists of three catalytic reversible reactions driven to yield the desired product, hydrogen, by the thermal energy generated from the combustion chamber, and therefore, the assumption of fast reaction rates is not applicable, so the FR/ED model may not be accurate. In Sec. 3.5.1, we have demonstrated that the EDC model is an alternative turbulence-chemistry interaction model with the ability to account for multi-step reaction mechanisms. Nevertheless, the computational requirement is demanding, and therefore, it should only be used as the last resort if the FR/ED model yields unacceptably incorrect simulation results. It is noteworthy that the accuracy of the FR/ED model is questioned only for the reforming tubes, and therefore, the CFD model of the industrial-scale reforming tube provides an effective means (based on the reasons stated in Sec. 3.6) for choosing the most suitable turbulence-chemistry interaction model for the reforming tubes of the pilot-scale reformer CFD model.

In this effort, two potential turbulence-chemistry interaction models, i.e., the EDC model and the FR/ED model, are implemented in the CFD model of the industrial-scale reforming tube.

Table 3.8: Simulation results of the reforming tube with the selected interaction models. % difference with respect to EDC. Heat flux ( $H$ )

<b>Turbulent-chemistry interaction model</b>	<b>EDC</b>	<b>FR/ED</b>	<b>% difference</b>
$\Delta P$ (kPa)	208.3	212.8	2.2
$\bar{P}_{outlet}$ (kPa)	3044.0	3044.0	0.0
$H_{average}$ (kW/m <sup>2</sup> )	66.484	68.942	3.7
$\bar{x}_{H_2}^{outlet}$	0.453	0.464	2.4
$\bar{x}_{H_2O}^{outlet}$	0.356	0.347	2.4
$\bar{x}_{CH_4}^{outlet}$	0.049	0.043	12
$\bar{x}_{CO}^{outlet}$	0.082	0.087	6.0
$\bar{x}_{CO_2}^{outlet}$	0.060	0.059	1.9

It is important to note that for this study using the CFD model of the industrial-scale reforming tube, all boundary conditions, i.e., the outer reforming tube wall temperature and the tube-side feed conditions, and other simulation settings, are the same as in the pilot-scale reforming tubes. The comparison between the simulation results generated by the two turbulence-chemistry models is shown in Table 3.8, where the differences (%) are computed by dividing the deviation between data extracted from the two sets of simulation results by the corresponding values generated by the CFD model implemented with the EDC model.

The differences between the simulation result generated by the CFD model implemented with the FR/ED model and the result generated by the CFD model implemented with the EDC model are negligible as shown in Table 3.8. Therefore, the errors associated with the FR/ED model are determined to be insignificant compared to the reduction in the required computation time. Specifically, the former CFD model takes  $\sim 2000$  iterations to determine the converged solution while the latter CFD model takes  $\sim 6500$  iterations. As a result, the FR/ED model is adopted in the pilot-scale reformer CFD model to describe the reaction rates of individual species in the turbulent reacting flows of both the tube-side and furnace-side mixtures.

## 3.8 Governing Equation of Pilot-scale SMR Unit

Based on the inlet information of the furnace-side feed (Sec. 3.4.1) and tube-side feed (Sec. 3.5.1), the flow profiles inside the combustion chamber and reforming tubes are speculated to be turbulent. Additionally, the catalyst network inside the reforming tubes plays the role of a physical obstacle interfering with the tube-side mixture flow, which generates turbulent flow patterns and enhances mixing for the tube-side mixture. Therefore, it is essential that a proper turbulence model is implemented within the CFD model of the pilot-scale reformer in order to accurately capture the characteristic parameters of the turbulent reacting flow profiles, i.e., the turbulence kinetic energy and turbulence dissipation rate; as a result, a standard  $k-\epsilon$  turbulence model is adopted. This turbulence model, presented in Eq. 3.9e and Eq. 3.9f,<sup>30,40</sup> is developed from the Reynolds-averaged Navier-Stokes (RANS) equations and can yield reasonably accurate estimates of characteristic parameters of the turbulent reacting flow, while it is also computationally inexpensive compared to other turbulence models, i.e., the realizable  $k-\epsilon$  and RNP  $k-\epsilon$  models. In the remainder of the section, the equations used to describe the complex physical phenomena within the combustion chamber and reforming tubes are described.

### 3.8.1 Furnace Chamber

In the combustion chamber, predicting the temperature field remains the most difficult modeling task because of the coupling between the mass, momentum and energy transport phenomena, the exothermic oxidation of the fuel stream and the thermal coupling of the combustion chamber with the reforming tubes. Specifically, these processes must be accurately modeled in order to produce a realistic temperature field, which can only be obtained by solving for the steady-state solution of the complete reformer model. Based on the above considerations and those discussed in Sec. 3.4, Sec. 3.6 and Sec. 3.7, the governing equations including the

continuity equation (Eq. 3.9a) and the momentum (Eq. 3.9b), energy (Eq. 3.9c) and species (Eq. 3.9d) balances, and the turbulence model (Eq. 3.9e and Eq. 3.9f) required for characterizing the heat and fluid-flow fields inside the combustion chamber are formulated. It is worth recalling that due to the mixing-limited nature of the combustion process, the detailed combustion kinetic models of hydrogen and methane, i.e., models including kinetics for free radicals, are rendered unnecessary for the purpose of this work because the formation/consumption rates of all furnace-side species are directly controlled by the rate of turbulent mixing, which in turn justifies the implementation of computationally efficient global kinetic models for these processes. note that all scalar variables are time-averaged variables It is important to realize that in the turbulent reacting fluid flow, velocity components, pressure, energy, temperature, density and species concentration fluctuate about their corresponding time-averaged values, and therefore, their instantaneous values are not well-defined. As a result, the governing equations of the furnace-side are written in terms of time-averaged variables as follows:

Continuity equation:

$$\frac{\partial}{\partial t}(\rho_{comb}) + \nabla \cdot (\rho_{comb} \vec{v}_{comb}) = 0 \quad (3.9a)$$

Momentum conservation equation:

$$\begin{aligned} \frac{\partial}{\partial t}(\rho_{comb} \vec{v}_{comb}) + \nabla \cdot (\rho_{comb} \vec{v}_{comb} \vec{v}_{comb}) = & -\nabla P_{comb} \\ & + \nabla \cdot \bar{\bar{\tau}}_{comb} + \rho_{comb} \vec{g} \end{aligned} \quad (3.9b)$$

Energy conservation equation:

$$\begin{aligned} \frac{\partial}{\partial t}(\rho_{comb} E_{comb}) + \nabla \cdot (\vec{v}_{comb} (\rho_{comb} E_{comb} + P_{comb})) = & \\ \nabla \cdot \left[ k_{comb}^{eff} \nabla T_{comb} - \left( \sum_i h_{comb}^i \vec{J}_{comb}^i \right) + (\bar{\bar{\tau}}_{comb} \cdot \vec{v}_{comb}) \right] & \\ + S_{comb}^{h,rxn} + \nabla \cdot \vec{q}_{rad} & \end{aligned} \quad (3.9c)$$

Species material conservation equation:

$$\frac{\partial}{\partial t}(\rho_{comb} Y_{comb}^i) + \nabla \cdot (\rho_{comb} \vec{v}_{comb} Y_{comb}^i) = -\nabla \cdot (\vec{J}_{comb}^i) + R_{comb}^i \quad (3.9d)$$

Transport equations of the standard  $k-\epsilon$  turbulence model:

$$\frac{\partial}{\partial t}(\rho_{comb} k_{comb}) + \nabla \cdot (\rho_{comb} k_{comb} \vec{v}_{comb}) = \quad (3.9e)$$

$$\nabla \cdot \left[ \left( \mu_{comb} + \frac{\mu_{comb}^t}{\sigma_k} \right) \nabla k_{comb} \right] + G_{comb}^k + G_{comb}^b - \rho_{comb} \epsilon_{comb}$$

$$\frac{\partial}{\partial t}(\rho_{comb} \epsilon_{comb}) + \nabla \cdot (\rho_{comb} \epsilon_{comb} \vec{v}_{comb}) = \quad (3.9f)$$

$$\nabla \cdot \left[ \left( \mu_{comb} + \frac{\mu_{comb}^t}{\sigma_\epsilon} \right) \nabla \epsilon_{comb} \right] + C_{1\epsilon} \frac{\epsilon_{comb}}{k_{comb}} G_{comb}^k - C_{2\epsilon} \rho_{comb} \frac{\epsilon_{comb}^2}{k_{comb}}$$

$$\vec{J}_{comb}^i = \left( \rho_{comb} D_{comb}^{m,i} + \frac{\mu_{comb}^t}{Sc_{comb}^t} \right) \nabla Y_{comb}^i - D_{comb}^{T,i} \frac{\nabla T_{comb}}{T_{comb}} \quad (3.10a)$$

$$\overline{\vec{\tau}}_{comb} = \mu_{comb} \left[ (\nabla \vec{v}_{comb} + \nabla \vec{v}_{comb}^T) - \frac{2}{3} \nabla \cdot \vec{v}_{comb} I \right] \quad (3.10b)$$

$$E_{comb} = h_{comb} + \frac{v_{comb}^2}{2} - \frac{P_{comb}}{\rho_{comb}} \quad (3.10c)$$

$$h_{comb} = \sum_j Y_{comb}^j h_{comb}^j \quad (3.10d)$$

$$h_{comb}^j(T_{comb}) = \int_{T_{ref}}^{T_{comb}} C_{p,comb}^j dT \text{ with } T_{ref} = 298.15 \text{ K} \quad (3.10e)$$

$$S_{comb}^{h,rxn} = - \sum_j \frac{h_j^f}{M_j} R_{comb}^j \quad (3.10f)$$

$$R_{comb}^j = \sum_k \nu_{comb}^{k,j} R_{comb}^{k,j} \quad (3.10g)$$

$$k_{comb}^{eff} = k_{comb}^l + k_{comb}^t \quad (3.10h)$$

$$k_{comb}^t = \frac{C_p \mu_{comb}^t}{Pr_t} \quad (3.10i)$$

$$\mu_{comb}^t = \rho_{comb} C_\mu \frac{k_{comb}^2}{\epsilon_{comb}} \quad (3.10j)$$

$$G_{comb}^k = - \rho_{comb} \frac{v'_{comb,i} v'_{comb,j}}{v'_{comb,i} v'_{comb,j}} \frac{\partial v_{comb,j}}{\partial x_i} \quad (3.10k)$$

$$G_{comb}^b = \beta g_i \frac{\mu_{comb}^t}{Pr_t} \frac{\partial T_{comb}}{\partial x_i} \quad (3.10l)$$

where  $\rho_{comb}$ ,  $\vec{v}_{comb}$ ,  $\mu_{comb}$ ,  $\mu_{comb}^t$ ,  $k_{comb}^{eff}$ ,  $k_{comb}^l$ ,  $k_{comb}^t$ ,  $C_p$ ,  $T_{comb}$  and  $P_{comb}$  are the furnace-side mixture density, mass-averaged velocity, laminar mixture viscosity, turbulent mixture viscosity (calculated as shown in Eq. 3.10j), effective thermal conductivity (estimated as shown in Eq. 3.10h), laminar thermal conductivity, turbulent thermal conductivity (estimated as shown in Eq. 3.10i), heat capacity, temperature and pressure of the furnace-side mixture in the combustion chamber, respectively,  $\vec{g}$  is the universal gravitational acceleration,  $\overline{\vec{\tau}}_{comb}$  is the stress tensor (estimated as shown in Eq. 3.10b), and  $I$  is the unit tensor. It is noteworthy that the aforementioned

governing equations are capable of characterizing the turbulent reacting furnace-side flow under the influence of complex interactions of mass, momentum and energy transport, reaction and turbulence, and also accounting for the major microscopic/macroscale phenomena that yield the heat and fluid-flow fields inside the combustion chamber. Specifically, the turbulent mass diffusion flux of species  $i$ ,  $\vec{J}_{comb}^i$ , driven by concentration and temperature gradients, is shown in Eq. 3.10a, where  $Y_{comb}^i$ ,  $D_{comb}^{m,i}$  and  $D_{comb}^{T,i}$  are the furnace-side mass fraction, laminar mass diffusion coefficient and laminar thermal diffusion coefficient of species  $i$ . It is necessary to note that the ratio  $\frac{\mu_{comb}^t}{Sc_{comb}^t}$ , in which  $Sc_{comb}^t$  and  $\mu_{comb}^t$  are the turbulent Schmidt number and turbulent viscosity of the furnace-side mixture, is used to account for the effect of turbulence on the mass diffusion flux of species  $i$ , and therefore, it can be written as  $\rho_{comb} D_{comb}^{m,t}$  where  $D_{comb}^{m,t}$  is the turbulent mass diffusion coefficient. Additionally, the specific internal energy ( $E_{comb}$ ) of the furnace-side mixture which can be computed as the sum of the furnace-side specific sensible enthalpy ( $h_{comb}$ ) which depends on the furnace-side specific sensible enthalpy of species  $j$  at temperature  $T_{comb}$  ( $h_{comb}^j(T_{comb})$ ), specific kinetic energy ( $v_{comb}^2/2$ ) and external work per unit weight of the furnace-side mixture ( $-P_{comb}/\rho_{comb}$ ), is shown in Eq. 3.10c, Eq. 3.10d and Eq. 3.10e. It is important to note that the value of  $T_{ref}=298.15$  K in Eq. 3.10e is chosen automatically by *ANSYS Fluent's* parallel/pressure based solver, and  $C_{p,comb}^j$  is the heat capacity of species  $j$  in the combustion chamber. In addition, from Eq. 3.9c,  $\nabla \cdot (k_{comb}^{eff} \nabla T_{comb})$ ,  $-\nabla \cdot (\sum_i h_{comb}^i \vec{J}_{comb}^i)$ ,  $\nabla \cdot (\bar{\tau}_{comb} \cdot \vec{v}_{comb})$  and  $\nabla \cdot \vec{q}_{rad}$  represent four distinct mechanisms, i.e., conduction, species diffusion, viscous dissipation and radiation respectively, through which energy is transferred. Furthermore, the overall rate at which thermal energy is generated from combustion processes inside the combustion chamber,  $S_{comb}^{h,rxn}$ , is computed as shown in Eq. 3.10f in which  $R_{comb}^j$  and  $h_j^f$  represent the overall volumetric consumption/formation rate and enthalpy of formation of species  $j$ , and  $\nu_{comb}^{k,j}$  and  $R_{comb}^{k,j}$  are the stoichiometric coefficient and volumetric consumption/formation rate of species  $j$  in reaction  $k$ . It is noteworthy that  $R_{comb}^{k,j}$  is determined by the FR/ED turbulence-chemistry interaction model (Sec. 3.4.1). Transport equations of the standard  $k-\epsilon$  turbulence model are presented in Eq. 3.9e and Eq. 3.9f, in which  $k_{comb}$



and  $\epsilon_{comb}$  are the turbulence kinetic energy and turbulence dissipation rate of the furnace-side mixture,  $\beta$  is the coefficient of thermal expansion of the furnace-side mixture,  $\sigma_k = 1.3$  and  $\sigma_\epsilon = 1.0$  are the default values of the turbulent Prandtl numbers for  $k_{comb}$  and  $\epsilon_{comb}$ ,  $C_{1\epsilon} = 1.44$ ,  $C_{2\epsilon} = 1.92$ ,  $C_\mu = 0.09$  and  $Pr_t = 0.85$  are default constants of the standard  $k-\epsilon$  turbulence model, respectively, and  $G_{comb}^k$  and  $G_{comb}^b$  represent the generation of turbulence kinetic energy in the furnace-side mixture due to the mean velocity gradients (Eq. 3.10k) and buoyancy effect (Eq. 3.10l). We would like to point out that the standard  $k-\epsilon$  turbulence model can capture the characteristic parameters of turbulent reacting flow profiles. Specifically, in Eq. 3.10k, the term  $-\rho_{comb} \overline{v'_{comb,i} v'_{comb,j}}$  is the Reynolds stress representing the effect of turbulence on the velocity profile of the furnace-side mixture that arises from the Reynolds-averaged Navier-Stokes (RANS) equations, and  $\overline{v'_{comb,i}}$  is the time-averaged fluctuating component of  $\vec{v}_{comb}$  in the  $x_i$  direction. It is worth noting that all default constants of the standard  $k-\epsilon$  turbulence model are determined empirically by experiments for fundamental turbulent flows, and have been proven to be suitable for a wide range of wall-bounded and free shear flow applications.<sup>26</sup>

### 3.8.2 Reforming Tube

In the reforming tubes, the most challenging modeling task is to accurately simulate the formation/consumption rates of the tube-side species in turbulent flow as they undergo a series of microscopic processes. Specifically, the reactants including methane and steam from the bulk tube-side mixture are convectively driven to the stationary layer around the catalyst network by reactant concentration gradients generated by the external mass transfer resistance of the catalyst network. Then, these reactants are diffusively driven by the reactant concentration gradient generated by the internal mass transfer resistance of the catalyst network and by temperature gradients generated by the SMR process to the catalyst active sites, where the aforementioned endothermic reactions take place generating hydrogen and byproducts. These products diffuse back out of the catalyst and stationary layer to reenter the bulk tube-side mix-

ture. It is noteworthy that the effects of the internal and external mass transfer resistances and the presence of the catalyst network on the tube-side mixture are taken into account in the tube-side governing equations of this CFD model by the porosity, viscous resistance coefficient, inertial resistance coefficient of the catalyst network and the universal effectiveness factor (as mentioned in Sec. 3.5.1 and Sec. 3.5.2). Based on the above considerations and those discussed in Sec. 3.5, Sec. 3.6 and Sec. 3.7, the governing equations including the continuity equation and the momentum, energy and tube-side species balances, and the turbulence model required to simulate the SMR process inside the reforming tubes, are constructed in a similar manner to that of the combustion chamber, which has been described in Sec. 3.8.1. Additionally, the governing equations of the tube-side mixture have also been explicitly presented in our recent publication,<sup>37</sup> and therefore, they are not repeated here for brevity.

### 3.9 Simulation Results

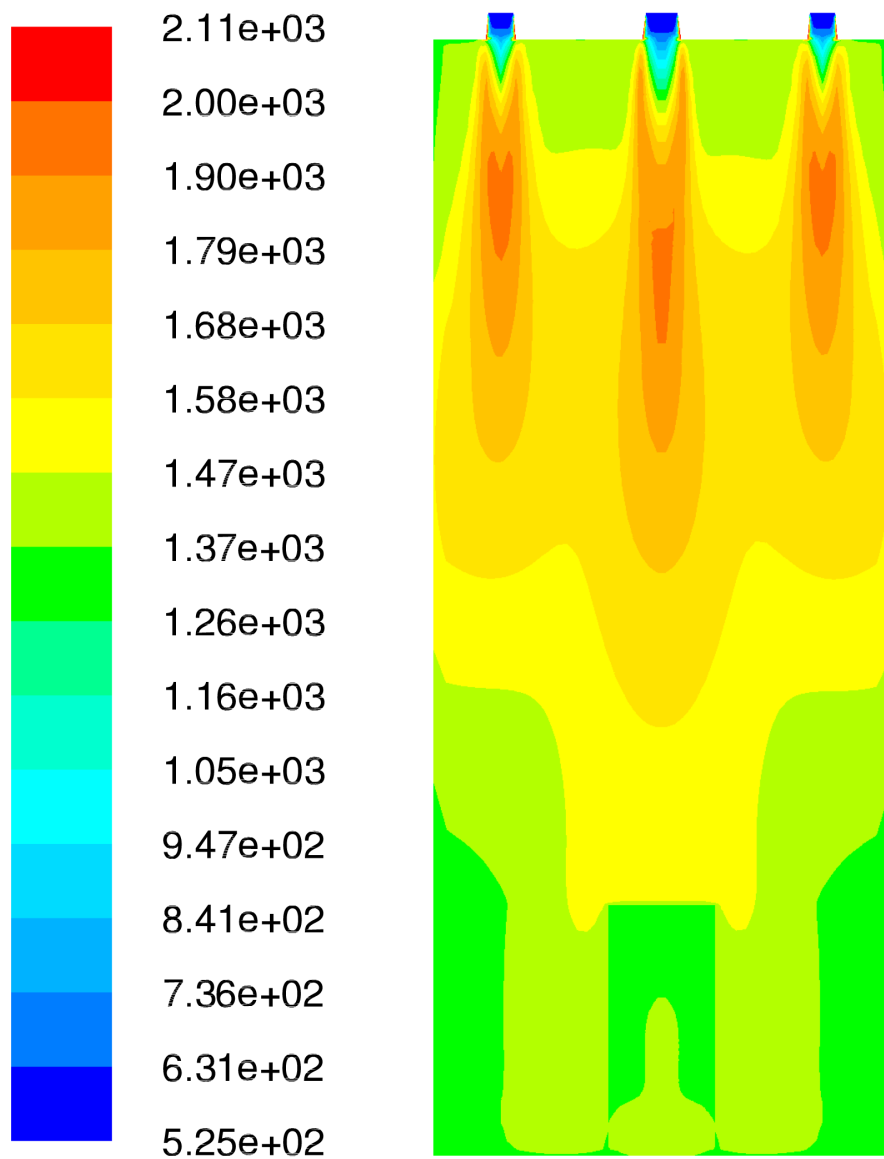
The solution of the pilot-scale reformer CFD model is computed in  $\sim 24$  hours by ANSYS Fluent's parallel solver with 48 cores on UCLA's Hoffman2 Cluster for which an arbitrarily chosen core is designated as a host process, and the remaining 47 cores are compute-node processes. Under ANSYS Fluent's parallel solver, the pilot-scale reformer mesh is partitioned into 47 parts for which each partition is assigned to a different compute-node process. It is noteworthy that the host process does not participate in the computing task to determine the converged solution. Instead, it is responsible for interpreting commands given in the graphical user interface (GUI), then redistributing them to all compute-node processes by a message-passing library, e.g., the Message Passing Interface (MPI).

In the remainder of this section, the steady-state simulation results of the pilot-scale reformer CFD model are presented. Based on the inlet information for the furnace-side feed (Sec. 3.4) and tube-side feed (Sec. 3.5), the steady-state furnace-side temperature field and oxidized

species distributions are shown in Figs. 3.9–3.12. Additionally, the corresponding tube-side temperature, pressure, and major species distributions are presented in Figs. 3.13–3.17. We would like to point out that due to the high heated reforming tube length to reforming tube diameter ratio,  $\sim 85 : 1$ , the radial direction is scaled up by 20 times in Figs. 3.13–3.17 for display purposes only. It is worth noting that the radially uniform pressure profile inside the reforming tubes is the result of the uniformly packed catalyst network assumption, and the definition of the porous zone with uniform coefficients of viscous resistance and inertial resistance of the catalyst network along the axial and radial directions as presented in Section 3.5.2. Lastly, the average temperature profiles of the outer and inner reforming tube wall and flue gas in the vicinity of the reforming tubes is shown in Fig. 3.18, and the corresponding steady-state heat flux profile through the reforming tube wall is displayed in Fig. 3.19. Fig. 3.18 suggests that the maximum temperature of the outer reforming tube wall of 1177.48 K is below the maximum allowable operating temperature, which if the maximum temperature of the outer reforming tube wall were to exceed for a sufficient length of time, the reforming tube would rupture. The presented simulation results of the pilot-scale reformer CFD model are consistent with the publicly available plant data,<sup>38</sup> many sources in the literature<sup>17,21,54,58</sup> and well-established knowledge about the SMR process, which supports the validity of the assumptions that we have made while constructing this CFD model. For instance, inside the combustion chamber, the furnace-side feed is fully oxidized to generate the necessary thermal energy required to drive the reversible endothermic SMR reactions in order to produce the desired hydrogen. The kinetic models for the chemical processes inside the combustion chamber required to construct this pilot-scale reformer CFD model were selected based on the assumption that methane, hydrogen and carbon monoxide are completely consumed prior to exiting the reformer. Figs. 3.10–3.12 demonstrate that the mol fractions of these species are effectively zero outside of the flame region, and as a result, the assumption of a lean combustion process is validated. Additionally, it is important to note that the outer-lane burners and inner-lane burner have the estimated lengths of 4 m and 6 m, respectively, which are visible in Fig. 3.9.

These results also match well with those observed in industry. Furthermore, the highest temperature inside the pilot-scale reformer is located at 1/3 of the combustion chamber's height from the ceiling as shown in Figs. 3.9-3.18, which is consistent with that observed and reported in industry.

Furthermore, the validation of the simulation results generated by the pilot-scale reformer CFD model is performed by comparing its tube-side mixture data at the reforming tube outlet to that generated by the industrial-scale reforming tube CFD model as shown in Table 3.9. The industrial-scale reforming tube CFD model is constructed with the same modeling parameters as described in Sec. 3.3, Sec. 3.5, Sec. 3.6 and Sec. 3.7, and implemented with the same tube-side inlet conditions and outer reforming tube wall profile as those in the pilot-scale reformer CFD model.<sup>37</sup> We found that the differences between the simulation results generated by the industrial-scale reforming tube CFD model and the pilot-scale reformer CFD model are negligible. Finally, the simulation results generated by this pilot-scale reformer are further justified by comparing the area-weighted average heat flux across the reforming tube wall with that reported in the literature as shown in Table 3.10. In addition to the average heat flux results reported in this table, the average heat flux for the reformer described by Latham<sup>38</sup> is estimated to be  $\sim 65.6 \text{ kW/m}^2$  based on the outer and inner reforming tube wall temperature profiles, the reforming tube thermal conductivity of  $106.500 \text{ J/mhK}$  and the reforming tube wall thickness of  $0.015 \text{ m}$ , which is an average heat flux that is consistent with the results of the pilot-scale CFD model and thus supports the accuracy of the pilot-scale reformer CFD model. The heat flux profile of the pilot-scale CFD model and the average heat flux are shown in Fig. 3.19.



Contours of Total Temperature (k)

Figure 3.9: Temperature field inside the combustion chamber from the pilot-scale reformer CFD simulation, where the parameters of the tube-side feed, furnace-side feed and combustion chamber refractory walls are consistent with typical plant data.<sup>38</sup>

Table 3.9: Validation of pilot-scale reformer CFD model by the industrial-scale reforming tube CFD model. Heat flux ( $H$ )

	Industrial-scale reforming tube CFD model (*)	Pilot-scale unit CFD model	% difference with respect to (*)
$\Delta P$ (kPa)	212.83	201.73	5.215
$\bar{P}_{outlet}$ (kPa)	3044.0	2942.94	3.320
$H_{average}$ (kW/m <sup>2</sup> )	68.972	69.523	0.799
$\bar{x}_{H_2}^{outlet}$	0.4645	0.4625	0.431
$\bar{x}_{H_2O}^{outlet}$	0.3467	0.3483	0.461
$\bar{x}_{CH_4}^{outlet}$	0.0426	0.0436	2.347
$\bar{x}_{CO}^{outlet}$	0.0873	0.0867	0.687
$\bar{x}_{CO_2}^{outlet}$	0.0588	0.0588	0.000

Table 3.10: Validation of pilot-scale reformer CFD model by available plant data from literature

	Average Heat Flux (kW/m <sup>2</sup> )
Pilot-scale reformer CFD model	69.5
Industrial-scale reforming tube CFD model <sup>37</sup>	69.0
Rostrup-Nielsen <sup>58</sup>	45–90
Dybkjaer <sup>17</sup>	78.5
Froment and Bischoff <sup>21</sup>	75.6
Pantolontos <sup>54</sup>	< 80.0

### 3.10 Sample Parametric Study Case

We are primarily interested in developing a pilot-scale reformer CFD model that can be employed for reformer parametric study which has been traditionally conducted by on-site experiments. The necessity and motivation for reformer parametric study has been discussed in great depth in Sec. 3, and specifically, it allows chemical process plants to determine the optimized and more profitable operating conditions, which result in an increase of profit margin for the plant. Nevertheless, the traditional on-site parametric study must be conducted over a long time period with small changes in the parameter of interest throughout time in order to avoid unit failure which can result in significant production and capital losses (Sec. 3). On the other hand, it is noteworthy that a well-developed CFD model of a reformer can generate simulation

data that reasonably resembles data that would be collected from on-site experiments, and this idea in turn motivates us to construct a CFD model of a pilot-scale reformer.

This task is successfully accomplished by the detailed analysis of physical phenomena, i.e., the transport of momentum, material, and energy in addition to turbulence, and chemical reactions taking place inside the reformer and furnace, and allows us to select the most suitable models, e.g., the  $P-1$  radiation model (Sec. 3.4.2), standard  $k-\epsilon$  turbulence model, compressible ideal gas equation of state (Sec. 3.6) and FR/ED turbulence-chemistry interaction model (Sec. 3.7), to simulate the macroscopic and microscopic events in the reformer. Simulation data generated by the resulting pilot-scale reformer CFD model is consistent with that of publicly available plant data reported in the literature and also with the simulation data generated by a well-developed industrial-scale single reforming tube CFD model as discussed in Sec. 3.9. As a result, this pilot-scale reformer CFD model is adopted for a reformer parametric study of the burner furnace-side feed.

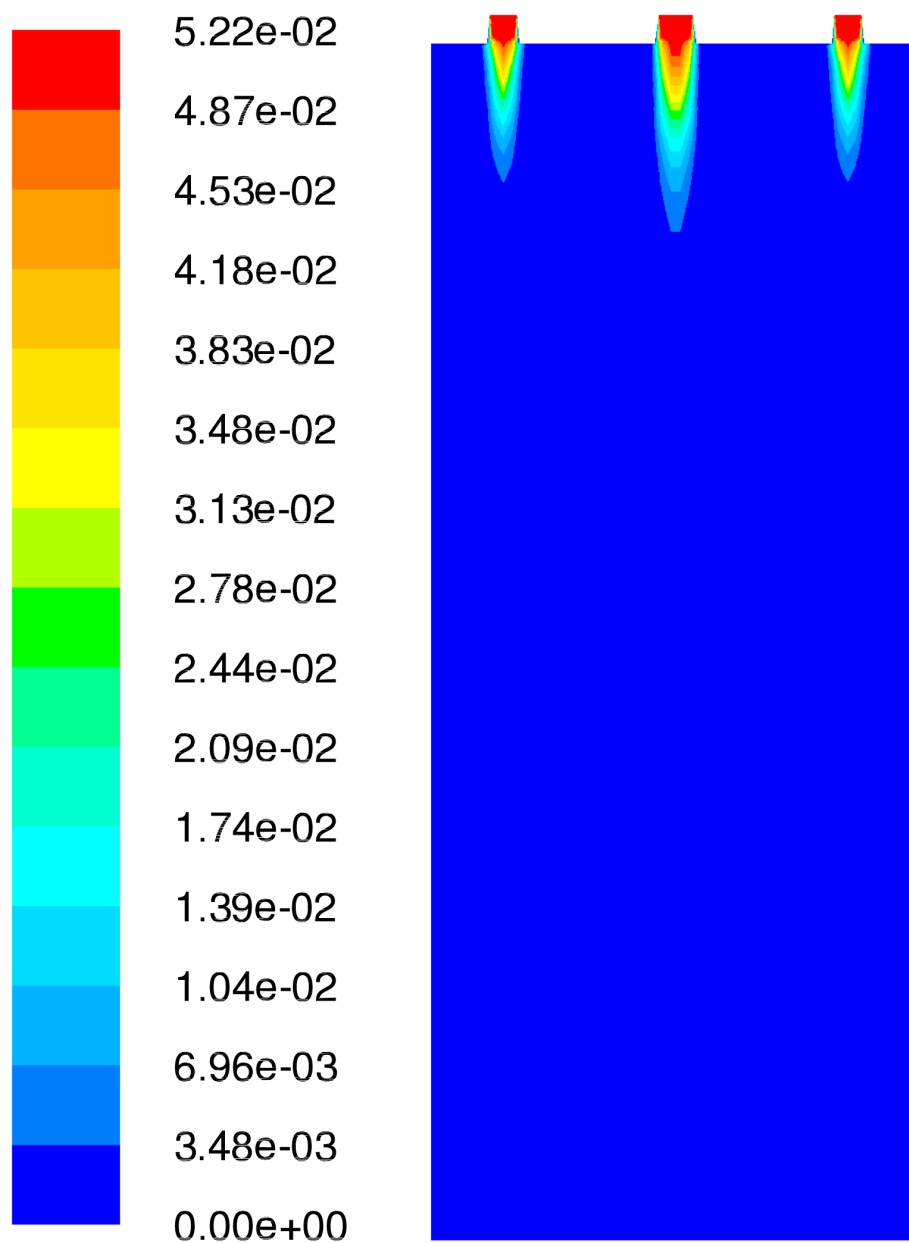
In this effort, a 20% increase in the furnace-side feed mass flow rate of each burner is implemented, which results in changes in the furnace-side feed mass flow rates of the inner-lane burner and outer-lane burners from 0.4056 kg/s to 0.4867 kg/s, and from 0.2434 kg/s to 0.2920 kg/s, respectively. During the parametric study of the furnace-side feed mass flow rate, the temperature, pressure and composition of the furnace-side feed, and all parameters of the tube-side feed and of the combustion chamber refractory walls, are kept constant, so that the effect of increasing the furnace-side feed mass flow rate can be identified and quantified. The simulation results generated by the pilot-scale reformer CFD model indicate that the maximum outer reforming tube wall temperature exceeded the maximum allowable operating temperature of the reforming tube as shown in Fig 3.21. This method for conducting parametric study has a number of advantages over the traditional on-site method. Firstly, it did not require that only incremental increases in the parameters (e.g., furnace-side feed mass flow rate) be implemented, allowing the study to be completed efficiently. In addition, the study

can be performed without risk to the equipment, and thus reasonably large variations in the parameters as in the above parametric study can be evaluated without concern.

### 3.11 Conclusion

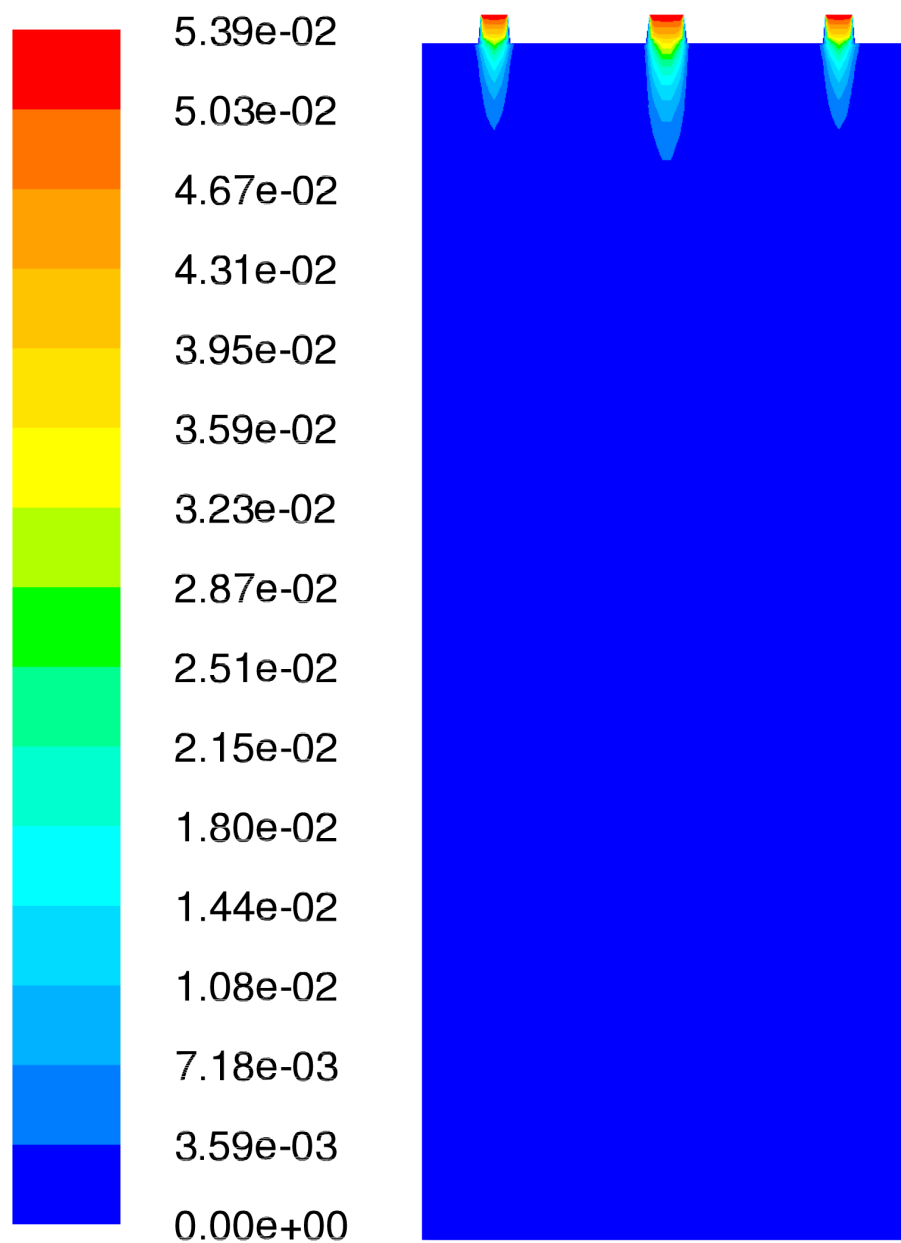
The present work initially described the detailed procedure for CFD modeling of a pilot-scale reformer, and subsequently demonstrated that the pilot-scale reformer CFD model could be employed for reformer parametric study. Specifically, the  $k - \epsilon$  turbulence model, FR/ED turbulence-chemistry interaction model and global kinetic models of combustion<sup>649</sup> were selected for use in the furnace side of the CFD model by studying the physical and chemical phenomena inside the combustion chamber, and were demonstrated to successfully capture the reaction rates of the furnace-side species and the thermal energy released by combustion in the turbulent reacting flow. The applicability of the FR/ED turbulence-chemistry interaction model was evaluated for the tube side of the CFD model due to the form of the global kinetic model of the SMR process.<sup>70</sup> Simulations with a previously developed and validated industrial-scale reforming tube CFD model suggested that the errors due to implementing FR/ED as the turbulence-chemistry interaction model were negligible. The simulation results generated by the pilot-scale reformer CFD model were in agreement with available plant data from literature, and also with the simulation results generated by the industrial-scale reforming tube CFD model. Lastly, we employed the pilot-scale reformer CFD model to conduct a sample parametric study in which the mass flow rate of the furnace-side feed was increased by 20% from its original value. We demonstrated that conducting the parametric study with the CFD model has a number of advantages compared to conducting it with the traditional on-site method, in particular that it allows for efficient testing of even reasonably large changes in the process parameters, without risk to the equipment.





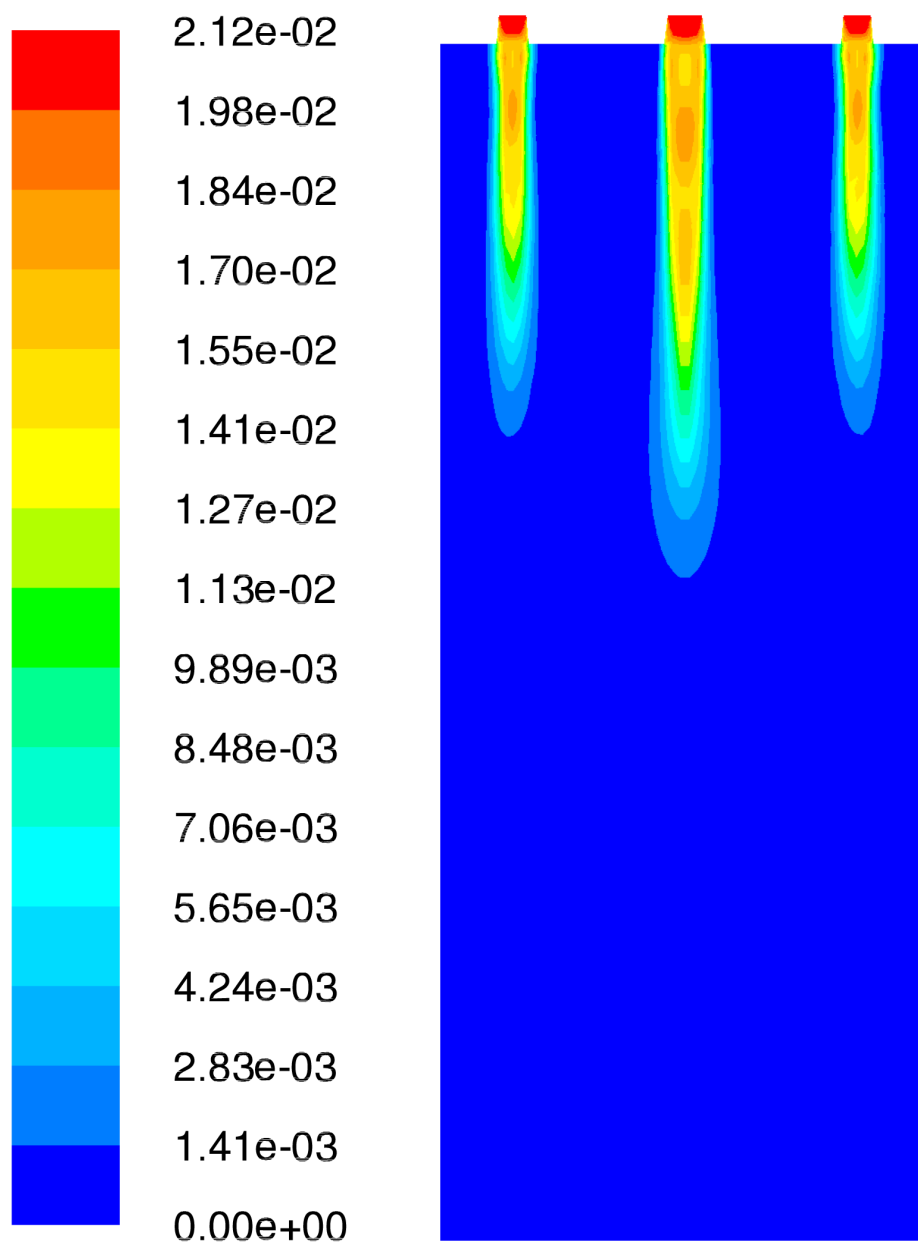
Contours of Mole fraction of ch4

Figure 3.10: Methane mole fraction profile inside the combustion chamber from the pilot-scale reformer CFD simulation, where the parameters of the tube-side feed, furnace-side feed and combustion chamber refractory walls are consistent with typical plant data.<sup>38</sup>



Contours of Mole fraction of h2

Figure 3.11: Hydrogen mole fraction profile inside the combustion chamber from the pilot-scale reformer CFD simulation, where the parameters of the tube-side feed, furnace-side feed and combustion chamber refractory walls are consistent with typical plant data.<sup>38</sup>



Contours of Mole fraction of co

Figure 3.12: Carbon monoxide mole fraction profile inside the combustion chamber from the pilot-scale reformer CFD simulation, where the parameters of the tube-side feed, furnace-side feed and combustion chamber refractory walls are consistent with typical plant data.<sup>38</sup>

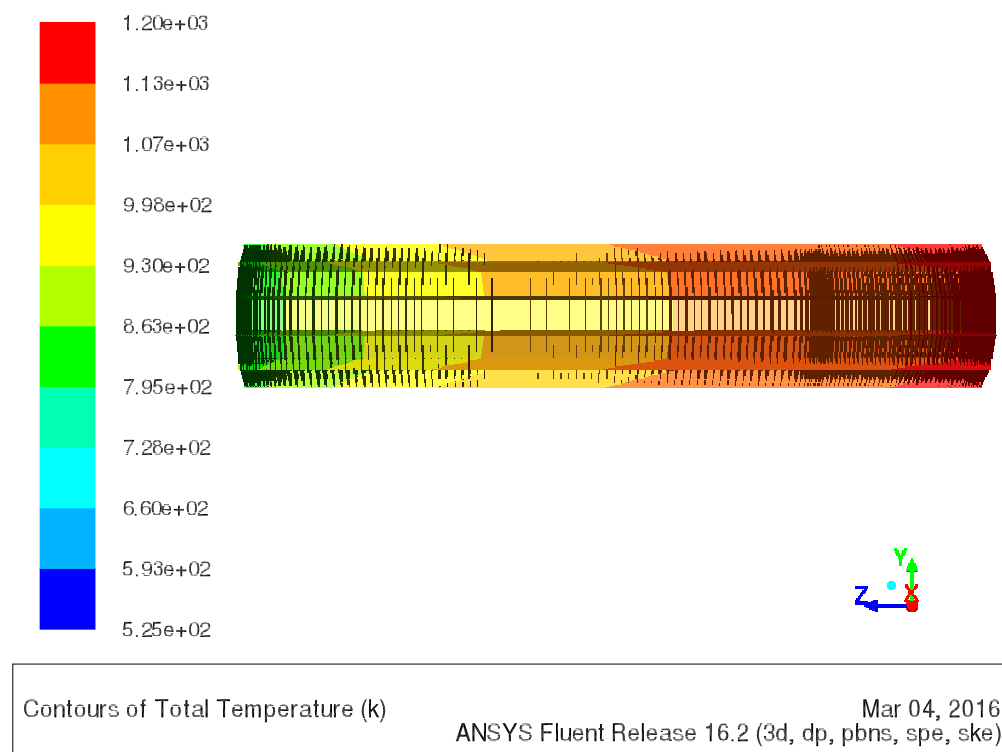


Figure 3.13: Temperature profile inside the reforming tube from the pilot-scale reformer CFD simulation, where the parameters of the tube-side feed, furnace-side feed and combustion chamber refractory walls are consistent with typical plant data.<sup>38</sup>

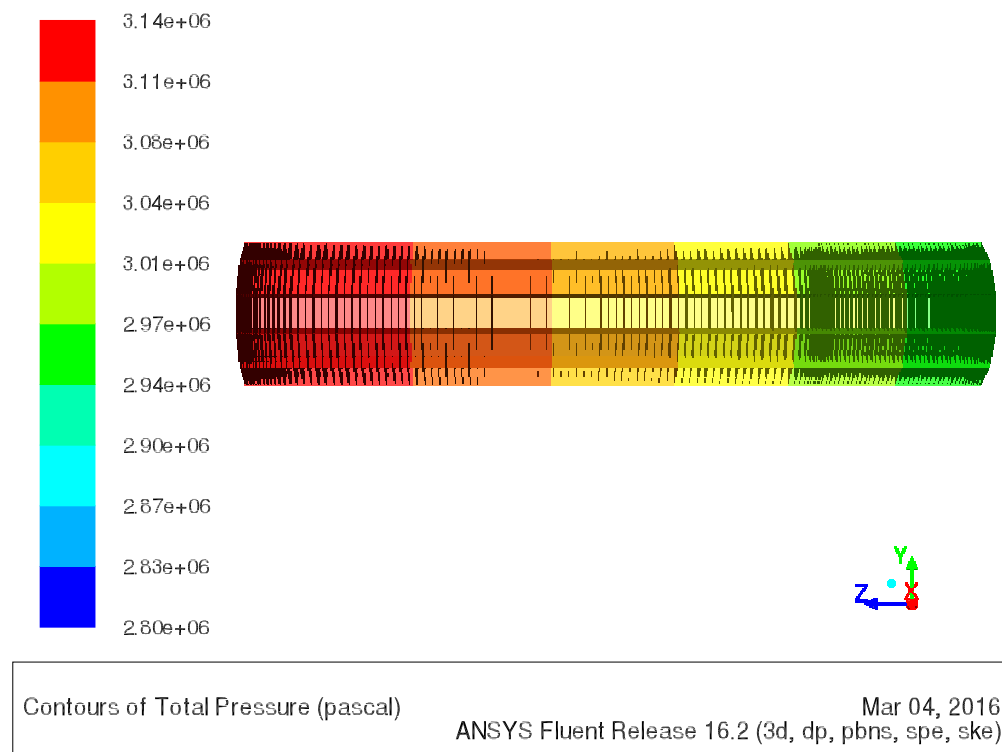


Figure 3.14: Pressure profile inside the reforming tube from the pilot-scale reformer CFD simulation, where the parameters of the tube-side feed, furnace-side feed and combustion chamber refractory walls are consistent with typical plant data.<sup>38</sup>

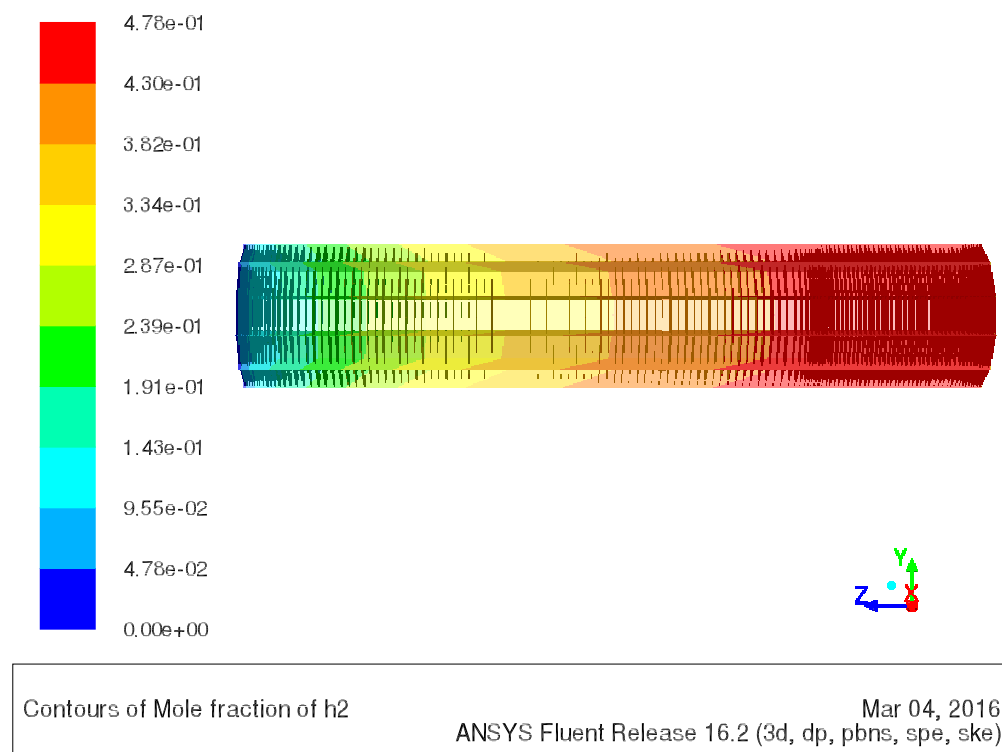


Figure 3.15: Hydrogen mole fraction profile inside the reforming tube from the pilot-scale reformer CFD simulation, where the parameters of the tube-side feed, furnace-side feed and combustion chamber refractory walls are consistent with typical plant data.<sup>38</sup>

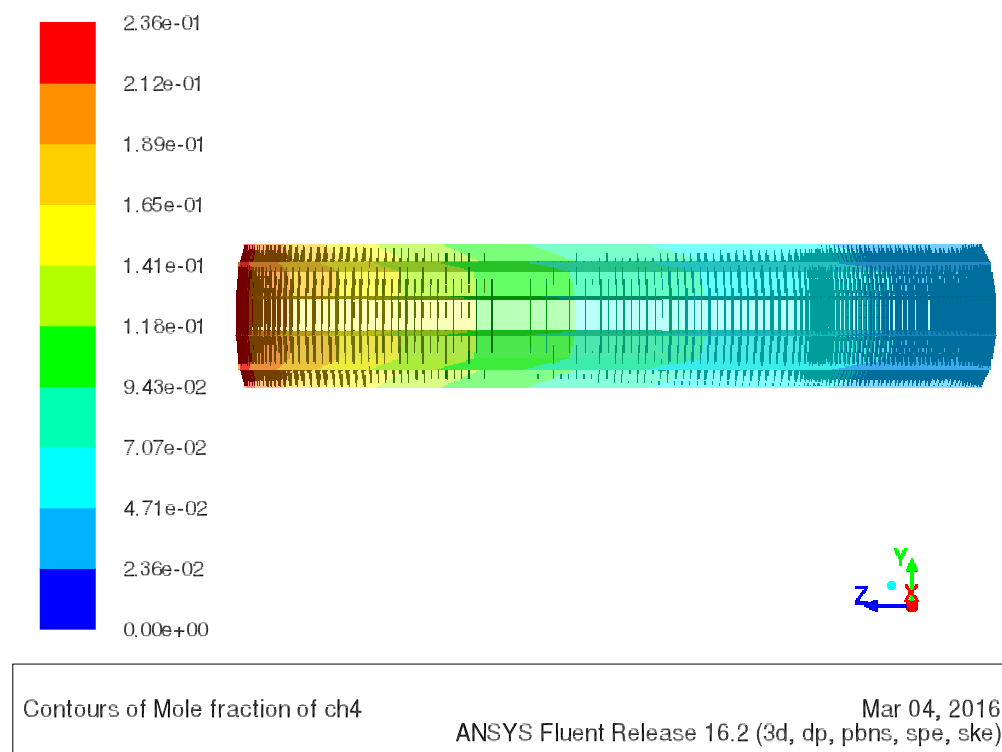


Figure 3.16: Methane mole fraction inside the reforming tube from the pilot-scale reformer CFD simulation, where the parameters of the tube-side feed, furnace-side feed and combustion chamber refractory walls are consistent with typical plant data.<sup>38</sup>

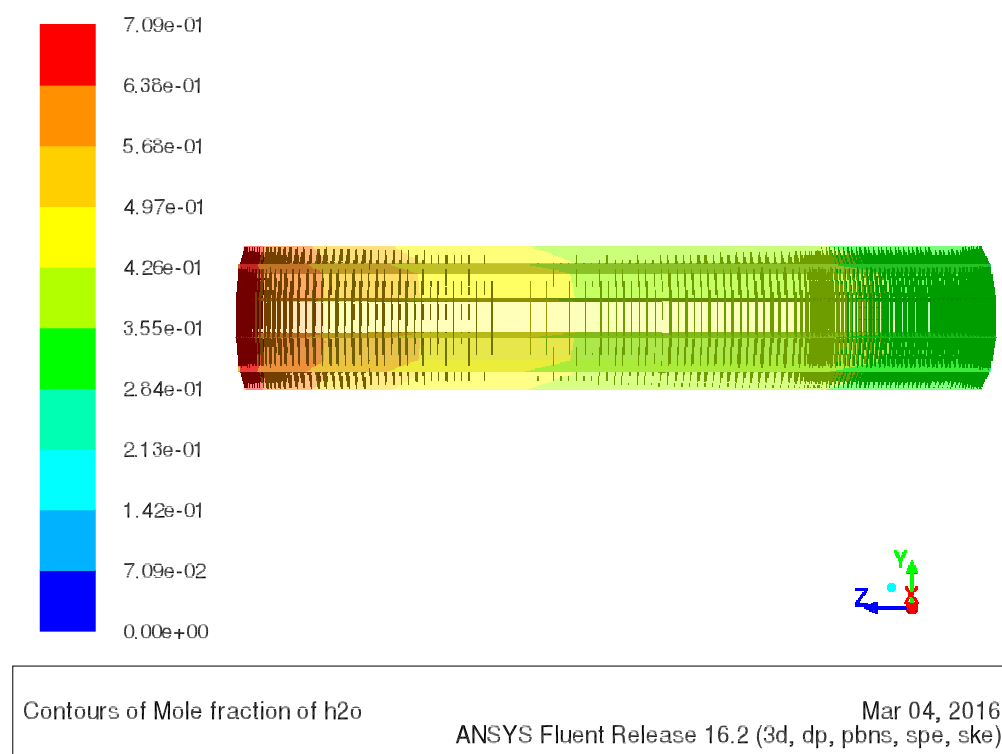


Figure 3.17: Superheated steam mole fraction profile inside the reforming tube from the pilot-scale reformer CFD simulation, where the parameters of the tube-side feed, furnace-side feed and combustion chamber refractory walls are consistent with typical plant data.<sup>38</sup>



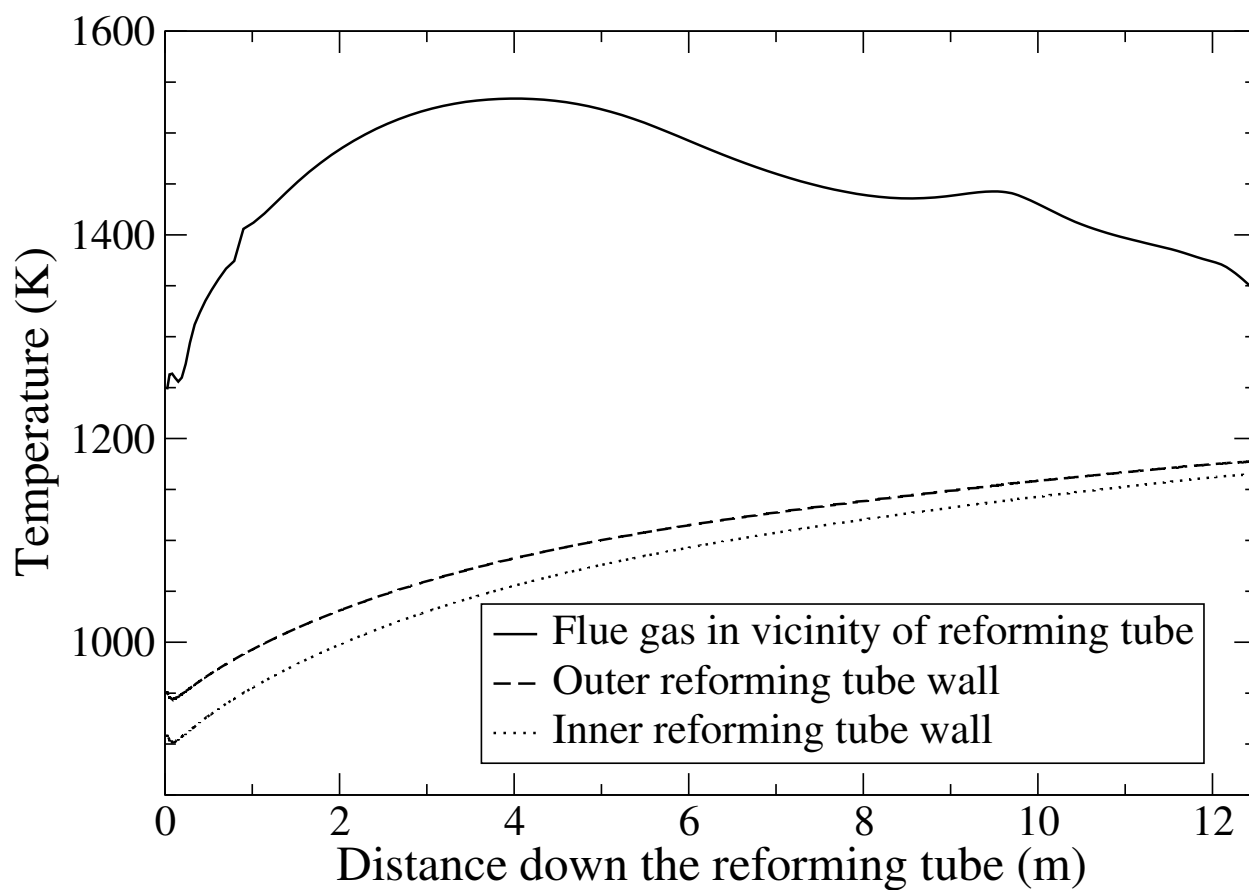


Figure 3.18: Temperature profiles of flue gas in the vicinity of the reforming tube (solid line), of the outer reforming tube wall (dashed line) and of the inner reforming tube wall (dotted line) from the pilot-scale reformer CFD simulation, where the parameters of tube-side feed, furnace-side feed and combustion chamber refractory walls are consistent with typical plant data.<sup>38</sup>

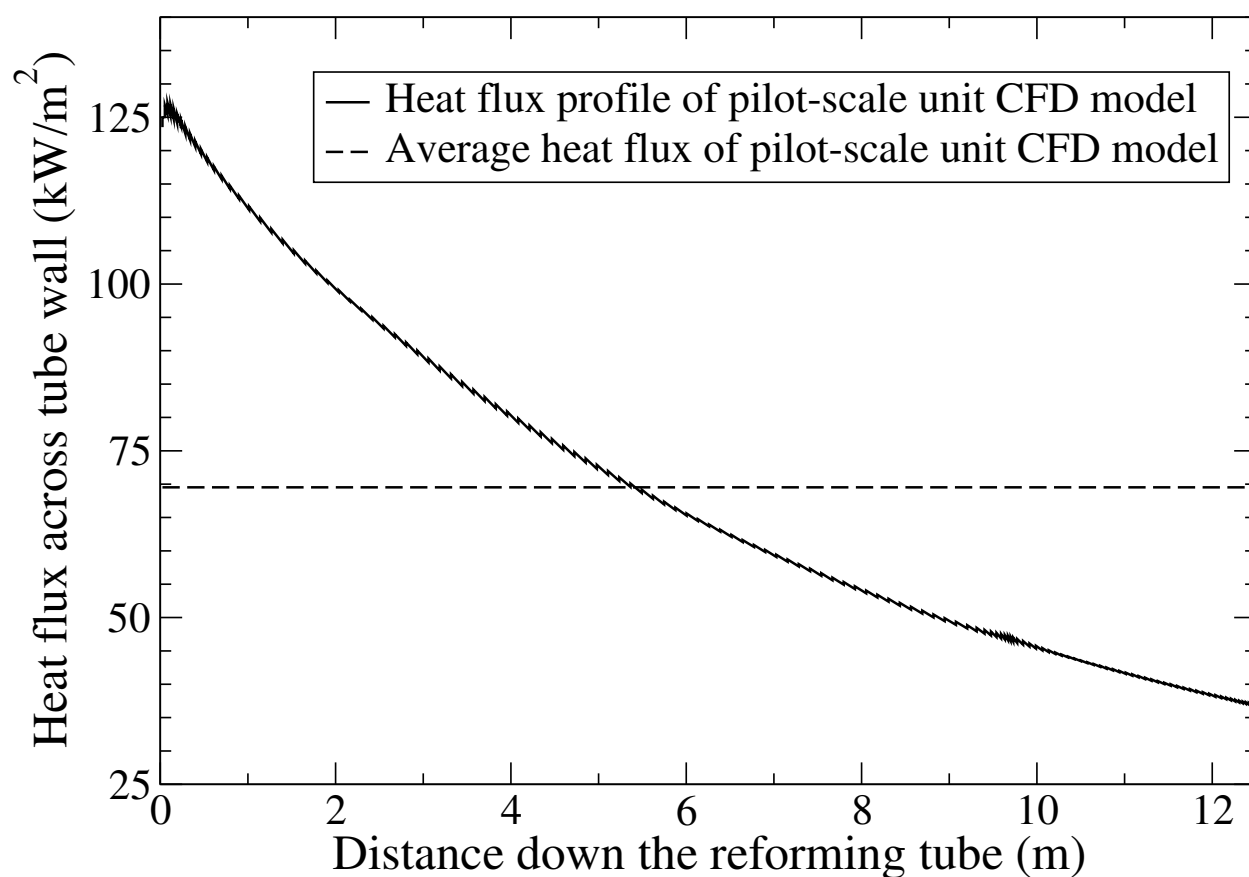


Figure 3.19: Heat flux profile (solid line), and average heat flux (dashed line) across the reforming tube wall from the pilot-scale reformer CFD simulation, where the parameters of the tube-side feed, furnace-side feed and combustion chamber refractory walls are consistent with typical plant data.<sup>38</sup>

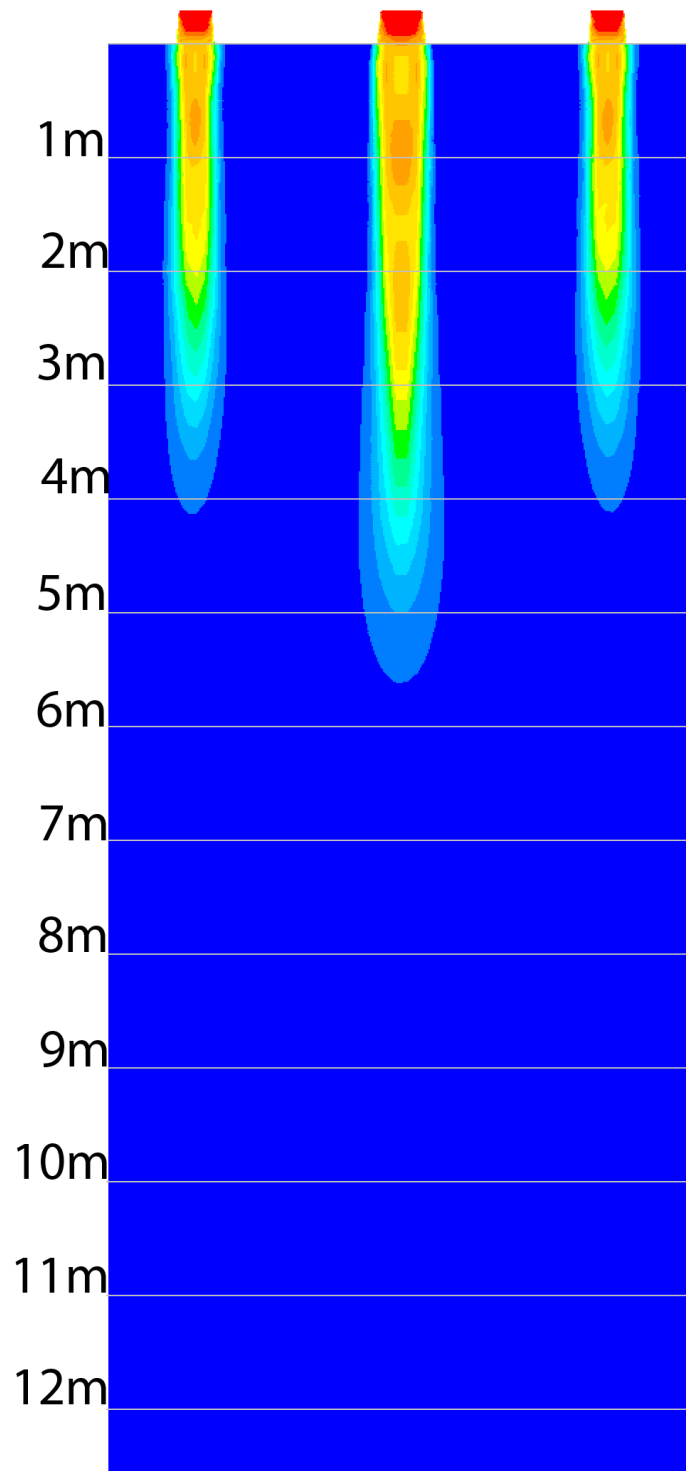


Figure 3.20: Flame length inside the combustion chamber from the pilot-scale reformer CFD simulation, where the parameters of the tube-side feed, furnace-side feed and combustion chamber refractory walls are consistent with typical plant data.<sup>38</sup>

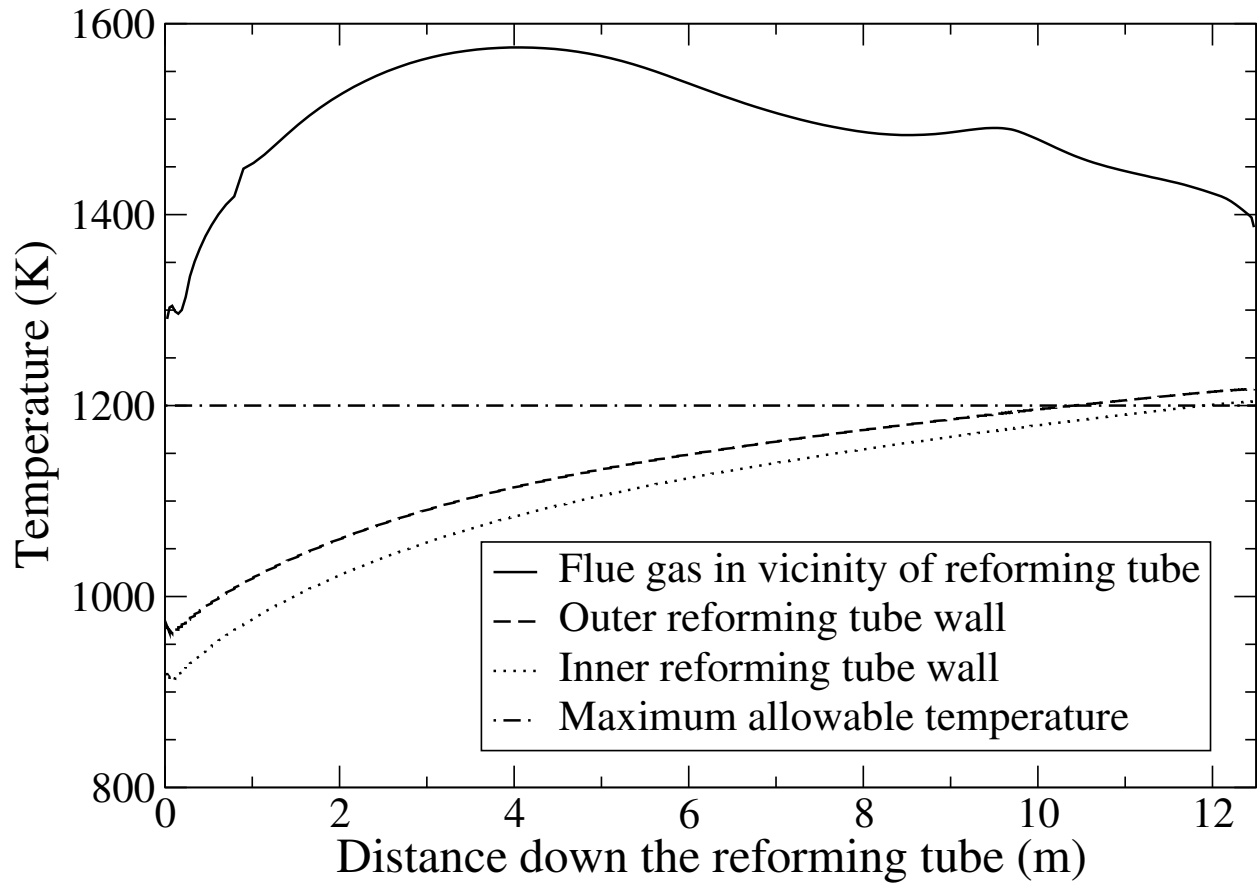


Figure 3.21: Temperature profiles of the flue gas in the vicinity of the reforming tube (solid line), of the outer reforming tube wall (dashed line) and of the inner reforming tube wall (dotted line) from the pilot-scale reformer CFD simulation, where the furnace-side feed mass flow rate is increased by 20% from its nominal value and all other parameters of the tube-side feed, furnace-side feed and combustion chamber refractory walls are consistent with typical plant data.<sup>38</sup>

# Chapter 4

## CFD of the full-scale furnace

### 4.1 Introduction

The development of large scale model that capture the physiochemical phenomena in chemical processes for parametric studies has been developing since the earlier 1900s. In the 1960s<sup>46</sup> the first mathematical model of a complete reformer was developed.

The mathematical models of reformers gradually became more sophisticated and highly complex in order to account for physical (i.e., the transport of momentum, material and energy) and chemical (i.e., combustion processes and the SMR process) phenomena taking place inside the unit. As a result, the mathematical model of the complete reformer

is defined by two sets of highly non-linear coupled partial integro-differential equations with seven independent variables including the three spatial coordinates, the temporal variable, the wave number of electro-magnetic waves and its corresponding two angular coordinates.<sup>47</sup> Therefore, characterizing the reformer by numerically determining the solution of the mathematical model of the complete reformer is a formidable task. In the effort to characterize reformers, previous studies of reformer modeling simplify the reformer mathematical model by avoiding simulating the combustion phenomena, and assume a profile for the energy re-

leased in the reaction zone due to the furnace-side oxidation<sup>38,39,72</sup> or a profile for the outer reforming tube wall temperature.<sup>54,55</sup> Specifically, these assumptions

substantially reduce the workload of the numerical solver. However, these profiles are often developed by extrapolating the scarcely available experimental data of bench-scale or pilot-scale versions of the system and, therefore, cannot be assumed to accurately represent the profiles that would be observed in an on-line reformer.

With improvements in technological performance, computational fluid dynamics (CFD) modeling became a powerful tool for predicting fluid behavior with a high level of accuracy.

Specifically, CFD modeling can capture all geometry characteristics of systems of interest through design software, which in turn allows CFD models to generate simulation results that can be expected to serve as reasonable substitutes for experimental data.<sup>73</sup>

Therefore, it is reasonable to assume that simulation results generated by a well-designed reformer CFD model, which simulates typical transport and chemical phenomena observed in reformers while accurately accounting for the reformer geometry, are expected to be consistent with experimental data collected from industrial-scale plants.

Furthermore, a well-designed CFD model of a reformer can provide insights into the system which cannot be captured in experimental data recorded from an on-site parametric study.

Motivated by the above considerations, we employ ANSYS Fluent CFD software to develop an industrial-scale reformer CFD model (for brevity, the CFD model is referred to as the “reformer CFD model”) that is composed of 336 reforming tubes, 96 burners and 8 flue gas tunnels (details given in Sec. 4.2). Initially, we discuss the modeling methodology for the reformer CFD model including kinetic models of methane/hydrogen combustion phenomena, radiative heat transfer modeling, global kinetic model of the SMR process, turbulence-chemistry interaction modeling and thermodynamic modeling. The selection of appropriate models to simulate all essential transport phenomena and chemical reactions of the reformer with an affordable

computational cost and reasonable computing time is based on expected transport and chemical reaction phenomena typically observed in the reformer. Specifically, the standard  $k-\epsilon$  turbulence model with the ANSYS Fluent enhanced wall treatment function, finite rate/eddy dissipation (FR/ED) turbulence-chemistry interaction model and global kinetic models of combustion<sup>649</sup> are integrated to simulate the non-premixed combustion characteristics (details given in Sec. 4.4.1). Additionally, an empirical correlation between the furnace-side radiative properties and temperature,<sup>45</sup> Kirchhoff's law, Lambert Beer's law and the discrete ordinate method<sup>26</sup> are adopted to simulate and quantify the rates of radiative heat transfer within the furnace-side mixture and between the furnace-side mixture and solid surfaces inside the reformer (i.e., combustion chamber refractory walls and outer reforming tube walls) (details given in Sec. 4.4.2). Furthermore, the reformer CFD model adopts the reforming tube modeling strategies developed in our previous work;<sup>37</sup> specifically, the reforming tubes are modeled by the pseudo-homogeneous reactor model, the reforming tube walls are modeled by the ANSYS Fluent thin wall model, the catalyst network is modeled by the continuum approach and its effects on the tube-side flow are modeled by the ANSYS Fluent porous zone function. In the reforming tubes, the standard  $k-\epsilon$  turbulence model with the ANSYS Fluent enhanced wall treatment function, global heterogeneous catalysis kinetic model of the SMR process<sup>70</sup> and FR/ED model are implemented to simulate the formation and consumption rates of the tube-side species in the turbulent reacting flow (details given in Sec. 4.5.1).

The boundary conditions for the reforming tube inlet (referred to in the following text as “tube-side feed”), burner inlet (referred to in the following text as “furnace-side feed”), and combustion chamber refractory walls are derived from typical plant data.<sup>38</sup> Finally, the simulation results generated by the reformer CFD model are rigorously validated by comparing them with the available data in the literature, converged solution produced by a single reforming tube CFD model and simulation results generated by a reforming Gibbs reactor of a commercial steady-state process simulator.

## 4.2 Industrial-scale Steam Methane Reformer Geometry

The reformer investigated in this work is developed based on an industrial-scale top-fired, co-current reformer designed by Sela Fluid Processing Corporation (Fig. 4.1). The reformer is approximately 16 m wide, 16 m long and 13 m tall.

The reformer contains seven rows of forty-eight reforming tubes of which the external diameter, internal diameter and exposed length are 14.6 cm, 12.6 cm and 12.5 m, respectively. Inside these reforming tubes, commercial nickel-based catalyst pellets (i.e., alpha-alumina-supported nickel oxide denoted as  $NiO-\alpha Al_2O_3$ ) are used as packing material. At the combustion chamber ceiling, these rows of reforming tubes are separated by eight rows of twelve burners which are fed with a furnace-side feed composed of a fuel stream containing methane, hydrogen and carbon monoxide, and an oxidizer stream containing combustion air ( $Ar$ ,  $N_2$  and  $O_2$ ).

The rows of burners which are adjacent to the combustion chamber refractory walls and a single row of reforming tubes (for brevity these burners are denoted as “outer-lane burners”), are fed with a lower furnace-side feed flow rate than the rows of burners which are adjacent to two rows of reforming tubes (for brevity, these burners are denoted as “inner-lane burners”). Specifically, the furnace-side feed flow rate of the outer-lane burners is 60% of that of the inner-lane burners to avoid causing “over-firing” in the outer lanes and “under-firing” in the inner lanes, which would occur if the total furnace-side feed flow rate were evenly distributed to all burners.

At the reformer floor, the rows of reforming tubes are separated by the rectangular intrusions known as flue gas tunnels or coffin boxes which extend from the front to the back of the combustion chamber along the rows of reforming tubes with a height of 3 m from the floor. Additionally, there are thirty-five extraction ports evenly distributed in a row along each side of the flue gas tunnels that allow the furnace-side mixture to enter the flue gas tunnels, and then to exit the combustion chamber through the front openings of the flue gas tunnels. In this



work, we will focus on the development of a CFD model of the reformer described above.

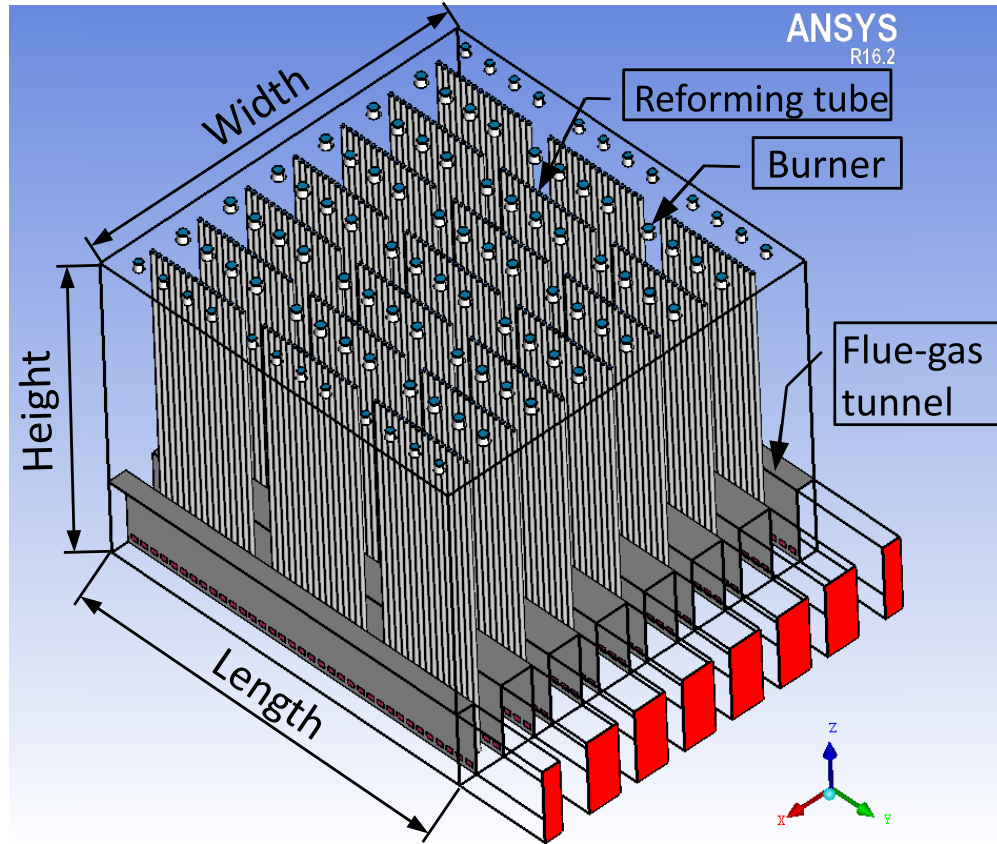


Figure 4.1: The isometric view of an industrial-scale, top-fired, co-current reformer with 336 reforming tubes, which are symbolized by 336 smaller circles, 96 burners, which are denoted by 96 larger circles, and 8 flue gas tunnels, which are represented by 8 rectangular intrusions. The outer-lane burners are burners on the right and left boundaries of the figure, while the inner-lane burners are slightly larger than the outer-lane burners in the figure.

### 4.3 Industrial-scale Steam Methane Reformer Mesh

In the CFD study of the reformer, the reformer volume is divided into small and discrete subdomains also known as grids (a collection of grids is referred to as a mesh), within which spatial variations are, though not negligible, significantly less drastic than those in the overall domain. Then, the reformer mathematical model (i.e., two sets of highly non-linear coupled integro-differential equations with seven independent variables) is discretized and numerically solved

within each grid to characterize the fluid-flow and temperature fields. Then, the numerical solutions of the grids are patched together to reconstruct the solution of the original domain.

Hence, creating a mesh with acceptable mesh quality is a critical task that determines the success level of CFD modeling because a CFD model built from a poor quality mesh has a slow speed of convergence<sup>7</sup> and is more likely to converge to an inaccurate solution as mesh quality directly determines solver discretization error.<sup>26</sup>

There are two major classes of meshing strategies in ANSYS ICEM, i.e., the unstructured tetrahedral meshing strategy (for simplicity, it is denoted as “unstructured meshing”) and the multi-block structured hexahedral meshing strategy (for simplicity, it is denoted as “structured meshing”). The unstructured meshing procedure creates a collection of predominantly tetrahedral grids that are arranged in an irregular pattern, while the structured meshing procedure creates a collection of hexahedral grids that are arranged in a pattern specified by the user of the mesh creation software. Although unstructured meshing is generally more proficient at approximating complicated geometries than structured meshing, the ANSYS ICEM environment offers an O-grid Block function that can be utilized to enhance the ability of structured meshing to approximate curvy geometry characteristics by re-arranging existing grid lines into an O shape to effectively improve the overall hexahedral mesh quality. In the creation of the reformer hexahedral mesh in this work, the O-grid Block function can be used for meshing of the burner geometries, which have a frustum-like structure, and the reforming tubes, which have a cylindrical structure. As shown in Figs. 4.2(a), 4.2(b) and 4.2(c), the structured meshing procedure with the O-grid Block function can capture the geometries of the reformer components (e.g., the inner-lane burners, outer-lane burners and reforming tubes) that cannot be represented with straight lines.

Therefore, because we can capture all aspects of the reformer geometry with the structured meshing technique, and because for wall-bounded systems like the reforming tubes, a CFD model built from structured meshing generally generates a converged solution closer to ex-

perimental data and also is expected to have a superior speed of convergence compared to other CFD models built from unstructured meshing when the system is decomposed into the same number of discrete grids,<sup>16,26,37</sup> the reformer mesh is created using structured meshing in this work. The good agreement of our CFD results (presented in Sec. 4.8) with typical plant data (compared in Sec. 4.10) utilizing this meshing strategy shows that the meshing method employed was adequate for obtaining results that are consistent with typical plant data.

In the reformer mesh, the grids are not uniformly distributed, but are more dense in regions expected to have large momentum, material, and temperature gradients, such as in the neighborhood of the reforming tube walls (where heat transfer from the furnace-side to the tube-side is expected to create temperature gradients that must be captured through a denser mesh as shown in Fig. 4.3) and in the regions directly under the burners that correspond to the flames (where the mixing-limited nature of non-premixed combustion is expected to create species and flow characteristics that should be captured with a denser mesh as shown in Fig 4.4). This design of the reformer mesh aims to reduce the stiffness of the spatial gradients of the transport variables, which allows the ANSYS Fluent CFD solver to obtain the numerical solution of the reformer CFD model with a shorter computing time.

In CFD, the reformer mesh must be discretized into a sufficient number of grids so that the CFD simulation data becomes mesh-independent. Our studies with three different mesh sizes of approximately 13, 29 and 41 million cells indicated that a mesh size of about 29 million cells produces mesh-independent results. Specifically, the reformer mesh contains 29,099,252 hexahedral grids, 88,798,168 quadrilateral faces and 30,584,930 nodes. The quality of the resulting mesh is evaluated utilizing the three mesh quality evaluation criteria (the minimum orthogonal factor, maximum ortho skew and aspect ratio) suggested by the manufacturer ANSYS Inc. of the commercial CFD software package utilized to develop the reformer CFD model in this work (other potential mesh evaluation criteria not specified by ANSYS Inc. were not utilized because ANSYS Inc. did not indicate recommended ranges for such properties that

would suggest appropriate mesh quality based on such other criteria). ANSYS Inc. suggests that if the values of the three suggested criteria for all subdomains (i.e., mesh quality) are within the recommended ranges shown in Table 4.1, the mesh can be considered to have reasonably good quality and can be used to generate CFD results (regardless of whether some subdomains have values close to the boundary of the recommended range, which would cause the values in Table 4.1 to be closer to the limits of the recommended ranges since the ANSYS Inc. criteria are for the worst-case values among all subdomains). Because the values of the minimum orthogonal factor, maximum ortho skew, and maximum aspect ratio among all subdomains are within the ranges recommended by ANSYS Inc., the mesh of the industrial-scale reformer is considered to have reasonably good quality (this is further validated by the good agreement of the CFD data generated using this mesh and typical plant data as discussed in Sec. 4.10). Although the minimum orthogonal factor and maximum ortho skew of the reformer mesh are close to the lower limits as shown in Table 4.1, the average orthogonal factor (0.965) and average ortho skew (0.035) of the reformer mesh are close to the ideal values of 1.000 and 0.000, respectively. Hence, we use the reformer mesh with approximately 29 million cells to create the reformer CFD model.

Table 4.1: Mesh quality of the reformer mesh.

	The reformer mesh	Recommended range
Minimum orthogonal factor	0.181	0.167 – 1.000
Maximum ortho skew	0.819	0.000 – 0.850
Maximum aspect ratio	28.5	1.000 – 100.0

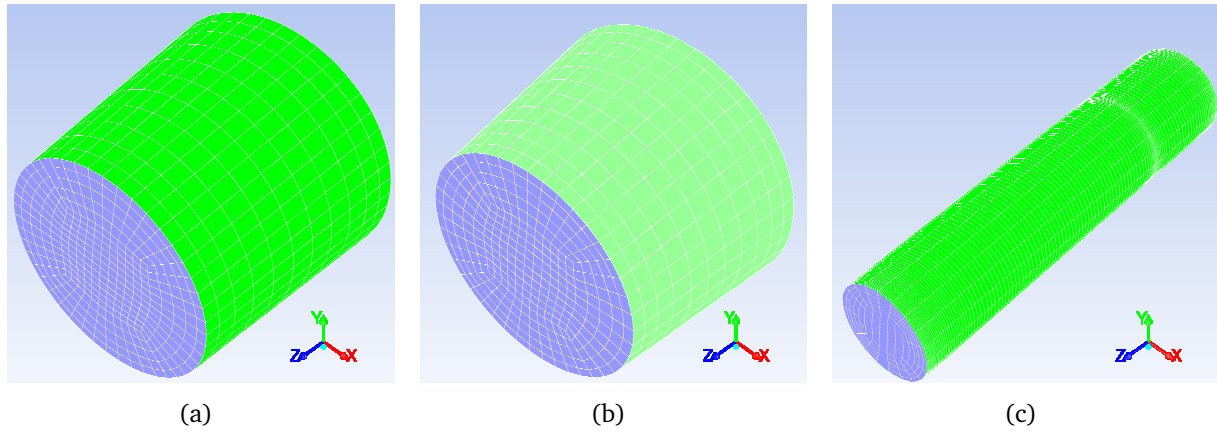


Figure 4.2: Isometric view of the hexahedral structured mesh of the outer-lane burner (a), inner-lane burner (b) and reforming tube (c). This figure demonstrates that the meshes of both the inner-lane and outer-lane burners, as well as the mesh of the reforming tubes, created by the O-grid Block function of ANSYS ICEM have the exact geometries of the corresponding components. In Fig. 4.2(c), the radial direction of the reforming tube is scaled up by 20 times for display purposes.

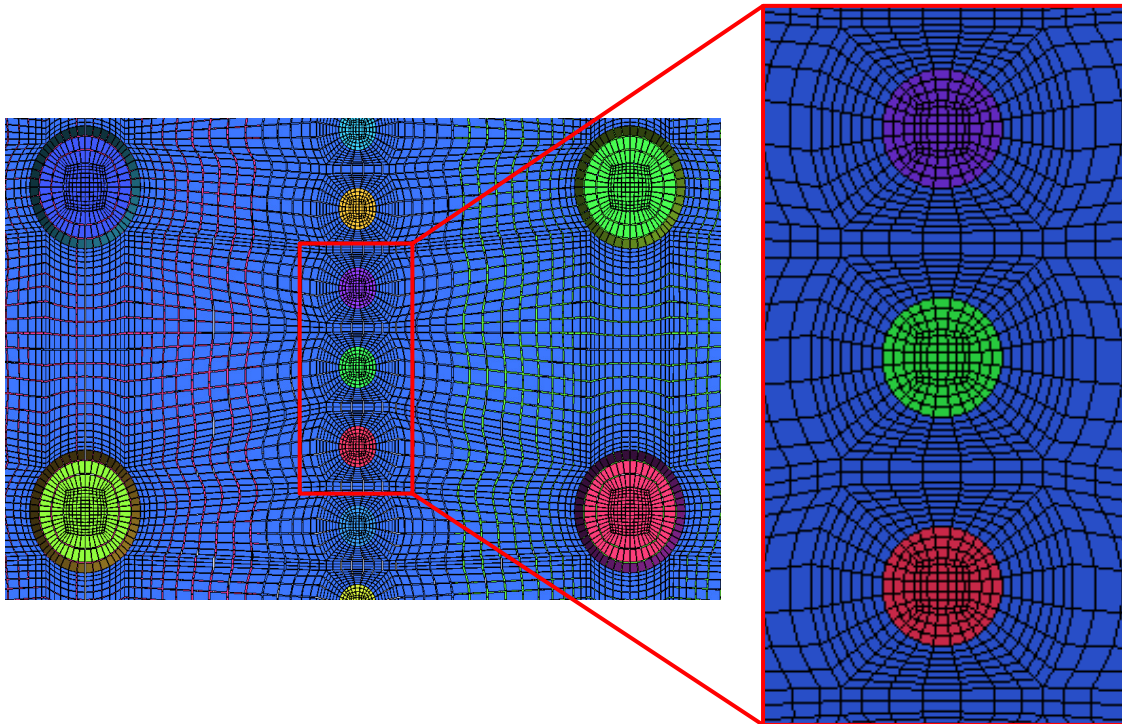


Figure 4.3: A sample of the top view of the hexahedral structured mesh of the reformer, where a row of reforming tubes is adjacent to two inner-lane burners. In Fig. 4.3, the reforming tube inlets and burner inlets are assigned with different color for display purposes.

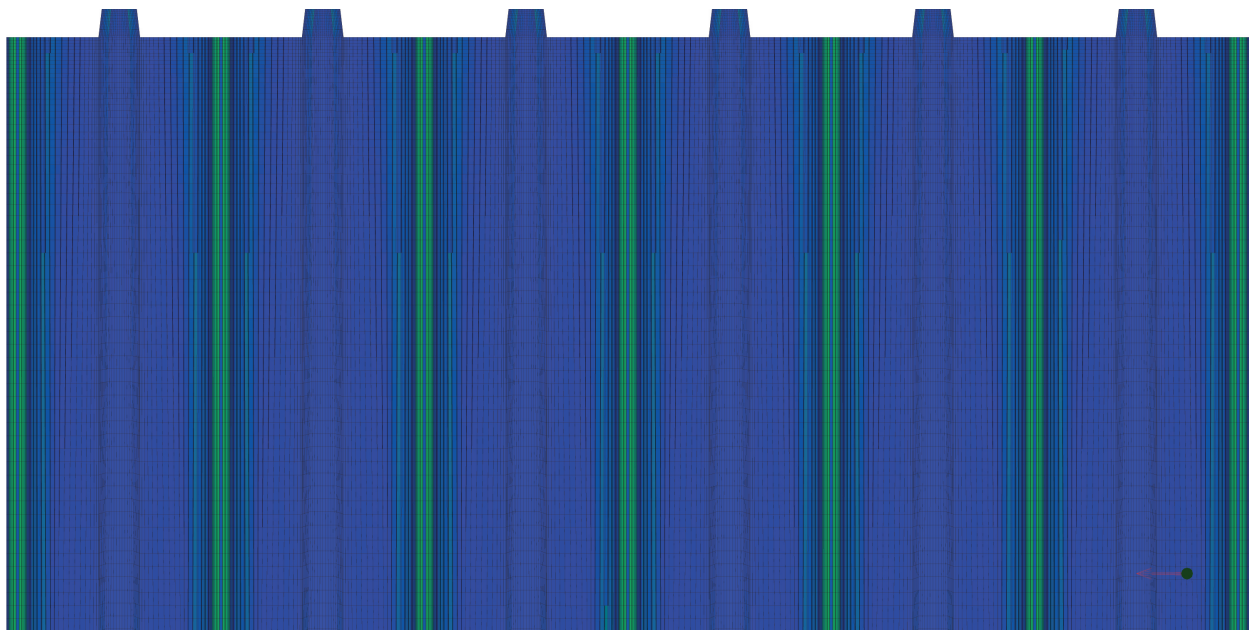


Figure 4.4: A sample of the vertical cross section of the hexahedral structured mesh of the reformer.

## 4.4 Furnace Chamber Modeling

### 4.4.1 Combustion Reaction Kinetic Model and Turbulence-Chemistry Model

In the combustion chamber, reducing agents in the furnace-side feed are oxidized to their highest oxidation states generating carbon dioxide, water and a large amount of thermal energy, which is used to drive the SMR process inside the reforming tubes.

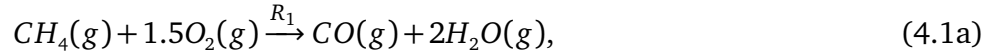
The chemistry of the combustion phenomena is a complex network of sequential elementary reactions governed by the concentrations of free radicals. For instance, the complete mechanism of the hydrogen combustion phenomena generating water involves more than 20 elementary reactions with various intermediates, and the corresponding detailed kinetic model consists of more than 20 distinct reaction rates.<sup>65</sup>

Although it is possible to implement such a detailed kinetic model in the reformer CFD model,

the CFD model would be no longer meaningful for industrial applications as it would take a long computing time to generate the CFD simulation data.

As a result, global kinetic models for the combustion of methane<sup>49</sup> and hydrogen<sup>6</sup> are adopted to reduce the computational requirement for simulating the reformer CFD model to model the combustion of the furnace-side feed:

Global kinetic model of methane combustion:



$$R_1 = 10^{15.22} [CH_4]^{1.46} [O_2]^{0.5217} \exp(-20643/T_{comb}) \quad (4.1b)$$



$$R_2 = 10^{14.902} [CO]^{1.6904} [O_2]^{1.57} \exp(-11613/T_{comb}) \quad (4.1d)$$

$$R_3 = 10^{14.349} [CO_2] \exp(-62281/T_{comb}) \quad (4.1e)$$

Global kinetic model of hydrogen combustion:



$$R_4 = 4.61 \times 10^{15} [H_2][O_2] \exp(-10080/T_{comb}) \quad (4.2b)$$

where checked the combustion model of ch4 but not h2 where  $R_1$ ,  $R_2$ ,  $R_3$  and  $R_4$  ( $\text{kmol m}^{-3} \text{s}^{-1}$ ) are the intrinsic volumetric reaction rates,  $T_{comb}$  (K) and  $[i]$ ,  $i = CO_2, CO, CH_4, H_2, O_2$  ( $\text{kmol m}^{-3}$ ) are the temperature and species molar concentrations of the furnace-side mixture. It is worth noting that because the empirical kinetic formulas (Eqs. 4.1–4.2) are in the Arrhenius form, they can be directly integrated into the reformer CFD model to simulate the formation and consumption rates of the furnace-side species.

Table 4.2: Furnace-side inlet operating conditions of the inner-lane burner in which  $x_{comb,inlet}^i$  represents the mole fraction of species  $i$  in the furnace-side feed.

Pressure (kPa)	131.3
Temperature (K)	532.9
Flow rate (kg/s)	1.1358
$x_{comb,inlet}^{H_2O}$	0.0039
$x_{comb,inlet}^{O_2}$	0.1610
$x_{comb,inlet}^{Ar}$	0.0071
$x_{comb,inlet}^{N_2}$	0.6008
$x_{comb,inlet}^{H_2}$	0.0592
$x_{comb,inlet}^{CO_2}$	0.0972
$x_{comb,inlet}^{CO}$	0.0208
$x_{comb,inlet}^{CH_4}$	0.0501

In the reformer, the furnace-side feed composed of two separate streams, i.e., the fuel stream and the oxidizer stream, is combusted inside the combustion chamber to generate the required fired duty for the SMR process. The intrinsic nature of non-premixed combustion is turbulent mixing-controlled, i.e., the rate of the chemical reactions is relatively faster than that of mixing on which the observed reaction rates of furnace-side species depend. In the remainder of this section, we demonstrate a modeling strategy that allows the reformer CFD model to simulate the behavior of non-premixed combustion processes of the furnace-side feed.

Specifically, in the reformer CFD model, the fuel stream and air stream of the furnace-side feed are assumed to be well-mixed as shown in Table 4.2 prior to being fed into the combustion chamber, and the combustion phenomena of methane and hydrogen are modeled by the pre-mixed combustion model. However, the intrinsic nature of non-premixed combustion phenomena must be shown in the simulation results generated by the reformer CFD model. This issue is resolved by using the finite-rate/eddy-dissipation (FR/ED) model as the turbulence-chemistry interaction model to simulate the reaction rates of the furnace-side species. In particular, the FR/ED model utilizes the global kinetic models of methane/hydrogen combustion phenomena (shown in Eqs. 4.1 and 4.2), finite rate formula (shown in Eq. 4.3c) and eddy-dissipation rates (shown in Eqs. 4.3a–4.3b) to estimate the observed reaction rates of the furnace-side



species.<sup>26</sup> The formulation of the FR/ED model is presented as follows:

$$R_{i,j} = \nu_{i,j} M_i A \rho_{comb} \frac{\epsilon_{comb}}{k_{comb}} \min_{\mathcal{R}} \left( \frac{Y_{\mathcal{R}}}{\nu_{\mathcal{R},j} M_{\mathcal{R}}} \right) \quad (4.3a)$$

$$R_{i,j} = \nu_{i,j} M_i A B \rho_{comb} \frac{\epsilon_{comb}}{k_{comb}} \frac{\sum_{\mathcal{P}} Y_{\mathcal{P}}}{\sum_n^N \nu_{n,j} M_n} \quad (4.3b)$$

$$R_{i,j} = \nu_{i,j} M_i R_j \quad (4.3c)$$

where  $R_{i,j}$  ( $\text{kg m}^{-3} \text{s}^{-1}$ ) and  $\nu_{i,j}$  are the observed reaction rate and stoichiometric coefficient of species  $i$  in reaction  $j$ ,  $M_i$  ( $\text{kg kmol}^{-1}$ ) is the molecular weight of species  $i$ ,  $Y_{\mathcal{R}}$  and  $M_{\mathcal{R}}$  are the mass fraction and molecular weight of a specified reactant  $\mathcal{R}$ ,  $\nu_{\mathcal{R},j}$  is the stoichiometric coefficient of a specified reactant  $\mathcal{R}$  in reaction  $j$ ,  $A = 4.0$  and  $B = 0.5$  are the default empirical constants of the FR/ED model,<sup>44</sup>  $k_{comb}$  ( $\text{m}^2 \text{s}^{-2}$ ) and  $\epsilon_{comb}$  ( $\text{m}^2 \text{s}^{-3}$ ) are the turbulence kinetic energy and dissipation rate (which will be discussed in Sec. 4.7),  $Y_{\mathcal{P}}$  is the mass fraction of a product species  $\mathcal{P}$  in reaction  $j$ ,  $R_j$  ( $\text{kmol m}^{-3} \text{s}^{-1}$ ) is the intrinsic volumetric reaction rate of reaction  $j$  from Eqs. 4.1–4.2,  $\rho_{comb}$  ( $\text{kg m}^{-3}$ ) is the density of the furnace-side mixture,  $n$  is the index of the product species involved in reaction  $j$  and  $N$  represents the number of chemical species in reaction  $j$ .<sup>26</sup> When the FR/ED model is integrated in the reformer CFD model, the reaction rate of each furnace-side species is calculated based on the three different methods presented in Eqs. 4.3a, 4.3b and 4.3c for which the smallest estimate corresponding to the slowest rate is set as the observed rate.<sup>42</sup> In other words, in the reaction-limited zone, the observed reaction rates of the furnace-side species are computed by the finite rate formula (Eq. 4.3c), whereas in the transport-limited zone, they are computed by the eddy-dissipation formulas (Eqs. 4.3a and 4.3b). Particularly, because the furnace-side temperature of 532.9 K at the inner-lane/outer-lane burner inlets is relatively low compared to the typical operating furnace-side temperature, the finite rate formula is expected to predict slower reaction rates of furnace-side species than those estimated by the eddy-dissipation formulas. This is because

the activation temperature values of methane/hydrogen combustion phenomena derived from the chosen kinetic models (Eqs. 4.1–4.2) are substantially larger than the furnace-side feed temperature, and the concentrations of reacting species are diluted by the presence of inert furnace-side species (i.e., nitrogen and argon), which account for ~61% of the furnace-side feed molar flow rate. Furthermore, the contour plots of furnace-side compositions and energy released from the combustion of the furnace-side feed (presented in Sec. 4.8) generated by the reformer CFD model indicate that the oxidation rates of methane and hydrogen detected in the vicinity of the inner-lane/outer-lane burner inlets are slow, which matches well with the expected observations. The results suggest that the reaction rates of furnace-side species estimated by the FR/ED model in these regions mimic the effect of initial mixing of fuel and oxidizer streams in non-premixed combustion phenomena. As the oxidation of the furnace-side feed gradually proceeds to produce combustion products (i.e., carbon dioxide and water), the enthalpy of reactions is released causing the temperature of the furnace-side mixture to increase, which allows the methane/hydrogen combustion phenomena to eventually overcome the activation energy barrier. Therefore, in the flame bodies, the finite rate formula is expected to yield higher estimates for the reaction rates of the furnace-side species than those based on the eddy-dissipation formulas.

As a result, the premixed combustion model coupled with the FR/ED model allows the reformer CFD model to simulate the turbulent-mixing controlled characteristics of non-premixed methane/hydrogen combustion phenomena.

#### **4.4.2 Radiative Heat Transfer Modeling**

In high-temperature applications such as the SMR process, the contribution of thermal radiation to the total heat transfer rate cannot be neglected.

In,<sup>51</sup> thermal radiation has also been reported as the dominant mode of heat transfer in a reformer as it accounts for about ~95% of the total heat transfer rate to the tube side. This

is because the rates at which thermal energy is transferred by conduction and convection are known to be approximately proportional to the difference in temperature, while the rate of thermal energy transferred by radiation is proportional to the difference between the temperatures raised to the fourth power. Therefore, in the high-temperature combustion chamber of the reformer, thermal radiation would be expected to contribute significantly to heat transfer.

The study of radiative heat transfer is not often conducted experimentally for reformers because of the severe operating temperature of 2050 K inside the reformer and the absence of an accurate means to measure the radiative heat transfer rate. Additionally, the only experimental data type related to the total heat transfer rate which can be collected from an on-line reformer may be the outer reforming tube wall temperature at designated locations (e.g., three along the heated tube length of 12.5 m).<sup>39</sup> This data is expected to carry a high degree of uncertainty because of the way by which the outer reforming tube wall temperature is measured, which involves a system of infrared cameras that gains access into the reformer to monitor the outer reforming tube wall temperature through peepholes in the combustion chamber refractory walls.<sup>38</sup> Therefore, the study of radiative heat transfer in reformers has been conducted primarily by a modeling approach.

To model thermal radiation, it is essential that the role of radiating media in thermal radiation is well understood. Specifically, radiating media, which can consist of various particle types (e.g., neutral molecules, ionic molecules, free electrons and atoms), participate in thermal radiation by absorbing or emitting radiative energy in the form of electromagnetic waves for which the corresponding energy content denoted by  $E_{wave}$  can be evaluated as follows:

$$E_{wave} = h \cdot \nu_{wave} \quad (4.4)$$

where  $h$  is Plank's constant and  $\nu_{wave}$  ( $s^{-1}$ ) is the frequency of an electromagnetic wave. When a radiating particle absorbs/emits radiative energy, it absorbs/emits an electromagnetic wave,

and its energy increases/decreases correspondingly by the amount of the electromagnetic wave. In air-fired reformers, radiating media (e.g., the furnace-side mixture) can be assumed to be neutral molecules, and thus, the furnace-side mixture can absorb an electromagnetic wave if the radiative energy content of the electromagnetic wave is equal to the transition energy required for the energy level to elevate to higher discrete bound states which correspond to the vibrational, rotational and electronic modes. Hence, radiative heat transfer in the furnace-side mixture is spectrum dependent because the furnace-side mixture only absorbs/emits radiative energy at certain frequencies in the entire spectrum.

In the furnace-side mixture, monatomic molecules (e.g., argon) and diatomic molecules (e.g., oxygen, nitrogen, hydrogen and carbon monoxide) can be considered to be transparent to radiation.<sup>45</sup> As a result, the furnace-side mixture can be treated as a  $H_2O-CO_2$  mixture in the sense that the radiative properties of the furnace-side mixture can be considered to depend only on those of  $H_2O$  and  $CO_2$  (i.e., the furnace-side mixture must be modeled as a radiatively participating medium with radiative properties developed from those of  $H_2O$  and  $CO_2$ ).

The combustion modeling literature suggests that the radiative properties of the furnace-side mixture can be estimated with the line-by-line model (LBLM), statistical narrow band model (SNBM) and exponential wide band model (EWBM); nevertheless, because of the excessively high required computational cost of utilizing these models for large-scale systems, they are not compatible with CFD models developed for industrially-oriented applications.<sup>45</sup> In the present work, a more computationally efficient empirical model developed in,<sup>45</sup> which is designed for air-fired combustion systems, is utilized. The empirical model uses the temperature, composition and total pressure of the furnace-side mixture and the characteristic dimension of the combustion chamber in the estimation of the total emissivity of the furnace-side mixture. The results reported in<sup>45</sup> show that the total emissivity of an air-fired combustion system calculated from the empirical model is within  $\pm 5\%$  of the data generated by the SNBM, and the computing time is decreased by a factor of at least ten. Hence, the following empirical model

for the total emissivity of the furnace-side mixture is expected to offer a significant reduction in the computing time and to predict sufficiently accurate estimates of the furnace-side total emissivity:

$$a_i = a_{10,i} + a_{11,i} \cdot x_{comb}^{H_2O} + a_{12,i} \cdot x_{comb}^{CO_2} + a_{13,i} \cdot x_{comb}^{H_2O} \cdot x_{comb}^{CO_2} \quad (4.5a)$$

$$L = 3.6 \cdot \frac{V_{comb}}{A_{comb}} \quad (4.5b)$$

$$\begin{aligned} \epsilon_{rad} = & a_1 + a_2 \cdot \ln(T_{comb}) + a_3 \cdot \ln(P_{comb}^t L) + a_4 \cdot [\ln(T_{comb})]^2 \\ & + a_5 \cdot [\ln(P_{comb}^t L)]^2 + a_6 \cdot \ln(T_{comb}) \cdot \ln(P_{comb}^t L) \end{aligned} \quad (4.5c)$$

where  $a_{j,i}$  and  $a_i$  are the model constants of the empirical model as shown in Table 4.3,  $x_{comb}^{H_2O}$  and  $x_{comb}^{CO_2}$  are the mole fractions of water and carbon dioxide in the furnace-side mixture,  $V_{comb} \sim 3303.5 \text{ m}^3$ ,  $A_{comb} \sim 5204.4 \text{ m}^2$  and  $L \sim 2.3 \text{ m}$  are the volume, total surface area and characteristic dimension of the combustion chamber, respectively, and  $P_{comb}^t$  and  $\epsilon_{rad}$  are the total pressure and total emissivity of the furnace-side mixture. The empirical model of the furnace-side total emissivity is designed for air-fired combustion systems, and as a result, the total pressure inside the furnace chamber in<sup>45</sup> as well as in the present work is assumed to be constant and is taken to be near atmospheric pressure of 100 kPa (i.e., 1 bar).

Though the correlation of Eq. 4.5 depends on  $x_{comb}^{CO_2}$  and  $x_{comb}^{H_2O}$ , which vary in the flame region of the furnace-side, the flame physical volume (i.e., the reaction zones of the combustion of the furnace-side feed) accounts for a small fraction of the total volume of the combustion chamber. Therefore, the region within which  $\epsilon_{rad}$  would vary due to the changes in  $a_i$ ,  $i = 1, \dots, 6$ , would be expected to be small compared to the dimensions of the furnace-side within which radiation is occurring. Furthermore, the difference in the furnace-side composition between the combustion product and the furnace-side feed is small, which is due to the fact that the inert gases (i.e., nitrogen and argon) of the furnace-side feed account for  $\sim 61.0\%$  of the total molar flow

rate, while the fuel (i.e., methane and hydrogen) only accounts for  $\sim 11.0\%$ . Specifically, the differences in the average mole fractions of  $H_2O$  and  $CO_2$  between the furnace-side feed and the combustion product change from 0.0039 to  $\sim 0.170$  and from 0.0972 to  $\sim 0.175$ , respectively. As a result, the change in  $\epsilon_{rad}$  between its value at the furnace-side inlet conditions and the complete oxidation condition of the furnace-side feed is not expected to be necessary to account for within the radiation calculations, especially given the small flame volume over which  $\epsilon_{rad}$  varies. Therefore, to reduce computation time,  $x_{comb}^{H_2O}$  and  $x_{comb}^{CO_2}$  are both approximated as constants at 0.170 and 0.175, respectively, in calculating  $\epsilon_{rad}$  according to Eq. 4.5. Moreover, the characteristic dimension  $L$  of the reformer, which is estimated by Eq. 4.5b based on the volume and total enclosure surface area of the combustion chamber, is also a constant, as is  $P_{comb}^t$ . As a result, the furnace-side total emissivity reduces to a function only of the furnace-side temperature (it is noted that the approximation of a constant furnace-side composition in calculating  $\epsilon_{rad}$  does not imply that other properties of the furnace-side mixture should be modeled to be independent of composition; modeling the composition of the furnace-side is important in capturing, for example, the observed reaction rates of the furnace-side species, which determines the heat release profile of the combustion of the furnace-side feed).

Next, the absorption coefficient of the furnace-side mixture is related to the value of  $\epsilon_{rad}$  from the empirical model of Eq. 4.5 through Kirchhoff's law and Lamber Beer's Law as follows:

$$\sigma_a = -\frac{\ln(1 - \epsilon_{rad})}{L} \quad (4.6)$$

where  $\sigma_a$  is the absorption coefficient of the furnace-side mixture. It is important to note that the correlation of the absorption coefficient in Eq. 4.6 inherits all assumptions that are used to develop the correlation of the total emissivity, and therefore, it is also a function of only the furnace-side temperature. Subsequently, an absorption coefficient data set within the operating temperature range of the reformer is obtained by the correlations of Eqs. 4.5 and 4.6 and is fit with a second-order polynomial function by using a least-squares linear regression method.

Table 4.3: Empirical constants of the correlation of the furnace-side mixture total emissivity with temperature. These constants are used in the calculation of  $a_i$  (Eq. 4.5a).<sup>45</sup>

$a_i$	$a_{10,i}$	$a_{11,i}$	$a_{12,i}$	$a_{13,i}$
$i = 1$	-2.756	-12.091	-2.074	8.90
$i = 2$	1.0155	3.827	0.649	-2.48
$i = 3$	0.284	-1.024	0.421	-0.64
$i = 4$	-0.085	-0.286	-0.047	0.17
$i = 5$	0.0104	-0.067	-0.016	0.19
$i = 6$	-0.0272	0.162	-0.061	0.08

The result of this fit is

$$\sigma_a = 2.10 \times 10^{-8} \cdot T_{comb}^2 - 2.06 \times 10^{-4} \cdot T_{comb} + 0.456, \quad (4.7)$$

which will be utilized in the reformer CFD model.

The next step in modeling radiation within the furnace side is choosing a suitable radiation model. The present work is facilitated by the ANSYS Fluent CFD solver, which only supports a limited number of thermal radiation models. Specifically, ANSYS Fluent uses one of five radiative heat transfer models (i.e., Rosseland,  $P-1$ , discrete transfer radiation model (DTRM), surface to surface (S2S) model and discrete ordinate model (DOM)) to estimate the energy transferred by thermal radiation in high-temperature applications in which thermal radiation cannot be ignored. Among the five radiative heat transfer models, the DOM is the most versatile model.<sup>26</sup> In particular, the DOM can estimate heat transfer by radiation within absorbing, emitting and scattering media and between the participating media and opaque/semi-transparent walls. In addition, unlike the Rosseland and  $P-1$  approximation which are only applicable for high optical thickness systems, the DOM can be used in any high-temperature application including the reformer in which the optical thickness is not well-defined because of the complex reformer interior. Unlike the S2S model which ignores the presence of the participating media, the DOM can account for the effect of the absorbing and emitting furnace-side mixture. Additionally, unlike the DTRM which uses the ray tracing technique and is more prone to error

Table 4.4: Properties of the combustion chamber refractory walls.

Density ( $\text{kg m}^{-3}$ )	3950
Heat Capacity ( $\text{J kg}^{-1} \text{K}^{-1}$ )	718
Thermal Conductivity ( $\text{W m}^{-1} \text{K}^{-1}$ )	2.6
Emissivity	0.65

due to ray effects,

the DOM converts the partial integro-differential radiative transfer equation (RTE) with seven independent variables into a finite number of transport equations of radiation intensity, which depends on the solid angle discretization parameters of the DOM. In particular, by default in each octant space the azimuthal division is equal to two, and the polar division is equal to two, which allows the DOM to generate 32 partial differential equations of radiation intensity corresponding to 32 discrete direction vectors  $\vec{s}$  specifying the directions at which energy is transferred by radiation. As a result, the radiative heat transfer rate obtained by solving the equations of radiation intensity is expected to require a relatively lower computational cost than is required to directly solve the RTE. In this work, radiative heat transfer between the furnace-side mixture, combustion chamber refractory walls and outer reforming tube walls will be quantified by the discrete ordinate method (DOM). The description of the DOM of an absorbing, emitting and non-scattering gray gas can be found in.<sup>26</sup>

It is critical to a successful modeling task to realize that the internal emissivity of the wall surface is an intrinsic property of the surface, and therefore, it only depends on the surface's characteristics, e.g., the surface texture, instead of the surface material. In the reformer CFD model, the emissivity coefficients for the wall surfaces are assumed to be independent of the furnace-side temperature and are constant. Specifically, the emissivity coefficients of the reforming tubes, refractory wall and tunnel wall are chosen to be 0.85, 0.65 and 0.65, respectively, and additional physical properties of the refractory wall and tunnel wall are shown in Table 4.4.<sup>38</sup>



## 4.5 Reforming Tube Modeling

In the present work, the 336 reforming tubes are modeled by the pseudo-homogeneous reactor model, the reforming tube walls are modeled by the ANSYS Fluent thin wall model, the catalyst network is modeled by the continuum approach and its effects on the tube-side flow are modeled by the ANSYS Fluent porous zone function. These modeling strategies were utilized due to their success in generating CFD data with good agreement with typical plant data for a single reforming tube with an assumed outer reforming tube wall temperature profile (i.e., the furnace-side and its interactions through heat transfer with the tube-side were not simulated) in.<sup>37</sup> In the remainder of this section, the modeling strategies of the kinetic model of the SMR process and the catalyst network are presented.

### 4.5.1 Reforming Reaction Kinetic Model

On the macroscopic scale, the SMR process consumes the thermal energy produced by the combustion of the furnace-side feed to convert steam and methane into hydrogen and carbon oxides in the presence of a nickel-based catalyst network, and the tube-side composition is reported to be close to the equilibrium composition at the reforming tube exit.<sup>70</sup> On the microscopic scale, the reactants are transported from the bulk of the tube-side mixture to the surface of the catalyst network by convective mass transfer driven primarily by the reactant concentration gradients, which are generated by the external diffusion resistance of the catalyst network. Then, they diffuse down the second reactant concentration gradients from the surface of the catalyst network through the catalyst medium to the catalyst active sites, where the SMR process occurs to generate the desired hydrogen along with carbon oxides. The reactant concentration gradients within the catalyst are generated by the internal diffusion resistance of the catalyst network. Finally, the products diffuse from the catalyst active sites back to the surface of the catalyst network, and eventually emerge back into the tube-side mix-

ture. A kinetic model that provides a rate formula for each microscopic event of the SMR process is unsuitable for the reformer CFD simulation because it would be expected to require a significant computation time.

Therefore, a global kinetic model of the SMR process proposed in,<sup>70</sup> which is derived based on the Langmuir-Hinshelwood mechanism (i.e., the heterogeneous catalysis kinetic model) and is formulated in  $\text{kg} (\text{kg of catalyst})^{-1} \text{s}^{-1}$ , is utilized to lessen the computational demand without substantially sacrificing the accuracy of the simulation results:

$$\begin{aligned} \text{CH}_4(\text{g}) + \text{H}_2\text{O}(\text{g}) &\xrightleftharpoons{\text{C}} \text{O}(\text{g}) + 3\text{H}_2(\text{g}), \\ R_5 &= \frac{k_1}{(p_{\text{tube}}^{\text{H}_2})^{2.5}} \left( p_{\text{tube}}^{\text{CH}_4} p_{\text{tube}}^{\text{H}_2\text{O}} - \frac{(p_{\text{tube}}^{\text{H}_2})^3 p_{\text{tube}}^{\text{CO}}}{K_1} \right) / \text{DEN}^2 \end{aligned} \quad (4.8a)$$

$$\begin{aligned} \text{CO}(\text{g}) + \text{H}_2\text{O}(\text{g}) &\xrightleftharpoons{\text{C}} \text{O}_2(\text{g}) + \text{H}_2(\text{g}), \\ R_6 &= \frac{k_2}{p_{\text{tube}}^{\text{H}_2}} \left( p_{\text{tube}}^{\text{CO}} p_{\text{tube}}^{\text{H}_2\text{O}} - \frac{p_{\text{tube}}^{\text{H}_2} p_{\text{tube}}^{\text{CO}_2}}{K_2} \right) / \text{DEN}^2 \end{aligned} \quad (4.8b)$$

$$\begin{aligned} \text{CH}_4(\text{g}) + 2\text{H}_2\text{O}(\text{g}) &\xrightleftharpoons{\text{C}} \text{O}_2(\text{g}) + 4\text{H}_2(\text{g}), \\ R_7 &= \frac{k_3}{(p_{\text{tube}}^{\text{H}_2})^{3.5}} \left( p_{\text{tube}}^{\text{CH}_4} (p_{\text{tube}}^{\text{H}_2\text{O}})^2 - \frac{(p_{\text{tube}}^{\text{H}_2})^4 p_{\text{tube}}^{\text{CO}_2}}{K_3} \right) / \text{DEN}^2 \end{aligned} \quad (4.8c)$$

$$\begin{aligned} \text{DEN} &= 1 + \frac{K_{\text{H}_2\text{O}} p_{\text{tube}}^{\text{H}_2\text{O}}}{p_{\text{tube}}^{\text{H}_2}} \\ &\quad + K_{\text{CO}} p_{\text{tube}}^{\text{CO}} + K_{\text{H}_2} p_{\text{tube}}^{\text{H}_2} + K_{\text{CH}_4} p_{\text{tube}}^{\text{CH}_4} \end{aligned} \quad (4.8d)$$

where  $K_{\text{H}_2}$ ,  $K_{\text{CH}_4}$  and  $K_{\text{CO}}$  are adsorption constants for  $\text{H}_2$ ,  $\text{CH}_4$  and  $\text{CO}$ ,  $K_{\text{H}_2\text{O}}$  is a dissociative adsorption constant of  $\text{H}_2\text{O}$ ,  $K_1$ ,  $K_2$ , and  $K_3$  are equilibrium constants of the reactions in Eqs. 4.8a, 4.8b and 4.8c,  $k_1$ ,  $k_2$  and  $k_3$  are forward kinetic constant coefficients of the reactions in Eqs. 4.8a, 4.8b, and 4.8c, respectively,  $\text{DEN}$  is a dimensionless parameter and  $p_{\text{tube}}^{\text{H}_2}$ ,  $p_{\text{tube}}^{\text{CH}_4}$ ,  $p_{\text{tube}}^{\text{H}_2\text{O}}$ ,  $p_{\text{tube}}^{\text{CO}}$  and  $p_{\text{tube}}^{\text{CO}_2}$  are the partial pressures of  $\text{H}_2$ ,  $\text{CH}_4$ ,  $\text{H}_2\text{O}$ ,  $\text{CO}$  and  $\text{CO}_2$  in the tube-side mixture, respectively. This kinetic model is widely accepted<sup>36</sup> and is frequently used in CFD

modeling and first-principles modeling of the SMR process because it accounts for the amount of the available catalyst. The kinetic model can also be modified to account for the external and internal diffusion resistances of the catalyst network by multiplying the kinetic formulas with a universal effectiveness factor of 0.1.<sup>69</sup> However, unlike the global kinetic models of the methane and hydrogen combustion phenomena, because the empirical kinetic formulas shown in Eq. 4.8 are not in the Arrhenius form, they cannot be directly integrated into the reformer CFD model. Nevertheless, ANSYS Fluent allows these non-Arrhenius form kinetic formulas to be integrated into the CFD model by means of user-defined functions, i.e., *DEFINE\_VR\_RATE* and *DEFINE\_NET\_REACTION\_RATE*, to simulate the formation and consumption rates of the tube-side components. In,<sup>70</sup> the complete list of the possible chemical reactions in the SMR process is provided, which does not contain any gas phase reaction. Additionally, the components of the tube-side mixture (i.e., methane, superheated steam, carbon oxides and hydrogen) of the SMR process are naturally stable and will not undergo chemical reaction in the absence of the nickel-based catalyst. Therefore, gas phase reactions are not considered in the present work.

Inside the reforming tubes, the catalyst network with a uniform packing pattern disrupts the tube-side flow and enhances the mixing processes of the tube-side mixture, and the Reynolds number at the reforming tube entrances is calculated to be ~70,000 based on the tube-side feed information detailed in.<sup>37</sup> Therefore, the tube-side flow is expected to be turbulent, and it is necessary to utilize a suitable turbulence-chemistry interaction model to simulate the tube-side species reaction rates under the influence of turbulent effects. Two turbulence-chemistry interaction models offered by ANSYS Fluent that may be appropriate for modeling turbulent effects on the tube-side species reaction rates are the FR/ED model and the EDC model.

On one hand, the FR/ED model is expected to require less computation time, but is known to estimate observed reaction rates that deviate significantly from experimental data for some reactions with multiple dependent elementary reaction rates.<sup>26</sup> In contrast, the EDC model is

expected to be more accurate because it can utilize detailed multi-step reaction kinetic models to determine the formation and consumption rates of the tube-side species in the turbulent reacting flow, but is computationally expensive. Additionally, the EDC model with default parameters is a robust turbulence-chemistry interaction model, and can be directly applied for a wide variety of reaction-limited and diffusion-limited systems.<sup>43</sup> The description of the EDC model can be found in.<sup>26</sup>

Although the observed reaction rates of the tube-side species calculated from the EDC model are expected to have higher accuracy than those calculated from the FR/ED model of Eq. 4.3, it is preferable for industrial applications to avoid integrating the EDC model in the reformer CFD model when that does not significantly impact the solution accuracy due to the corresponding increase in the required computational cost. In Sec. 4.6, the numerical error associated with the FR/ED model in the solution of the reformer CFD model is evaluated to determine that the FR/ED model is an appropriate chemistry-turbulence interaction model for the tube-side flow.

#### **4.5.2 Porous Zone Design**

In the reforming tubes, the nickel-based catalyst pellets are used as the packing material, and hence, it is essential to the development of the reformer CFD model that the effects of the catalyst network on the SMR process are well understood. Specifically, the catalyst network facilitates the formation of hydrogen from the naturally stable and slowly-reacting tube-side reactants, i.e., steam and methane, and it also enhances the rate of convective energy transfer from the reforming tube walls to the tube-side mixture by increasing the contact area. Additionally, the catalyst network interferes with the tube-side flow, increases the residence time of the tube-side species and reduces the free volume. Furthermore, a pressure difference between the tube-side mixture at the reforming tube inlet and outlet cannot be neglected due to the presence of the catalyst network inside the reforming tubes. Therefore, the effects of the

catalyst on the momentum and energy transport equations of the tube-side must be accounted for. In the present work, the reforming tubes are modeled by the pseudo-homogeneous reactor model in which the solid phase (i.e., the catalyst network) is modeled by the continuum approach, and the effects of the catalyst network on the tube-side flow are modeled by the ANSYS Fluent porous zone function. The porous zone function modifies the standard governing equations of the pseudo-homogeneous reactor model to account for the presence and effects of the catalyst network on the tube-side flow (which will be discussed in Sec. 4.7.2). Although the modeling strategy does not require the catalyst pellets and the random packing pattern of the catalyst network to be modeled, the simulation data generated by the reforming tube CFD model is expected to capture the gradients of the tube-side composition and state variables at the macroscopic scale typically larger than the equivalent dimension of the catalyst pellet.<sup>48</sup> The modeling strategy has been shown to be valid for packed-bed reactors in which the effective characteristic dimension of the catalyst pellets is less than 5 mm.<sup>61</sup> We have found that a reforming tube CFD model created from this modeling approach can simulate the macroscopic effects of the catalyst network on the tube-side mixture (e.g., the pressure drop across the catalyst network and the increase of the tube-side residence time generated by the reforming tube CFD model are consistent with the typical plant data).<sup>37</sup>

In the reformer CFD model, the modeling parameters of the porous zone function are estimated from the semi-empirical Ergun equation:<sup>18</sup>

$$\frac{\Delta P_{tube}}{L_{tube}} = \frac{150\mu_{tube}}{D_p^2} \frac{(1-\gamma)^2}{\gamma^3} v_{\infty,tube} + \frac{1.75\rho_{tube}}{D_p} \frac{(1-\gamma)}{\gamma^3} v_{\infty,tube}^2 \quad (4.9)$$

where  $\Delta P_{tube}$  (kPa) is the pressure difference of the tube-side mixture across the catalyst network,  $v_{\infty,tube}$  (m s<sup>-1</sup>),  $\rho_{tube}$  (kg m<sup>-3</sup>) and  $\mu_{tube}$  (kg m<sup>-1</sup> s<sup>-1</sup>) are the average superficial velocity, density and viscosity of the tube-side mixture at the reforming tube inlet and outlet, respectively,  $L_{tube}$  of 12.5 m is the reforming tube length,  $\gamma=0.609$  is the porosity of the catalyst network and  $D_p$  (m) is an effective diameter of the catalyst pellets.

Based on the pressure drop of the tube-side mixture across the catalyst network from typical plant data, reforming tube geometry and available physical properties of the catalyst network reported in,<sup>37</sup> the Ergun equation is employed to estimate the effective diameter of the catalyst pellets. Then, the modeling parameters of the porous zone function required by the reformer CFD model are calculated as follows,

$$\alpha = \frac{D_p^2}{150} \frac{\gamma^3}{(1-\gamma)^2} \quad (4.10a)$$

$$\beta = \frac{3.5}{D_p} \frac{(1-\gamma)}{\gamma^3} \quad (4.10b)$$

where  $\alpha^{-1} \sim 8,782,800 \text{ m}^{-2}$  is the viscous resistance coefficient of the catalyst network and  $\beta \sim 1,782 \text{ m}^{-1}$  is the inertial resistance coefficient of the catalyst network.

It is noteworthy that because the semi-empirical Ergun equation is suitable for a wide range of Reynolds numbers and various packing patterns,<sup>26</sup> it is not necessary to model the detailed packing of the catalyst network within the reformer. In this CFD model, the catalyst network inside each reforming tube is assumed to have a uniform packing structure and to be functioning properly (i.e., no deactivation or sintering occurs). Hence, the coefficients of viscous resistance and inertial resistance of the catalyst network can be assumed to be constant and uniform along the axial and radial directions.

## 4.6 Equation of State and Turbulence-Chemistry Interaction Model

In this section, we present the procedure by which the thermodynamic and turbulence-chemistry interaction models are selected for the reformer CFD model. The modeling considerations that motivate the analysis of multiple equations of state and turbulence-chemistry

interaction models are discussed. Finally, a strategy to obtain the necessary numerical evidence, which is subsequently analyzed to determine the solutions for the modeling challenges, is proposed.

The first modeling consideration is the choice of an equation of state for describing the thermodynamics of the furnace-side and tube-side flows in the reformer. In the combustion chamber of the reformer, the maximum temperature of the furnace-side mixture is approximately 2050 K due to the thermal energy released by the rapid oxidation of the furnace-side feed, and the operating pressure is designed to be nearly at atmospheric pressure at  $\sim 132$  kPa. Therefore, the furnace-side mixture can be assumed to possess incompressible ideal gas characteristics. On the contrary, the thermodynamic behavior of the tube-side mixture is speculated to deviate significantly from that governed by the incompressible ideal gas law due to the high operating pressure inside the reforming tubes (i.e.,  $\sim 3,000$  kPa), which is  $\sim 25$ - $28$  times higher than that of the combustion chamber.<sup>38</sup> Specifically, the tube-side density at high operating pressure of the reforming tubes is expected to be significantly different from the estimated density by the incompressible ideal gas law using the reference state of 298 K.

It is critical to the development of the reformer CFD model that the adopted equation of state accurately predicts the thermodynamics of turbulent reacting flows inside both the combustion chamber and reforming tubes because the SMR process is expected to reach equilibrium at the reforming tube outlets. In an effort to choose an appropriate equation of state, two potential thermodynamic models, i.e., the compressible ideal gas and the real gas Soave-Redlich-Kwong (SRK) equations of state, are selected. It is important to note that the real gas SRK model predicts more accurate fluid properties than the compressible ideal gas model and is frequently employed for determining fluid thermodynamic properties for industrial applications. Nevertheless, the required computational cost of the real gas SRK model is higher than that of the compressible ideal gas model; the former thermodynamic model should be integrated into the reformer CFD model only when the latter model is proven to be inadequate for obtaining

accurate results.

The second modeling consideration is the selection of an appropriate turbulence-chemistry interaction model. As discussed in Secs. 4.4.1 and 4.5.1, the FR/ED and EDC models are two viable models for these phenomena, but the FR/ED model may produce inaccurate results, though it is expected to have a lower computational time than the EDC model.

To evaluate whether the less computationally intensive modeling strategies (compressible ideal gas and FR/ED models) can be expected to produce sufficiently accurate results, we could develop one reformer CFD model that uses the more computationally intensive modeling strategies (i.e., the SRK and EDC models) and one that uses the less computationally intensive modeling strategies. The results could then be compared to analyze the impact on the CFD numerical results of utilizing the more rigorous SRK and EDC models compared to utilizing the less accurate (but more suitable in terms of computational cost, computing time, and memory capacity for industrial applications) compressible ideal gas and FR/ED models. Nevertheless, the available computational power (i.e., 80 cores on UCLA's Hoffman2 Cluster) and memory capacity (i.e., 20.0 GB on UCLA's Hoffman2 Cluster) are not expected to be sufficient to simulate the reformer CFD model with the more computationally intensive modeling strategies in a timely manner because the reformer mesh is composed of 29,099,252 hexahedral grids, 88,798,168 quadrilateral faces and 30,584,930 nodes. Consequently, it is not practical to employ the reformer CFD model that uses the more computationally intensive modeling strategies as a means to obtain the necessary numerical evidence, which would subsequently be used as a basis for selection of the appropriate models. As an alternative for assessing the expected order of magnitude of differences in the CFD numerical results when employing the more computationally intensive versus less computationally intensive modeling strategies, we would like to use a part of the reformer domain (e.g., a single reforming tube) to analyze both types of thermodynamic and chemistry-turbulence interaction models. However, the transport phenomena of the reforming tubes of the reformer CFD model are coupled and thus a single



reforming tube from the reformer model could not be simulated individually. Therefore, a CFD model of a single industrial-scale reforming tube developed from our previous work<sup>37</sup> using modeling strategies similar to those employed for modeling the reforming tubes of the reformer CFD model is readily available and will be used in the remainder of this section for assessing whether the more or less computationally intensive modeling strategies will be chosen for the reformer CFD model.

Before utilizing the industrial-scale reforming tube from<sup>37</sup> to assess the appropriateness of the more and less computationally intensive thermodynamic and turbulence-chemistry interaction models for the reformer CFD model, the differences between the industrial-scale reforming tube mesh and modeling strategies and those of the reformer CFD model are discussed to demonstrate the large reduction in the computation time offered by the industrial-scale reforming tube CFD model. Three key differences between the reformer mesh and industrial-scale reforming tube mesh are the shape of the subdomains, the number of the subdomains and the mesh quality. Specifically, the industrial-scale reforming tube mesh developed in<sup>37</sup> is the 2-D axisymmetric quadrilateral structured mesh, and the reformer CFD mesh is the 3-D hexahedral structured mesh. Additionally, the industrial-scale reforming tube mesh consists of  $\sim 23$  thousand subdomains, and the reformer mesh has  $\sim 29$  million subdomains, which corresponds to a cell count that is  $\sim 1264$  times higher than that of the former mesh. Moreover, the mesh quality of the industrial-scale reforming tube mesh reported in<sup>37</sup> is nearly ideal based on the three suggested criteria (i.e., the orthogonal factor, aspect ratio and ortho skew) and is better than that of the reformer mesh shown in Table 4.1. Therefore, the industrial-scale reforming tube CFD model serves as an effective tool to quantify the magnitude of the numerical error introduced in the CFD simulation data when the computationally less intensive modeling strategies (i.e., the compressible ideal gas model and the FR/ED model) are implemented, and the industrial-scale reforming tube CFD model is expected to have a faster speed of convergence than that of the reformer CFD model, making the analysis possible in a reasonable time frame.

In this effort, two industrial-scale reforming tube CFD models are developed, one of which utilizes the SRK and EDC models, and the other of which uses the compressible ideal gas and FR/ED models (for brevity, the former and latter CFD models will be referred to as the original and simplified tube CFD models, respectively). In this study, all boundary conditions of the tube CFD models (i.e., the outer reforming tube wall temperature and the tube-side feed conditions) are derived from typical plant data,<sup>37</sup> and the modeling strategies are identical to those of the reformer CFD model. The simulation results generated by the original and simplified tube CFD models are shown in Table 4.5.

The deviations of the simulation results generated by the simplified tube CFD model with respect to the data generated by the original tube CFD model are considered to be insignificant. However, the computational benefits of utilizing the simplified tube CFD model compared to using the original tube CFD model are noticeable. Specifically, the original tube CFD model takes 1100 iterations and 650 seconds of computing time to reach the converged solution, while the simplified tube CFD model only takes 871 iterations and 320 seconds. This result shows that the simplified tube CFD model offers a 20% reduction in the number of iterations and a 50% reduction in the computing time required for the simulation to reach the converged solution and yields similar simulation data compared to the original tube CFD model. As a result, the compressible ideal gas and FR/ED models are integrated in the reformer CFD model to describe the thermodynamics and reaction rates of individual species in the turbulent reacting flows of both the tube-side and furnace-side mixtures.

**Remark 4.1** *The most prominent difference in the modeling strategies of the industrial-scale reforming tube mesh and of a reforming tube in the reformer CFD model is that the industrial-scale reforming tube assumes a tube wall temperature profile along the reforming tube length whereas the reforming tubes in the reformer exhibit a temperature profile dependent on the furnace-side environment which is simultaneously calculated. Though these differences in the mesh and modeling strategies exist, they are not expected to significantly impact the order of magnitude of numerical*

Table 4.5: Simulation results of the original and simplified tube CFD models in which  $H \bar{P}_{tube,inlet}$  and  $\bar{x}_{tube,outlet}^i$  represent the heat flux, average inlet pressure and outlet mole fraction of species  $i$  in the tube-side mixture,

	Original tube CFD model [∗]	Simplified tube CFD model	Difference (%, with respect to ∗)
$\Delta P_{tube}$ (kPa)	204.2	210.3	3.00
$\bar{P}_{tube,inlet}$ (kPa)	2958.2	2964.3	0.21
$H_{average}$ (kW/m <sup>2</sup> )	69.506	68.423	1.56
$\bar{x}_{tube,outlet}^{H_2}$	0.470	0.469	0.33
$\bar{x}_{tube,outlet}^{H_2O}$	0.341	0.341	0.00
$\bar{x}_{tube,outlet}^{CH_4}$	0.043	0.044	3.44
$\bar{x}_{tube,outlet}^{CO}$	0.088	0.087	1.18
$\bar{x}_{tube,outlet}^{CO_2}$	0.058	0.059	1.43

differences in the CFD results for the industrial-scale reforming tube using the more and less computationally intensive modeling strategies compared to the order of magnitude of the differences that would be observed using a reforming tube from the reformer model. Furthermore, the order of magnitude of the results utilizing a single reforming tube would be expected to be indicative of the order of magnitude of differences that would be expected on the furnace-side as well, particularly since the equation of state is not expected to pose an issue on the furnace side due to the relatively low pressures in that domain.

## 4.7 Governing Equations of Industrial-scale SMR Unit

The reformer mathematical model consists of two sets of highly non-linear coupled partial integro-differential equations with seven independent variables as discussed in Sec. 4.1. Specifically, one of the two equation sets represents the combustion chamber model, and the other is the reforming tube model. In this section, we present the equations of continuity and of momentum, energy, and species material conservation that employ parameters or variables calculated from the modeling strategies discussed in the prior sections to characterize the mass, flow, heat and species transport within the reformer. The physical properties of individual

species in these equations in the tube-side and furnace-side mixtures are imported from the ANSYS Fluent database materials. Subsequently, the physical properties of the tube-side and furnace-side mixtures are computed based on those of the corresponding constituents, ideal gas mixing law (in the case of the thermal conductivities and viscosities) and kinetic theory (in the case of the diffusion coefficients).

Inside the combustion chamber and reforming tubes, the flow profiles are speculated to be turbulent as discussed in Secs. 4.4.1 and 4.5.1, and thus, the state variables (e.g., temperature, pressure, internal energy, enthalpy, and entropy) and fluid properties (i.e., velocity, density and species concentration) fluctuate about their corresponding time-averaged values.

In the present work, the standard  $k-\epsilon$  turbulence model developed from the Reynolds-averaged Navier-Stokes (RANS) equations and the Boussinesq hypothesis is integrated in the reformer CFD model to characterize the furnace-side and tube-side turbulent reacting flows, which allows the reformer CFD model to simulate the effects of turbulence on the transport and chemical reaction phenomena.<sup>26,30,40</sup> The standard  $k-\epsilon$  model is selected because it is a robust turbulence model, it requires lower computational resources compared to the realizable  $k-\epsilon$  model (i.e., relatively longer computing time), RNG  $k-\epsilon$  model (i.e., 15% more computing time) and Reynolds stress model (i.e., 50%-60% more computing time), and it is expected to yield reasonably accurate predictions for a wide range of turbulent flows.<sup>26</sup> Additionally, the  $k-\epsilon$  model is expected to be suitable when there are not extreme pressure gradients within the fluid,<sup>26</sup> which we do not expect to observe on either the tube side or furnace side of the reformer because the ratios between the pressure drop and the inlet pressure of the tube-side feed and furnace-side feed are  $\sim 5\%$  and  $\sim 0\%$ , respectively, based on the typical plant data<sup>38</sup>. In the present work, the enhanced wall treatment option of the standard  $k-\epsilon$  model is used to improve the model accuracy at the regions near the walls. Therefore, though the ideal dimensionless distance from the wall to the first interior node (denoted by  $y^+$ ) everywhere in the reformer mesh is recommended by ANSYS Fluent to be  $\sim 1$ , the use of the  $k-\epsilon$  model

with enhanced wall treatment allows the accuracy of the CFD data to be less sensitive to the  $y^+$  value, which allows for the  $y^+$  value of the reformer mesh to be greater than 1 and allows the cell count in the reformer mesh to be reduced compared to the case that the  $y^+$  value is  $\sim 1$ . In the present work, the initial guess of the grid size is obtained from NASA's viscous grid spacing calculator based on the Reynolds number of the furnace-side mixture at the inner-lane burner inlet ( $Re = 240,000$ ), the diameter of the inner-lane burner inlet and the desired value of  $y^+$ , which varies between 30 and 60. The grid size is further adjusted by a trial-and-error approach during the trial simulations of the reformer CFD model to ensure that the convergence criteria defined in Sec. 4.8 can be reached. From the simulation results, the average  $y^+$  values at the outer reforming tube wall and the interior wall of the combustion chamber obtained from the CFD simulation data were 20.8 and 58.9, respectively. The reformer mathematical model accounts for transport phenomena frequently observed in high-operating-temperature applications in addition to the essential reformer-related considerations discussed at length in Secs. 4.4.1, 4.4.2, 4.5.1 and 4.5.2. In the remainder of this section, the combustion chamber model and the reforming tube model are presented.

#### **4.7.1 Furnace Chamber**

The combustion chamber model developed in this work can simulate the mixing-controlled characteristics of non-premixed combustion phenomena, radiative heat transfer between the furnace-side mixture, outer reforming tube walls and combustion chamber refractory inner walls, in addition to other heat transfer mechanisms observed in reformers (e.g., convective and conductive heat transfer). Based on the above considerations and those discussed in Sec. 4.4 and Sec. 4.6, the combustion chamber model including the continuity equation (Eq. 4.11a), the momentum (Eq. 4.11b), energy (Eq. 4.11c) and species (Eq. 4.11d) conservation equations, and the turbulence model (Eq. 4.11e and Eq. 4.11f) required for characterizing the heat and fluid-flow fields as well as composition inside the combustion chamber are formulated as

follows:

Continuity equation:

$$\frac{\partial}{\partial t}(\rho_{comb}) + \nabla \cdot (\rho_{comb} \vec{v}_{comb}) = 0 \quad (4.11a)$$

Momentum conservation equation:

$$\begin{aligned} \frac{\partial}{\partial t}(\rho_{comb} \vec{v}_{comb}) + \nabla \cdot (\rho_{comb} \vec{v}_{comb} \vec{v}_{comb}) = & -\nabla P_{comb} \\ & + \nabla \cdot \bar{\bar{\tau}}_{comb} + \rho_{comb} \vec{g} \end{aligned} \quad (4.11b)$$

Energy conservation equation:

$$\begin{aligned} \frac{\partial}{\partial t}(\rho_{comb} E_{comb}) + \nabla \cdot (\vec{v}_{comb} (\rho_{comb} E_{comb} + P_{comb})) = & \\ \nabla \cdot \left[ k_{comb}^{eff} \nabla T_{comb} - \left( \sum_i h_{comb}^i \vec{J}_{comb}^i \right) + (\bar{\bar{\tau}}_{comb} \cdot \vec{v}_{comb}) \right] & \\ + S_{comb}^{h,rxn} + \nabla \cdot \vec{q}_{rad} & \end{aligned} \quad (4.11c)$$

Species material conservation equation:

$$\frac{\partial}{\partial t}(\rho_{comb} Y_{comb}^i) + \nabla \cdot (\rho_{comb} \vec{v}_{comb} Y_{comb}^i) = -\nabla \cdot (\vec{J}_{comb}^i) + R_{comb}^i \quad (4.11d)$$

Transport equations of the standard  $k-\epsilon$  turbulence model:

$$\begin{aligned} \frac{\partial}{\partial t}(\rho_{comb} k_{comb}) + \nabla \cdot (\rho_{comb} k_{comb} \vec{v}_{comb}) = & \\ \nabla \cdot \left[ \left( \mu_{comb} + \frac{\mu_{comb}^t}{\sigma_k} \right) \nabla k_{comb} \right] + G_{comb}^k + G_{comb}^b - \rho_{comb} \epsilon_{comb} & \end{aligned} \quad (4.11e)$$

$$\begin{aligned} \frac{\partial}{\partial t}(\rho_{comb} \epsilon_{comb}) + \nabla \cdot (\rho_{comb} \epsilon_{comb} \vec{v}_{comb}) = & \\ \nabla \cdot \left[ \left( \mu_{comb} + \frac{\mu_{comb}^t}{\sigma_\epsilon} \right) \nabla \epsilon_{comb} \right] + C_{1\epsilon} \frac{\epsilon_{comb}}{k_{comb}} G_{comb}^k - C_{2\epsilon} \rho_{comb} \frac{\epsilon_{comb}^2}{k_{comb}} & \end{aligned} \quad (4.11f)$$

$$\vec{J}_{comb}^i = \left( \rho_{comb} D_{comb}^{m,i} + \frac{\mu_{comb}^t}{Sc_{comb}^t} \right) \nabla Y_{comb}^i \quad (4.12a)$$

$$\overline{\vec{\tau}}_{comb} = \mu_{comb} \left[ (\nabla \vec{v}_{comb} + \nabla \vec{v}_{comb}^T) - \frac{2}{3} \nabla \cdot \vec{v}_{comb} I \right] \quad (4.12b)$$

$$E_{comb} = h_{comb} + \frac{v_{comb}^2}{2} - \frac{P_{comb}}{\rho_{comb}} \quad (4.12c)$$

$$h_{comb} = \sum_j Y_{comb}^j h_{comb}^j \quad (4.12d)$$

$$h_{comb}^j(T_{comb}) = \int_{T_{ref}}^{T_{comb}} C_{p,comb}^j dT \text{ with } T_{ref} = 298.15 \text{ K} \quad (4.12e)$$

$$S_{comb}^{h,rxn} = - \sum_j \frac{h_j^f}{M_j} R_{comb}^j \quad (4.12f)$$

$$R_{comb}^j = \sum_k \nu_{comb}^{k,j} R_{comb}^{k,j} \quad (4.12g)$$

$$k_{comb}^{eff} = k_{comb}^l + k_{comb}^t \quad (4.12h)$$

$$k_{comb}^t = \frac{C_{p,comb} \mu_{comb}^t}{Pr_t} \quad (4.12i)$$

$$\mu_{comb}^t = \rho_{comb} C_\mu \frac{k_{comb}^2}{\epsilon_{comb}} \quad (4.12j)$$

$$G_{comb}^k = -\rho_{comb} \overline{v'_{comb,i}} \overline{v'_{comb,j}} \frac{\partial v_{comb,j}}{\partial x_i} \quad (4.12k)$$

$$G_{comb}^b = \beta' g_i \frac{\mu_{comb}^t}{Pr_t} \frac{\partial T_{comb}}{\partial x_i} \quad (4.12l)$$

where  $\vec{v}_{comb}$  (m/s),  $\mu_{comb}$  (kg/ms),  $\mu_{comb}^t$  (kg/ms),  $k_{comb}^{eff}$  (W/mK),  $k_{comb}^l$  (W/mK),  $k_{comb}^t$  (W/mK),  $C_{p,comb}$  (J/kgK),  $T_{comb}$  (K) and  $P_{comb}$  (kPa) are the furnace-side mixture mass-averaged velocity, laminar mixture viscosity, turbulent mixture viscosity (calculated as shown in Eq. 4.12j), effective thermal conductivity (estimated as shown in Eq. 4.12h), laminar thermal conductivity, turbulent thermal conductivity (estimated as shown in Eq. 4.12i), specific heat capacity, temperature and pressure of the furnace-side mixture in the combustion chamber, respectively,  $\vec{g}$  is the universal gravitational acceleration,  $\overline{\vec{\tau}}_{comb}$  is the stress tensor (estimated as shown in

Eq. 4.12b), and  $I$  is the unit tensor.

The combustion chamber model accounts for all reformer-relevant modes of momentum, energy and material transport phenomena under the influence of chemical phenomena and turbulence to characterize the dynamics of the chamber.

Specifically, the turbulent mass diffusion flux of species  $i$ ,  $\vec{J}_{comb}^i$ , driven by concentration gradients, is shown in Eq. 4.12a, where  $Y_{comb}^i$  and  $D_{comb}^{m,i}$  are the furnace-side mass fraction and laminar mass diffusion coefficient of species  $i$ , respectively. It is necessary to note that the ratio  $\frac{\mu_{comb}^t}{Sc_{comb}^t}$ , in which  $Sc_{comb}^t$  and  $\mu_{comb}^t$  are the turbulent Schmidt number and turbulent viscosity of the furnace-side mixture, is used to account for the effect of turbulence on the mass diffusion flux of species  $i$ , and therefore, it can be written as  $\rho_{comb} D_{comb}^{m,t}$  where  $D_{comb}^{m,t}$  is the turbulent mass diffusion coefficient. Additionally, the specific internal energy ( $E_{comb}$ ) of the furnace-side mixture which can be computed as the sum of the furnace-side specific sensible enthalpy ( $h_{comb}$ ) which depends on the furnace-side specific sensible enthalpy of species  $j$  at temperature  $T_{comb}$  ( $h_{comb}^j(T_{comb})$ ), specific kinetic energy ( $v_{comb}^2/2$ ) and external work per unit weight of the furnace-side mixture ( $-P_{comb}/\rho_{comb}$ ), is shown in Eq. 4.12c, Eq. 4.12d and Eq. 4.12e. It is important to note that the value of  $T_{ref}=298.15$  K in Eq. 4.12e is chosen automatically by ANSYS Fluent's parallel/pressure based solver, and  $C_{p,comb}^j$  is the heat capacity of species  $j$  in the combustion chamber. In addition, from Eq. 4.11c,  $\nabla \cdot (k_{comb}^{eff} \nabla T_{comb})$ ,  $-\nabla \cdot (\sum_i h_{comb}^i \vec{J}_{comb}^i)$ ,  $\nabla \cdot (\bar{\tau}_{comb} \cdot \vec{v}_{comb})$  and  $\nabla \cdot \vec{q}_{rad}$  represent four distinct mechanisms, i.e., conduction, species diffusion, viscous dissipation and radiation respectively, through which energy is transferred.

Furthermore, the overall rate at which thermal energy is released from combustion processes inside the combustion chamber,  $S_{comb}^{h,rxn}$ , is computed as shown in Eq. 4.12f in which  $R_{comb}^j$  and  $h_j^f$  represent the overall volumetric consumption/formation rate and enthalpy of formation of species  $j$ , and  $\nu_{comb}^{k,j}$  and  $R_{comb}^{k,j}$  are the stoichiometric coefficient and volumetric consumption/formation rate of species  $j$  in reaction  $k$ . It is noteworthy that  $R_{comb}^{k,j}$  is determined by the FR/ED turbulence-chemistry interaction model (Sec. 4.4.1). Transport equations of the stan-



standard  $k-\epsilon$  turbulence model are presented in Eq. 4.11e and Eq. 4.11f, in which  $k_{comb}$  and  $\epsilon_{comb}$  are the turbulence kinetic energy and turbulence dissipation rate of the furnace-side mixture,  $\beta'$  is the coefficient of thermal expansion of the furnace-side mixture,  $\sigma_k = 1.3$  and  $\sigma_\epsilon = 1.0$  are the default values of the turbulent Prandtl numbers for  $k_{comb}$  and  $\epsilon_{comb}$ ,  $C_{1\epsilon} = 1.44$ ,  $C_{2\epsilon} = 1.92$ ,  $C_\mu = 0.09$  and  $Pr_t = 0.85$  are default constants of the standard  $k-\epsilon$  turbulence model, respectively, and  $G_{comb}^k$  and  $G_{comb}^b$  represent the generation of turbulence kinetic energy in the furnace-side mixture due to the mean velocity gradients (Eq. 4.12k) and buoyancy effect (Eq. 4.12l). The standard  $k-\epsilon$  turbulence model can capture the characteristic parameters of turbulent reacting flow profiles. Specifically, in Eq. 4.12k, the term  $-\rho_{comb} \overline{v'_{comb,i}} \overline{v'_{comb,j}}$  is the Reynolds stress representing the effect of turbulence on the velocity profile of the furnace-side mixture that arises from the RANS equations, and  $\overline{v'_{comb,i}}$  is the time-averaged fluctuating component of  $\vec{v}_{comb}$  in the  $x_i$  direction. It is worth noting that all default constants of the standard  $k-\epsilon$  turbulence model are determined empirically by experiments for fundamental turbulent flows, and have been shown to be suitable for a wide range of wall-bounded and free shear flow applications.<sup>26</sup>

### 4.7.2 Reforming Tube

In the present work, the effects of the catalyst network on the tube-side transport phenomena are accounted for by the ANSYS Fluent porous zone function, which includes the additional momentum sink term in the momentum conservation equation of the reforming tube model to simulate the interference effect of the catalyst network, which decreases the superficial velocity and increases the residence time of the tube-side species. In addition, the energy conservation equation of the reforming tube model is affected by the porous zone function to include an additional transient term to account for the thermal inertia of the catalyst network and to use the effective thermal conductivity to account for the presence of the catalyst network. Moreover, the tube-side species material balances of the reforming tube model use the overall

effectiveness factor ( $\eta$ ) to account for the internal and external mass transfer resistances of the catalyst network and the catalyst packing factor  $((1-\gamma)\rho_{cat})$  to convert the surface reaction rates from Eq. 4.8 to volumetric reaction rates (i.e., kg/m<sup>3</sup>h) that are employed within the FR/ED turbulence-chemistry interaction model for use within the species material balances. These approximations of the effects of the catalyst network on the transport equations and species balances were also utilized in the development of the industrial-scale reforming tube CFD model for which the simulation results have been shown to be in good agreement with typical plant data,<sup>37</sup> and thus these approximations are expected to be sufficient for the reforming tubes of the reformer CFD model. The reforming tube walls are modeled by the ANSYS Fluent thin wall model in which the thermal resistance of the reforming tube wall and the temperature profile across the reforming tube wall thickness can be estimated without meshing the reforming tube wall explicitly. In the simulation of the reforming tube CFD model, the ANSYS Fluent thin wall model creates an artificial wall thickness for the reforming tubes, and the ANSYS Fluent solver utilizes the 1-D steady heat conduction equation to determine the reforming tube wall thermal resistance based on the specified artificial wall thickness and material of the reforming tubes. This modeling strategy is utilized because the wall thickness is negligible compared to other dimensions of the system (the ratio of the reforming tube exposed length and wall thickness is  $\sim 1250:1$ , and the ratio of the reforming tube diameter and wall thickness is  $\sim 13:1$ ). This modeling strategy for the tube wall affects the boundary conditions of the reforming tube walls when solving the heat transfer equations. Radiation is neglected in the energy balance equation for the tube side<sup>36,48,61</sup> because the nickel-based catalyst network expands the contact area between the tube-side mixture and the inner reforming tube wall, with the result that convective heat transfer is expected to be the dominant mode. Based on the above considerations and those discussed in Sec. 4.5 and Sec. 4.6, the governing equations including the continuity equation and the momentum, energy and tube-side species balances, and the turbulence model required to simulate the SMR process inside the reforming tubes, are constructed in a similar manner to that of the combustion chamber, which has been described

in Sec. 4.7.1. Additionally, the governing equations of the tube-side mixture have also been explicitly presented in our recent publication,<sup>37</sup> and therefore, they are not repeated here for brevity.

## 4.8 Process Simulation

Intuitively, the CFD solution of the reformer CFD model would be obtained by simulating the reformer CFD model until convergence criteria are satisfied. However, the reformer CFD model has been found to be very sensitive to the initial guess (e.g., the simulation of the reformer CFD model with the initial guess automatically generated by the ANSYS Fluent standard initialization function based on the boundary conditions of the CFD model is often unstable and is likely to quickly diverge). Although ANSYS Fluent allows a conservative mode of the ANSYS Fluent solver to be selected to prevent the reformer CFD simulation from diverging, this strategy often results in a substantial increase in the required computing time to calculate the converged solution of the reformer CFD model, and therefore, forfeits the potential of the reformer CFD model for industrial interests. In this work, a step-by-step converging strategy that allows the implementation of an aggressive mode of the ANSYS Fluent solver to compute the reformer CFD steady-state solution is proposed as shown in Fig. 4.5. Specifically, the step-by-step converging strategy is an optimized procedure that is designed to resolve the instability issue of the reformer CFD simulation, to accelerate the rate of convergence and to minimize the required computing time to obtain the converged solution of the reformer CFD model. Initially, an isothermal, non-reacting (INR) reformer CFD model is created by deactivating the combustion phenomena, radiative heat transfer and SMR kinetic models in addition to excluding the energy conservation equations from the furnace-side and tube-side models. Then, the simulation of the INR reformer CFD model is initialized with the initial guess generated by the ANSYS Fluent standard initialization function based on the tube-side and furnace-side feeds, and is solved by the aggressive mode of the ANSYS Fluent solver. In this work, the reformer CFD

simulation is said to reach the converged solution when the global normalized residuals of all transport variables computed over all subdomains of the reformer between two consecutive iterations are less than  $10^{-4}$ , the mass flow rate integrated over all boundaries of the reformer CFD model is approximately zero, the total heat transfer rate integrated over all boundaries of the reformer CFD model is less than 1% of the reformer total fired duty and the absolute residuals of the furnace-side temperature at five different locations inside the combustion chamber are less than 1 K. Next, the converged solution of the INR reformer CFD model is utilized as an initial guess for the succeeding non-reacting (NR) CFD model because even though the composition and temperature fields in the INR reformer CFD model are different from those in the NR reformer CFD model, their velocity and turbulence fields are expected to be similar.<sup>26,68</sup> Analogously, the converged reformer CFD solution in each preceding step is utilized as an initial guess for the reformer CFD model in the subsequent step until the converged solution of the complete reformer CFD model is obtained.

The solution of the reformer CFD model is obtained after  $\sim 72$  hours of computing time by the ANSYS Fluent parallel solver with a computational power of 80 cores on UCLA's Hoffman2 Cluster. During the initialization procedure of the reformer CFD model, the ANSYS Fluent solver arbitrarily selects one of the available 80 cores as a host process and designates the remaining 79 cores as compute-node processes. It is noteworthy that the host process is only responsible for interpreting the user's commands given in the graphical user interface (GUI), then redistributing them to all compute-node processes by a message-passing library, e.g., the Message Passing Interface (MPI). Thus, the reformer mesh is partitioned into 79 parts corresponding to the number of available compute-node processes, and each partition consisting of  $\sim 368,345$  grids is assigned to a different compute-node process. Then, the compute-node processes consider each grid within the corresponding partitions as an open system in which the reformer mathematical model is discretized by the finite differences method and numerically solved until the convergence criteria are satisfied. The corresponding solutions of the grids are recombined to generate the simulation results of the reformer CFD model.

## 4.9 Simulation Results

In this section, the steady-state simulation results of the reformer CFD model with the furnace-side and tube-side operating conditions and properties as shown in Tables 4.2–4.6 are presented.

Two cross-sectional planes (i.e., the frontal and lateral planes) of the combustion chamber as shown in Fig. 4.6 are designated along which the properties of the furnace-side mixture are presented. Specifically, the furnace-side temperature contour maps (lateral and frontal planes) are shown in Fig. 4.7. The contour maps of the thermal energy released by the oxidation of the furnace-side feed are shown in Fig. 4.8. In addition, the furnace-side velocity magnitude vector plots are shown in Fig. 4.9, and the furnace-side species contour maps are shown in Figs. 4.10–4.13.

The properties of the interior of a reforming tube are displayed for a cross-sectional plane along the axial direction of a reforming tube. Because the dimension of the heated reforming tube length is  $\sim 85$  times longer than that of the reforming tube diameter, the radial dimension of the reforming tube cross section is scaled up by 20 times for display purposes.

The tube-side pressure contour map is shown in Fig. 4.14. The radially uniform pressure profile inside the reforming tubes is the result of the uniformly packed catalyst network assumption, and the definition of the porous zone with uniform coefficients of viscous resistance and inertial resistance of the catalyst network along the axial and radial directions as presented in Sec. 4.5.2.

Lastly, the average composition profiles of the tube-side mixture are shown in Fig. 4.15, and the average temperature profiles of the outer and inner reforming tube walls and the furnace-side and tube-side mixtures are shown in Fig. 4.16.

Fig. 4.16 suggests that the maximum temperature of the outer reforming tube wall of  $\sim 1180$  K is below the maximum allowable operating temperature of  $\sim 1300$  K;<sup>59</sup> if the outer reforming

tube wall were to exceed the maximum temperature for a sufficient length of time, the reforming tube would rupture more quickly than if it were kept below this maximum temperature.

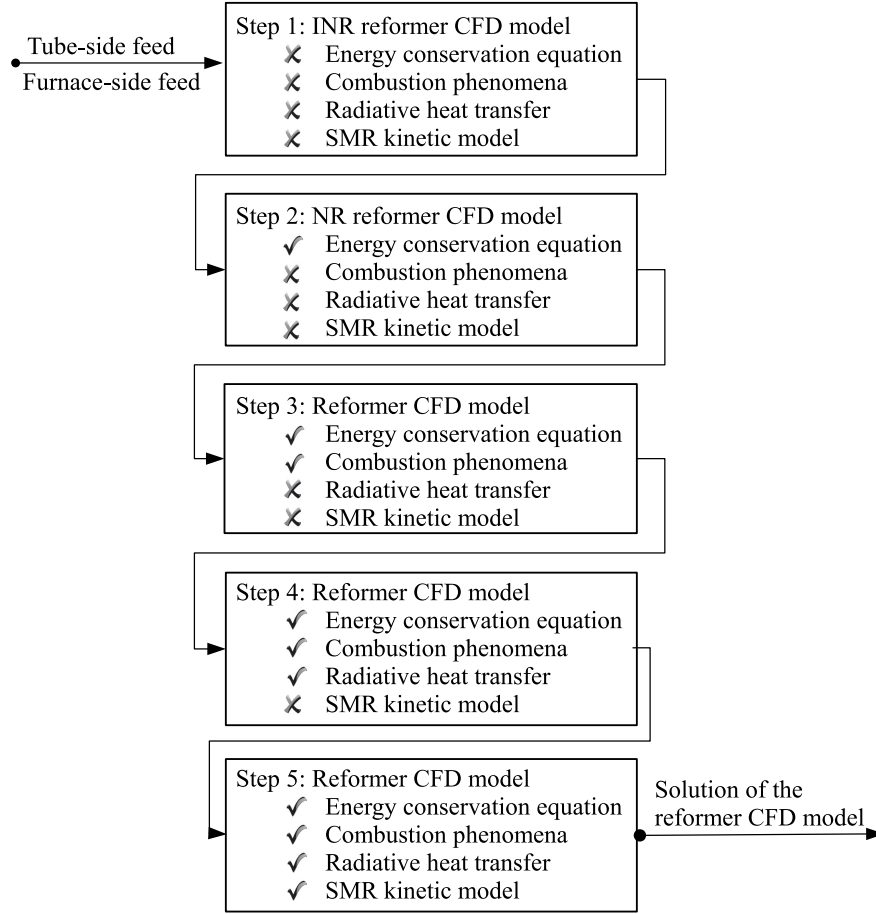


Figure 4.5: Step-by-step converging strategy designed to resolve the initial instability issue of the reformer CFD simulation, accelerate the rate of convergence and minimize the required computing time to obtain the converged solution of the reformer CFD model in which the models with ✓ are activated, and those with ✗ are disabled.

## 4.10 Discussion

In computational fluid dynamics study, a converged solution is not necessarily a physically correct solution, and therefore, the simulation results produced by the reformer CFD model are inspected by the well-established knowledge of the phenomena typically observed in reformers and validated by the typical plant data<sup>17,21,38,39,54,58</sup> in the remainder of this section.

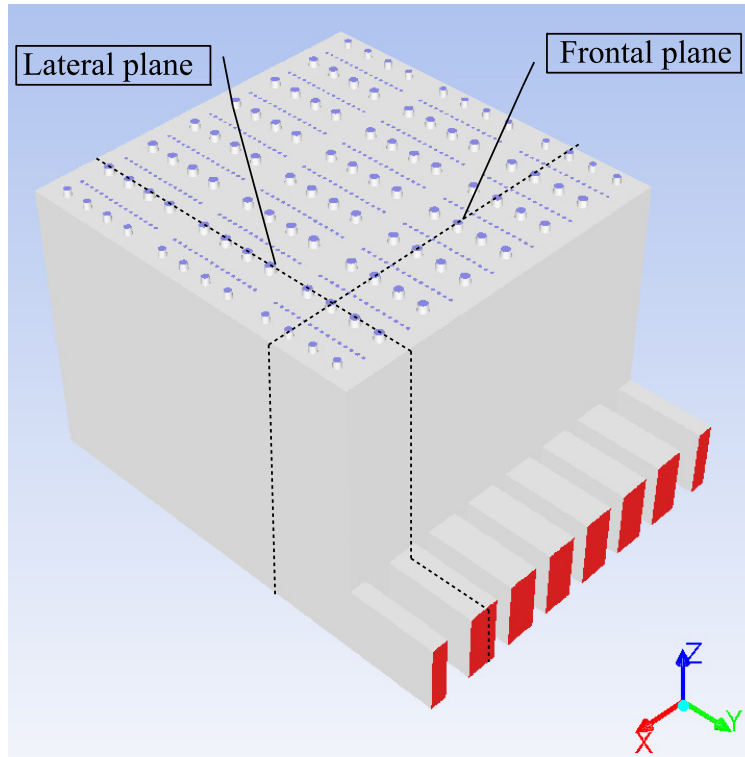


Figure 4.6: The frontal and lateral cross-sectional plane of the combustion chamber.

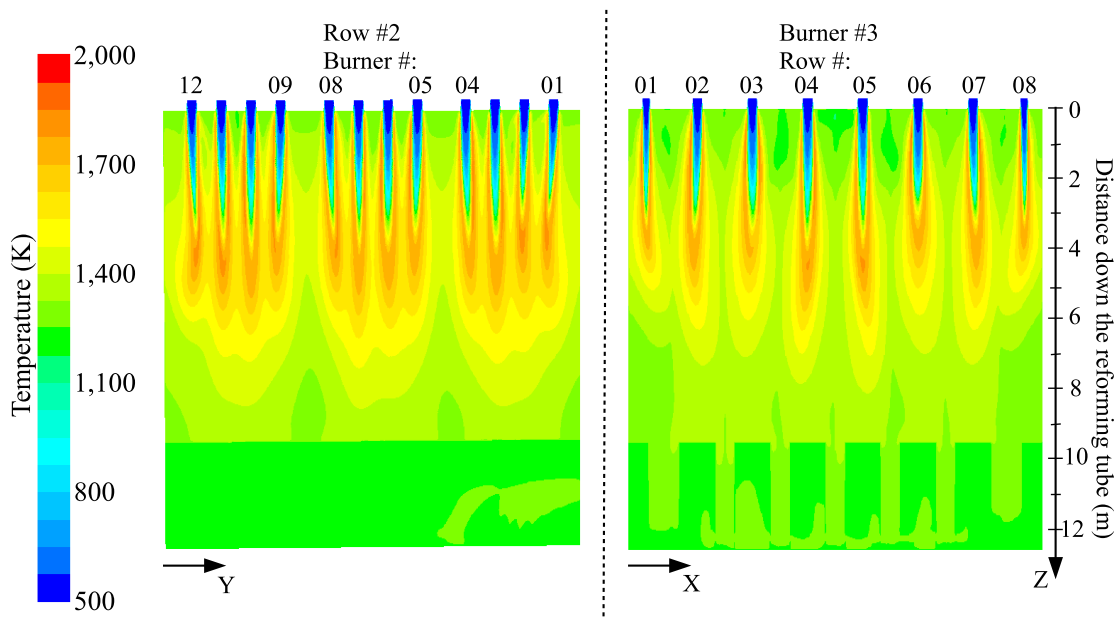


Figure 4.7: Lateral (left) and frontal (right) furnace-side temperature contour maps predicted by the reformer CFD simulation in which the parameters of the tube-side feed, furnace-side feed and combustion chamber refractory walls are consistent with typical plant data.<sup>38</sup>

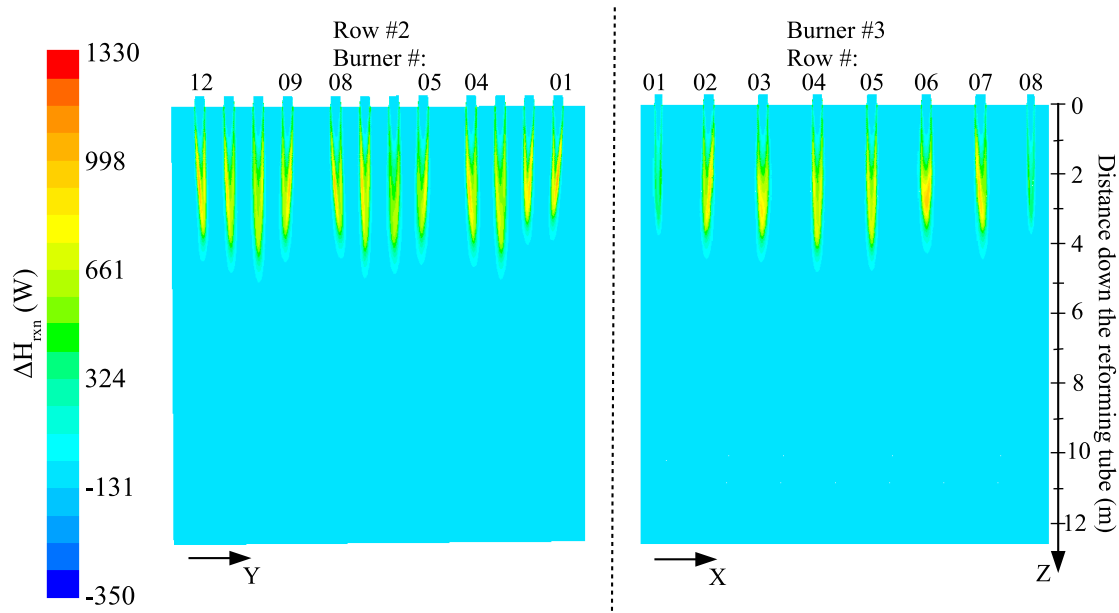


Figure 4.8: Lateral (left) and frontal (right) contour maps of energy released by the furnace-side oxidation predicted by the reformer CFD simulation in which the parameters of the tube-side feed, furnace-side feed and combustion chamber refractory walls are consistent with typical plant data.<sup>38</sup>

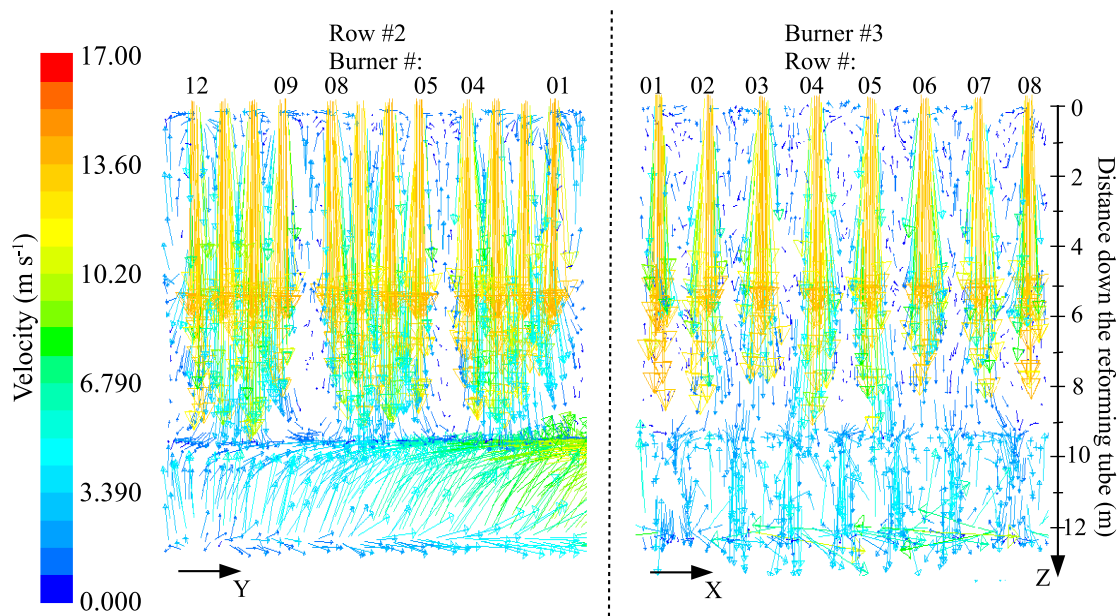


Figure 4.9: Lateral (left) and frontal (right) contour maps of the furnace-side velocity magnitude predicted by the reformer CFD simulation in which the parameters of the tube-side feed, furnace-side feed and combustion chamber refractory walls are consistent with typical plant data.<sup>38</sup>



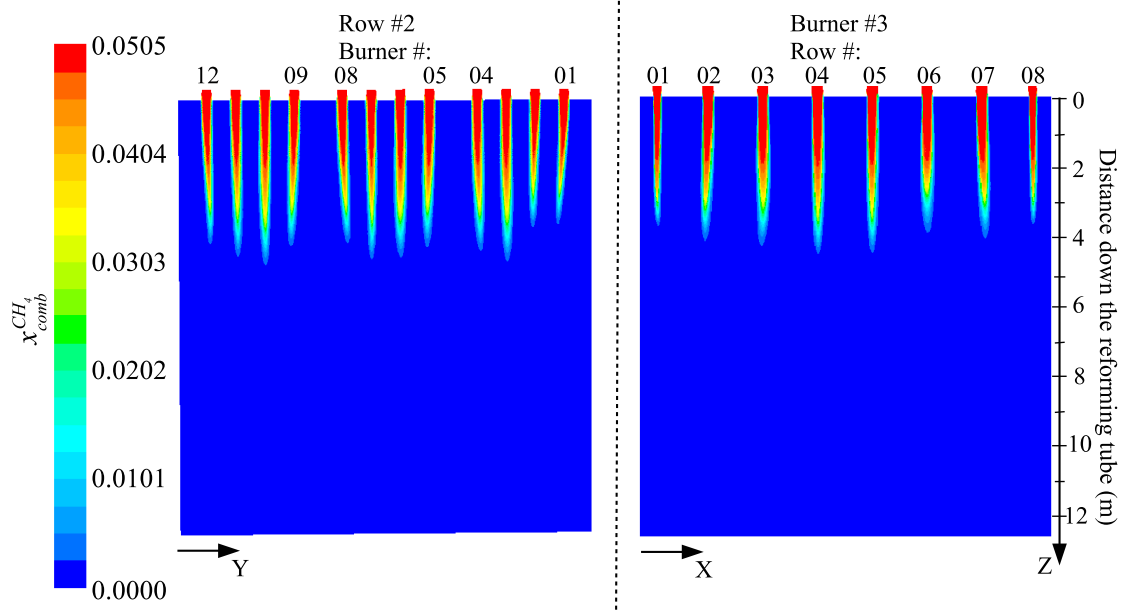


Figure 4.10: Lateral (left) and frontal (right) methane mole fraction contour maps inside the combustion chamber predicted by the reformer CFD simulation in which the parameters of the tube-side feed, furnace-side feed and combustion chamber refractory walls are consistent with typical plant data.<sup>38</sup>

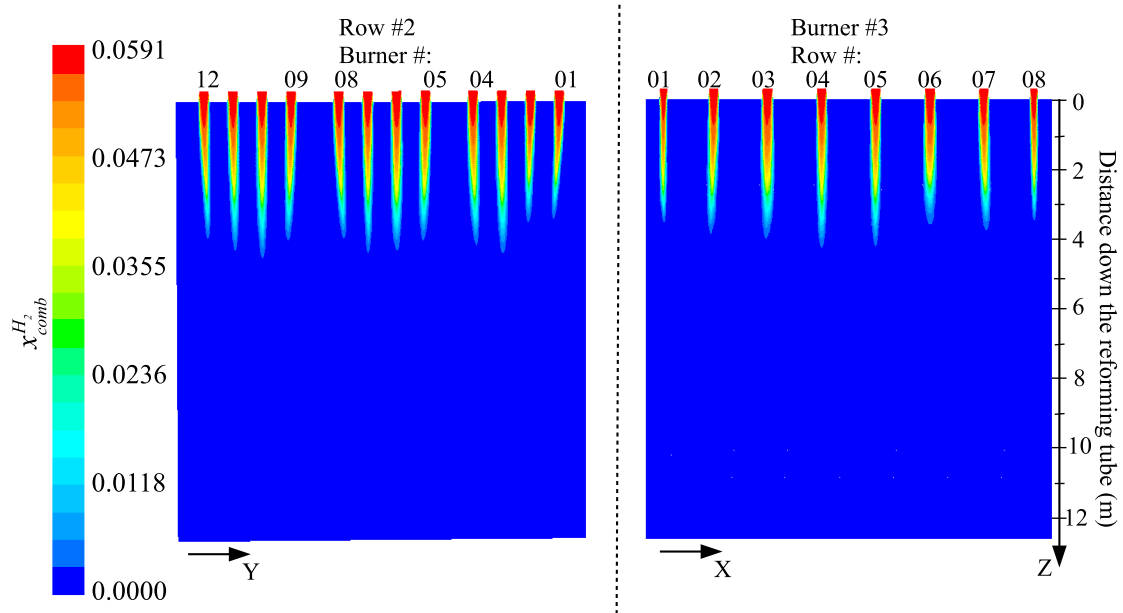


Figure 4.11: Lateral (left) and frontal (right) hydrogen mole fraction contour maps inside the combustion chamber predicted by the reformer CFD simulation in which the parameters of the tube-side feed, furnace-side feed and combustion chamber refractory walls are consistent with typical plant data.<sup>38</sup>

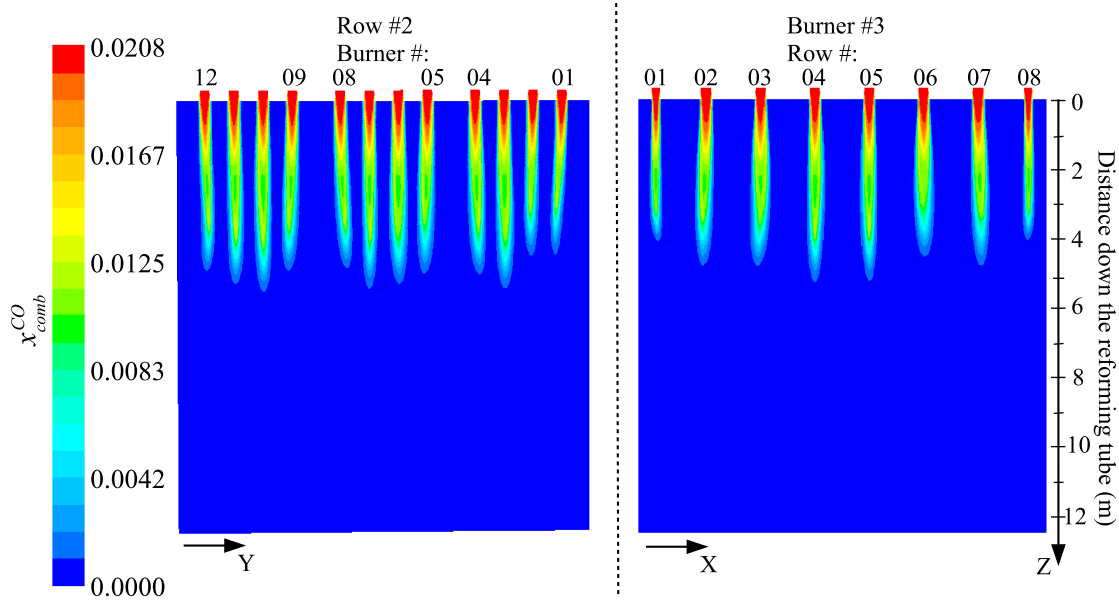


Figure 4.12: Lateral (left) and frontal (right) carbon monoxide mole fraction contour maps inside the combustion chamber predicted by the reformer CFD simulation in which the parameters of the tube-side feed, furnace-side feed and combustion chamber refractory walls are consistent with typical plant data.<sup>38</sup>

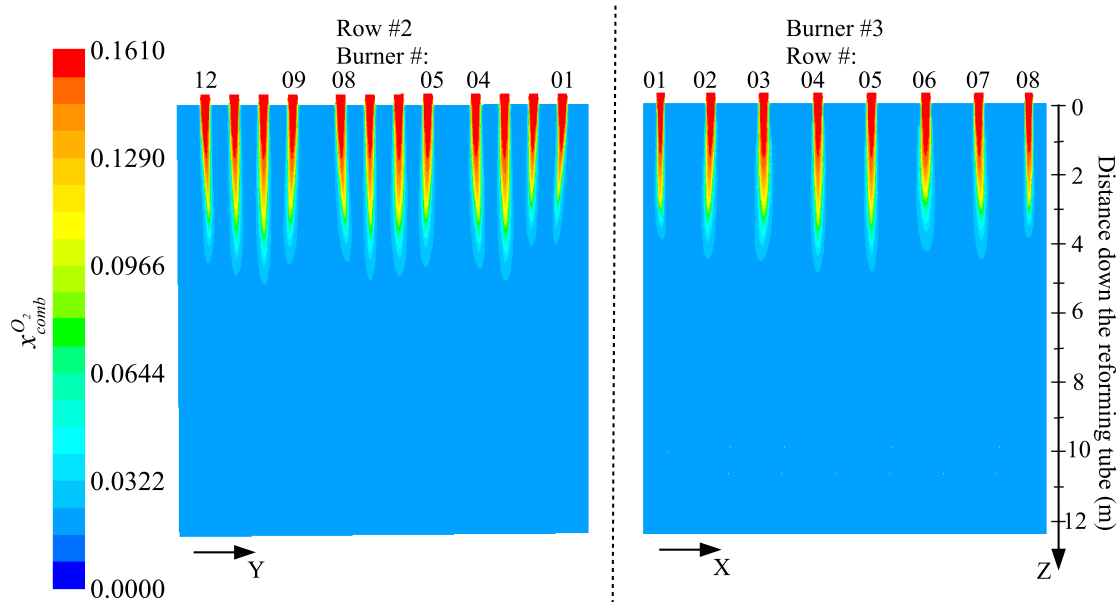


Figure 4.13: Lateral (left) and frontal (right) oxygen mole fraction contour maps inside the combustion chamber predicted by the reformer CFD simulation in which the parameters of the tube-side feed, furnace-side feed and combustion chamber refractory walls are consistent with typical plant data.<sup>38</sup>

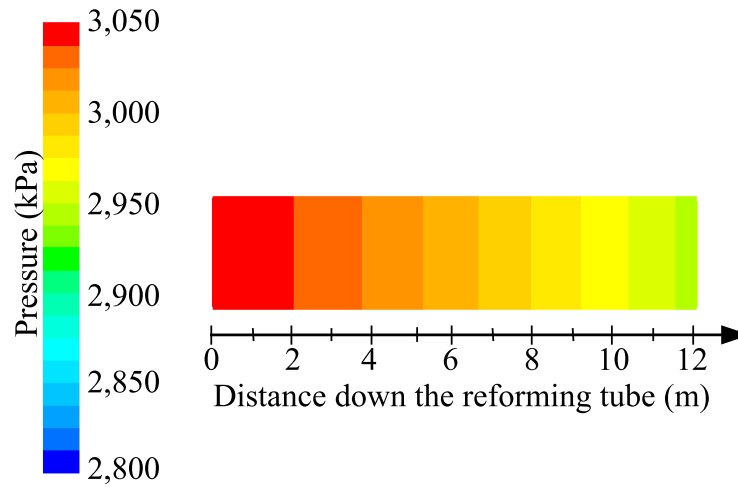


Figure 4.14: Tube-side pressure contour map predicted by the reformer CFD simulation in which the parameters of the tube-side feed, furnace-side feed and combustion chamber refractory walls are consistent with typical plant data.<sup>38</sup>

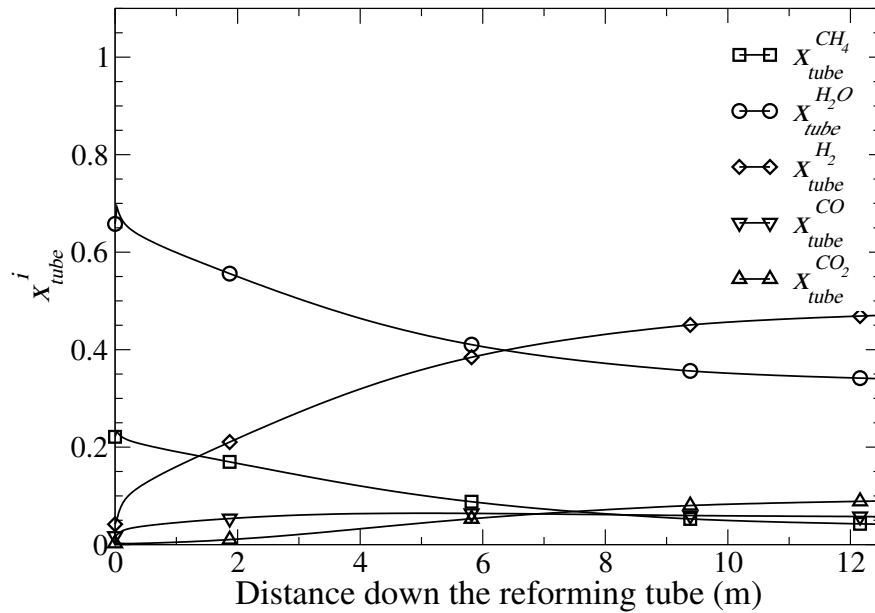


Figure 4.15: Radial-weighted average tube-side compositions predicted by the reformer CFD simulation in which the parameters of the tube-side feed, furnace-side feed and combustion chamber refractory walls are consistent with typical plant data.<sup>38</sup>

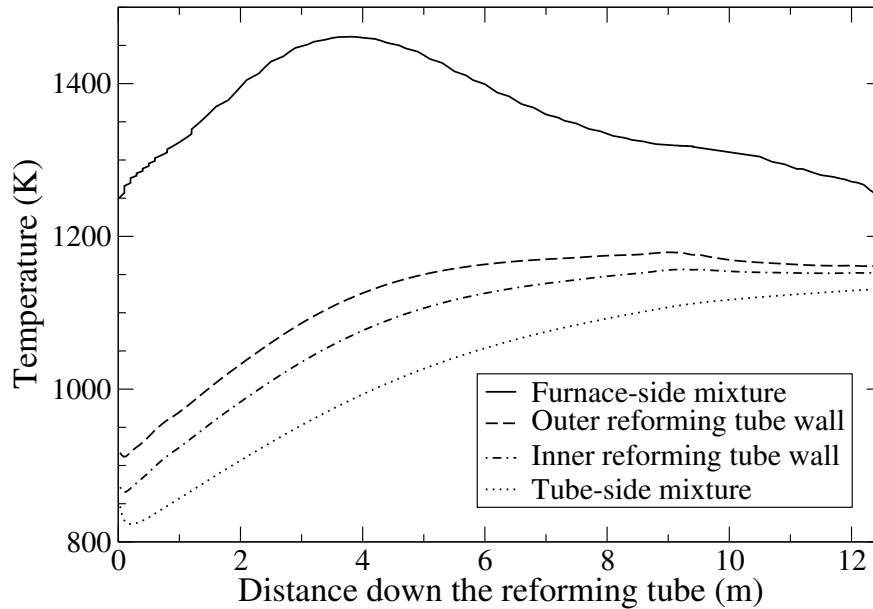


Figure 4.16: Average temperature profiles of the furnace-side mixture (solid line), outer reforming tube wall (dashed line), inner reforming tube wall (dash-dotted line) and tube-side mixture (dotted line) predicted by the reformer CFD simulation in which the parameters of the tube-side feed, furnace-side feed and combustion chamber refractory walls are consistent with typical plant data.<sup>38</sup>

We begin by checking that the modeling strategies employed produced the effects expected. For instance, the furnace-side feed composition in Table 4.2 indicates that it is lean-fuel (i.e., the ratio of air to fuel of the furnace-side feed is higher than the stoichiometric ratio). Therefore, it is expected that the fuel will be fully oxidized and that oxygen will remain in the flue gas. Figs. 4.10, 4.11 and 4.12 demonstrate that the composition of the furnace-side reducing agents in the CFD solution are effectively zero everywhere except in the reaction zones, and Fig. 4.13 shows that oxygen is not completely consumed, as expected. Additionally, the characteristics of non-premixed combustion phenomena that are expected in the furnace-side as discussed in Sec. 4.4.1 can be observed in the converged reformer CFD solution. In particular, Figs. 4.10–4.12 reveal that the furnace-side compositions in the vicinities of the inner-lane and outer-lane burners are almost identical to those in the furnace-side feed, and Fig. 4.8 shows that the oxidation rate of the furnace-side feed in these regions is close to zero. These results suggest that the reformer CFD model correctly simulates the initial mixing of the fuel and

air streams of the furnace-side feed, in which the observed oxidation rate of the furnace-side species is expected to be relatively slow. Moreover, the characteristics of top-fired reformers can be seen in the presented solution of the reformer CFD model. Particularly, Figs. 4.7 and 4.16 indicate that the maximum furnace-side temperature is located in the upper part of the reformer,<sup>14,39</sup> and Fig. 4.8 demonstrates that the flame length is consistent with the typical values between  $\sim 4.5$  m and  $\sim 6.0$  m.<sup>38</sup>

Furthermore, the simulation data of the reformer CFD model indicates that approximately 55.1% of the thermal energy released by this process is transferred to the reforming tubes, 3% of which dissipates to the surrounding air through the chamber refractory walls and the remainder of which exits the reformer at the combustion chamber outlets, which is in close agreement with typical plant data.<sup>14,38</sup> Finally, the solution of the reformer CFD model suggests that the SMR process is near equilibrium at the reforming tube outlets as expected. Specifically, Fig. 4.15 shows that the slopes of the composition profiles, which are indicative of the net reaction rates of the tube-side species at the reforming tube outlet, are close to zero.

We next compare our numerical results with those from typical plant data. When typical plant data is employed to justify the validity of the simulation results produced by the reformer CFD model, the data needs to be normalized to unity as follows:

$$\tilde{z}^* = \frac{\tilde{z} - \tilde{z}_{min}}{\tilde{z}_{max} - \tilde{z}_{min}} \quad (4.13)$$

where  $\tilde{z}$  and  $\tilde{z}^*$  are the original data and corresponding normalized data, respectively, and  $\tilde{z}_{max}$  and  $\tilde{z}_{min}$  are the maximum and minimum values of the data set of interest. This is because many variations of top-fired reformer geometries are employed in the previous experimental and computational works of the SMR process, and the typical plant data are commonly reported in deviation forms for proprietary reasons.

Fig. 4.17 and Fig. 4.18 compare the normalized CFD data with the normalized typical plant data presented in<sup>38</sup> and<sup>39</sup>. It is noted that we refer to the data from<sup>38</sup> and<sup>39</sup> as typical plant

data though it is generated from a first-principles reformer model in which the combustion of the furnace-side feed was not simulated simultaneously with the reforming tubes, and a predefined heat released profile was used. In addition, the reforming tube models from those works are modeled by the 1-D plug flow reactor model and thus ignore the radial spatial gradients of transport variables and the effect of the flow pattern on the reforming tubes. Nevertheless, the models from<sup>38</sup> and<sup>39</sup> employ a number of adjustable empirical constants (e.g., the heat-release length, the predefined parabolic heat-release profile, the gray gas model, and the convective heat transfer coefficients) that are tuned so that the estimated temperature profile of the outer reforming tube wall is consistent with the experimental data recorded by the high-cost monitoring IR cameras of an on-line reformer. Thus, we consider that the data from these works can be considered to be sufficiently close to experimental plant data to be utilized in validating the reformer CFD model. Therefore, the data from<sup>38</sup> and<sup>39</sup> is used to validate the proposed modeling strategies that lead to the development of the reformer CFD model from Sec. 4.4, Sec. 4.5, Sec. 4.6 and 4.7. Specifically, Fig. 4.17 shows that the composition profiles of the tube-side species along the reforming tube length vary in a manner that is consistent with the previous work, which justifies the choice of the global kinetic model of the SMR process with the universal effectiveness factor and the FR/ED model for accounting for turbulence-chemistry interaction. Additionally, Fig. 4.18 demonstrates that the average temperature profiles of the furnace-side mixture and outer reforming tube wall along the length of the reforming tube closely resemble the corresponding profiles reported in the previous reformer study, which validates the choice of the radiative property correlation and heat transfer model, as well as the neglect of radiation in the tube side and the use of the porous zone function for modifying the heat transfer equations in the reforming tubes. Specifically, the outer reforming tube wall temperatures from the reformer CFD model and<sup>39</sup> are similar, and the temperature profiles for the furnace-side mixture have a similar shape in the sense that both demonstrate a maximum furnace-side temperature that is located in the upper part of the reformer (i.e., a characteristic of top-fired reformers). Differences between the furnace-side mixture temperature profiles

of the CFD simulation and<sup>39</sup> are expected since in,<sup>39</sup> the effects of the furnace-side flow pattern on the temperature of the furnace-side mixture are ignored as the combustion chamber is assumed to behave like a plug flow reactor.

As additional validation of the reformer CFD simulation results, the values of a number of properties of the tube-side mixture from<sup>38</sup> are compared with those from the reformer CFD model in Table 4.6 and show good agreement.

The converged reformer CFD solution is validated by the CFD data generated by the industrial-scale reforming tube CFD model developed in.<sup>37</sup> The industrial-scale reforming tube CFD model is updated with the same modeling parameters as described in Sec. 4.2, Sec. 4.5 and Sec. 4.6, and implemented with the tube-side feed conditions and outer reforming tube wall profile (Fig. 4.16) of the reformer CFD model. Table 4.6 indicates that the differences between the CFD data generated by the reformer CFD model and updated industrial-scale reforming tube CFD model are not significant.

Furthermore, the converged reformer CFD solution is validated by the data generated by a standard reforming Gibbs reactor model of a steady-state process simulator (e.g., Pro/II) as shown in Table 4.6. Because the tube-side reactions have been demonstrated above through Fig. 4.15 to have approximately reached equilibrium at the reactor outlet, it is expected that the mole fractions at the tube outlet from the CFD simulation would correspond with the results from the Gibbs reactor simulation. The reforming Gibbs reactor model is provided with the Gibbs reactor feed stream and duty, which are set to the tube-side feed and the average thermal energy absorbed by each reforming tube of 345 090 kW derived from the reformer CFD solution, respectively. The differences in the results between the reformer CFD model and the reforming Gibbs reactor model are demonstrated in Table 4.6 to be small. It is important to note that the solution of the reforming Gibbs reactor model can only be obtained after the solution of the reformer CFD model has already been computed from which the total energy absorbed by each reforming tube is extracted. One might suggest that the total energy ab-

sorbed by each reforming tube can be back-calculated given the tube-side composition at the reforming tube outlets; however, prior to the completion of the reformer CFD simulation, neither the amount of thermal energy absorbed by the reforming tubes (i.e., the energy uptake of a reforming Gibbs reactor model) nor the tube-side composition at the reforming tube outlets (i.e., the approximated yield of the SMR process) are available to be used as inputs. Hence, it is evident that the reforming Gibbs reactor model is not designed to replace the reformer CFD model, and more details are given in Remark 4.4.

Next, the area-weighted average heat flux across the reforming tube wall predicted by the reformer CFD model is compared to that of the typical plant data reported in the literature as shown in Table 4.7. The average heat flux in Table 4.7 from<sup>38</sup> is estimated based on the outer and inner reforming tube wall temperature profiles reported in that work, the reforming tube thermal conductivity of 106500 J/mhK) and the typical reforming tube wall thickness of 0.015 m. From Table 4.7, the area-weighted average heat flux across the reforming tube wall predicted by the reformer CFD model is consistent with that of the typical plant data.

Finally, the reformer CFD model is implemented with the furnace-side feed distribution of an on-line reformer provided by a third party, and the corresponding converged CFD data is obtained by the proposed step-by-step convergence strategy as discussed in Sec. 4.8. Subsequently, the CFD data is compared with the recorded plant data, which is an outer reforming tube wall temperature distribution at a fixed axial location (as shown in Fig. 4.19) and is collected by a system of IR cameras situated around the reformer as discussed in Sec. 4.4.2. The outer reforming tube wall temperature distribution constructed based on the CFD simulation and information of the approximate views of the IR cameras is consistent with the plant data provided by the third party as the maximum deviation at any location is  $\sim 3\%$  and the average deviation is  $\sim 1.2\%$  as shown in Fig. 4.20.

The blank spaces shown in Fig. 4.20 represent reforming tubes for which no temperature measurements were provided from the reported data. However, from the good agreement of our



CFD data with the available data, we can be confident that our CFD results for these additional reforming tubes are indicative of the actual operating conditions. This highlights the utility of CFD modeling for obtaining information regarding operating conditions that are perhaps not available from standard process monitoring techniques (e.g., the outer wall temperature at all  $z$  locations down the reforming tube length, for every reforming tube) which may be required for assessing whether potentially dangerous operating conditions exist (e.g., any reforming tube outer wall temperature exceeding the maximum operating temperature at any  $z$  location) and modifying the process inputs to ameliorate such conditions when they are detected.

Based on the above, the simulation results produced by the reformer CFD model are demonstrated to be consistent with phenomena observed in reformers and to be in close agreement with the typical plant data. As a result, the converged solution of the reformer CFD model can be considered to be a reasonably reliable representation of experimental data and can be utilized to characterize the velocity, turbulence, composition and temperature fields inside the reformer.

**Remark 4.2** *In this work, we focus on presenting only modeling strategies that are expected to be most suitable for modeling the expected transport and reaction phenomena among the choices offered by Fluent for the purpose of demonstrating how a high-fidelity CFD model of a reformer can be devised. Showing how initial modeling strategies can be selected for reasonably accurate results within a reasonable time frame is a significant contribution of the present work, because the coupling between the various transport and reaction phenomena in and between the tube and furnace sides prevents CFD results of the entire SMR from being generated for comparison with typical plant data until all phenomena have been included within the CFD simulation. Therefore, we focus only on the selection of initial modeling strategies that allow CFD data to be obtained that shows good agreement with typical plant data. Fine-tuning of the models for various phenomena (e.g., re-running the CFD simulation with alternative models such as alternative turbulence-chemistry interaction models to analyze whether this improves the agreement of the CFD results with typical*

plant data) could be performed, particularly by industry with significant plant data that can be used for distinguishing between the differences in accuracy at this fine-tuning step, but given the already significant agreement with typical plant data, changing the modeling strategies chosen would not conceptually change the novelty of the work (developing a step-by-step guide for obtaining a high-fidelity CFD model of an industrial-scale reformer), and thus is not pursued. The good agreement of the typical plant data with our CFD simulation results indicates that all simplifications and assumptions made in the development of the reformer CFD modeling strategies and meshing as described in Secs. 4.2-4.7 were sufficient for obtaining a CFD model that can be considered to be a reasonable substitute for experimental data.

**Remark 4.3** *In this work, we assume that the furnace-side feed is uniformly distributed among all inner-lane burners and among all outer-lane burners, which results in symmetry in the furnace-side feed distribution and geometry that could have been exploited for the simulation. However, the intended application of the reformer CFD model is for allowing the evaluation of reformer operating parameters to improve the economics of operation when such operating changes cannot be fully evaluated any other way (for example, furnace balancing, which is optimizing the furnace-side feed distribution so that the temperature distribution of the outer reforming tube wall at a given length down the reforming tubes becomes more uniform). Evaluating the most optimal operating conditions may require the flexibility of simulating asymmetry within the reactor (e.g., an asymmetrical furnace-side feed distribution). Furthermore, the furnace-side feed flow rate to each burner is controlled by the percent opening of the corresponding valve, and therefore, valve-related disturbances (e.g., the valve stickiness) can cause an unintended asymmetric furnace-side feed distribution. For such reasons, it is beneficial to simulate the entire reformer, without exploiting symmetry, in the development of the reformer CFD model.*

**Remark 4.4** *The comparison of the Gibbs reactor simulation results and those from the outlet of a reforming tube in the reformer CFD model in Table 4.6 does not indicate that steady-state simulations that are standard in the chemical process industries can serve as substitutes for a*

*CFD model of a reformer. The CFD simulations reveal details about the reactor operation (e.g., the flame length, maximum and minimum temperatures of the reforming tube walls at any given axial location in the reformer, and the effect of changes in the burner feed flow rates on these maximum and minimum temperatures) that cannot be obtained from steady-state simulations such as a Gibbs reactor, and cannot even be obtained from standard experimental measurements that are taken at SMR plants (e.g., temperatures of specific reforming tube walls at specific axial locations determined from infrared cameras). It is also notable that due to the effects of the geometry on the flows and heat transfer within the SMR (for example, asymmetry in the flow field within the furnace side is observed in Fig. 4.9 due to the flue gas tunnel exits being located on only one side of the reformer, which creates non-identical environments for the reforming tubes throughout the reformer despite the fact that they are fed with identical feeds), as well as the interactions of the flow and heat transfer with the observed reaction rates, our prior works (<sup>3,37</sup>) cannot predict the effects seen in a reformer as the present work can because they utilize different geometries and modeling strategies. Therefore, the novelty of the present work hinges on the fact that because it demonstrates how a reformer CFD model can be developed and validated (i.e., it develops neither a simplified model like a Gibbs reactor nor even a smaller-scale CFD model), it demonstrates a methodology for obtaining high-fidelity data regarding the operating conditions throughout a reformer that can be considered to be representative of the actual conditions within the SMR but cannot be obtained any other way. The development of such a model is significant therefore for industry, because it provides a methodology for optimizing process operation with highly reliable data that is not otherwise available and allows problematic operating conditions to be evaluated and mitigated. Furthermore, the discussion of why the CFD modeling strategies were chosen demonstrates how expected phenomena within a reactor can be evaluated to allow for appropriate modeling strategies to be chosen for CFD simulation of other reactors of industrial interest for which such high-fidelity data would be beneficial.*

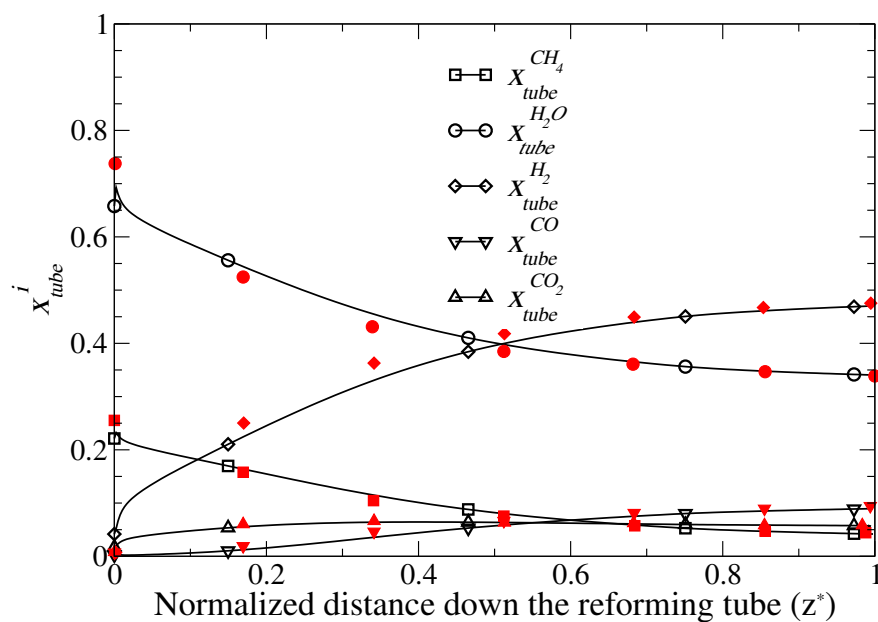


Figure 4.17: Radial-weighted average tube-side compositions along the reforming tubes produced by the reformer CFD model (black) versus those derived from typical plant data of the SMR process (red).<sup>38</sup>

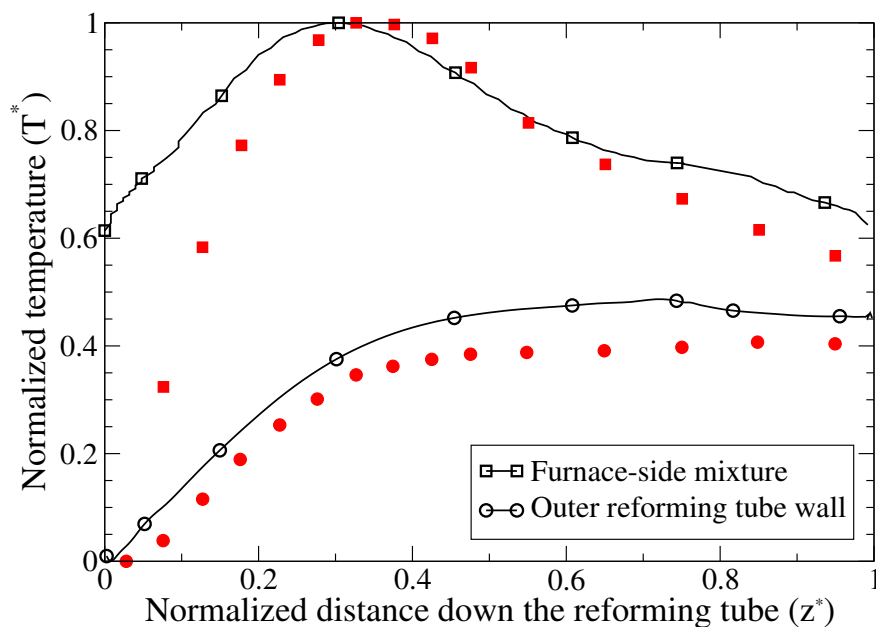


Figure 4.18: Average temperature profiles of the furnace-side mixture and outer reforming tube wall produced by the reformer CFD model (black) versus those derived from typical plant data of the SMR process (red).<sup>39</sup>

Table 4.6: Validation of reformer CFD model. Heat flux (H)

	Industrial-scale reforming tube CFD model	Reformer CFD model	Reforming Gibbs reactor model	Typical plant data <sup>38</sup>
$\Delta P_{tube}$ (kPa)	194.29	106.22	N/A	146.9
$\bar{P}_{tube,outlet}$ (kPa)	2955.2	3044.0	N/A	2879.8
$H_{average}$ (kW/m <sup>2</sup> )	70.659	69.523	N/A	67.125
$\bar{x}_{tube,outlet}^{H_2}$	0.4734	0.4687	0.4686	0.4713
$\bar{x}_{tube,outlet}^{H_2O}$	0.3380	0.3419	0.3411	0.3377
$\bar{x}_{tube,outlet}^{CH_4}$	0.0389	0.0430	0.0433	0.0453
$\bar{x}_{tube,outlet}^{CO}$	0.0905	0.0883	0.0872	0.0889
$\bar{x}_{tube,outlet}^{CO_2}$	0.0574	0.0576	0.0589	0.0559

Table 4.7: Validation of reformer CFD model by available plant data from literature

	Average heat flux (kW/m <sup>2</sup> )
Reformer CFD model	70
Industrial-scale reforming tube CFD model <sup>37</sup>	71
D. Latham <sup>38</sup>	67
J. R. Rostrup-Nielsen <sup>58</sup>	45–90
I. Dybkjaer. <sup>17</sup>	79
G. F. Froment & K. B. Bischoff <sup>21</sup>	76
G. Pantoleontos et al <sup>54</sup>	< 80

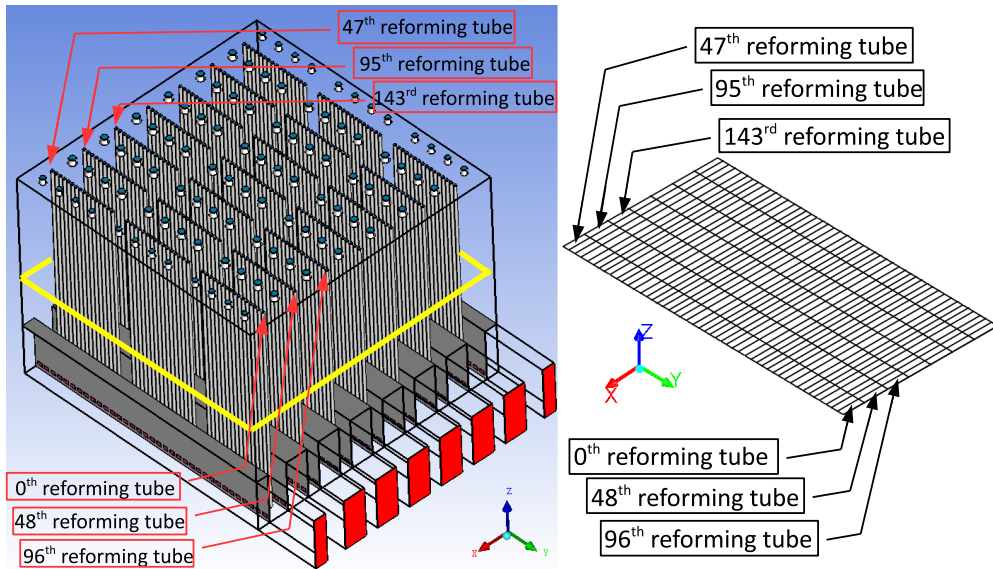


Figure 4.19: Description of the layout of the outer reforming tube wall temperature distribution, in which each grid contains an average outer reforming tube wall temperature of the corresponding reforming tube recorded by a system of IR cameras situated around the reformer.

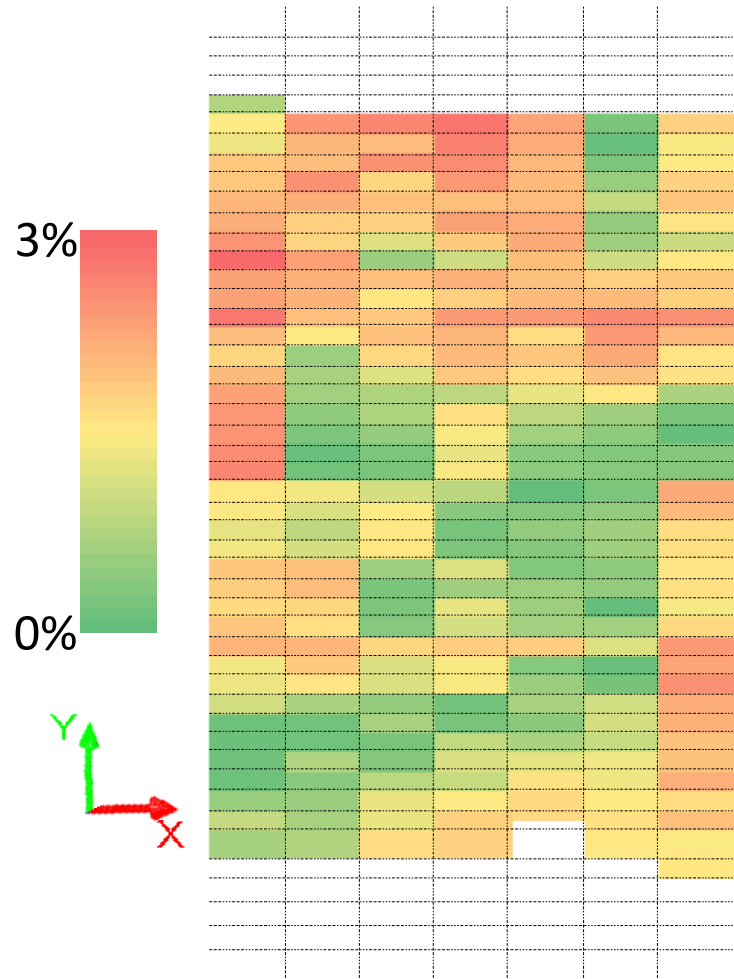


Figure 4.20: Distribution of the percent difference in the outer reforming tube wall temperature between the reformer CFD data and the plant data provided by the third party. The percent difference of each reforming tube is computed by the ratio of the deviation of the CFD data from the corresponding plant data to the corresponding plant data.

## 4.11 Conclusion

The present work detailed the development of a CFD model of a steam methane reformer and presented a methodology for analyzing expected transport and reaction phenomena to choose modeling strategies within the CFD software that result in CFD simulation data that can be considered to be a substitute for experimental data. The reformer model simulates the essential transport phenomena observed in industrial high-temperature applications as well as reformer-relevant physical and chemical phenomena. Specifically, the standard  $k-\epsilon$  turbulence model, FR/ED model and global kinetic models of hydrogen/methane combustion were selected to simulate the non-premixed combustion characteristics, the reaction rates of the furnace-side species and the thermal energy released from the oxidation of the furnace-side feed under the influence of turbulence. Then, a correlation between the furnace-side radiative properties and temperature, Kirchhoff's law, Lambert Beer's law and the discrete ordinate method were chosen to simulate radiative heat transfer within the furnace-side mixture and between the furnace-side mixture and solid surfaces inside the reformer. Next, the standard  $k-\epsilon$  turbulence model, FR/ED model and global kinetic model of the SMR process were utilized to simulate the reaction rates of the tube-side species under the influence of turbulence. Lastly, the modeling strategy of the reforming tubes utilized an approximate representation of the catalyst network to simulate the presence of catalyst particles inside the reforming tube and the effect of internal and external diffusion limitations on the observed reaction rates of the tube-side species. We recognize that the computing time required to complete a simulation of the reformer CFD model by ANSYS Fluent on 80 cores of UCLA's Hoffman2 cluster is significant (i.e., approximately three full days), yet the upfront investment (i.e., time) makes it possible for us to determine the optimized operating conditions of the reformer. Specifically, the simulation results generated by the reformer CFD model with the tube-side and furnace-side feed derived from typical plant data are demonstrated to be consistent with phenomena observed in reformers and to be in close agreement with typical plant data. In addition, the

simulation data generated by the reformer CFD model, in which the tube-side and furnace-side feed distributions provided by a third party are used as boundary conditions, is shown to be in close agreement with the plant data recorded from the on-line reformer at the hydrogen manufacturing plant. Therefore, the reformer CFD model can be considered to be an adequate representation of the on-line reformer and can be used to determine the risk to operate the on-line reformer at un-explored and potentially more beneficial operating conditions.

$A_{comb}$	total surface area of the combustion chamber ( $m^2$ )
$C_p$	specific heat capacity of the mixture (J/kgK)
$C_{p,comb}^j$	heat capacity of species $j$ in the mixture (J/kgK)
$D_p$	effective diameter of the catalyst pellets (mm)
$D_{comb}^{m,i}$	mass diffusion coefficient of the species $i$ in the mixture ( $m^2/s$ )
$D_{comb}^{m,t}$	turbulent mass diffusion coefficient of the mixture ( $m^2/s$ )
$E_{comb}$	specific internal energy of the mixture (J/kg)
$E_{wave}$	energy of electromagnetic waves (J)
$P_{comb}$	pressure of the mixture (kPa)
$p_{tube}^i$	partial pressure of the species $i$ in the mixture (kPa)
$\vec{g}$	universal gravitational acceleration vector ( $m/s^2$ )
$h$	Plank's constant Js
$h_{comb}$	specific sensible enthalpy of the mixture (J/kg)
$h_{comb}^j$	specific sensible enthalpy of species $j$ in the mixture (J/kg)
$K_{H_2}$	adsorption constants for $H_2$ ( $bar^{-1}$ )
$K_{CH_4}$	adsorption constants for $CH_4$ ( $bar^{-1}$ )
$K_{CO}$	adsorption constants for $CO$ ( $bar^{-1}$ )
$K_{H_2O}$	dissociative constants for $H_2O$
$K_1$	equilibrium constant of the reaction 5 ( $bar^2$ )
$K_2$	equilibrium constant of the reaction 6
$K_3$	equilibrium constant of the reaction 7 ( $bar^2$ )



$k_1$	forward kinetic constant coefficient of the reaction 5 ( $\text{kmol bar}^{0.5}/\text{kg}_{\text{catalyst}} \text{h}$ )
$k_2$	forward kinetic constant coefficient of the reaction 6 ( $\text{kmol bar}^{0.5}/\text{kg}_{\text{catalyst}} \text{h}$ )
$k_3$	forward kinetic constant coefficient of the reaction 7 ( $\text{kmol bar}^{0.5}/\text{kg}_{\text{catalyst}} \text{h}$ )
$k_{comb}^{eff}$	effective thermal conductivity of the mixture ( $\text{W/mK}$ )
$k_{comb}^l$	thermal conductivity of the mixture ( $\text{W/mK}$ )
$k_{comb}^t$	turbulent thermal conductivity of the mixture ( $\text{W/mK}$ )
$k_{comb}$	turbulence kinetic energy of the mixture ( $\text{m}^2/\text{s}^2$ )
$I$	unit tensor (kPa)
$\vec{J}_{comb}^i$	turbulent mass diffusion flux of species $i$ of the mixture ( $\text{kg}/\text{m}^2 \text{s}$ )
$R_i, i = 1, \dots, 4$	intrinsic volumetric reaction rate of the $i^{th}$ reaction ( $\text{kmol m}^{-3} \text{s}^{-1}$ )
$R_i, i = 5, \dots, 7$	intrinsic volumetric reaction rate of the $i^{th}$ reaction ( $\text{kmol (kg of catalyst)}^{-1} \text{s}^{-1}$ )
$R_{i,j}$	observed volumetric rate of species $i$ in reaction $j$ ( $\text{kg m}^{-3} \text{s}^{-1}$ )
$M_i$	molecular weight of species $i$ ( $\text{kg kmol}^{-1}$ )
$M_{\mathcal{R}}$	molecular weight of a specified reactant $\mathcal{R}$ ( $\text{kg kmol}^{-1}$ )
$L$	characteristic dimension of the combustion chamber (m)
$L_{tube}$	heated reforming tube length (m)
$Sc_{comb}^t$	turbulent Schmidt number of the mixture
$T_{comb}$	temperature of the mixture (K)
$T_{wall}$	temperature of the solid surfaces (K)
$T_{ref}$	reference temperature (K)
$[i]$	molar concentrations of the species $i$ of the mixture ( $\text{kmol m}^{-3}$ )
$x_{tube}^i$	mole fractions of species $i$ in the mixture
$x_{comb}^i$	mole fractions of species $i$ in the mixture
$Y_i$	mass fraction of species $i$
$Y_{comb}^i$	mass fraction of species $i$ in the mixture
$Y_{\mathcal{R}}$	mass fraction of a specified reactant $\mathcal{R}$ in reaction $j$
$Y_{\mathcal{P}}$	mass fraction of a specified product species $\mathcal{P}$ in reaction $j$

$V_{comb}$	volume of the combustion chamber ( $m^3$ )
$v_{\infty, tube}$	superficial velocity of the mixture ( $m\ s^{-1}$ )
$\vec{v}_{comb}$	velocity vector of the mixture ( $m\ s^{-1}$ )
$v_{comb}^2/2$	specific kinetic energy of the mixture ( $J\ kg^{-1}$ )
$\alpha$	permeability coefficient of the catalyst network ( $m^2$ )
$\beta$	inertial resistance coefficient of the catalyst network ( $m^{-1}$ )
$\beta'$	coefficient of thermal expansion of the mixture ( $K^{-1}$ )
$\nu_{i,j}$	stoichiometric coefficient of species $i$ in reaction $j$
$\nu_{\mathcal{R},j}$	stoichiometric coefficient of a specified reactant $\mathcal{R}$ in reaction $j$
$\nu_{wave}$	frequency of electromagnetic waves ( $s^{-1}$ )
$\rho_{tube}$	density of the mixture ( $kg\ m^{-3}$ )
$\rho_{comb}$	density of the mixture ( $kg\ m^{-3}$ )
$\epsilon$	total emissivity of the mixture
$\epsilon_{comb}$	dissipation rate of the mixture ( $m^2\ s^{-3}$ )
$\epsilon_{wall}$	internal emissivity coefficient of the solid surfaces
$\sigma_a$	absorption coefficient of the mixture
$\overline{\tau}_{comb}$	stress tensor (kPa)
$\gamma$	porosity of the catalyst network
$\mu_{comb}$	molecular viscosity of the mixture ( $kg\ m^{-1}\ s^{-1}$ )
$\mu_{comb}^t$	eddy viscosity of the mixture ( $kg\ m^{-1}\ s^{-1}$ )
$\mu_{tube}$	molecular viscosity of the mixture ( $kg\ m^{-1}\ s^{-1}$ )
$-\nabla \cdot \vec{q}_{rad}$	radiative heat transfer rate ( $J\ m^{-3}\ s^{-1}$ )
$\Delta P_{tube}$	pressure difference of the mixture across the catalyst network (kPa)

Table 4.8: Notations

## Chapter 5

# Smart Manufacturing Workflow to Model a Steam Methane Reforming Furnace Using Computational Fluid Dynamics

### 5.1 Introduction

In the previous chapters, we developed a model of the steam methane reformer with the goal to capture the transport phenomena while maintaining the simulation size, and computational time reasonable for our design target to run on Hoffman2 computing cluster at UCLA. In Chapter 2, we developed a single reforming-tube 2D axisymmetric model which allowed us to learn how to set up the chemical reactions necessary and validated the model output for the steam methane reforming process based on global intrinsic kinetics models.<sup>70</sup> Then, in Chapter 3, we expanded the process model considered to a model containing four reforming tubes and three burners. In doing so, the new model also increased in complexity as it became a 3D model that also included combustion from 3 burners of which, two are outer-lane burners and one is inner-lane burner. This work allowed us to understand the complexities associated with

combining two computational domains and also implementing methane combustion along with steam methane reforming. In Chapter 4, the reforming furnace model was finally scaled up to the full steam methane reformer furnace developed by Selas-Linde GmbH. This new model brought new knowledge such as developing a step by step converging strategy that allowed us to deal with the instability issues of the initial steps of the simulation while bringing significant computational performance increase. Finally, in,<sup>63</sup> we implemented a temperature balancing strategy improved upon our convergence strategy from<sup>64</sup> by utilizing a two-step strategy for the data generation. In the current chapter, we present a workflow for a non-expert user of our steam methane reforming furnace computational modeling and operation methodologies where a user can simply visit our Smart Manufacturing Platform resource, choose a model and appropriate input data and run the model to balance the furnace temperature. The importance of this approach is detailed in<sup>11</sup> “The SM Platform also shortens the development time for the model and data management configuration process to bring the SM system into production sooner.”

## 5.2 Smart Manufacturing

Smart manufacturing (SM) is the practice of generating and applying manufacturing intelligence to the manufacturing life cycle and supply chain enterprise, allowing for an increase of operational freedom. Manufacturing intelligence (MI) includes two components: (1) the intensified and pervasive application of networked information based technologies, and (2) the extensive use of data analysis, modeling and optimization. The application of manufacturing intelligence requires the real-time understanding, reasoning, planning, and management of all aspects of the manufacturing process. Smart Manufacturing<sup>11, 12</sup> is aimed at addressing manufacturing needs driven by competitive markets that are influenced by legislation and social pressures. Manufacturing needs include producing the best value for customers in a short and flexible time frame, maintaining a flexible and agile production, while decreasing main-

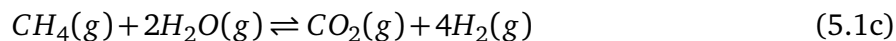
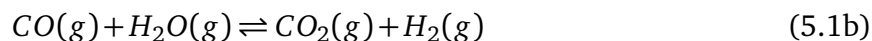
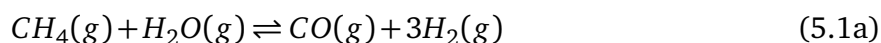
tenance, incidents, and operational cost. Davis *et al.*<sup>11</sup> refer to manufacturing test beds as a concept to classify and identify industrial needs and propose four potential test bed scenarios in which smart manufacturing can be implemented using the Smart Manufacturing Platform (SM Platform).

A SM platform is designed as an open, shared and reusable, software and IT infrastructure. It is designed for the development and deployment of components necessary for smart manufacturing. SM Platform is a cloud-based service that also acts as an application store which resembles popular cell-phone app stores. The SM platform combines the management of actionable information and the procurement of necessary IT infrastructure by meeting three key requirements.<sup>11,12</sup> First, it supports the development of an accessible SM intelligence to understand the manufacturing process, increased accessibility and availability of software and data by applying modeling, data analysis, and fostering and sharing of knowledge and software. Second, it is encouraging the proliferation of integrated, sensor-based, data-driven Manufacturing Intelligence. Third, the SM Platform, which is built upon an open, shareable, secure and manageable architecture, allows for the development of data independent applications. Davis *et al.*<sup>11</sup> proposed a steam methane reformer as one of the Test Beds for the initial development of the SM Platform because it is a very energy-intensive process and it is deployed around the world in over 900 facilities.<sup>11</sup> In the present Chapter, we are presenting a workflow for a hydrogen steam methane reformer furnace producing  $2.8 \times 10^6 \text{ Nm}^3$   $2.8 \times 10^6 \text{ Nm}^3$  per day.

### 5.3 Steam Methane Reforming (SMR)

Steam methane reforming is a prolific process in downstream petroleum industry accounting for approximately 48%<sup>19</sup> of the worldwide molecular hydrogen production. Its widespread deployments across worldwide plant sites is a result of its economic viability due to low production cost. Petroleum refining consumes large amounts of hydrogen in various catalytic pro-

cesses (e.g., hydrocracking, hydrotreating, desulfurization). Hydrocracking and hydrotreating are used in bottom of the barrel processing to convert residual feed into higher grade products. Hydrocracking cleaves sigma carbon-carbon bonds and hydrotreating converts olefins to paraffins. Hydro-desulfurization is used to treat sour natural gas by removing thiol compounds from natural gas.<sup>29</sup> Steam methane reforming is a set of reactions 5.1a - 5.1c in which water vapor reacts with methane in a net endothermic set of reactions to produce molecular hydrogen and carbon oxides.



Steam methane reforming typically takes place in an industrial unit named the reformer. This unit consists of two closed domains: (1) The first domain is a furnace chamber where fuel and excess atmospheric oxygen combust to generate thermal energy, (2) the second domain named reforming-tube in which the steam methane reforming reactions take place. Four configurations named after the locations of the burners inside the reformer furnace are most common for industrial plants, bottom-fired, terrace wall-fired, sided-fired, and top-fired reformer. Bottom-fired and terrace wall-fired reformers are known for their uniform heat flux along the reforming tubes.<sup>20</sup> Side-fired reformers have flexible temperature adjustments. Top-fired reformers, increase the heat available near the entrance to the tubes.<sup>63,64</sup> In this work, we focus on a top-fired reformer for the net endothermic nature of the SMR process. Heat transfer near the entrance to the reforming-tube is most desirable to minimize the reforming-tube length. Moreover, to increase the conversion of methane to hydrogen by SMR, a higher tube-wall temperature is required.<sup>41</sup> However, as desirable as it is to operate at high temperatures for SMR process, careful temperature control and furnace balancing is necessary because permanent

increase of 20K above the designed operating tube wall temperature value can reduce the expectancy of a reforming-tube to half.<sup>54</sup>

### 5.3.1 Steam Methane Reformer

The steam methane reformer in this work is based on a design by Selas-Linde GmbH.<sup>38</sup> The operational cost and production of this steam methane reformer is 62 million USD and 2800000 Nm<sup>3</sup> of hydrogen and 1700000 kg of superheated steam per day, respectively. The reformer physical dimensions are 16.3m length, 16m width, 12.7m height. The reformer components are: 96 burners, 336 reforming-tubes and eight flue-gas tunnels. The burners are distributed on eight rows of 12 burners, and the 24 burners adjacent to the refractory walls (outer-lane burners) are of smaller diameters than the 48 burners adjacent to two rows of tubes (inner-lane burners). The reforming tubes are distributed over seven rows of 48 burners and are in between of two rows of burners. The reforming-tube's dimension are 12.5 m length, 12.6 cm inner diameter and 1.0 cm tube-wall. The reforming-tubes are packed with alpha-alumina-supported nickel oxide ( $NiO-\alpha Al_2O_3$ ). The flue-gas tunnels are part of eight coffin boxes at the bottom of the furnace and span across the length of the furnace, and are 3m in height. The refractory walls are perforated by 35 evenly spaced extraction ports with a dimension of 22 cm  $\times$  30.5 cm. The flue gas enters the coffin boxes perpendicularly and exits the furnace through the flue-gas tunnels.<sup>63,64</sup>

## 5.4 Smart Manufacturing Workflow

Our work is designed to take external dynamic inputs from industrial data as shown in Fig.5.2. The data can be originated by industrial equipment readings, sensors, cameras or any type of metrics appropriate to the process. The data used in this study was stored at the source location and transmitted in real time to a OSI/PI<sup>52</sup> historian on a private cloud resource. Historian is a

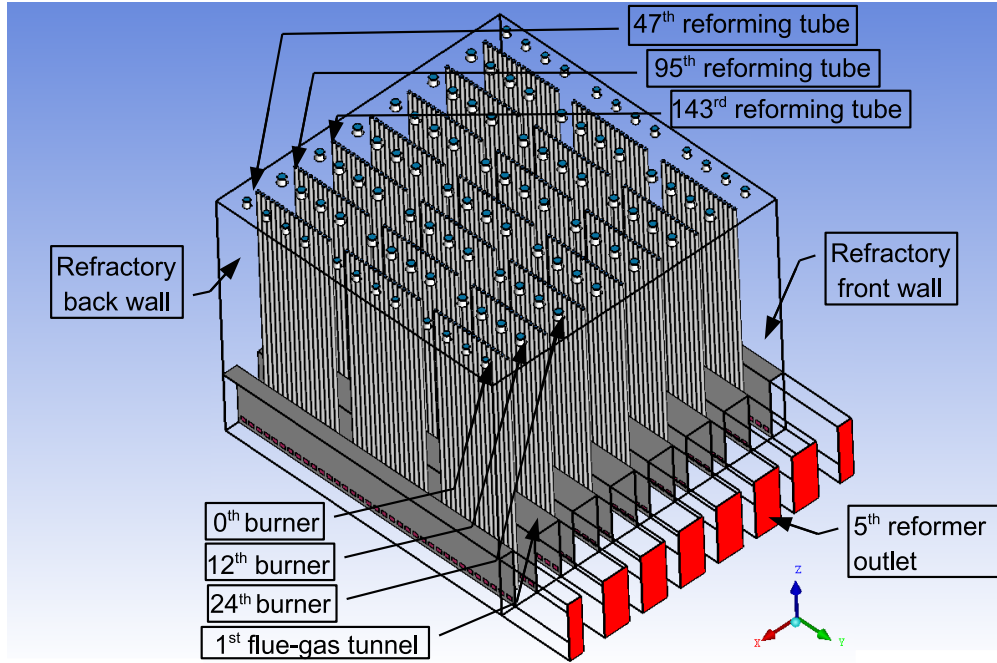


Figure 5.1: The isometric view of an industrial-scale, top-fired, co-current reformer with 336 reforming tubes, which are represented by 336 slender cylinders, 96 burners, which are represented by 96 frustum cones, and 8 flue-gas tunnels, which are represented by 8 rectangular intrusions.

time series database that is optimized to handle time sensitive information and it is indexed by time, so that we can query historical data at the particular time point. We used passwordless secure shell protocol (scp) to transfer input data from the factory and output data back to the source.



Figure 5.2: Smart Manufacturing workflow

To develop a workflow to automate the computation process in a high-performance computing (HPC) environment, we used the Hoffman2 cluster at UCLA. The Hoffman2 cluster is a HPC resource at UCLA with Infiniband interconnects<sup>22</sup> and a high-performance storage server from Panasas.<sup>53</sup> In this computation, we utilized 128 cores of computing power from this cluster. The CPU cores are based on the Intel Xeon architecture and include 4 GB RAM per core. ANSYS



Fluent makes use of the Infiniband interconnects when multiple nodes are used in a message passing interface (MPI) calculation environment.

We used Kepler scientific workflow software package to automate the creation and deployment of our CFD-based model mainly because of our earlier expertise in the use of Kepler software package.<sup>32,33</sup> Our past experience has taught us that using an automated workflow will eliminate possible human error when a process has to be repeated many times. It will also free modelers to carry other research work, adding productivity to the bottom line. The parametrization feature of the workflow will allow us to run the code in a completely different computational environment by providing different run time parameters. The parameters are run time variables that can be supplied as an argument to the workflow. Kepler software is written in Java and can be deployed in Linux, MAC OS, or Windows operating system. In the simplest form, a scientific workflow can be a series of commands for the appropriate operating system. Kepler provides users an easy to use graphical environment with pre-defined execution files and logic symbols that can be dragged and dropped to canvas and connected to create a flowchart like a sequence of operations. The software uses concepts of *directors* and *actors* with *directors* determining when an *actor* performs its part. Examples of some of the *actors* used in this workflow are *scp actor*, *ssh-execution actor*, *boolean job-completion-check actor*, *conditional actor*, *display actor*, *composite actor*, etc. The *ssh-execution actor* when called with a host-name and user credential will log into a remote host and execute the command given to that actor, and the *display actor* will simply display the standard output.<sup>31</sup> Since in a workflow like ours many actors may be performing work at the same time, we used a *parallel director*. The workflow composed for this study is deployed in a Linux computing environment to take advantage of HPC resource. The schematic diagram of this workflow is given in Fig. 5.3. In the very first step, a *scp actor* is configured to transfer files using ssh passwordless authentication method from a location where input files from a OSI/PI historian database is available. The IP address for the OSI/PI historian resource can be either set as default or changed at run time as a command line argument to the workflow instructions which are written as an *xml* file.

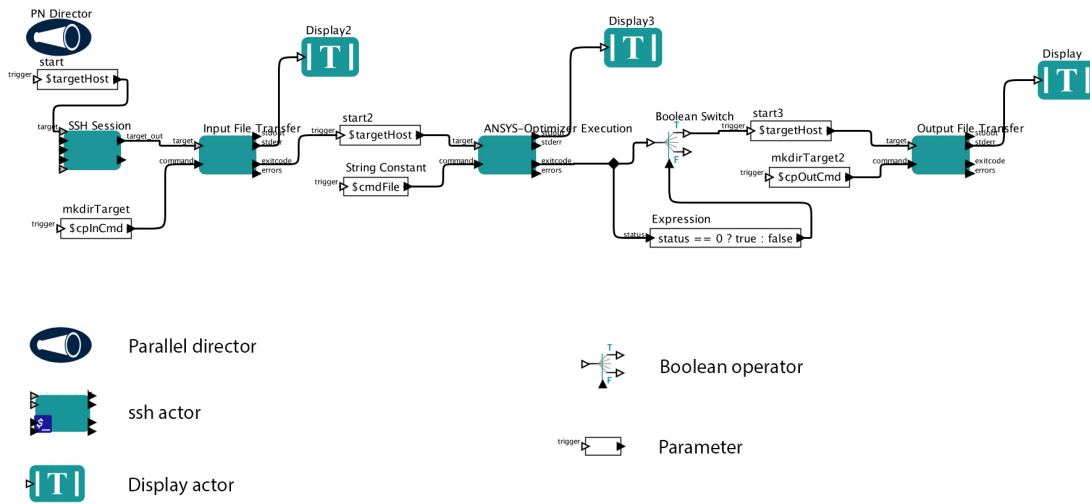


Figure 5.3: Kepler workflow screenshot provides.

Once file transfer is complete, in the event the input files are given as valve position expressed as percentage opening, we will have to call another execution actor that will convert the percentage opening of valve position to mass flow rate in units of  $kg/second$ . The next step is to call an ssh execution actor that runs an ANSYS Fluent calculation and monitors the progress of the calculation. In order to run ANSYS Fluent, this actor needs to be provided several environmental variables such as the path of ANSYS Fluent binary installation, location (full path) of the working directory and setup LD\_LIBRARY\_PATH which tells ANSYS the exact location of the UDF that Fluent will be using during the CFD calculation process. Additionally, since this is a distributed computing process, Fluent needs to be provided with a *hostfile* which contains the IP address of all the hosts involved in the computation process. During the creation of the workflow many of these parameters are given a default value but due to the nature of HPC or cloud computation almost all of these parameters may be different during the actual deployment of the workflow. So these parameters can also be given as command line arguments to the XML workflow instruction.

While the ANSYS Fluent calculation is going on, within Fluent itself, we run a mini workflow with the details of this workflow given in the next section called "Internal Balancing Workflow"

which essentially involves three steps which are: (1) data generation, (2) model identification and (3) model-based control scheme. The data generation part is done by ANSYS Fluent which is the computationally intensive part of the calculation. For the steps 2 and 3, we call the linear programming solver packages CPLEX.<sup>25</sup> Since CPLEX is not distributed as a package available inside ANSYS, we need to make use of the user defined function capability of ANSYS Fluent to call these packages at run time. The IPOPT is another open source package which needs to be compiled in advance with a gcc compiler and the resulting dynamic library path location is added to the LD\_LIBRARY\_PATH that Kepler workflow sets up for the Fluent calculation. The CPLEX libraries are downloaded as it is and require no additional compilation other than adding the location of the library to the LD\_LIBRARY\_PATH. An overall view of the Kepler workflow and the mini-ANSYS based workflow inside the Kepler workflow is given in the Fig. 5.4 below. Once the ANSYS based workflow completes, the Kepler workflow will move on to the next actor which is an *scp actor* that transfers the output files to a location where users can view the file. Optionally, we can also add an actor that will display the resultant file in a format that is familiar for the user.

#### **5.4.1 Smart Manufacturing Workflow Convergence Criterion**

The workflow convergence criteria, i.e., outer loop termination criteria determines if sufficient trials have been performed to achieve the optimal solution. At the end of each trial in the outer loop, the final standard deviation is recorded. If the difference between two consecutive trials is below 0.5%, the outer loop is considered to be converged. Usually convergence is achieved within five trials, and upon which an optimized valve percentage opening would be returned to the user.

## 5.5 Internal Balancing Workflow

The Internal Balancing Workflow implemented in ANSYS Fluent is an internal step of the entire Smart Manufacturing workflow. This workflow includes the iterative optimization-computation routine for SMR and the automatic exit criteria. From a high level perspective, the workflow optimizes the result of the converged simulation and uses the optimized flow rate as a new starting point for the simulation. This procedure is repeated automatically until the difference between simulation temperature standard deviation and optimization temperature standard deviation is below 3%.

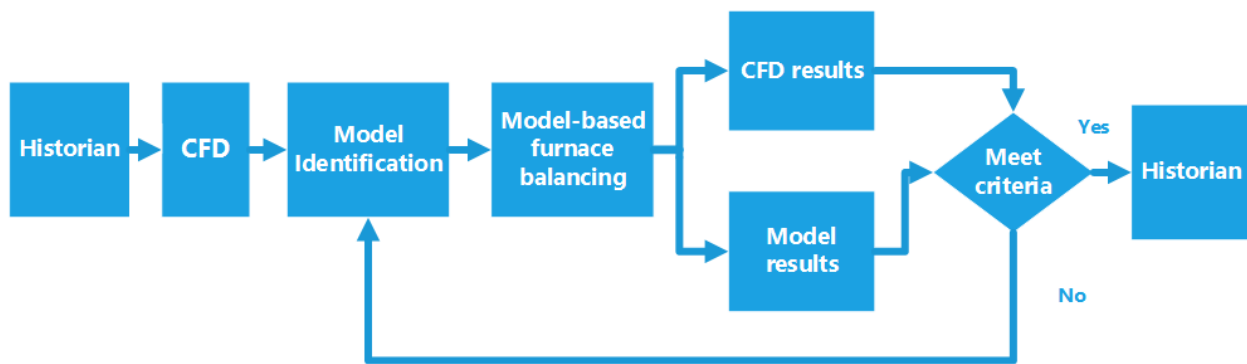


Figure 5.4: Inner workflow schematic using ANSYS fluent orchestrate the optimization via scheme language and optimization packages

The implementation of Fluent workflow involves two types of files: Journal files and Scheme files. A journal file is loaded upon the startup of the Fluent application and is used to load the case and data of the current simulation. It also loads the scheme files into the current simulation environment. The scheme files, which use Fluent scheme as a scripting language, serve as the main body of the workflow that includes the essential loops for the optimization routine. The workflow is characterized by two nested loops. The outer loop determines the number of trials to be performed. A trial represents a steady-state indicated by the input flow rate. In the outer loop, first, we set the RP Variable, can be accessed by the fluent UDF, to the current number of trials, and we output the temperature of every single tube and the flow rate of every single burner. RP variables are user defined and executed by a scheme interpreter and

are identified by *rp-var-define*.<sup>27</sup> Next, we perform the optimization, using an on-demand UDF that calls a shared object created using the IBM CPLEX optimization API. This step gives an output of the optimized burner flow rates, which is updated into FLUENT as the new burner flow rates using another scheme function. Then, the inner loop will determine the arrival of steady state by the furnace CFD model, which is indicated by the fluctuation of the standard deviation of tube wall temperatures. When the standard deviation between two iteration is below 1%, the inner loop will exit and release the control back to the outer loop. The outer loop then compares the final standard deviation of the current trial with the previous trial. If the difference is below 3%, the outer loop will exit.

### 5.5.1 Fluent User-Defined Function (UDF) and Implementation Scheme

In our implementation of the workflow, we use the User Defined Function (UDF)<sup>27</sup> feature provided by Fluent to call the external utility that performs the optimization over the burner flowrates and tube temperatures. In Fluent, UDF is a powerful tool to access the current case parameters, including the physical models, result access and post-processing. Fluent UDF is implemented in C-language and there are many types of UDFs serving various purposes. For example, in our case, another UDF we used to provide the reaction kinetics of steam methane reforming reaction is a *VR\_RATE* UDF<sup>27</sup> which specializes in the specification of volumetric reaction rate. In the workflow, we used an Execute On-Demand (EOD) UDF as a switch to call the optimization toolpack. The Execute On-Demand UDF is handy in a workflow because it can be called at any point defined by the user, and in our case, the UDF is called right after the burner flowrates and tube temperature data are exported.

The Fluent Scheme is also a very important feature in Fluent, and it is used extensively in our workflow. Scheme is a LISP language dialect, and ANSYS provides a Domain-Specific Language version of Scheme that serves as the scripting language of Fluent. The Fluent Scheme provides the access to application flow control, such as the control of numerical method convergence,

file storage management, iteration control, etc. The Fluent Scheme also provides the communication between the Fluent application and UDF, which often has external dependencies, through RP-variables. RP-variables are usually used in Fluent as fundamental application parameters. However, their low-level accessibility made it handy to be captured by Fluent UDF. By adding RP-variables, we were able to construct a workflow that is able to continuously provide and receive information between Fluent and external optimization utility, without human input.

### 5.5.2 Model Identification

The second step of the furnace-balancing scheme (i.e., the model identification process) utilizes the cumulative reformer CFD database collected from the data generation process to derive a data-driven model describing the relationship between the outer reforming tube wall temperature (OTWT) distribution at a specified distance away from the reforming tube inlets and the FSF distribution. In the present work, we have found that the relationship can be assumed to be linear, and the data-driven model can still provide a reasonably accurate prediction of the OTWT distribution, which is generated by the reformer CFD model, given a sufficiently large reformer CFD database. Therefore, the radially averaged outer reforming tube wall temperature of the  $i^{th}$  reforming tube at the fixed distance away from the reforming tube inlet ( $T_i$  (K)), which is an element of the OTWT distribution, can be approximated by a linear combination of the FSF flow rates of all 96 burners (i.e., the FSF distribution) as follows,

$$T_i = \sum_{j=0}^{95} \alpha_{ij} F_j \quad (5.2)$$

where  $F_j$  ( $\text{kg s}^{-1}$ ) is the furnace-side feed flow rate of the  $j^{th}$  burner and  $\alpha_{ij}$  ( $\text{K kg}^{-1}\text{s}$ ) is the empirical coefficient of the data-driven correlation corresponding to the  $i^{th}$  reforming tube and  $j^{th}$  burner, which is to be determined by the model identification process. In this study,

the outer-lane/ inner-lane burners and reforming tubes are indexed from  $0^{th} - 95^{th}$  and  $0^{th} - 335^{th}$  in the specified patterns as shown in Fig. 5.1. As a result, the model identification process created based on our assumption of the linear relationship between the OTWT and FSF distributions is an optimization problem with 32256 decision variables. Due the sheer number of decision variables, the model identification process is expected to be a computationally expensive algorithm. Hence, in the remainder of this section, the concept of a heating zone is introduced in an effort to decrease the computational time for deriving the data-driven model, and a modified formulation of the model identification process is presented.

In high-temperature applications, thermal radiation is the dominant mode of heat transfer, and the reformers are commonly referred to as radiant heat exchangers.<sup>35</sup> Olivieri et al.<sup>51</sup> shows that radiative heat transfer accounts for  $\sim 95\%$  of the total heat transfer in the top-fired reformer investigated in that work, which suggests that the OTWT distribution is primarily controlled by thermal radiation. This is because the rate of energy transferred by thermal radiation between two blackbodies at different temperatures is commonly modeled as being proportional to the difference in temperatures raised to the fourth power (i.e.,  $\Delta(T^4)$ ), while the rate of heat transfer by conduction and convection between them is proportional to the temperature difference (i.e.,  $\Delta(T)$ ). However, the rate of heat transfer by thermal radiation decreases drastically with increasing distance between two blackbodies because it is proportional to the radiation intensity, which is inversely proportional to the distance between the two blackbodies raised to the second power. This idea allows us to assume that when the distance between a specified burner and reforming tube is sufficiently large, the furnace-side feed flow rate of the burner has negligible impact on the average outer reforming tube wall temperature. In this study, the distance between a specified burner and reforming tube is defined as the distance between the projection of the burner centroid and the projection of the reforming tube centroid onto any 2-D horizontal cross-sectional plane. To quantitatively determine the local radiative heating effect on the OTWT distribution due to the furnace-side feed flow rate of each burner, we consider the following simplifying assumptions: each burner creates a heating

zone represented by a blue cylindrical volume as shown in Fig. 5.7, the heating zones of the burners have an identical size and shape, and the FSF flow rate of the  $j^{th}$  burner only affects the average outer wall temperature values of the reforming tubes which are located inside the heating zone of the  $j^{th}$  burner.

We begin by utilizing the existing reformer CFD data reported in<sup>64</sup> to construct the velocity vector fields of the furnace-side flow pattern as shown in Fig. 5.5, which allows us to form a hypothesis regarding the underlining mechanism by which the furnace-side flow field affects the OTWT distribution. Specifically, Fig. 5.5 indicates that the hot combustion products (i.e., the furnace-side flow) enter the flue-gas tunnels through the extraction ports and move toward the reformer outlets. The existing furnace-side flow pattern appears to cause the wall temperature of the flue-gas tunnels to increase with decreasing distance toward the reformer outlets as shown in Fig. 5.6. Additionally, Fig. 5.6 shows that the minimum wall temperature of the flue-gas tunnel of 1240 K is greater than the maximum temperature of the reforming tube wall of 1183 K,<sup>64</sup> so it is reasonable to assume that the reforming tubes might receive additional radiative heating from the neighboring flue-gas tunnels. However, the magnitude of the additional heating transferred to each reforming tube from the neighboring flue-gas tunnels depends on the location of the reforming tube with respect to the reformer outlets. Particularly, because the flue-gas tunnels are at higher temperature toward the reformer outlets, the reforming tubes that are situated closer to the reformer outlets are expected to receive higher amounts of additional radiative heating from the neighboring flue-gas tunnels. It is important to note that the existing furnace-side flow pattern (Fig. 5.5) also suggests that the additional radiative heating received by the reforming tubes that are situated near the reformer outlets can be from the combustion products of the burner that is situated near the reformer back wall. The analysis motivates us to develop heating zones with the shape shown in Fig. 5.7 in the effort of making the data-driven model aware of the furnace-side flow pattern and its effects on the OTWT distribution. It is important to note that when a larger cylindrical heating zone is utilized in the model identification process, each burner is assumed to influence more surrounding reforming



tubes in addition to those that are situated in the direction toward the reformer outlets and in the two adjacent rows of reforming tubes, which may allow the data-driven model to be more accurate with respect to the reformer CFD data at the cost of increased computational time. We conducted a study with various dimensions of the burner heating zone to determine the appropriate dimension of the cylindrical volume (i.e.,  $r_{cyl}$ ), and we have found that at  $r_{cyl} \sim 3.4$  m, we are able to form 336 sets of the tube-burner relationships, which are denoted by  $S_i$  and  $i \in [0, 335]$  such that  $S_i$  contains the FSF flow rates of the burners on which the outer wall temperature of the  $i^{th}$  reforming tube depends. The tube-burner relationships reduce the number of decision variables of the model identification algorithm from 32256 to 6865 and, thus, allow the data-driven model to be created within a reasonable computing time interval.

The data-driven model is designed to account for the reformer geometry characteristics (i.e., the burner and reforming tube arrangements) and is designed to have the potential to account for the influence of the furnace-side flow pattern on the OTWT distribution by using the concept of a heating zone. The data-driven model utilizes a given FSF distribution to predict an OTWT distribution that is close to that taken from a reformer CFD simulation result in the least squares sense. The model identification process based on  $n$  sets of the reformer CFD data taken from the reformer CFD database is formulated as follows,

$$\min_{\alpha_{ij} \in [0, \infty)} \sum_{m=0}^{n-1} \sum_{k=0}^{335} (T_{k,m} - T_{k,m}^{est})^2 \quad (5.3)$$

subject to

$$T_{k,m}^{est} = \sum_{j=0}^{95} \alpha_{kj} F_{j,m} \quad (5.4a)$$

$$\alpha_{kj} = 0 \quad \text{if } F_{j,m} \notin S_k \quad (5.4b)$$

$$\alpha_{kj} = \alpha_{ki} \quad \text{if } F_{j,m}, F_{i,m} \in S_k \text{ and } d_{kj} = d_{ki} \quad (5.4c)$$

$$\left( \frac{d_{kj}}{d_{ki}} \right)^\beta \cdot \alpha_{kj} \geq \alpha_{ki} \geq \alpha_{kj} \quad \text{if } F_{j,m}, F_{i,m} \in S_k \text{ and } d_{kj} > d_{ki} \quad (5.4d)$$

where  $T_{k,m}$  and  $T_{k,m}^{est}$  are the average outer wall temperature of the  $k^{th}$  reforming tube taken from the  $m^{th}$  reformer CFD data set and the corresponding value generated by the data-driven model given the  $m^{th}$  furnace-side feed distribution as shown in Eq. 5.4a, respectively,  $F_{j,m}$  is the furnace-side feed flow rate of the  $j^{th}$  burner derived from the  $m^{th}$  reformer CFD data set,  $\beta = 4.0$  is an empirical constant of the data-driven model estimated from the study of the burner heating zone,  $d_{kj}$  is the distance between the  $k^{th}$  reforming tube and the  $j^{th}$  burner and  $d_{ki}$  is the distance between the  $k^{th}$  reforming tube and the  $i^{th}$  burner. In Eqs 5.4a–5.4d, the ranges of  $k$ ,  $i$ ,  $j$  and  $m$  are 0–335, 0–95, 0–95 and 0– $n$ , respectively. The cost function (Eq. 5.3) of the model identification penalizes the deviation of the average outer wall temperature of each reforming tube generated by the data-driven model from that derived from the corresponding reformer CFD data set. Specifically, Eq. 5.4b suggests that if the  $k^{th}$  reforming tube is not situated within the heating zone of the  $j^{th}$  burner ( $T_{k,m} \neq T_{k,m}(F_{j,m})$ ), the data-driven model will assume that the furnace-side feed flow rate of the  $j^{th}$  burner does not affect the  $k^{th}$  outer reforming tube wall temperature. Additionally, Eq. 5.4c indicates that if the distance between the  $k^{th}$  reforming tube and the  $j^{th}$  burner is equal to that between the  $k^{th}$  reforming tube and the  $i^{th}$  burner, the data-driven model then presumes that the effects of the burners on the  $k^{th}$  outer reforming tube wall temperature are the same. Similarly, Eq. 5.4d shows that if the distance between the  $k^{th}$  reforming tube and the  $j^{th}$  burner is greater than that between the  $k^{th}$  reforming tube and the  $i^{th}$  burner, the data-driven model then infers that the effects of the

$j^{th}$  burner on the  $k^{th}$  outer reforming tube wall temperature are weaker than those of the  $i^{th}$  burner.

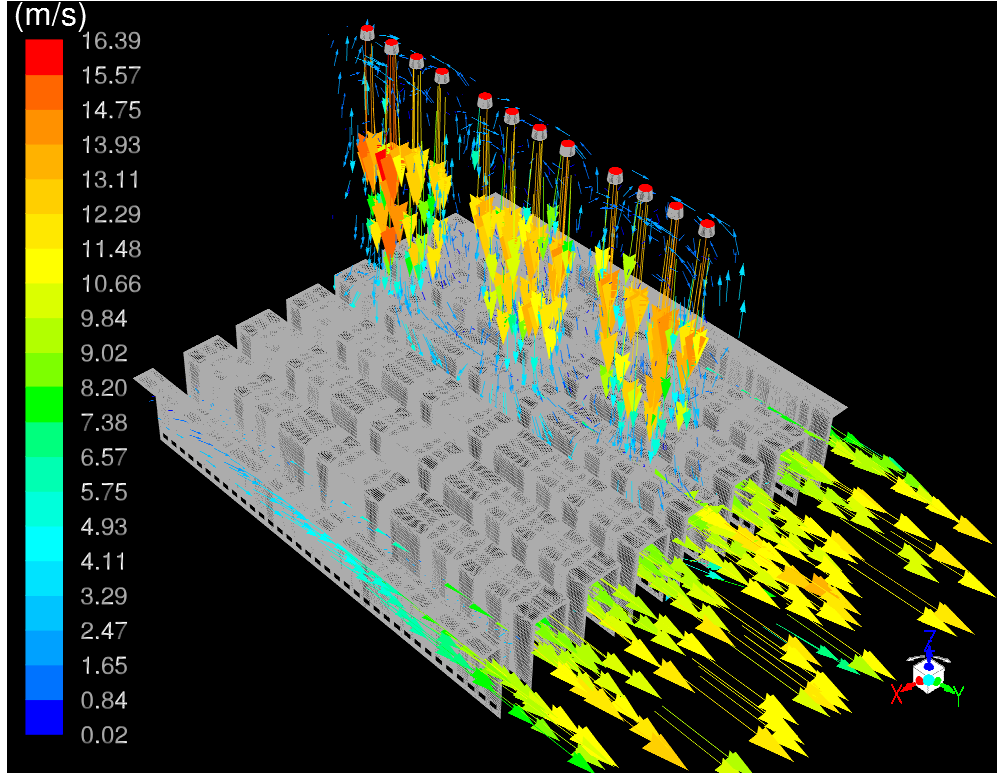


Figure 5.5: The velocity vector field of the furnace-side flow pattern in the vicinity of the 4<sup>th</sup> burner row in the reformer is constructed from the reformer CFD data.<sup>64</sup> The outlets of the reformer are situated at the bottom right corner and are placed in the direction of the velocity vectors inside the flue-gas tunnels.

### 5.5.3 Valves and flow rate relation

Although the FSF distribution is used as the boundary condition of the high fidelity reformer CFD model and is chosen as the input of the data-driven model, it cannot be directly controlled and is not typically measured in industrial practice. Indeed, the FSF distribution is controlled by a system of flow regulators consisting of a finite number of flow control valves. Specifically, because the burners in the reformer are interconnected, a fractional amount of the FSF flow rate of the  $j^{th}$  burner can be redistributed to other units by partially closing the corresponding flow control valve. This suggests that the optimized FSF distribution can be produced by ap-

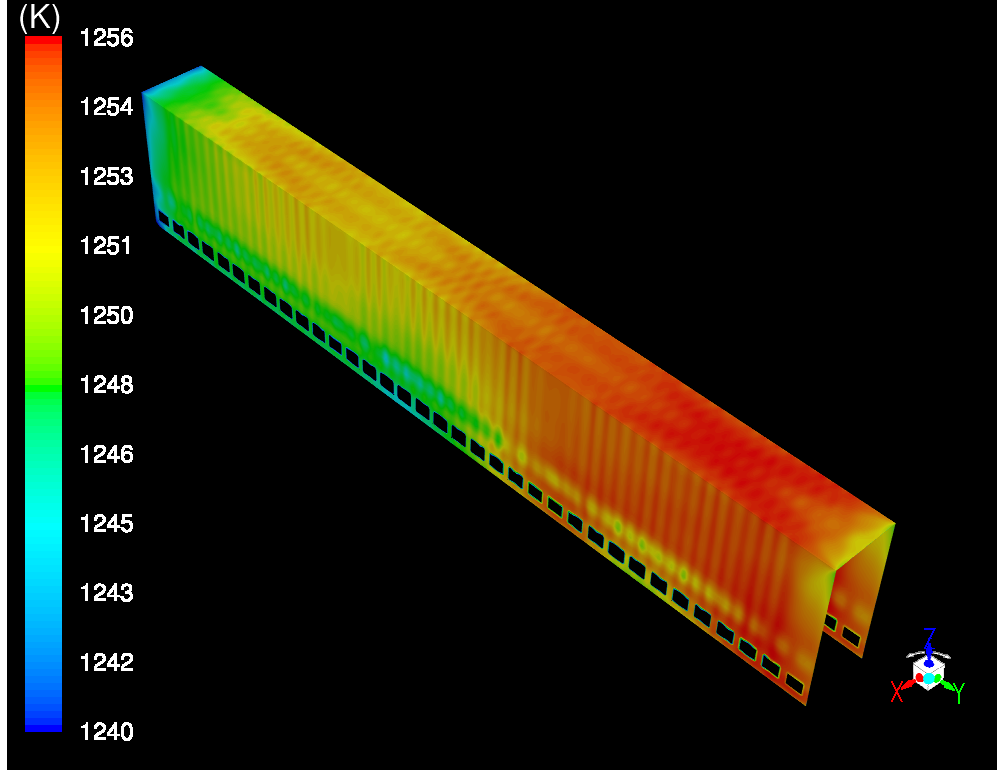


Figure 5.6: The temperature contour map of the 4<sup>th</sup> flue-gas tunnel, which is situated directly under the 4<sup>th</sup> burner row in the reformer, is shown. This contour map is created from the reformer CFD data in.<sup>64</sup> In Fig. 5.6, the outlets of the reformer are situated at the bottom right corner.

appropriately adjusting the percent open positions of all flow control valves in the flow regulator system, which is referred to as the valve position distribution. Hence, the merit of the high fidelity reformer CFD model and of the data-driven model for the furnace-balancing application, which aims to reduce the degree of the temperature nonuniformity in the combustion chamber and to increase the reformer thermal efficiency, is evident.

In an industrial setting of commercial-scale hydrogen production, it is unconventional for a furnace-side feed flow rate of a burner in the reformer to be individually regulated due to the sheer number of burners. In the present work, we assume that every set of two consecutive burners in a row of twelve burners is controlled by a flow control valve, and therefore, it is also reasonable to assume that the same FSF flow rate is delivered to these burners. Additionally, we assume that the FSF distribution is regulated by two distinct linear flow control valve models

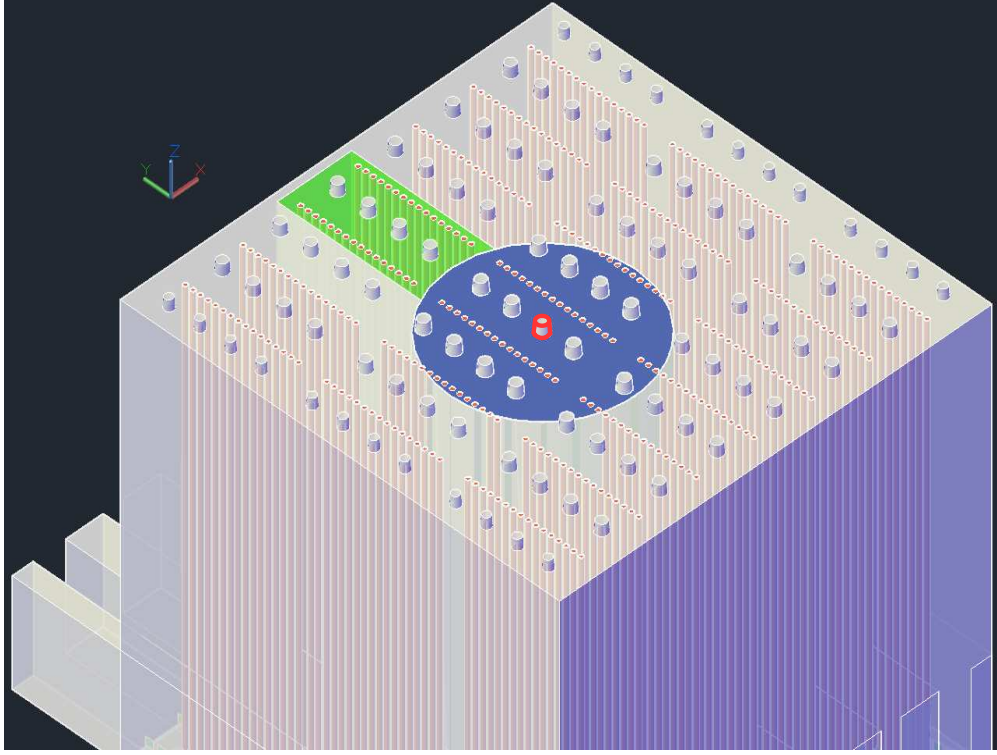


Figure 5.7: A representation of a burner heating zone which is created by the highlighted burner in red. The burner heating zones are displayed by a blue cylindrical volume (where the reforming tubes are heated via thermal radiation from the furnace-side flow) and a green rectangular volume (where the reforming tubes are heated via thermal radiation from the neighboring flue-gas tunnels). It is assumed that only the reforming tubes located within the burner heating zones have the outer wall temperature values dependent on the FSF flow rate of the burner.

with different maximum capacities. Among the flow control valve models, one valve model with a larger maximum capacity is used for the inner-lane burners, and the other valve model with a smaller maximum capacity is implemented in the outer-lane burners such that when valves are at the same opening position, the FSF flow rate of the outer-lane burners is 60% of that of the inner-lane burners. Based on the burner arrangement in the reformer and the capacity ratio of the inner-lane valve model and the outer-lane valve model, the valve-position-to-flow-rate converter is formulated as follows,

$$[F] = \delta \cdot [X] \cdot [Y] \cdot [V] \quad (5.5)$$

subject to

$$[V] \in \mathbb{R}^{48 \times 1} \quad (5.6a)$$

$$[X] \in \mathbb{R}^{96 \times 96} \quad (5.6b)$$

$$X_{ij} = 0.6; \quad i = j \text{ where } i \in [0, 11] \cup [84, 95]$$

$$X_{ij} = 1.0; \quad i = j \text{ where } i \in [12, 83]$$

$$X_{ij} = 0.0; \quad i \neq j$$

$$[Y] \in \mathbb{R}^{96 \times 48} \quad (5.6c)$$

$$Y_{ij} = 1.0; \quad i = 2j \cup i = 2j + 1 \text{ where } j \in [0, 47]$$

$$Y_{ij} = 0.0; \quad i \neq 2j \cap i \neq 2j + 1 \text{ where } j \in [0, 47]$$

$$[F] \in \mathbb{R}^{96 \times 1} \quad F_i \geq 0 \quad \forall i \in [0, 95] \quad (5.6d)$$

$$\delta = \frac{F_{tot}}{\|[X] \cdot [Y] \cdot [V]\|_1} \quad (5.6e)$$

where  $F_{tot}$  ( $\text{kg s}^{-1}$ ) is the total mass flow rate of the furnace-side feed to the reformer,  $\delta$  is the valve-to-flow-rate proportionality coefficient and is dependent on the valve position distribution,  $[F]$  is a vector of the FSF flow rate through each burner (the FSF distribution),  $[X]$  is a transformation matrix that identifies the types of the flow control valves (i.e., the inner-lane and outer-lane valves) in the reformer,  $[Y]$  is a transformation matrix that describes the burner arrangement in the reformer and  $[V]$  is a vector of valve positions (the valve position distribution). A characteristic of the valve-to-flow-rate converter is that an FSF distribution can be produced by different valve position distributions by changing the inlet pressure of the furnace-side feed to the reformer. To illustrate this idea, we utilize a fictitious simplified interconnected flow system which consists of four inner-lane burners and is supplied with the constant total FSF mass flow rate of  $4.0 \text{ (kg s}^{-1}\text{)}$ . When both flow control valves regulating the four inner-lane burners are at 100% open, the total FSF flow rate to the simplified interconnected flow

system is evenly distributed, i.e., the FSF flow rate to each inner-lane burner is expected to be  $1.0 \text{ (kg s}^{-1}\text{)}$ . When both flow control valves regulating the four inner-lane burners are 80% open, the FSF flow rate to each inner-lane burner is still required to be  $1.0 \text{ (kg s}^{-1}\text{)}$  to maintain the constant total FSF mass flow rate of  $4.0 \text{ (kg s}^{-1}\text{)}$  because of the two following reasons: the FSF flow rates of the two inner-lane flow control valves that are at the same valve position are equal, and the FSF flow rates of the two inner-lane burners that are regulated by a flow control valve are also assumed to be equal. The primary difference between the two case studies is in plant's efficiency, as the magnitude of the inlet pressure of the furnace-side feed to the reformer is expected to be higher in the second case study, which corresponds to a higher energy input to the compressor system leading to an increase in the operating cost of the reformer and a reduction in the plant's efficiency.

In the reformer, the flow control system has 48 flow control valves among which 36 valves are designated to regulate the FSF flow rates of the 72 inner-lane burners, and the valve position of each flow control valve must be adjusted to create the optimized FSF distribution. Therefore, the reformer thermal efficiency becomes susceptible to common valve-related problems (e.g., valve stickiness) as these disturbances prevent the valve position distribution that is designed to produce the optimized FSF distribution from being implemented. In this study, when a flow control valve is said to become defective, we assume that the flow control valve becomes stuck, and hence, the valve position cannot be adjusted, which prevents the furnace-side feed from being distributed according to the optimized distribution.

#### **5.5.4 Model-based furnace-balancing optimizer**

The third step of the furnace-balancing scheme (i.e., the model-based furnace-balancing optimizer) utilizes the data-driven model (Eq. 5.11b), the valve-position-to-flow-rate converter (Eq. 5.11a) to derive an optimized FSF distribution that aims to reduce the degree of nonuniformity in the OTWT distribution. The furnace-balancing optimizer is designed as a multivariable

optimization problem in which the decision variables are the positions of the properly functional flow control valves. Additionally, the furnace-balancing optimizer is designed to handle defective valves in the flow control system by adjusting the number of decision variables. For instance, if a flow control valve of the 0<sup>th</sup> and 1<sup>st</sup> outer-lane burners becomes defective, there are 47 functional valves in the flow control system, and therefore, the number of decision variables decreases from 48 (which corresponds to the total number of the flow control valves in the reformer) to 47. During the initialization of the furnace-balancing optimizer, a text file documenting the current status of the flow control valves is provided, based on which the furnace-balancing optimizer identifies the defective valve(s) and the corresponding stuck valve position(s) to determine the number of decision variables. The decision variables of the furnace-balancing optimizer are subjected to the practical constraint of the flow control valves (i.e., Eq. 5.11f, which is enforced to avoid extinguishing the flame) and the physical constraint of the flow control valves (i.e., Eq. 5.11e). In addition, we assume that the total furnace-side feed derived based on typical industrial data is kept constant at  $F_{tot}$  (i.e., Eq. 5.11c), when the optimized FSF distribution is computed. This strictly controlled operating window of the reformer allows the radial average temperature of the  $i^{th}$  reforming tube at a fixed distance away from the reforming tube inlet to be expressed as a linear combination of the FSF distribution as shown in Eq. 5.11b.

In the development of the furnace-balancing optimizer, careful considerations regarding the characteristic of the valve-to-flow-rate converter must be given. Specifically, the valve-to-flow-rate converter allows a FSF distribution to be produced by different valve position distributions between which the primary difference is in the plant's efficiency because the valve position distribution deviates further away from the default distribution (i.e., in which flow control valves are fully open) and thus requires a higher inlet pressure of the furnace-side feed to the reformer leading to a higher energy input to the compressor system, an increase in the operating cost of the reformer and a reduction in the plant's efficiency. In the present work, a quantitative assessment of the deviation of a valve position distribution ( $[V]$ ) from the default



distribution ( $[V]_0$ ) is computed as the 1-norm of the difference between  $[V]_0$  and  $[V]$ , i.e.,  $\|[V]_0 - [V]\|_1$ . Therefore, the furnace-balancing optimizer is designed to minimize the degree of nonuniformity in the OTWT distribution in a manner that requires the least duty of the compressor system to maximize the plant's efficiency and reformer service life by penalizing the weighted quadratic deviation of the outer wall temperature values of all reforming tubes from the set-point temperature ( $T_{AVE}$ ),

$$\sum_{k=0}^{335} w_k (T_{AVE} - T_k^{est})^2, \quad (5.7)$$

and also penalizing the deviation of the optimized valve position distribution ( $[V]$ ) from  $[V]_0$ ,

$$\|[V]_0 - [V]\|_1 = \sum_{i=0}^{47} (V_{i,max} - V_i). \quad (5.8)$$

The objective function of the furnace-balancing optimizer must signify that minimizing the degree of nonuniformity in the OTWT distribution has by far the highest priority and should not be compromised by the minor benefit of minimizing the duty of the compressor system. This idea is translated into mathematical expression of the penalty associated with the task of minimizing the compressor duty in the objective function of the furnace-balancing optimizer by normalizing the deviation of the optimized valve position distribution from  $[V]_0$ , which is subsequently scaled by multiplying with the product of the penalty associated with the task of minimizing the degree of nonuniformity in the OTWT distribution and a weighting factor ( $\gamma$ ),

$$\gamma \cdot \sum_{k=0}^{335} w_k (T_{AVE} - T_k^{est})^2 \cdot \frac{\sum_{i=0}^{47} (V_{i,max} - V_i)}{\sum_{i=0}^{47} (V_{i,max} - V_{i,min})}. \quad (5.9)$$

As a result, the objective function of the furnace-balancing optimizer is formulated as shown in Eq. 5.10, in which the first term represents the penalty associated with the task of minimizing

the degree of nonuniformity in the OTWT distribution, and the second term represents the penalty associated with the task of minimizing the compressor duty. The set-point temperature ( $T_{AVE}$ ) can be computed based on the OTWT distribution from any of the previous CFD data sets from the reformer CFD database as shown in Eq. 5.11d because the overall average outer wall temperature at the fixed distance away from the reforming tube inlets is expected to be constant despite the degree of nonuniformity in the OTWT distribution. Additionally, the initial guesses for the decision variables of the furnace-balancing optimizer are set to be 100% open (i.e., when the penalty on the control action is minimized) to allow the furnace-balancing optimizer to initially shift the focus on minimizing the degree of nonuniformity in the OTWT distribution and to avoid being stuck, which could happen when it is initially forced to accomplish both objectives simultaneously. The model-based furnace-balancing optimizer is formulated as follows,

$$\min_{\substack{V_j \in [60, 100] \\ j = \{0, \dots, 47\} \setminus V_{def}}} \sum_{k=0}^{335} w_k (T_{AVE} - T_k^{est})^2 + \gamma \sum_{k=0}^{335} w_k (T_{AVE} - T_k^{est})^2 \cdot \frac{\sum_{i=0}^{47} (V_{i,max} - V_i)}{\sum_{i=0}^{47} (V_{i,max} - V_{i,min})} \quad (5.10)$$

subject to

$$[F] = \delta \cdot [X] \cdot [Y] \cdot [V] \quad (5.11a)$$

$$T_k^{est} = \sum_{j=0}^{95} \alpha_{kj} F_j \quad \forall F_j \in [F] \quad (5.11b)$$

$$\sum_{j=0}^{95} F_j = F_{tot}, j = \{0, \dots, 95\} \quad (5.11c)$$

$$T_{AVE} = \frac{1}{336} \sum_{k=0}^{335} T_{k,m} \quad (5.11d)$$

$$V_{i,max} = 100\% \quad i = \{0, \dots, 47\} \quad (5.11e)$$

$$V_{i,min} = 60\% \quad i = \{0, \dots, 47\} \quad (5.11f)$$

$$V_{i,max} \leq V_{i,max} \leq V_{i,max} \quad i = \{0, \dots, 47\} \setminus V_{def} \quad (5.11g)$$

$$V_{i,def} \quad (5.11h)$$

where  $V_{def}$  is the set of indices of defective control valves,  $w_k$  is the weighting factor of the  $k^{th}$  reforming tube (which is used to compute the penalty associated with the deviation of the predicted outer wall temperature of the  $k^{th}$  reforming tube ( $T_k^{est}$ ) from  $T_{AVE}$ ),  $\gamma$  is the weighting factor of the penalty associated with the control action,  $V_i$  (the  $i^{th}$  component of  $[V]$ ) is the valve position of the  $i^{th}$  flow control valve (which regulates the FSF flow rates of the  $(2i)^{th}$  and  $(2i+1)^{th}$  burners) and  $F_j$  (the  $j^{th}$  component of  $[F]$ ) is the optimized FSF flow rate of the  $j^{th}$  burner. The idea of assigning the deviations of  $T_k^{est}$  from  $T_{AVE}$  of the reforming tubes different weights in the penalty associated with the degree of nonuniformity in the OTWT distribution is motivated by the fact that the local environments of the reforming tubes are not all identical, and specifically, the additional radiative heating provided for the reforming tubes from the neighboring flue-gas tunnels is expected to decrease with increasing distance away from the reformer outlets. Hence, we want to compensate for the nonuniform

additional radiative heating along the rows of 48 reforming tubes by giving the most weight to the offsets of the reforming tubes that are the furthest away from the reformer outlets (e.g., the 47<sup>th</sup> reforming tube). Specifically,  $w_k$  is designed to monotonically decrease with the position ( $p_k$ ) of the  $k^{th}$  reforming tube in a row of 48 reforming tubes as follows,

$$p_k = k - 48 \cdot \left\lfloor \frac{k}{48} \right\rfloor \quad k \in \{0, 1, \dots, 335\} \quad (5.12a)$$

$$w_k = w_k^{max} \cdot \exp[-\beta_w \cdot (47 - p_k)] \quad p_k \in \{0, 1, \dots, 47\} \quad (5.12b)$$

where  $\lfloor \cdot \rfloor$  represents the ‘floor’ operator, and  $w_k^{max}$  and  $\beta_w$  are the parameters of  $w_k$ . These weights, combined with the form of the heating zones for the data-driven model discussed in Sec. 5.5.2, allow the furnace-balancing optimizer to account to some extent for the reformer geometry, furnace-side flow pattern and its potential influence on the OTWT distribution. Therefore, the furnace-balancing optimizer is expected to realize that the burners situated near the refractory back wall might have long range effects on the outer wall temperature of the reforming tubes near the reformer outlets. As a result, the optimized FSF distribution is expected to lessen the degree of nonuniformity in the OTWT distributions along the reforming tubes and to reduce the overall maximum temperature of the outer reforming tube wall, which creates room for improving the thermal efficiency of the reformer. It is important to note that  $w_{k,1}^{max} = 10.0$ ,  $\beta_w = 0.05$  and  $\gamma = 0.1$  are determined based on a trial-and-error approach until the largest reduction in the degree of nonuniformity in the predicted OTWT distribution is observed.

### 5.5.5 Internal Balancing Workflow Convergence Criterion

The inner loop termination criteria determines the convergence of CFD computation. For each iteration in the inner loop, a scheme function is written to calculate the current temperature distribution standard deviation, and an average of standard deviation over 25 iterations serves

as the termination criteria. If the difference between three consecutive averaged standard deviations is under 0.2%, we consider an inner loop trial to be converged. Sometimes the change in temperature profile in the first couple hundred iterations might be small. To make sure that the new temperature profile would be sufficiently developed without accidentally triggering the termination criteria, we first let Fluent run 800 iterations without applying any termination detection mechanism. At the end of each inner loop convergence, an optimized furnace mass flow rate is returned as the input to the next inner loop iteration.

## 5.6 Results

In this section, we study the ability of our automated workflow to pull data pushed by industrial processes and autonomously execute a series of steps aimed at fulfilling SM objectives such as optimization of the process. In this case, we are balancing the temperature for our SMR process and comparing it with similar results to our previous user generated and supervised work on Tran *et al.*<sup>63</sup> The outputs of the optimization are in turn formatted appropriately in compliance with the user's requirements and pushed back to the historian for immediate usage.

In Fig. 5.8, we display the convergence criterion for one iteration of the internal balancing workflow going from trial 3 to 4. After meeting our initial criteria of running for 800 iterations, the percent difference of the standard deviation is tracked between iterations 800-875 while maintaining a threshold of lower than 0.2% change as specified in sec. 5.5 over a period of approximately  $\approx 30$  h.

The smart manufacturing workflow runs over 5 trials of the internal balancing workflow ( $Trial_0$ - $Trial_4$ ), starting from a typical burner distribution. Each time the temperature balancing workflow is terminated, the standard deviation of the last reading is compared to the standard deviation of the previous trial Fig. 5.9. The exit criterion stipulated in sec. 5.4 as shown in Fig. 5.9 going from inner-loop trial 3 to trial 4. The decrease in standard deviation



Figure 5.8: Evolution of the OTWT standard deviation at 6.5 m from the top and its percent change going from trial 3 to 4.

of the average temperature of the OTWT measured at 6.5m from the tube entrance between  $Trial_0$  and  $Trial_4$  is 42%.

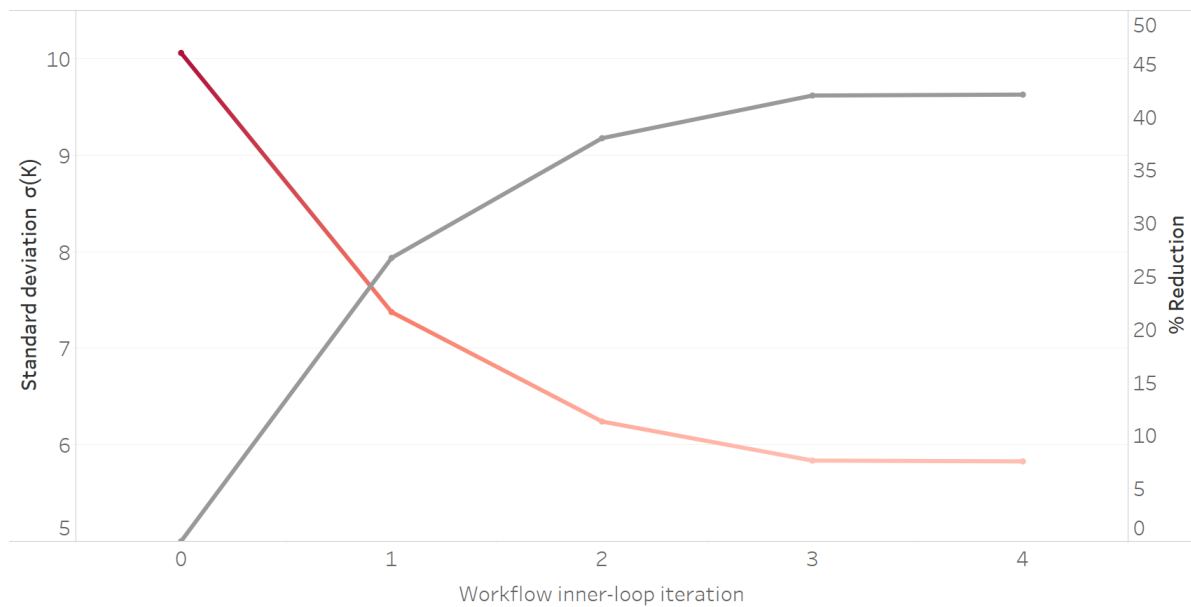


Figure 5.9: Standard deviation (red-gold) and percent reduction of the standard deviation (grey) during the internal balancing workflow execution.

Our automated approach has generated similar tube temperature distribution as the human-supervised method in Tran *et al.*<sup>63</sup> In Figure 5.10, the estimated temperature derived from the data-driven model is compared with the temperature calculated from the CFD model. Figure 5.11 shows the heat map of the temperature distribution inside the furnace and the evolution over different trials to a more uniform temperature. As we can see, the temperature trend matches closely with the result by Tran *et al.*<sup>63</sup> The minimal tube temperature is greatly improved through the trials, which contributes to the smaller standard deviation and the reduction of cold spot. As approaching the end of iteration, the difference between estimated and simulation result is below 1%. Figure 5.9 shows the development of standard deviation of the OTWT over the five furnace balancing iterations. In our simulation, the standard deviation of tube temperature distribution stabilized at 5.83, which is higher than in,<sup>63</sup> which has a final standard deviation of 4.7. The different ways of exporting temperature data accounts for this discrepancy. Since we used the iso-surface method to capture the OTWT that performs a surface integration of the mesh grid, it would be an accurate representation of the temperature at the very surface of the reforming tube. However, in,<sup>63</sup> the post-processing method would perform an average over a range of data points near the tube surface. Statistically, an averaged data set would have a lower standard deviation than the original data set even if intrinsically they represent the same result. The iso-surface method should be preferred as it shows the actual temperature of the reforming tube, thereby reducing the possibility of potential hot/cold spot omission. Our result is further confirmed to match<sup>63</sup> data when we exported the temperature using the post-processing method.

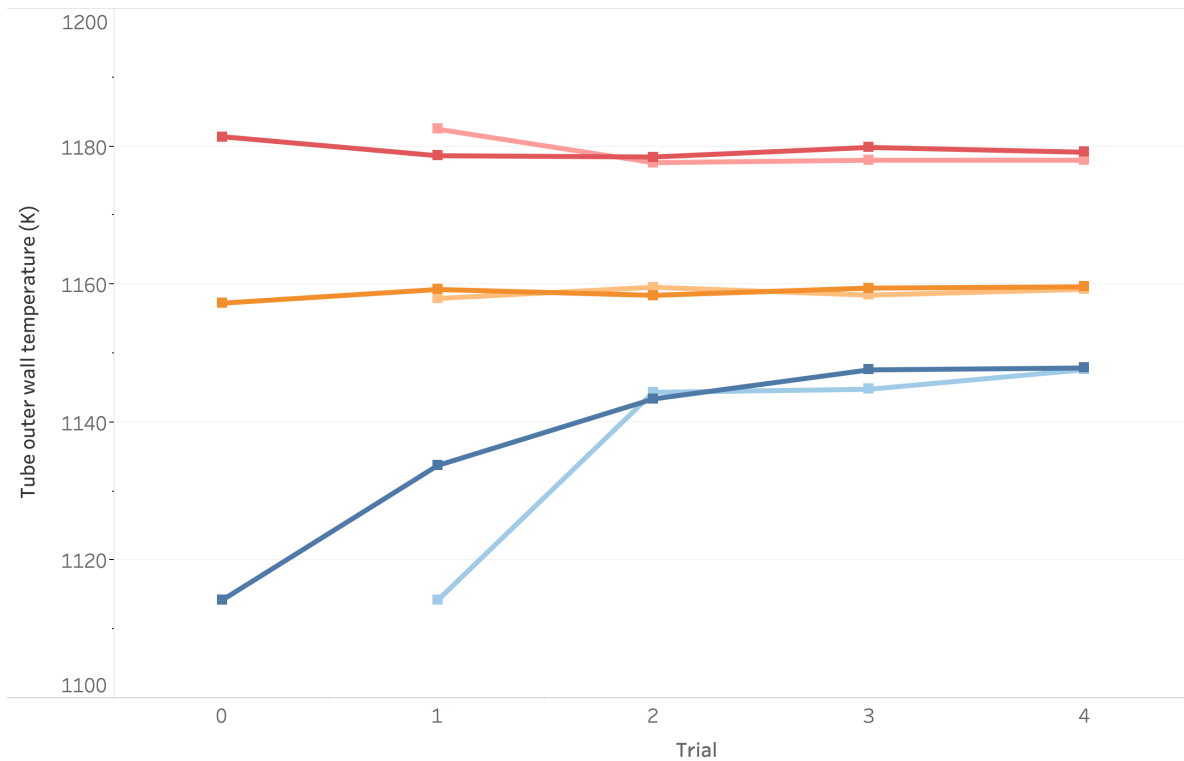


Figure 5.10: Tube outer tube wall temperature measured at the end of trials at a distance of 6.5 m away from the reforming tube inlets. The dark shade represent data obtained from the CFD simulations and the light shade the furnace-balancing scheme. The maximum, average and minimum temperature of the OTWT are represented in red, orange and blue respectively.



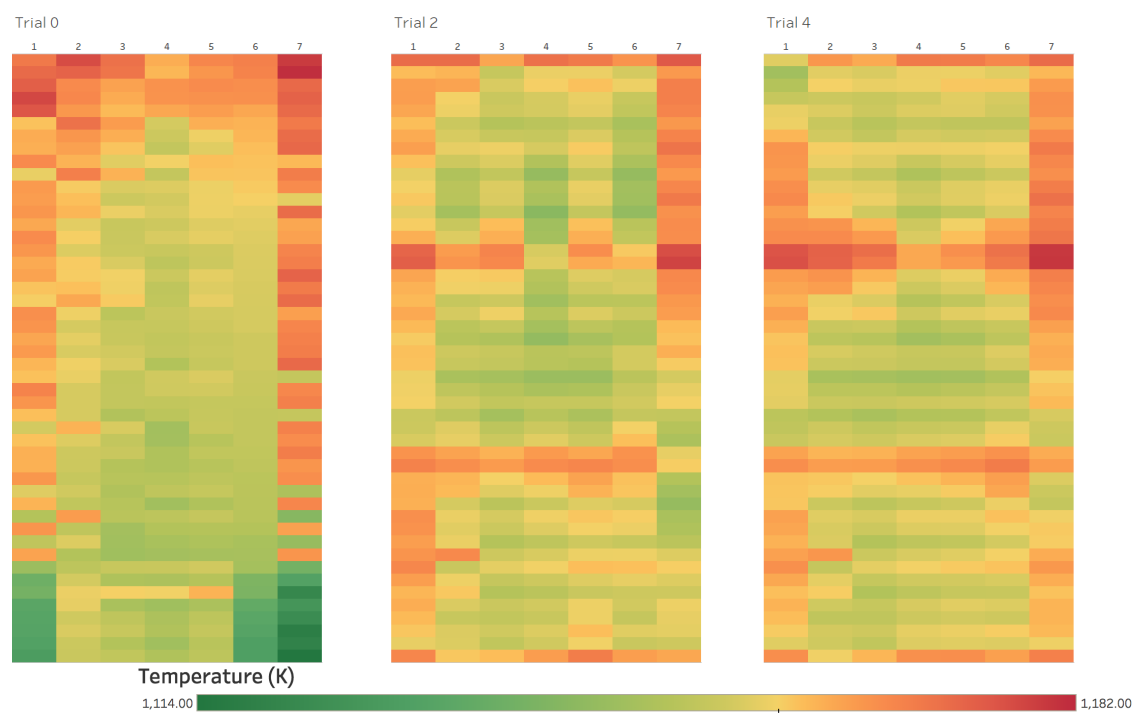


Figure 5.11: Temperature distribution inside the furnace for the OTWT.

## 5.7 Conclusion

In this chapter, we replicated the result from<sup>63</sup> CFD model of the steam methane reforming furnace balancing using an automated workflow, which enabled us to perform the furnace balancing trials without active human involvement. This workflow involves Kepler workflow interface and the Fluent Scheme/UDF programming. Upon successful implementation, our workflow was able to take an input of percentage valve opening for burner fuel provided by the plant, and goes through CFD calculation and furnace balancing optimization routine to find the optimal percentage valve opening for the operation automatically. Our results showed that, after five furnace balancing trials, we were able to obtain a stable reformer tube temperature distribution, which has a standard deviation of 5.8. Different ways of exporting tube temperatures from Fluent justifies the small difference between our result and,<sup>63</sup> which has a standard deviation of 4.7. Simulation details show high correspondence with previous manual studies. Within each trial, the termination criteria was satisfied where the difference of averaged standard deviation over 100 CFD iterations is controlled to be below 0.5%. Similarly, between trials, convergence is determined by a difference of standard deviation below 3.0% for two consecutive trials. For the entire simulation starting from a typical temperature distribution, approximately 30 hours were required for the simulation and optimization to achieve convergence, and by adopting shared objects in the optimization programming, only 0.06% of the entire time was used for valve percentage opening optimization. Therefore, a future suggestion for study in this process would be the speed-up of the CFD calculation, and one possible way would be the smart-determination of variable numerical computation parameters, which could be readily implemented by the Fluent Scheme.

## Chapter 6

### Conclusion

This dissertation developed Computational Fluid Dynamics models for steam methane reforming reactors and furnaces and a framework for developing an automated workflow of a testbed for the Smart Manufacturing Platform. Chapter 2 developed a detailed CFD model of a single industrial scale two-dimensional axisymmetric steam methane reforming reactor (tube). The CFD model results matched closely with industrial data and demonstrated its application for control design for the reactor. Chapter 3 developed a model that allowed for simultaneous chemical reactions and transport phenomena in different computational domains while producing results consistent with available plant data from literature and the model from Chapter 2. This model showed its ability to be utilized for parametric studies of a steam methane reforming furnace using a CFD model. Chapter 4 developed a CFD model for an industrial scale steam methane reformer furnace which captured the physical dimensions, transport phenomena, and core components of a reformer utilized in an industrial plant. The reformer CFD model can be considered an adequate representation of the on-line reformer after thorough comparison with industrial plant data for consistent operating conditions; therefore, it was used as a tool for operational conditions studies. Finally, Chapter 5 compiled all the knowledge and experience gained from the design and implementation of the previous chapters to

accomplish our objective to design a workflow for automated model implementation and operation condition determination on the SM platform. The workflow was designed to be executed without the need for an expert user, to be deployed in a cloud environment and to be fully or partially used.

# Bibliography

- [1] T. A. Adams and P. I. Barton. A dynamic two-dimensional heterogeneous model for water gas shift reactors. *International Journal of Hydrogen Energy*, 34(21):8877–8891, 2009.
- [2] N. Aeronautics and S. Administration. NASA's viscous grid spacing calculator. <http://geolab.larc.nasa.gov/APPS/YPlus/>, 2015.
- [3] A. Aguirre, A. Tran, L. Lao, H. Durand, M. Crose, and P. D. Christofides. CFD modeling of a pilot-scale steam methane reforming furnace. In *Advances in Energy Systems Engineering*, pages 75–117. Springer, 2017.
- [4] H. Amirshaghaghi, A. Zamaniyan, H. Ebrahimi, and M. Zarkesh. Numerical simulation of methane partial oxidation in the burner and combustion chamber of autothermal reformer. *Applied Mathematical Modelling*, 34:2312–2322, 2010.
- [5] M. Baburić, N. Duić, A. Raulot, and P. J. Coelho. Application of the conservative discrete transfer radiation method to a furnace with complex geometry. *Numerical Heat Transfer, Part A: Applications*, 48:297–313, 2005.
- [6] S. P. M. Bane, J. L. Ziegler, and J. E. Shepherd. Development of one-step chemistry models for flame and ignition simulations. Technical report, GALCIT Report GALCITFM:2010.002, Mar. 2010.
- [7] M. Batdorf, L. A. Freitag, and C. Ollivier-Gooch. Computational study of the effect of unstructured mesh quality on solution efficiency. In *Proceedings of the 13th AIAA Computational Fluid Dynamics Conference*, Snowmass, CO, 1997.
- [8] N. Behnam, A. G. Dixon, P. M. Wright, M. Nijemeisland, and E. H. Stitt. Comparison of CFD simulations to experiment under methane steam reforming reacting conditions. *Chemical Engineering Journal*, 207-208:690–700, 2012.
- [9] F. Beyer, J. Brightling, P. Farnell, and C. Foster. Steam reforming - 50 years of development and the challenges for the next 50 years. In *AIChE 50th Annual Safety in Ammonia Plants and Related Facilities Symposium*, Toronto, Canada, Sept. 2005.
- [10] H. P. A. Calis, J. Nijenhuis, B. C. Paikert, F. M. Dautzenberg, and C. M. van den Bleek. CFD modelling and experimental validation of pressure drop and flow profile in a novel structured catalytic reactor packing. *Chemical Engineering Science*, 56:1713–1720, 2001.

- [11] J. Davis, T. Edgar, R. Graybill, P. Korambath, B. Schott, D. Swink, J. Wang, and J. Wetzel. Smart manufacturing. *Annual Review of Chemical and Biomolecular Engineering*, 6(1):141–160, 2015. PMID: 25898070.
- [12] J. Davis, T. Edgar, J. Porter, J. Bernaden, and M. Sarli. Smart manufacturing, manufacturing intelligence and demand-dynamic performance. *Computers & Chemical Engineering*, 47:145–156, 2012.
- [13] J. R. Davis. *Alloy Digest Sourcebook: Stainless Steels (Alloy Digest)*. ASM International, Materials Park, OH, 2000.
- [14] H. I. de Lasa, G. Dogü, and A. Ravella, editors. *Chemical Reactor Technology for Environmentally Safe Reactors and Products*, volume 225 of *NATO ASI Series*. Springer Science & Business Media, Dordrecht, The Netherlands, 1992.
- [15] A. G. Dixon. CFD study of effect of inclination angle on transport and reaction in hollow cylinder catalysts. *Chemical Engineering Research and Design*, 92:1279–1295, 2014.
- [16] R. Duan, W. Liu, L. Xu, Y. Huang, X. Shen, C.-H. Lin, J. Liu, Q. Chen, and B. Sasanapuri. Mesh type and number for the CFD simulations of air distribution in an aircraft cabin. *Numerical Heat Transfer, Part B: Fundamentals*, 67:489–506, 2015.
- [17] I. Dybkjaer. Tubular reforming and autothermal reforming of natural gas - an overview of available processes. *Fuel Processing Technology*, 42:85–107, 1995.
- [18] S. Ergun and A. A. Orning. Fluid flow through randomly packed columns and fluidized beds. *Industrial & Engineering Chemistry*, 41:1179–1184, 1949.
- [19] B. Ewan and R. Allen. A figure of merit assessment of the routes to hydrogen. *International Journal of Hydrogen Energy*, 30(8):809 – 819, 2005.
- [20] D. P. FerreiraAparicio, M. J. Benito, and J. L. Sanz. New trends in reforming technologies: from hydrogen industrial plants to multifuel microreformers. *Catalysis Reviews*, 47(4):491–588, 2005.
- [21] G. F. Froment and K. B. Bischoff. *Chemical Reactor Analysis and Design*. Wiley, New York, 1990.
- [22] P. Grun. Introduction to infiniband for end users. Technical report, Infiniband Trade Association, 2010.
- [23] A. Guardo, M. Coussirat, M. A. Larrayoz, F. Recasens, and E. Egusquiza. CFD flow and heat transfer in nonregular packings for fixed bed equipment design. *Industrial & Engineering Chemistry Research*, 43:7049–7056, 2004.
- [24] Y. Han, R. Xiao, and M. Zhang. Combustion and pyrolysis reactions in a naphtha cracking furnace. *Chemical Engineering & Technology*, 30:112–120, 2006.
- [25] IBM. CPLEX:high-performance mathematical programming solver for linear programming, mixed integer programming, and quadratic programming, 2017.
- [26] A. Inc. *ANSYS Fluent Theory Guide 15.0*, Nov. 2013.

- [27] A. Inc. *ANSYS Fluent UDF Manual 15.0*, Nov. 2013.
- [28] A. Inc. *ANSYS Fluent User's Guide 15.0*, Nov. 2013.
- [29] D. S. Jones and P. P. Pujadó. *Handbook of petroleum processing*. Springer Science & Business Media, 2006.
- [30] W. P. Jones and B. E. Launder. The prediction of laminarization with a two-equation model of turbulence. *International Journal of Heat and Mass Transfer*, 15:301–314, 1972.
- [31] Kepler-project. Documentation - kepler, 2017. [Online; accessed 07/12/2017] <https://kepler-project.org/users/documentation>.
- [32] P. Korambath, J. Wang, A. Kumar, R. Graybill, B. Schott, M. Baldea, and J. Davis. A smart manufacturing use case: Furnace temperature balancing in steam methane reforming process via kepler workflows. *Procedia Computer Science*, 80:680–689, 2016.
- [33] P. Korambath, J. Wang, A. Kumar, L. Hochstein, B. Schott, R. Graybill, M. Baldea, and J. Davis. Deploying kepler workflows as services on a cloud infrastructure for smart manufacturing. *Procedia Computer Science*, 29:2254, 2014.
- [34] J. I. Kroschwitz and M. Howe-Grant, editors. *Kirk-Othmer Encyclopedia of Chemical Technology*. John Wiley and Sons Inc., New York, NY, 1999.
- [35] A. Kumar, M. Baldea, T. F. Edgar, and O. A. Ezekoye. Smart manufacturing approach for efficient operation of industrial steam-methane reformers. *Industrial & Engineering Chemistry Research*, 54:4360 – 4370, 2015.
- [36] M. Kuroki, S. Ookawara, and K. Ogawa. A high-fidelity CFD model of methane steam reforming in a packed bed reactor. *Journal of Chemical Engineering of Japan*, 42:S73–S78, 2009.
- [37] L. Lao, A. Aguirre, A. Tran, Z. Wu, H. Durand, and P. D. Christofides. CFD modeling and control of a steam methane reforming reactor. *Chemical Engineering Science*, 148:78–92, 2016.
- [38] D. Latham. *Masters Thesis: Mathematical Modeling of An Industrial Steam Methane Reformer*. Queen's University, 2008.
- [39] D. A. Latham, K. B. McAuley, B. A. Peppley, and T. M. Raybold. Mathematical modeling of an industrial steam-methane reformer for on-line deployment. *Fuel Processing Technology*, 92(8):1574–1586, 2011.
- [40] B. E. Launder and B. I. Sharma. Application of the energy dissipation model of turbulence to the calculation of flow near a spinning disc. *Letters in Heat and Mass Transfer*, 1:131–138, 1974.
- [41] J. S. Lee, J. Seo, H. Y. Kim, J. T. Chung, and S. S. Yoon. Effects of combustion parameters on reforming performance of a steam methane reformer. *Fuel*, 111:461 – 471, 2013.

- [42] Y.-T. Luan, Y.-P. Chyou, and T. Wang. Numerical analysis of gasification performance via finite-rate model in a cross-type two-stage gasifier. *International Journal of Heat and Mass Transfer*, 57:558–566, 2013.
- [43] B. F. Magnussen. The eddy dissipation concept: A bridge between science and technology. In *ECCOMAS Thematic Conference on Computational Combustion*, Lisbon, Portugal, 2005.
- [44] B. F. Magnussen and B. H. Hjertager. On mathematical modeling of turbulent combustion with special emphasis on soot formation and combustion. In *Symposium (International) on Combustion*, volume 16, pages 719–729. Elsevier, 1977.
- [45] A. Maximov. *Thesis for the Degree of Doctor of Science: Theoretical Analysis and Numerical Simulation of Spectral Radiative Properties of Combustion Gases in Oxy/air-fired Combustion Systems*. Lappeenranta University of Technology, 2012.
- [46] C. McGreavy and M. W. Newmann. Development of a mathematical model of a steam methane reformer. In *Institution of Electrical Engineering, Conference on the Industrial Applications of Dynamic Modelling*, Durham, NC, Sept. 1969.
- [47] S. C. Mishra and M. Prasad. Radiative heat transfer in participating media—A review. *Sadhana*, 23(2):213–232, 1998.
- [48] E. M. Mokheimer, M. I. Hussain, S. Ahmed, M. A. Habib, and A. A. Al-Qutub. On the modeling of steam methane reforming. *Journal of Energy Resources Technology*, page 012001, 2015.
- [49] D. G. Nicol. *Ph. D. Thesis: A Chemical Kinetic and Numerical Study of NO<sub>x</sub> and Pollutant Formation in Low-emission Combustion*. University of Washington, 1995.
- [50] M. M. Noor, P. W. Andrew, and T. Yusaf. Detail guide for CFD on the simulation of biogas combustion in bluff-body mild burner. In *International Conference on Mechanical Engineering Research*, Kuantan, Malaysia, Jul. 2013.
- [51] A. Olivieri and F. Vegliò. Process simulation of natural gas steam reforming: Fuel distribution optimisation in the furnace. *Fuel Processing Technology*, 89:622–632, 2008.
- [52] OSIsoft. Pi system, 2017. <http://www.osisoft.com/pi-system/> [Online, accessed July 20, 2017 ].
- [53] Panasas. Panasas activestor turbocharges ansys fluent in hpc. Technical report, Panasas, Inc, 2013.
- [54] G. Pantoleontos, E. S. Kikkinides, and M. C. Georgiadis. A heterogeneous dynamic model for the simulation and optimisation of the steam methane reforming reactor. *International Journal of Hydrogen Energy*, 37:16346–16358, 2012.
- [55] M. N. Pedernera, J. Piña, D. O. Borio, and V. Bucalá. Use of a heterogeneous two-dimensional model to improve the primary steam reformer performance. *Chemical Engineering Journal*, 94(1):29–40, 2003.
- [56] K. P. R. and V. P. *Stochastic systems: estimation, identification and adaptive control*. Prentice-Hall, Inc., Upper Saddle River, NJ, 1986.



- [57] A. Rogers and K. Steiglitz. Maximum likelihood estimation of rational transfer function parameters. *IEEE Transactions on Automatic Control*, 12:594–597, 1967.
- [58] J. R. Rostrup-Nielsen. Catalytic steam reforming. In *Catalysis*, pages 1–117. Springer, 1984.
- [59] J. R. Rostrup-Nielsen and T. Rostrup-Nielsen. Large-scale hydrogen production. *Cattech*, 6:150–159, 2002.
- [60] P. Sadooghi and R. Rauch. Pseudo heterogeneous modeling of catalytic methane steam reforming process in a fixed bed reactor. *Journal of Natural Gas Science and Engineering*, 11:46–51, 2013.
- [61] Y.-S. Seo, D.-J. Seo, Y.-T. Seo, and W.-L. Yoon. Investigation of the characteristics of a compact steam reformer integrated with a water-gas shift reactor. *Journal of Power Sources*, 161:1208–1216, 2006.
- [62] G. D. Stefanidis, B. Merci, G. J. Heynderickx, and G. B. Marin. CFD simulations of steam cracking furnaces using detailed combustion mechanisms. *Computers & Chemical Engineering*, 30:635–649, 2006.
- [63] A. Tran, A. Aguirre, M. Crose, H. Durand, and P. D. Christofides. Temperature balancing in steam methane reforming furnace via an integrated CFD/data-based optimization approach. *Computers & Chemical Engineering*, 104:185–200, 2017.
- [64] A. Tran, A. Aguirre, H. Durand, M. Crose, and P. D. Christofides. CFD modeling of a industrial-scale steam methane reforming furnace. *Chemical Engineering Science*, 171:576–598, 2017.
- [65] S. R. Turns. *An Introduction to Combustion: Concepts and Applications*. McGraw-Hill, Boston, MA, 1996.
- [66] N. R. Udengaard. Hydrogen production by steam reforming of hydrocarbons. *Preprint Papers-American Chemical Society, Division of Fuel Chemistry*, 49:906–907, 2004.
- [67] I. Uriz. Computational fluid dynamics as a tool for designing hydrogen energy technologies. In L. M. Gandía, G. Arzamendi, and P. M. Diéguez, editors, *Renewable Hydrogen Technologies: Production, Purification, Storage, Applications and Safety*, pages 401–435. Elsevier, Oxford, UK, 2013.
- [68] R. Vuthaluru and H. Vuthaluru. Modelling of a wall fired furnace for different operating conditions using FLUENT. *Fuel Processing Technology*, 87(7):633–639, 2006.
- [69] M. H. Wesenberg and H. F. Svendsen. Mass and heat transfer limitations in a heterogeneous model of a gas-heated steam reformer. *Industrial & Engineering Chemistry Research*, 46:667–676, 2007.
- [70] J. Xu and G. F. Froment. Methane steam reforming, methanation and water-gas shift: I. intrinsic kinetics. *AIChE journal*, 35(1):88–96, 1989.

- [71] A. Zamaniyan, A. Behroozsarand, and H. Ebrahimi. Modeling and simulation of large scale hydrogen production. *Journal of Natural Gas Science and Engineering*, 2:293–301, 2010.
- [72] A. Zamaniyan, H. Ebrahimi, and J. S. S. Mohammadzadeh. A unified model for top fired methane steam reformers using three-dimensional zonal analysis. *Chemical Engineering and Processing: Process Intensification*, 47(5):946–956, 2008.
- [73] J. Zhang, B. Dai, Y. Meng, X. Wu, J. Zhang, X. Zhang, Y. Ninomiya, Z. Zhang, and L. Zhang. Pilot-scale experimental and cfd modeling investigations of oxy-fuel combustion of victorian brown coal. *Fuel*, 144:111–120, 2015.